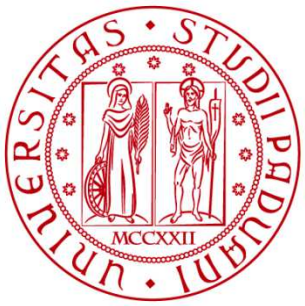

UNIVERSITÀ DEGLI STUDI DI PADOVA

Sede Amministrativa: Università degli Studi di Padova

DIPARTIMENTO DI GEOSCIENZE

SCUOLA DI DOTTORATO DI RICERCA

IN SCIENZE DELLA TERRA

CICLO XXIV

CHARACTERIZATION STUDIES ON CEMENT CONGLOMERATES FROM HISTORIC REINFORCED CONCRETE STRUCTURES

Direttore della Scuola: Ch.mo Prof. Gilberto Artioli

Supervisori: Ch.mo Prof. Gilberto Artioli, Ch.mo Prof. Claudio Mazzoli

Dottorando: Michele Secco

ABSTRACT

Patented by Joseph Monier in 1867, reinforced concrete became a highly successful material during the 20th century, capable of satisfying the most challenging demands of designers and engineers. However, even though its introduction in construction paved the way for a century of continuous technological innovation in the building industry, the mechanical behaviour of structures made with this material has not been fully understood for a long time, giving rise to a variety of structural problems of the buildings built in the first decades of the 20th century. At the roots of the problem there was not only the empirical conception of the structural calculations, but also the lack of development of standard concrete production technology and the poor attention paid to the choice of raw materials and their mixing methodology. Furthermore, the problem of reinforced concrete behavior to external chemical-physical degrading agents was not considered during most of the 20th century, due to the wrong assumption of "infinite durability" of this material.

One and a half century after its invention, reinforced concrete is considered a cultural heritage material, being the structural core of the 20th century contemporary architecture. The characterization of this heterogeneous artifact has been for decades exclusive competence of structural engineers, but, over the last fifteen years, it has become one of the main fields of study of material scientists, due to its mineralogical, textural and chemical complexity and high susceptibility to the action of external chemical-physical degrading agents.

Given the complexity of the material, a combined multidisciplinary approach, covering the engineering and material science fields, is necessary to obtain a full mechanical and microstructural characterization of reinforced concrete structures and, consequently, to plan and perform proper interventions with adequate restoration materials for the rehabilitation and structural improvement of this modern heritage.

This research project is aimed at the multi-analytical characterization of cement conglomerates from five historical structures located in north-eastern Italy and built between the end of the 19th and the middle of the 20th century, paying attention to the

determination of the original mix designs, to the study of their conservation state and to the development of novel medium invasive analytical techniques.

The materials were first of all characterized according to a multi-analytical approach; in this part of the study, the classic petrographic characterization of the conglomerates following the guidelines of the American standard ASTM C856 was deeply integrated with the results obtained from mineralogical analyses by X-ray Powder Diffraction (XRPD) and from microstructural-microchemical analyses by Scanning Electron Microscopy and Energy-dispersive X-ray Microfluorescence (SEM-EDS). This integrated methodology of analysis allowed to broaden the spectrum of the analytical results obtained, fully characterizing the materials and their constituents in a broad dimensional, compositional and textural range.

The data obtained, even though highly accurate, are still strictly qualitative, in particular as regards the determination of several parameters, fundamental for the reconstruction of the original mix designs (e.g. water/cement ratio, cement/aggregate ratio, granulometric distribution curve of the inert fraction). In this respect, several recent studies tested 2D digital image analysis procedures for the study of several concrete components, obtaining reliable and unbiased results. Nevertheless, despite the promising data obtained, the analytical procedures were never applied to the whole concrete constituents, mainly due to intrinsic limitations of the technique related both to the high polydispersity of the constituents and to the absence of clear colorimetric tracers to allow rapid and clear digital discriminations. Despite these problems, at the state of the art 2D digital image analysis is the only analytical technique theoretically capable of giving reliable, rapid and unbiased results on a such polydisperse material. Consequently, one of the main objectives of this research project consisted in the development of a valid and multiscale protocol of sample preparation, image acquisition, and analysis, in order to fully and quantitatively reconstruct mix designs of the studied historical concretes. The novel approach proved to be extremely reliable to fully characterize these heterogeneous and poorly standardized materials, and the analytical results obtained were successfully crosschecked with the ones obtained with the multi-analytical study.

Finally, an accurate study of the conservation state and degradation phenomena acting on the materials was performed. The materials were studied according to a multi-analytical approach articulated in a preliminary petrographic study, integrated by profile XRPD analyses on the finer fractions of the materials and SEM-EDS analyses both on massive

and thin section samples. The results highlighted the incidence of several alteration phenomena on the materials, strictly related to their compositional and textural characteristics and to the environmental conditions of exposure. Besides the identification of the occurrence of common forms of concrete alteration - namely carbonation, sulfate attack, chloride attack, alkali-aggregate reactions and soluble salts crystallization phenomena – a novel type of degradation was observed and described for the first time in the concrete samples of the Ex-Agrimont Area, the synergic sulfate-phosphate attack. This form of alteration was thoroughly investigated through an extended profile multi-analytical approach consisting of a combination of optical microscopy, synchrotron-based micro-XRPD, SEM-EDS microanalyses, *in situ* thermal XRPD, simultaneous thermogravimetric and differential thermal analyses (TGA-DTA), inductively coupled plasma atomic emission spectroscopy (ICP-OES) and thermodynamic modeling. This form of alteration resulted to be strongly related to the interaction between sulfate-rich atmospheric multipollutants and phosphate-ammonia-rich solutions leached from the fertilizers production plant, and caused severe decalcification of the cement matrices and formation of secondary sulfates and phosphates according to a marked mineralogical and textural zoning, with stabilization of metastable phases thanks to the peculiar pH and concentration gradients developed in the materials. Furthermore, rare solid solution phases formed, undergoing partial dehydration phenomena related to the conditions of exposure.

RIASSUNTO

Brevettato da Joseph Monier nel 1867, il conglomerato cementizio armato (comunemente definito calcestruzzo armato, o cemento armato) è diventato un materiale da costruzione di grandissimo successo nel corso del XX secolo, capace di soddisfare le richieste più impegnative di progettisti e ingegneri. Tuttavia, nonostante la sua introduzione e diffusione abbia spianato la strada a un secolo di continue innovazioni tecnologiche nell'ambito dell'industria delle costruzioni, il comportamento meccanico degli edifici costruiti con tale materiale non è stato compreso a pieno per lungo tempo, con conseguente incidenza di una serie di problemi strutturali interessanti gli edifici costruiti nei primi decenni del XX secolo. Alle radici del problema non vi era soltanto la concezione empirica dei calcoli strutturali, ma anche la mancanza di una tecnologia standardizzata di produzione del calcestruzzo e la scarsa attenzione posta nella scelta delle materie prime e delle strategie di miscelazione. Inoltre, le problematiche relative alla resistenza del conglomerato cementizio armato all'azione degradante di agenti chimico-fisici esterni non sono state considerate per gran parte del XX secolo, a causa dell'errata assunzione di "durabilità infinita" del materiale.

Un secolo e mezzo dopo la sua invenzione, il cemento armato è al giorno d'oggi considerato un materiale di interesse culturale, costituendo il nucleo strutturale dell'architettura contemporanea. La caratterizzazione di questo materiale eterogeneo è stata per decenni di competenza esclusiva degli ingegneri strutturali, ma, nel corso degli ultimi quindici anni, è diventata una delle principali tematiche di studio degli scienziati dei materiali, a causa della complessità mineralogica, tessiturale e chimica del calcestruzzo e della sua suscettibilità all'azione di agenti alterativi esterni di natura chimico-fisica.

Considerata la complessità del materiale, un approccio analitico combinato e multidisciplinare, comprendente campi sia ingegneristici sia della scienza dei materiali, risulta necessario al fine di ottenere una completa caratterizzazione meccanica e microstrutturale delle strutture in cemento armato e, conseguentemente, di progettare ed eseguire interventi di restauro con materiali adeguati per la riabilitazione e il miglioramento strutturale di questi moderni beni culturali.

Tale progetto di ricerca è stato volto alla caratterizzazione multi-analitica di conglomerati cementizi appartenenti a cinque edifici storici in cemento armato, tutti localizzati nell'Italia nordorientale e costruiti tra la fine del XIX secolo e la metà del XX secolo, prestando particolare attenzione alla determinazione dei mix design originari, allo studio del loro stato di conservazione e allo sviluppo di tecniche analitiche innovative di natura mediamente distruttiva.

I materiali sono stati anzitutto caratterizzati tramite un approccio multi-analitico; in questa parte dello studio, la classica caratterizzazione petrografica dei conglomerati secondo le linee guida dello standard americano ASTM C856 è stata integrata con i risultati ottenuti tramite analisi mineralogiche in diffrazione ai raggi X delle polveri (XRPD) e analisi microstrutturali e microchimiche in microscopia elettronica a scansione e microfluorescenza ai raggi X a dispersione di energia (SEM-EDS). La metodologia analitica integrata ha permesso un notevole allargamento dello spettro dei risultati ottenuti, consentendo una caratterizzazione completa dei materiali e dei loro costituenti in un ampio intervallo dimensionale, composizionale e tessiturale.

I risultati ottenuti, sebbene altamente accurati, sono strettamente qualitativi, in particolare per quanto concerne la determinazione di una serie di parametri fondamentali per la ricostruzione dei mix design originari (quali i rapporti acqua/cemento e cemento/aggregato e la curva di distribuzione granulometrica degli inerti). A tal riguardo, diversi studi hanno recentemente testato procedure di analisi di immagine 2D per lo studio di componenti del calcestruzzo indurito, ottenendo risultati affidabili e oggettivi. Ciononostante, tali procedure analitiche non sono mai state applicate al sistema calcestruzzo nel suo insieme, a causa di limitazioni intrinseche delle tecniche di studio legate sia all'alto grado di polidispersione delle componenti del conglomerato cementizio, sia all'assenza di chiari traccianti colorimetrici in grado di consentire una rapida e chiara discriminazione digitale delle stesse. Al di là di tali problematiche, allo stato dell'arte l'analisi di immagine 2D risulta essere l'unica tecnica analitica in grado, almeno in via teorica, di fornire risultati rapidi, attendibili e oggettivi su un materiale caratterizzato da un grado di polidispersione così elevato. Conseguentemente, uno degli obbiettivi principali di questo progetto di ricerca è consistito nello sviluppo di un valido protocollo multiscala di preparazione dei campioni e acquisizione e analisi delle immagini per ricostruire completamente e quantitativamente i mix design dei calcestruzzi storici studiati. Tale approccio analitico innovativo si è dimostrato estremamente affidabile per l'ottenimento di una

caratterizzazione completa di questi materiali eterogenei e poco standardizzati, e i risultati ottenuti sono stati confrontati con successo con quelli ottenuti tramite lo studio multi-analitico.

Infine, è stato effettuato uno studio dettagliato dello stato di conservazione e dei fenomeni di degrado agenti sui materiali. I calcestruzzi sono stati studiati con un approccio multi-analitico articolato in uno studio petrografico preliminare, integrato da analisi XRPD di profilo della frazione fine dei materiali e da analisi SEM-EDS sia su campioni massivi che in sezione sottile. I risultati hanno evidenziato l'incidenza nei materiali di molteplici fenomeni di alterazione, strettamente correlati alle loro caratteristiche composizionali e tessiturali e alle condizioni ambientali di esposizione. Oltre all'individuazione di forme comuni di alterazione del calcestruzzo, quali la carbonatazione, l'attacco solfatico, l'attacco da cloruri, le reazioni alcali-aggregato e di ricristallizzazione di sali solubili, una nuova tipologia di degrado è stata per la prima volta osservata e studiata nei campioni di calcestruzzo dell'Area Ex-Agrimont, l'attacco sinergico solfatico-fosfatico. Questa forma di alterazione è stata investigata approfonditamente attraverso un approccio multi-analitico di profilo, consistente in una combinazione di microscopia ottica, micro-XRPD in luce di sincrotrone, microanalisi SEM-EDS, XRPD termica *in situ*, analisi termogravimetriche e termiche differenziali simultanee (TGA-DTA), spettroscopia di emissione atomica a plasma accoppiato induttivamente (ICP-OES) e modeling termodinamico. Tale forma di alterazione è risultata essere strettamente legata all'interazione tra inquinanti atmosferici ricchi in solfati e soluzioni ricche in fosfati e ioni ammonio rilasciati dall'impianto di produzione di fertilizzanti, e ha causato una grave decalcificazione delle matrici cementizie e la formazione di fosfati e solfati secondari secondo una marcata zonazione mineralogica e tessiturale, con associata stabilizzazione di fasi metastabili a causa dei particolari gradienti di pH e concentrazione degli inquinanti venutisi a stabilire all'interno dei materiali. Inoltre, si sono formate rare fasi in soluzione solida, le quali hanno successivamente subito fenomeni di parziale disidratazione correlati alle condizioni di esposizione.

TABLE OF CONTENTS

CHAPTER 1: THE REINFORCED CONCRETE

1.1	***DEFINITION***	*1*
1.2	***A BRIEF HISTORY***	*1*
1.3	***THE MAIN COMPONENTS OF CONCRETE AT FRESH AND HARDENED STATE***	*6*
1.3.1	***Portland cement***	*6*
1.3.1.1	*Production process*	*6*
1.3.1.2	*Nomenclature*	*8*
1.3.1.3	*The main clinker phases*	*8*
1.3.1.4	*The hydration of Portland cement*	*10*
1.3.2	***Aggregate***	*13*
1.3.3	***Water***	*19*
1.3.4	***Chemical admixtures: plasticizers and superplasticizers***	*20*
1.3.5	***Pore network***	*21*
1.3.6	***Interfacial transition zone***	*24*
1.4	***MIX DESIGN***	*25*
1.5	***REINFORCED CONCRETE***	*26*
1.6	***CONCRETE DEGRADATION***	*29*
1.6.1	***Acidic attack***	*29*
1.6.2	***Carbonation***	*31*
1.6.3	***Corrosion of reinforcement bars***	*32*
1.6.4	***Chloride attack***	*33*
1.6.5	***Sulfate attack***	*34*
1.6.6	***Alkali-related attacks***	*36*
1.6.7	***Freeze-thaw cycles***	*38*
1.6.8	***Physical-mechanical alterations related to environmental causes***	*38*

CHAPTER 2: THE STUDIED STRUCTURES

2.1 ***INTRODUCTION*** *41*

2.2 ***NORTHERN WING OF THE CARRARESI CASTLE*** *42*

2.2.1 ***Historical background*** *42*

2.2.2 ***Structural and architectural features*** *45*

2.3 ***VICTORY MONUMENT*** *48*

2.3.1 ***Historical background*** *48*

2.3.2 ***Structural and architectural features*** *50*

2.4 ***EX-AGRIMONT AREA, C3 BUILDING*** *52*

2.4.1 ***Historical background*** *52*

2.4.2 ***Structural and architectural features*** *54*

2.5 ***EX-ZWEIFEL EMBROIDERY PLANT*** *58*

2.5.1 ***Historical background*** *58*

2.5.2 ***Structural and architectural features*** *59*

2.6 ***EX-FORO BOARIO*** *62*

2.6.1 ***Historical background*** *62*

2.6.2 ***Structural and architectural features*** *63*

CHAPTER 3: MULTI-ANALYTICAL CHARACTERIZATION OF THE CONGLOMERATES

3.1 ***INTRODUCTION*** *67*

3.2 ***THE SAMPLING CAMPAIGNS*** *68*

3.2.1 ***Preliminary surveys*** *68*

3.2.2 ***Sampling operations*** *72*

3.3 ***EXPERIMENTAL*** *74*

3.3.1 ***Materials*** *74*

3.3.2 ***Methods*** *79*

3.4 ***RESULTS*** *80*

3.4.1 ***Northern Wing of the Carraresi Castle*** *80*

3.4.1.1 *Compressive strength values* *80*

3.4.1.2 *Concrete of the first constructive phase* *81*

3.4.1.3 *Concrete of the second constructive phase* *85*

3.4.1.4 *Concrete of the third constructive phase* *89*
3.4.2 ***Victory Monument*** *92*
3.4.2.1 *Compressive strength values* *92*
3.4.2.2 *Concrete of the walls* *93*
3.4.2.3 *Concrete of the vaulted slab* *96*
3.4.2.4 *Concrete of the stairway beams and slabs* *98*
3.4.3 ***Ex-Agrimont Area, C3 building*** *100*
3.4.3.1 *Compressive strength values* *100*
3.4.3.2 *Mineral-petrographic features* *101*
3.4.4 ***Ex-Zweifel Embroidery Plant*** *105*
3.4.4.1 *Compressive strength values* *105*
3.4.4.2 *Concrete of the columns* *106*
3.4.4.3 *Concrete of the beams and the riddle* *108*
3.4.4.4 *Concrete of the arches* *111*
3.4.5 ***Ex-Foro Boario*** *114*
3.4.5.1 *Compressive strength values* *114*
3.4.5.2 *Mineral-petrographic features* *114*
3.4.6 ***Binder hydration*** *118*
3.5 ***CONCLUSIONS*** *122*

CHAPTER 4: MIX DESIGNS RECONSTRUCTION BY MULTISCALE IMAGE ANALYSIS

4.1 ***INTRODUCTION*** *127*
4.2 ***EXPERIMENTAL*** *129*
4.2.1 ***Materials*** *129*
4.2.2 ***Samples treatment and images acquisition*** *130*
4.2.3 ***Images segmentation*** *135*
4.2.4 ***Mix designs reconstructions*** *142*
4.2.5 ***Reconstruction of the aggregate granulometric curves and pore network characterization*** *152*
4.3 **RESULTS** *155*
4.3.1 ***Verification of the accuracy of the image analysis protocol*** *155*

4.3.2 Northern Wing of the Carraresi Castle 158
4.3.3 Victory Monument 169
4.3.4 Ex-Agrimont Area, C3 building 180
4.3.5 Ex-Zweifel Embroidery Plant 185
4.3.6 Ex-Foro Boario 195
4.4 CONCLUSIONS 199

CHAPTER 5: STUDY OF THE DEGRADE OF THE CONCRETE ELEMENTS

5.1 THE CONSERVATION STATE OF THE STRUCTURES 201
5.1.1 Northern Wing of the Carraresi Castle 201
5.1.2 Victory Monument 203
5.1.3 Ex-Agrimont Area, C3 building 205
5.1.4 Ex-Zweifel Embroidery Plant 206
5.1.5 Ex-Foro Boario 208
5.2 EXPERIMENTAL 209
5.3 RESULTS 210
5.3.1 Northern Wing of the Carraresi Castle 210
5.3.2 Victory Monument 215
5.3.3 Ex-Agrimont Area, C3 building 224
5.3.4 Ex-Zweifel Embroidery Plant 229
5.3.5 Ex-Foro Boario 232
5.4 CONCLUSIONS 240

CHAPTER 6: CONCRETE DEGRADATION BY COMBINED SULFATE-PHOSPHATE ATTACK

6.1 INTRODUCTION 243
6.2 PRODUCTION OF PHOSPHATE-BASED FERTILIZERS 244
6.3 ENVIRONMENTAL SETTING OF THE AREA 246
6.4 CONSERVATION STATE OF THE STRUCTURE 248
6.5 CHARACTERIZATION OF THE ALTERED MATERIALS 250
6.5.1 Experimental 250

6.5.2 Results *253*
6.5.2.1 Explorative petrographic and mineralogical analyses *253*
6.5.2.2 Profile mineralogical analyses *256*
6.5.2.3 SEM-EDS analyses *259*
6.6 EXPERIMENTAL STUDY OF THE DEHYDRATION BEHAVIOUR OF GYPSUM-BRUSHITE SOLID SOLUTION *265*
6.6.1 Experimental *265*
6.6.2 Results *268*
6.6.2.1 First experiment *268*
6.6.2.2 Second experiment: characterization of the synthesized phases *269*
6.6.2.3 Second experiment: thermal analyses and in situ thermal XRPD *272*
6.6.2.4 Second experiment: study of the influence of kinetics and crystal size *277*
6.7 THE ALTERATION MODEL *284*
6.8 CONCLUSIONS *287*

CONCLUSIONS

REFERENCES

ACKNOWLEDGEMENTS

CHAPTER 1

The reinforced concrete

1.1 DEFINITION

Concrete is a heterogeneous construction material made of a mixture of Portland cement, an aggregate fraction made of pebbles of rocks and minerals of different grain sizes, and water. The combination of these components provides a hydraulic material capable to set and harden thanks to the hydration reaction of the binder, which causes strong interconnection between the aggregate particles. Various admixtures, both organic and inorganic, can be added to the mixtures, to improve the characteristics of the conglomerates, both at the fresh state - e.g. workability - and at the hardened one - e.g. mechanical resistance and durability (St John et al., 1998). Nowadays, concrete is the most used material in the field of construction technology, thanks to its excellent mechanical and durability properties.

The diffusion of this material in the constructions field is strictly related to the production of structural elements made of reinforced concrete, obtained by incorporating steel bars in the fresh conglomerate, in the areas most subjected to tensile stresses, to improve the low tensile strength of the material (Barbisan & Guardini, 2007). Reinforced concrete is a complex and heterogeneous material: to understand fully its properties, it is fundamental to consider its evolution over time, as well as the main characteristics of its components and its subjectivity to alteration phenomena of various nature.

1.2 A BRIEF HISTORY

The first account for the utilization of an inorganic binder in the human culture dates back to 5600 B.C.: it was found in archaeological remains of domestic settlements in the Middle East. The use of various types of binders was largely diffused in ancient cultures, especially among the Egyptians, who used mortars made of a mixture of lime and gypsum

as binder with the addition of straw and *cocciopesto* (made of brick fragments of different grain size) for the lining of masonry structures. Lime mortars were widely used by the ancient Greeks, too (Barbisan & Guardini, 2007).

Concrete was produced for the first time by the Romans during the 4th century B.C., a mixture of lime and coarse tuff aggregate, *cocciopesto* and volcanic ashes called *opus caementicium* (Pecchioni et al., 2008). Later on, they started utilizing pozzolana in the binder mixtures, a volcanic sand of fine pyroclastite grains mined in Pozzuoli, near Naples, and mainly constituted of vitreous matrices of amorphous silica. Many famous roman monuments, such as the Coliseum and the Pantheon, are made with pozzolanic binders. Pozzolana, mixed with lime and water, produces a pozzolanic reaction which creates a hydraulic binder with properties similar to the modern Portland cement.

During the Middle Ages the construction tradition of the ancient Romans was forgotten and the quality of the binder was very poor. Only in the course of the 14th century were hydraulic and pozzolanic binders used again in the construction technology.

Great innovations in the field of hydraulic binders occurred during the 18th century, with a noteworthy development of scientific studies on the properties of cements (Barbisan & Guardini, 2007). In 1793, J. Smeaton produced a lime obtained by the calcination of marls, capable of setting and hardening under water. This hydraulic lime can be considered the real progenitor of modern Portland cement, with hydraulic properties related to the formation of calcium aluminosilicates during the calcination process. In 1802, L. Vicat produced the first hydraulic lime obtained by calcination of mixtures of limestone and clay, his studies were crucial for the comprehension of chemical properties of hydraulic binders. After these pioneering studies, the use of hydraulic binders became widespread in the construction technology field, both in Europe and the United States (Barbisan & Guardini, 2007).

Portland cement was officially patented by W. and J. Aspdin in 1824, and was obtained by thermal treatment at 850^{o}C from a mixture of limestone and clay. Due to the low calcination temperature, the properties of this cement were distant from the ones of modern Portland cement, so it is now called "proto-Portland cement". A product with characteristics similar to the modern cements was obtained by I.C. Johnson in 1845, raising the firing temperatures, and it is now called "meso-Portland cement". A further step in the evolution of cement production technology was the introduction of rotary kilns at the end

of the 19th century, which were able to produce cements with compositional characteristics and properties fully comparable to modern binders.

Reinforced concrete was officially patented by J. Monier in 1867, after fifteen years of experimentations by a number of French and English scientists and technologists. Originally conceived for the production of non-structural artifacts, the system was soon introduced in construction technology; reinforced with steel bars, concrete was mainly used for the construction of ceilings and roofs, structural elements widely exposed to tensile stresses.

Reinforced concrete was widely used during the second half of the 19th century, and more than fifty construction systems were patented during those years. The most common one was the Hennebique construction system, patented in France in 1892 (figure 1.1). Even though it was conceived according to empiric methods, the system was based on an accurate disposition of the reinforcement bars in the areas of structural elements more subjected to tensile stresses, and adopted for the first time a well-conceived disposition of stirrups, to withstand shear stresses (Nelva & Signorelli, 1990; Barbisan & Guardini, 2007).

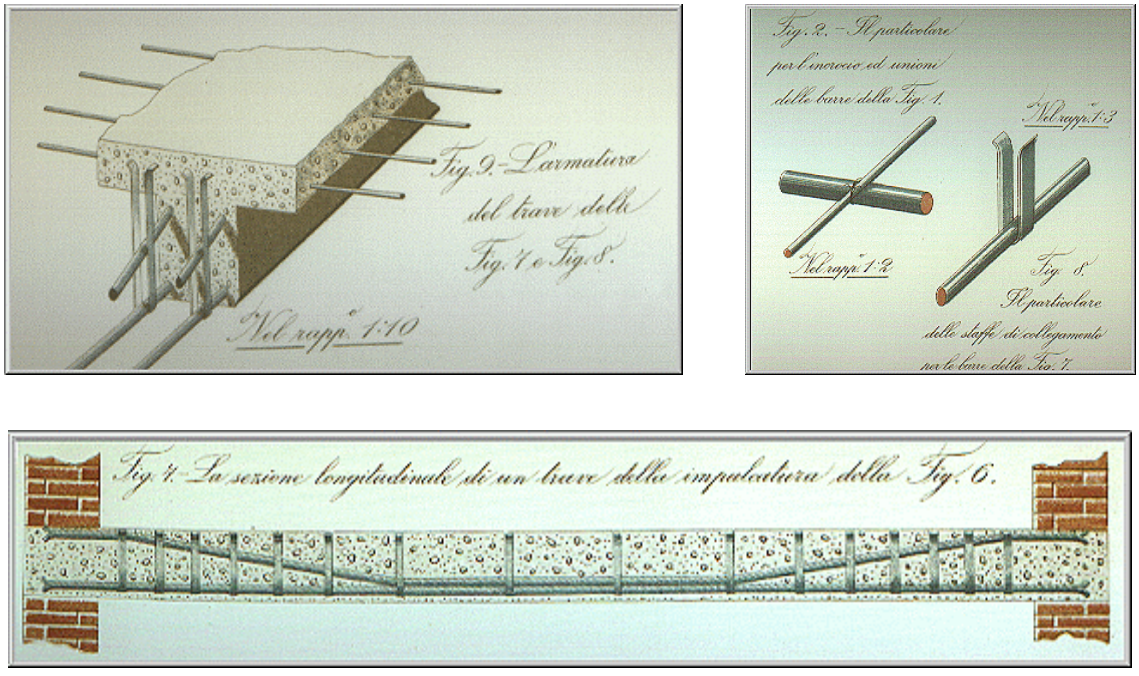

Figure 1.1. The Hennebique construction system, disposition of reinforcement bars in slabs and beams (from Nelva & Signorelli, 1990)

The system knew a worldwide diffusion thanks to a capillary network of local sales representatives. Porcheddu company, based in Turin, was the Italian holder of the construction system. Many famous Italian structures were made with this technique, for example the Carlo Emanuele I bridge in Turin (1902) and the Risorgimento bridge in Rome (1911) (Nelva & Signorelli, 1990; Barbisan & Guardini, 2007*)*.

Great innovations in the field of reinforced concrete construction technique were brought by the French architect A. Perret, who constructed the first complex building with a structural frame entirely made of reinforced concrete, the Rue Franklin apartment house in Paris (1903). The architect constructed numerous buildings in the French capital, and his structures influenced the contemporary architecture for decades, paving the road to the construction of building without load-bearing walls, substituted by columns, beams and slabs (Barbisan & Guardini, 2007).

Prestressed reinforced concretes were patented by E. Freyssinet in 1928, even if the first experimentations were carried out at the end of the 19th century by American engineer P.H. Jackson. The idea of Freyssinet consisted in placing fresh concrete in formworks where the reinforcement bars were subjected to a tensile stress. In this way, a tension transferring from steel to concrete occurred, capable of increasing the overall mechanical strength of the material. FIAT Lingotto factory in Turin was designed and built by Italian architect M. Trucco in 1916 using this technique, becoming one of the masterpieces of 20th century Italian architecture (figure 1.2).

Figure 1.2. FIAT Lingotto factory, Turin (from Nelva & Signorelli, 1990)

Reinforced concrete soon became the most used construction system by architects and engineers, who were fascinated by an easy-to-cast material, with excellent mechanical properties and with low production costs.

Italian engineer P.L. Nervi was a pioneer in the structural utilization of reinforced concrete, with the conception of the concrete shells, used for the construction of valuable buildings like the Fair Pavilion in Turin (1948-50), the Palasport in Rome (1959) and the George Washington Bridge Bus Station in New York (1962). French architect Le Corbusier used reinforced concrete for the construction of some of his most famous buildings, like Villa Savoye (1931), the La Tourette Monastery (1959) and the Notre-Dame du Haut Chapel (1957) (figure 1.3). F.L Wright was the first architect to exploit the versatility of reinforced concrete for the construction of non-linear buildings, perfectly integrated with the surrounding environment and similar to design artifacts. His most famous buildings are the Kaufman House (1936) (figure 1.4) and the Guggenheim Museum of New York (1956-59) (Barbisan & Guardini, 2007).

Figure 1.3. Le Corbusier, Notre Dame Du Haut Chapel (from Nelva & Signorelli, 1990)

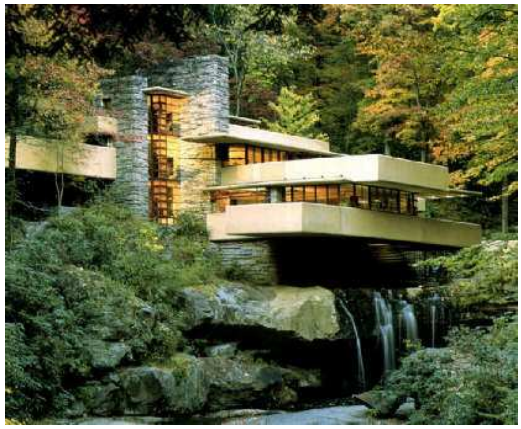

Figure 1.4. F.L. Wright, Kaufman House (from Nelva & Signorelli, 1990)

The latest evolution in the history of reinforced concrete occurred during the 70s, with the first application of fiber reinforced concretes. These composite materials, obtained by adding fibers of various nature (asbestos, glass, carbon and polymeric fibers) to the fresh conglomerate, can withstand even more intense tensile stresses, broadening the application field of concrete to the construction of thin structural elements previously made of steel only.

Nowadays, the optimization of mix designs and the conceiving of new generation conglomerates like self-compacting concretes led to reaching extraordinary performances

in terms of both mechanical properties and durability, enhancing the crucial role of this material in the contemporary building technology.

1.3 THE MAIN COMPONENTS OF CONCRETE AT FRESH AND HARDENED STATE

1.3.1 Portland cement

1.3.1.1 Production process

Portland cement is an inorganic hydraulic binder constituted by a mixture of Portland cement clinker, calcium sulphates and other minor constituents in limited amounts, finely ground together (Taylor, 1990; Hewlett, 2007). When mixed with water, the binder sets and hardens thanks to the hydration reaction occurring at the interface between dissolving particles and water, and in solution, with the development of a dense network of hydrated phases constituting a material with excellent mechanical properties. Ordinary Portland cement clinker is mainly constituted by two calcium silicates phases, named alite (Ca_3SiO_5) and belite (Ca_2SiO_4), which constitute at least two-thirds of the total mass of the material. The remaining fraction is mainly constituted by calcium aluminate and calcium aluminoferrite phases, plus other minor compounds.

The raw mix for the production of Portland cement clinker is generally constituted by a mixture of limestone, with a smaller fraction of clay materials. Some argillaceous limestones and marls may show compositions very close to the one required for the production of the raw mixture, so they can be directly employed.

After extraction from the quarries, the raw materials undergo a series of crushing, drying, milling and blending cycles, to obtain a homogeneous powder with a mean grain size of about 160 μm. Then, the powder is gradually heated in a pre-heater system up to 800 °C, before passing in a pre-calciner and finally in a rotary kiln, typically 50-100 m long, sloping at a gradient of 3-4% and rotating at a few revolutions per minute. The raw material inside the kiln moves against a flow of hot gases, reaching a maximum temperature of about 1450°C.

During the firing process, a series of reactions takes place, which can be divided in three main groups:

- *Reactions below ~ 1300 °C*: calcination of carbonates and de-hydroxylation of clay minerals, with formation of new phases above 900 °C (mainly Al-Si spinel, cristobalite and mullite). The reactions of lime (CaO) with high-temperature polymorphs of SiO_2 and clay minerals decomposition products lead to the formation of high temperature polymorphs of belite (Ca_2SiO_4), aluminate ($Ca_3Al_2O_6$) and aluminoferrite (or simply ferrite, $Ca_4Al_2Fe_2O_{10}$). A considerable amount of free lime is still available at the end of this stage.
- *Reactions between 1300 and 1450 °C (clinkering)*: fusion of aluminate and ferrite and reaction between belite and lime to form alite (Ca_3SiO_5). The material starts to nodulize and forms the clinker.
- *Reactions during cooling*: crystallization of the liquid phase forming aluminate and ferrite, and polymorphic transitions of calcium silicates. During this stage, which takes place both at the end of the kiln and in the coolers, clinker solidifies completely in large nodules between 3 and 20 mm in diameter. The cooling process must be as rapid as possible, in order to avoid the decomposition of alite to belite and free lime.

After the production process, clinker is mixed with a small amount of calcium sulfate (gypsum, bassanite, anhydrite), finely ground (typically below 100 μm). Sulfates are fundamental during the setting process of the binder, to avoid “flash set” phenomena. Other inorganic materials, called supplementary cementitious materials (SCMs) may be mixed with Portland cement, obtaining composite cements. SCMs play a fundamental role in reducing the overall cost of binder, being mainly waste materials from specific industrial production processes, and can take part to the hydration process of the binder either by developing a pozzolanic reaction with portlandite to produce CSH or for their latent hydraulic properties. The main consequences on binder properties are a slower and decreased heat evolution, an improvement in durability and in some cases higher mechanical strengths. The principal mineral additions are fly ash, blast furnace slag, natural and artificial pozzolana, silica fume and limestone.

A typical chemical composition of an ordinary clinker is the following: 67% CaO, 22% SiO_2, 5% Al_2O_3, 3% Fe_2O_3 and 3% of other components (mainly SO_3, MgO, Na_2O and K_2O). Besides the four major clinker phases (alite, belite, aluminate and ferrite), several other phases such as alkali sulfates, CaO and MgO are commonly present in minor amounts.

1.3.1.2 Nomenclature

A specific cement chemistry notation is commonly used to abbreviate the formulae of oxides to simple letters; the abbreviations for the main oxides, clinker phases and hydration phases are reported in Tables 1.1 and 1.2.

$CaO = C$	$Fe_2O_3 = F$	$K_2O = K$	$CO_2 = Č$
$SiO_2 = S$	$MgO = M$	$Na_2O = N$	$TiO_2 = T$
$Al_2O_3 = A$	$SO_3 = Š$	$H_2O = H$	$P_2O_5 = P$

Table 1.1. Cement chemistry notation: abbreviations of common oxides

Phase	**Chemical formula**	**Cement notation**
Alite	Ca_3SiO_5	C_3S
Belite	Ca_2SiO_4	C_2S
Aluminate	$Ca_3Al_2O_6$	C_3A
Aluminoferrite	$Ca_4Al_2Fe_2O_{10}$	C_4AF
Gypsum	$CaSO_4 \cdot 2H_2O$	$CŠH_2$
Bassanite	$CaSO_4 \cdot 0.5H_2O$	$CŠH_{0.5}$
Anhydrite	$CaSO_4$	CŠ
Portlandite	$Ca(OH)_2$	CH
Calcium silicate hydrate	$(CaO)_x(SiO_2)_y \cdot z(H_2O)$	CSH
Ettringite	$Ca_6Al_2(SO_4)_3(OH)_{12} \cdot 26H_2O$	$C_6AŠ_3H_{32}$
Monosulfoaluminate	$Ca_4Al_2(SO_4)(OH)_{12} \cdot 6H_2O$	$C_4AŠH_{12}$
Hydrogarnet	$Ca_3[Al(OH)_6]_2$	C_3AH_6

Table 1.2. Chemical formulae and abbreviated notations of the most important cement-related phases

1.3.1.3 The main clinker phases

Tricalcium silicate alite (C_3S) is the most important constituent of Portland cement clinkers, ranging from 50 to 70% of the mass. Ionic substitutions (approximately 3-4%) are common in C_3S structure. The commonest are Na^+, K^+, Mg^{2+}, Fe^{3+} for Ca^{2+} and Al^{3+}, P^{5+}, S^{6+} for Si^{4+} (Taylor, 1990). Structural substitutions favor the stabilization at ambient temperature of high-temperature polymorphs. M_3 and M_1 polymorphs (monoclinic) are the most commonly present in industrial clinkers. Alite is characterized by fast hydration kinetics, thus it is the main responsible for strength development, especially in the short-term. About 70% of alite hydrates in the first 28 days, while the remaining fraction completely reacts within one year, provided water is available for reactions to take place.

Dicalcium silicate belite (C_2S) constitutes about 15-30% of Portland clinker. As for C_3S,

higher temperature polymorphs are stabilized by substituting ions. Polymorphic transition during cooling from monoclinic β-C_2S to orthorhombic γ-C_2S shall be avoided as it causes intense cracking of belite crystals, a phenomenon known as "dusting". Generally, common degrees of substitution with stabilizing ions are sufficient to avoid this destructive transformation. Belite has slower reaction kinetics with respect to alite, therefore it plays a minor role in the development of mechanical strength at early days of hydration, while its reaction is fundamental for the long-term strength development.

Aluminate (C_3A) is present in Portland cement clinkers in proportions from 5 to 10%. Pure C_3A has a cubic symmetry and does not exhibit polymorphism. However, Ca^{2+} can be considerably substituted by $2Na^{+}$, leading to a solid solution of general formula $Na_{2x}Ca_{3-x}Al_2O_6$, and consequent occurrence of a series of orthorhombic and monoclinic polymorphs. Aluminate is commonly found in clinkers in the cubic or orthorhombic form. C_3A is characterized by very fast reaction kinetics, leading to the undesired phenomenon of "flash set". This effect is controlled by adding an adequate amount of calcium sulfates as set-retarders.

Ferrite (C_4AF) is present in Portland cement clinkers in ratios between 5 and 15%. The phase is characterized by an orthorhombic structure, organized in several space groups according to Al/Fe ratio variations and ionic substitutions. The composition of ferrite is expressed by the solid solution series $Ca_2(Al_xFe_{1-x})_2O_5$, where $0 < x < 0.7$. Also, the incorporation of about 10% of other oxides usually occurs, mainly replacements of Fe^{3+} by Mg^{2+}, Si^{4+}, Ti^{4+} or Mn^{3+}. Ferrite has small effects on the mechanical properties of cement and shows fast reaction kinetics during early hydration, while it is almost inert later on. This phase is also the main responsible for the typical dark color of cement.

At microstructural level (figure 1.5), Portland cement clinker is constituted mainly by pseudo-hexagonal euhedral crystals of C_3S, with associated rounded subedral crystals of C_2S, often with inclusions of C_3S relicts. C_3A and C_4AF constitute an interstitial, very fine-grained material, often with incorporated accessory minerals such as free lime, periclase and alkaline sulfates (St John et al., 1998).

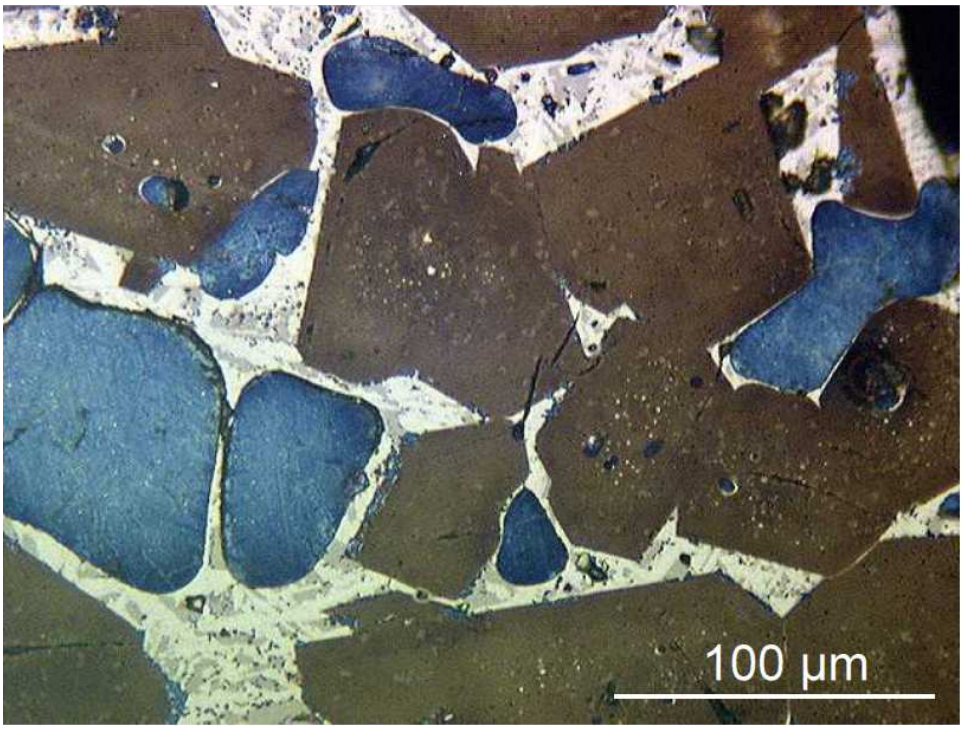

Figure 1.5. False colors micrograph of Portland cement clinker (Stutzman, 2009). It is possible to observe the presence of large euhedral alite crystals (brown), with associated subedral belite crystals (blue), dispersed in an interstitial matrix of aluminate (white) and ferrite (grey)

1.3.1.4 The hydration of Portland cement

The hydration process of Portland cement is based on a sequence of complex chemical reactions between clinker phases calcium sulfates and water, leading to the setting and hardening of the paste and the consequent development of mechanical strength. Due to the overall complexity, cross correlation and different kinetics of reaction sequences, the study of hydration of clinker phases is usually performed on a simplified system constituted by a single phase only. However, the general hydration behavior of constituents is basically the same: dissolution of anhydrous phases and precipitation of low solubility products forming the hardened paste. The setting process occurs during the first hours of hydration and consists in the transition from a concentrated suspension of flocculated particles to a viscoelastic solid capable of supporting shear stress. The hardening process is slower, and consists of the progressive development of a solid framework responsible for cement mechanical properties. The hydration reactions can last years, terminating only at the consumption of one of the two reactants, or when there is no space left for the deposition of new hydration products. The hydration behavior of clinker phases is strongly influenced

by several factors, the most important being w/c ratio, temperature, particle size distribution, mixing procedure, size of the hydrating sample and presence of admixtures.

The hydration of calcium silicates produces two main phases, calcium silicate hydrate (CSH) and calcium hydroxide portlandite (CH). The term CSH refers to a series of phases characterized by low crystallinity order and with variable stoichiometry, and thus commonly known as CSH gels. The development of highly interlocked fibers of CSH aggregates is the main responsible for the development of mechanical strength in cements. Portlandite, characterized by a layered hexagonal structure, does not contribute significantly to the development of mechanical strength. In very diluted solutions, CH forms euhedral hexagonal flakes, while in ordinary cement microstructures it is organized in massive microcrystalline aggregates without a well-defined shape. The hydration of C_3S and C_2S can be described by the following reactions:

$$C_3S + (3\text{-}x+n)H \rightarrow C_xSH_n + (3\text{-}x)CH \quad (\Delta H = -121 \text{ kJ/mol}) \quad \textit{(1.1)}$$

$$C_2S + (2\text{-}x+n)H \rightarrow C_xSH_n + (2\text{-}x)CH \quad (\Delta H = -43 \text{ kJ/mol}) \quad \textit{(1.2)}$$

When the solution is saturated with respect to CH, *x* and *n* are respectively 1.7 and 4, thus reactions 1.1 and 1.2 become:

$$3C_3S + 16H \rightarrow 3C_{1.7}SH_4 + 4CH \quad \textit{(1.3)}$$

$$3C_2S + 13H \rightarrow 3C_{1.7}SH_4 + CH \quad \textit{(1.4)}$$

As C_3S constitutes about 50 to 70% of the mass of normal clinkers, its hydration is the dominant process in Portland cement hydration, especially during the early stages of strength development.

C_3A is considered, by the scientific literature, to be the most reactive clinker phase: for this reason, its influence in the setting process of cement is crucial. In the absence of sulfates, the phase hydrolyzes and reacts with water to form amorphous hydrated calcium aluminates that progressively structure to form hexagonal hydrated phases, characterized by a layered structure and with compositions C_2AH_8, C_4AH_{13} and C_4AH_{19} (reactions 1.5, 1.6). The latter phase tends to lose part of its interlayer water to form C_4AH_{13}. Due to the metastability of these compounds, they tend to convert progressively into the stable phase C_3AH_6 (hydrogarnet, reaction 1.7), leading to an increase in porosity and a disruption of the microstructure with consequent loss of strength.

$$2C_3A + 27H \rightarrow C_4AH_{19} + C_2AH_8 \quad \textit{(1.5)}$$

$$C_3A + CH + 12H \rightarrow C_4AH_{13} \quad \textit{(1.6)}$$

$$C_4AH_{19} + C_2AH_8 \rightarrow 2C_3AH_6 \quad \textit{(1.7)}$$

These phases do not contribute significantly to the early development of mechanical properties, causing an undesired rapid setting of cement called "flash set". The addition of calcium sulfates in ordinary Portland cement prevents the development of such phenomenon. The first stable hydration product under these conditions is ettringite, a fibrous phase that grows at the beginning of hydration on C_3A surface, giving a fundamental contribution to the development of early strengths and preventing anticipated setting of the paste. Ettringite is one of a group of compounds known as AFt phases, and its reaction with C_3A and water can be represented by the following simplified reaction:

$$C_3A + 3C\check{S}H_2 + 26H \rightarrow C_6A\check{S}_3H_{32} \text{ (ettringite)} \quad (1.8)$$

With the increase of the alumina to sulfate ratio in the solution during hydration, related to sulfates consumption and progressive C_3A hydrolysis, ettringite becomes unstable and tends to convert into monosulfoaluminate (or simply monosulfate), according to the following reaction:

$$C_6A\check{S}_3H_{32} + 2C_3A + 4H \rightarrow 3C_4A\check{S}H_{12} \text{ (monosulfate)} \quad (1.9)$$

Monosulfate can form a solid solution with the isostructural compound C_4AH_{13}. Also CO_3^{2-} can partially substitute SO_4^{2-} in the interlayer position, and Fe^{3+} may substitute Al^{3+}, resulting in wide compositional variations. Such compounds are generally defined as AFm phases, where *m* stands for “mono”, which indicates the presence of a single anionic group in the structure (Matschei, 2007). In a similar way in AFt phases *t* stands for “tri” as they contain three anionic groups.

The hydration of ferrite is similar to that of aluminate and leads to the formation of iron-substituted AFt and AFm phases. Like C_3A, ferrite reaction kinetics are very fast during the first hydration stages, then the phase reaction almost completely stops, probably due to the formation of a passivating layer of iron hydroxides on the crystals, preventing further reactions.

A valid technique for the monitoring of overall reactions in a hydrating cement paste is the isothermal calorimetry, which measures the rate of heat evolution of the material over time. On the basis of calorimetric curves, the overall progress of hydration has been divided into four stages (Gartner et al., 2002), illustrated in figure 1.6 and summarized as follows:

1- *Initial reaction* (first minutes, corresponding to wetting and mixing): free lime, sulfates and aluminates rapidly hydrolyze, with immediate formation of AFt phases; C_3S starts to hydrate on its surface. The large initial burst of heat is mainly

due to the dissolution of C_3A and C_4AF and the formation of ettringite.

2- *Period of slow reaction* (also known as dormant or induction period): CSH gels form and CH nucleates, with progressive decrease of Si and Al concentrations in pore solution and limited increase in viscosity. A low heat evolution rate is observable during this stage.

3- *Acceleration period* (corresponding to setting and early hardening): C_3S rapidly hydrates to form CSH and CH, with a consequent rapid increase in heat flow. The paste starts to solidify and porosity significantly decreases (early strength development).

4- *Deceleration period*: C_3S and C_2S rate of reaction progressively decrease due to reactants' consumption. Ettringite converts into monosulfate and a renewed hydration of aluminates produces mainly AFm phases. The progressive growth of hydration phases and consequent reduction in overall porosity leads to a continuous increase in strength. Also, a shrinking of the paste is observed due to drying.

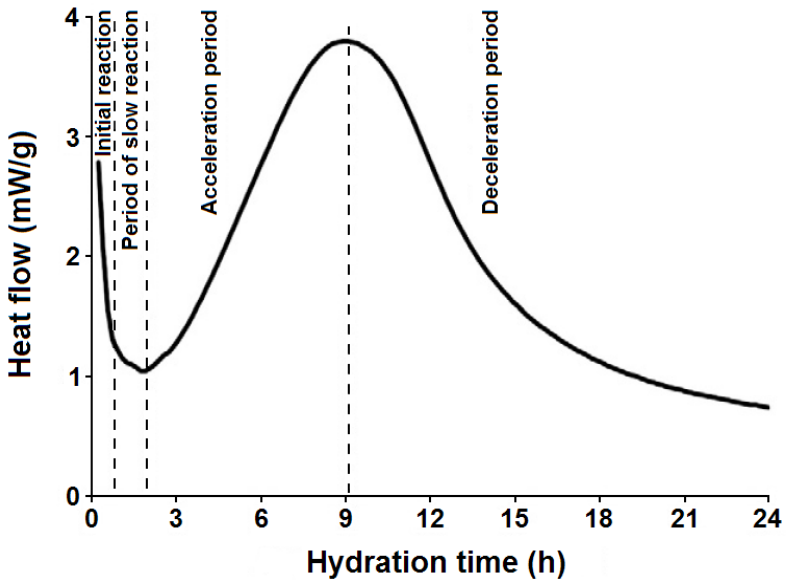

Figure 1.6. Calorimetric curve showing the rate of hydration of a pure C_3S paste (Bullard et al., 2010). A similar pattern can be obtained using normal Portland cements

1.3.2 Aggregate

The aggregate is a heterogeneous fraction constituted of rock fragments and minerals, inert to hydration processes and mixed together with cement and water to reduce the

manufacturing costs of concrete and to improve its mechanical properties. During setting and hardening, the aggregate buffers the overall shrinkage of the conglomerate due to cement chemical shrinkage, preventing the formation of diffuse cracking and reducing the tensile stresses inside the material. Moreover, its addition to the mixture does not affect significantly the variation of the mechanical properties of concrete, even at great concentrations (80 - 85% of the overall volume), so it is usually the dominant volumetric fraction of the material (Pecchioni et al., 2008). This component can be considered without doubts the structural skeleton of the conglomerate, and its correct selection and proportioning is fundamental to truly improve concrete overall properties. In modern concretes, aggregate is constituted by gravels, rubbles and sands from natural deposits (mainly alluvial fans) and, frequently, from crushing of quarry rocks (with consequent reduced mineral-petrographic heterogeneity and higher angularity of the clasts, figure 1.7). In historic concretes, supply from river beds adjacent to the construction site was frequent, with consequent higher mineral-petrographic heterogeneity and lower control on the quality assessment process.

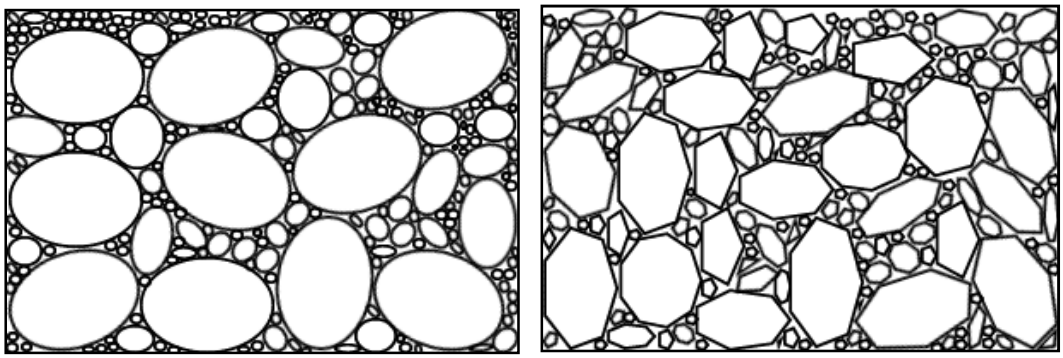

Figure 1.7. Left: natural gravel; right, rubble obtained by crushing of quarry rocks

In the selection process of aggregates, several compositional, textural and morphologic parameters need to be considered in order to guarantee a high standard of quality of the inert fraction.

- **Shape**. This parameter mainly influences concrete workability at the fresh state, and describes the aggregate according to two main parameters: roundness (the measure of the sharpness of a particle's edges and corners) and sphericity (the ratio of the surface area of a sphere with the same volume as the given particle to the surface area of the particle) (St John et al., 1998). According to these shape descriptors, aggregate can be rounded, angular, irregular, flat or elongated.

Generally, rounded and regular aggregates are preferable to increase concrete workability; moreover, flat particles may be interested by preferred orientation phenomena during the placing of concrete, creating discontinuity interfaces with lower overall strength.

- **Dimensions**. A first discrimination of the aggregate according to dimensions distinguishes fine aggregate (with dimensions between 0.063 mm and 2 mm) from coarse aggregate (with dimensions over 2 mm) (Standard UNI EN 933-1, 1999). Fine aggregate can be subdivided in very fine sand (0.063 mm-0.125 mm), fine sand (0.125 mm-0.25 mm), medium sand (0.25 mm-0.5 mm), coarse sand (0.5-1 mm) and very coarse sand (1-2 mm). Coarse aggregate can be subdivided in very fine gravel/rubble (2-4 mm), fine gravel/rubble (4-8 mm), medium gravel/rubble (8-16 mm), coarse gravel/rubble (16-32 mm), very coarse gravel/rubble (32-64 mm). The fraction under 0.063 mm is subdivided in silt, clay and colloid according to progressively lower medium dimensions. A correct grain size distribution of the aggregate fraction is fundamental for the improvement of concrete overall properties. Aggregate needs to be well sorted to reach a maximum packing and the minimum degree of voids, which can be achieved if the finer grains occupies the space between the coarse ones. A well-sorted aggregate gives compactness to the mixture, improving resistance at the hardened state (Pecchioni et al., 2008, St John et al., 1998). The descriptor parameter for the grain size distribution of the aggregate is the granulometric curve, which links the volume percentage of aggregate passing to a progressive series of standard sieves to the reference sieves aperture diameters. To determine a granulometric curve, the overall fraction of the aggregate is sieved on a set of sieves stacked according to progressively lower aperture diameters. For each sieve, the weight percentage of retained fraction is determined and considered comparable to the volume percentage. The data obtained are reported on a curve expressing the cumulative passing fraction through each standard sieve (Collepardi et al., 2008).

  The ideal granulometric curve, which expresses the reference granulometric distribution to obtain maximum aggregate packing, is the Füller & Thompson curve (1907) (figure 1.8), determined by the following equation (Collepardi et al., 2008, Pecchioni et al., 2008):

$$P = 100 \cdot (d/D_{max})^{1/2} \qquad (1.1)$$

Where d is the reference sieve aperture, P is the percentage of passing aggregate and D_{max} is the maximum diameter of aggregate.

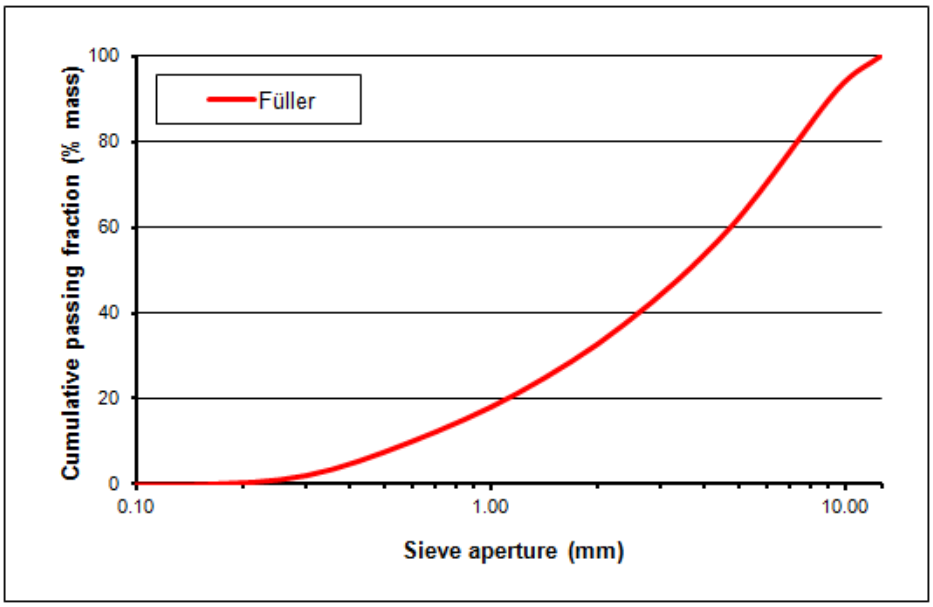

Figure 1.8. Füller & Thompson granulometric curve

The curve, besides its theoretical significance for the obtaining of a conglomerate with maximum packing, cannot be used in standard concretes due to the hard workability of a paste with such granulometric distribution. A variation of Füller & Thompson curve which takes into account workability factors was formulated also by Bolomey in 1935 (figure 1.9). The calculation of this curve introduces the so-called "workability factor" A, related to aggregate typology (natural or crushed stones) and consistency class of the paste to be obtained. In practice, Bolomey curve differs from Füller & Thompson curve for a greater quantity of fines and lower amounts of gravel, and is expressed by the following equation (Collepardi et al., 2008, Pecchioni et al., 2008):

$$P = A + (100-A) \cdot (d/D_{max})^{1/2} \quad (1.2)$$

Where *d* is the reference sieve aperture, P is the percentage of passing aggregate, D_{max} is the maximum diameter of the aggregate and A is the workability parameter. The values of A, according to aggregate typology and consistency class, are the following:

Aggregate Typology	A values according to consistency classes		
	S1	**S2, S3**	**S4, S5**
Natural	8	10	12
Crushed stone	10	12	14

Table 1.3. Values of workability coefficient parameter (Collepardi et al., 2008)

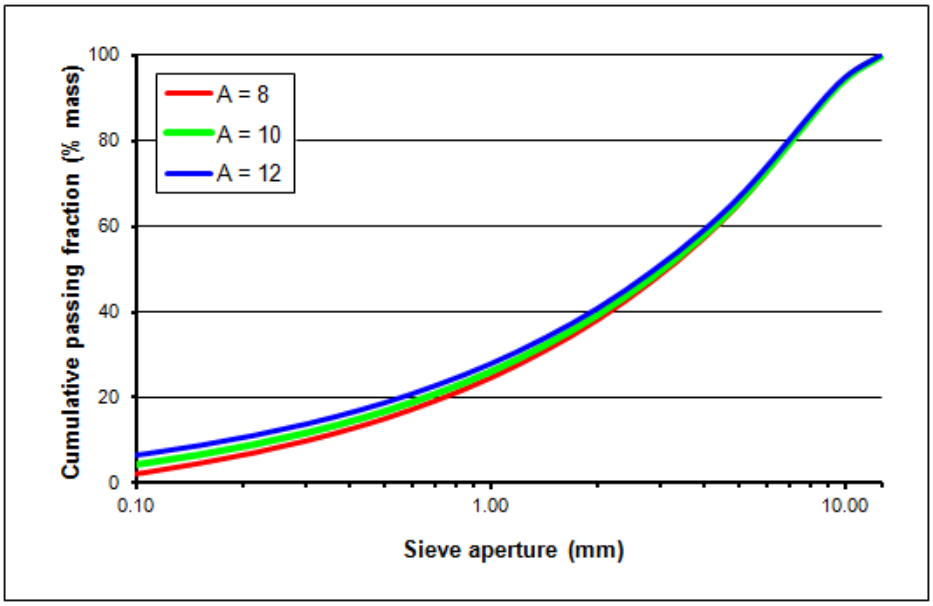

Figure 1.9: Bolomey granulometric curves according to three different A values

The reported equations are referred to the total solids of the paste (aggregate + cement). In order to refer them to the aggregate only, the determined values need to be normalized to a C factor, expressing the percentage of cement over total solids. Füller & Thompson and Bolomey curves, normalized according to C factor, are expressed by the following equations:

$$P = [(100 \cdot (d/D_{max})^{1/2} - C) / 100 - C] \cdot 100 \quad (1.3)$$

$$P = [(A - C + (100\text{-}A) \cdot (d/D_{max})^{1/2}) / 100 - C] \cdot 100 \quad (1.4)$$

- **Superficial texture**. This parameter mainly influences the adhesion between aggregate and hardened paste, and consequently tensile strength of concrete. Superficial texture may be vitreous, smooth, rough, crystalline and porous (St John et al., 1998; Pecchioni et al., 2008). Aggregates with rough surfaces guarantee better adhesion.
- **Porosity**. This parameter influences the physical, chemical, mechanical, thermal and durability properties of concrete. Generally, the use of compact aggregates is necessary.

- **Mechanical properties**. The properties usually monitored in aggregates are: compression strength, tensile strength, stiffness and resistance to abrasion. The higher the values, the better the aggregate quality.
- **Humidity and water absorption**. This parameter describes the attitude of an aggregate to absorb water, and is directly related to the total connected porosity of the material. The quantity of water absorbed by the aggregates shall be accurately evaluated not to influence the overall water to cement ratio of concrete. According to this parameter, appropriate corrections to the amount of water to be added to the mixture need to be performed, to guarantee an adequate setting of the paste (St John et al., 1998).
- **Composition**. For logistic reason, the supply of aggregate for concrete tends to be as close as possible to the site of manufacturing. A broad range of lithological species are suitable to be used as inert fraction for concrete. The most widely used are compact carbonate rocks such as micritic limestone and spathic dolostone. Igneous and metamorphic rocks are also widely used for their excellent mechanical properties. Yet, it is fundamental to verify, in the inert fraction, the absence of mineral phases and chemical compounds which may negatively influence concrete durability. Marine sands cannot be used before having performed accurate washing, due to the great amount of salts that can negatively influence cement hydration and, later on, concrete durability. Sulfates, sulfides, magnesium oxides and pyrite shall be avoided due to their high reactivity, which leads to the formation of expansive secondary compounds (Taylor, 1990; St John et al., 1998; Pecchioni et al., 2008). Rocks rich in amorphous silica (like ignimbrites, tuffs, opal and chalcedony) shall be avoided in presence of cements rich in alkalis or in structures subjected to capillary rise of solutions rich in alkaline salts, due to the possibility of formation of expansive alkaline silica gels for alkali-silica reactions (Rear et al., 1994). Clay minerals are potentially dangerous due to their properties of water absorption, with consequent deprivation of the water necessary for the hydration process (Fontanive, 1974; Taylor, 1990; St John et al., 1998).

1.3.3 Water

Water added to concrete should not influence the hydration process of cement and should not contain dissolved compound, which could affect the durability and mechanical properties of the materials. For this reason, it is necessary to use waters with reduced total dissolved solids and without organic admixtures that could interfere with conglomerate components during the setting and hardening process. Generally, waters are analyzed prior to their use, and total chlorides, sulfates and nitrates contents are determined, as these are the chemical species that mostly affect concrete durability and mechanical strength development. Saltwater is not used due to the high values of dissolved chlorides and sulfates. Rainwater cannot be used either, due to the presence of dissolved atmospheric pollutants. Generally, drinkable water from rivers, lakes and other natural continental deposits is used, after depuration from organic compounds (Marinoni et al., 2003, Pecchioni et al., 2008).

Water shall be added to the mix in the minimum quantity necessary to obtain full binder hydration and plastic, homogeneous, workable paste. The parameter expressing the quantity of water added to a specific conglomerate mix is the water to cement (w/c) ratio, the ratio between the mass of water and the mass of cement of a mixture. W/c ratio has crucial consequences not only on the degree of hydration of cement pastes, but also on the porosity of concrete and its mechanical strength. Water that is not consumed by the hydration reactions may evaporate from concrete during hardening, increasing the amount of capillary pores that will reduce the final strength of the material. A mix with an excessive amount of water will also experience higher shrinkage, with consequent higher cracking development.

A direct linear correlation between w/c ratio and capillary porosity of pastes is observable (Ingham, 2011), with progressive lowering of the overall volumetric amount of capillary pores with decreasing w/c ratios. Furthermore, there is an inverse exponential relation between w/c ratio and the compressive strength of concrete, expressed by the Abrams law (1918):

$$f_c = A/B^{w/c} \qquad (1.5)$$

where f_c is the compressive strength of concrete, w/c its water to cement ratio and A and B are constants for a given material, age and test conditions.

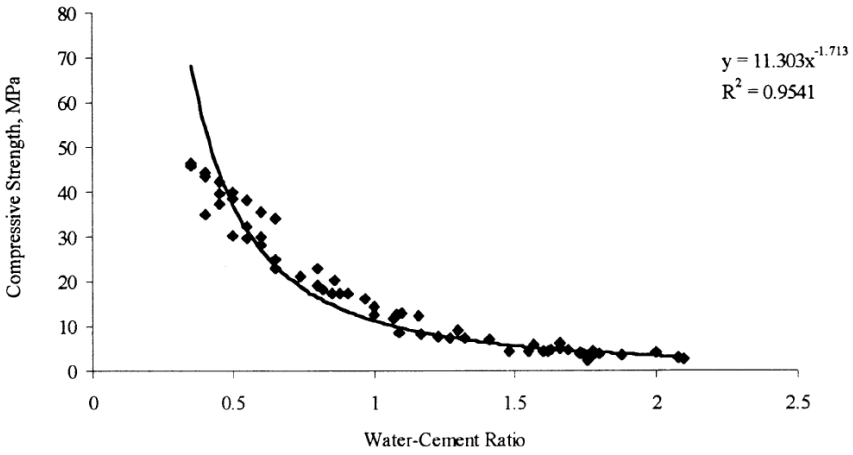

Figure 1.10. Variation of compressive strength with w/c ratio in cement mortars (Appa Rao, 2001)

An appropriate w/c ratio, necessary to guarantee full hydration of binder on a concrete paste, is between 0.38 and 0.42 (Taylor, 1990; St John et al., 1998), but commonly the flocculation of cement particles on a fresh concrete paste due to electrostatic interactions subtracts water to the system, with negative consequences both on workability and degree of hydration. To overcome these problems, in standard concretes usually water is added over the ideal quantities, commonly reaching w/c ratios of 0.5/0.6 and more, affecting mechanical performances and durability of materials consequently. The use of lower w/c ratios than these values is possible only by operating accurate compaction procedures during the manufacturing of concrete structural elements, or by adding in the mixtures organic additives capable of modifying the rheology of fresh pastes, the so-called plasticizers and superplasticizers.

1.3.4 Chemical admixtures: plasticizers and superplasticizers

All materials other than hydraulic cements, water or aggregates that are added to concrete immediately before or during mixing are defined “admixtures” (Taylor, 1990). A large variety of admixtures, both organic and inorganic, may be employed to achieve specific properties, such as an acceleration or delay of setting and hardening, a decrease of the amount of water needed to obtain a given level of workability or a modification of the entrained air content.

Water-reducing agents, also called plasticizers, were developed at the end of the 1930s, but were little used in the concrete technology field until 1970s. They are mainly based on

calcium and sodium lignosulfonates and they allow reducing the w/c ratio of a cement mixture (typically in the range of 5-15%) maintaining at the same time high levels of workability. The main limitation of conventional plasticizers is related to the fact that many of them also have retarding, accelerating or air-entraining properties. For this reason, to avoid undesired effects, they cannot be used at high dosages and are typically added as solutions in concentrations of up to 0.2% on the weight of cement. Since the 1980s, conventional plasticizers have been almost completely replaced by a novel generation of admixtures called superplasticizers (SPs), that allow overcoming the limitations of common admixtures. Superplasticizers allow producing high-strength and high-durability concretes by reducing the w/c ratio up to about 30%, or they can be used to improve the workability of concrete maintaining the desired w/c ratio. The so-called "first generation" SPs are the sulfonated melamine formaldehyde poly-condensates (SMF), sulfonated naphthalene formaldehyde poly-condensates (SNF) and modified lignosulfonate compounds. Since the beginning of the 1990s, a new class of superplasticizers based on polycarboxylate ethers (PCE) and characterized by improved performances and higher environmental compatibility has found increasing applications. Such molecules typically consist of an adsorptive backbone unit and a hydrophilic polyethylene-oxide (PEO) side chain (Plank et al., 2008, Zingg et al., 2009).

SPs allow reduction of water improving dispersion of cement grains and thus decreasing flocculation. In this way, a significant amount of water becomes available, allowing an increased fluidity of the paste. Adsorption of the admixture on the hydrating cement grains decreases flocculation by increasing the zeta-potential and the solid-liquid affinity and by steric hindrance (Daimon & Roy, 1978). Besides being adsorbed on particle surfaces, SP molecules can also be intercalated by co-precipitation with early hydration products or remain dispersed in the pore solution, influencing the nucleation of hydration phases as well as their growth and crystal shape.

1.3.5 Pore network

Pore network is a component of hardened concrete that plays a fundamental role on the mechanical performance of the material, as well as on its durability. Pore network constitutes a relevant volumetric fraction of concrete, from 10 to 30 % over the total volume. Concrete pore network is constituted by voids, with dimensions above 5 µm, and

capillary pores, with dimensions below this value. The main characteristics of capillary pores and voids are hereby reported:

- **Capillary pores**. They are characterized by irregular and dendritic shapes, with diameters smaller than 5 µm (figure 1.11). They generate during binder hydration, on areas previously occupied by mixing water (Walker, 1992).

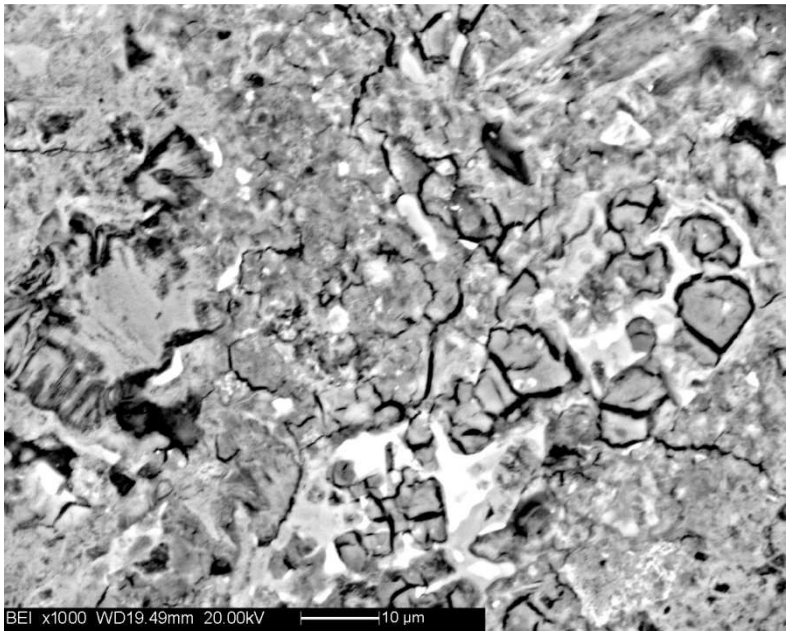

Figure 1.11. Concrete's hardened paste, capillary pores

- ***Entrained air voids***. They are sub-spherical voids, with dimensions under 1 mm (typically 100 µm) (figure 1.12). They originate during mixing, due to the inclusion of air bubbles in the paste. Their presence may be beneficial for concrete, as they tend to absorb tensile stresses caused by freezing/thawing cycles of saturation water in capillary pores. For this reason, their incidence is frequently favored by using air-entraining admixtures in fresh concrete pastes (Walker, 1992).

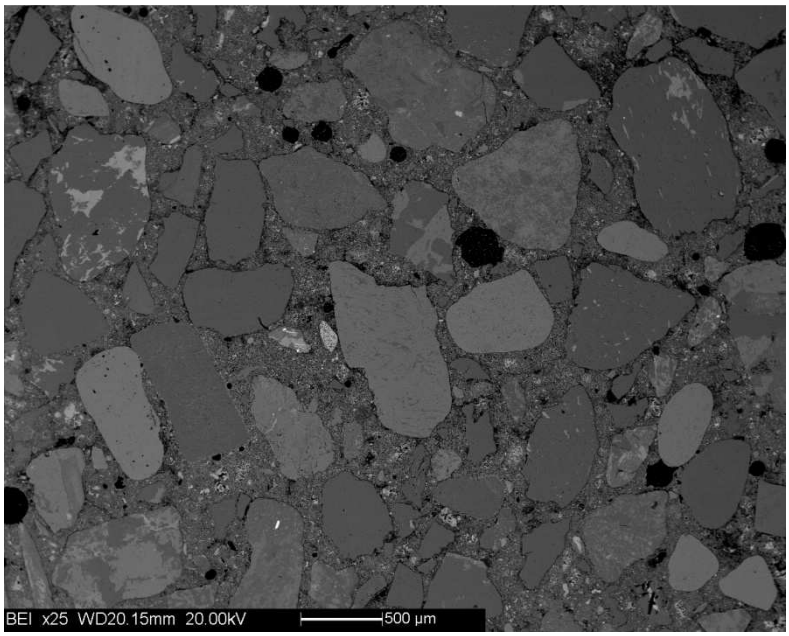

Figure 1.12. Concrete hardened paste, with entrained air voids

- ***Entrapped air voids/water voids***. They originate due to the inclusion of large air bubbles during mixing or for accumulation of excess and bleed water under big aggregate particles and reinforcement bars or at the interface with formworks. They are numerous in concretes manufactured with excessive w/c ratios. They are irregular in shape, with dimension from the millimetric to the centimetric scale. Due to their great dimensions, they are considered deleterious for both mechanical and durability properties of materials (Walker, 1992).

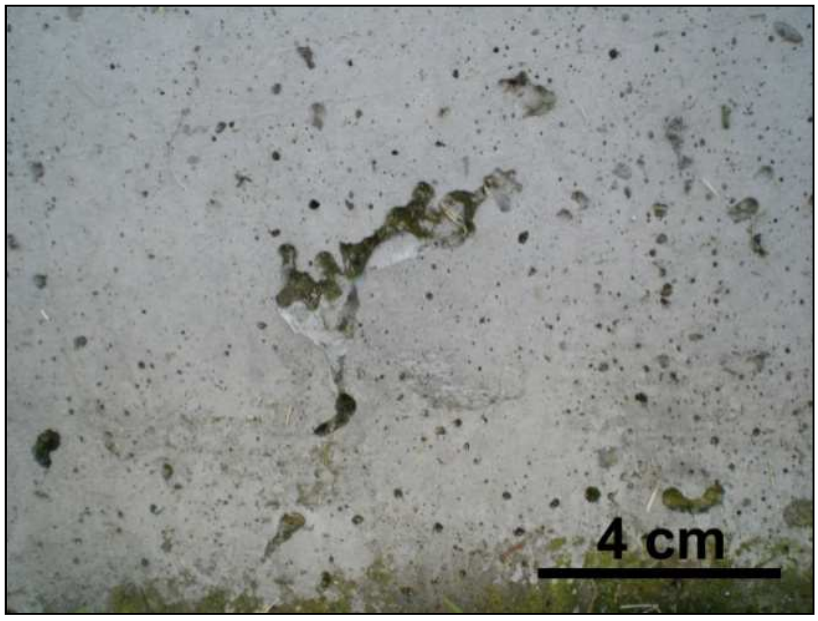

Figure 1.13: External surface of a concrete wall showing entrapped air voids/water voids

A further type of porosity is given by the so called CSH gel pores, with dimensions under 10 nm. Being part of the fibrous structure of aggregates of CSH particles, thus related to the cement matrix itself, they are not generally considered as constituents of the pore network and it is widely assumed that they cannot influence concrete properties significantly (Taylor, 1990; Walker, 1992; St John et al., 1998).
Another type of porosity that is not considered as part of concrete pore network are cracks. Dimensionally, they are divided in macrocracks (larger than 0.1 mm), fine cracks (between 0.01 and 0.1 mm) and microcracks (smaller than 0.01 mm). According to their origin, they are subdivided in plastic shrinkage cracks and drying shrinkage cracks. The former are located on the surfaces and they originate during the first hours of concrete placing due to an excessive superficial evaporation of water. The latter develop radially to the fine aggregate during advanced stages of hydration, and they are related to slow water evaporation. They are potentially dangerous as they both reduce mechanical performances of concrete and constitute a preferential way for the penetration of aggressive agents (Walker, 1992; Rear et al., 1994; St John et al., 1998). Their formation can be avoided through accurate curing of newly placed concrete elements.

1.3.6 Interfacial transition zone

The expression interfacial transition zone (ITZ) defines the volume of hardened cement paste surrounding for the first 50 µm the particles of medium and coarse aggregate (Bensted & Barnes, 2002). This portion is characterized by greater porosity and different occurrence and distribution of hydrated phases with respect to the undisturbed cement matrix. ITZ formation is mainly related to the accumulation of finer clinker particles around the inert fraction due to wall effects and micro-bleeding phenomena occurring during the first phases of hydration.
The microstructural consequences of these phenomena are the development of an anomalous porosity due to the greater availability of water, and an enrichment in AFm and AFt phases with respect to the undisturbed paste due to the greater exposure of interstitial phases on the finer particles. Moreover, great CH crystals can nucleate and grow due to the greater availability of space (figure 1.14).

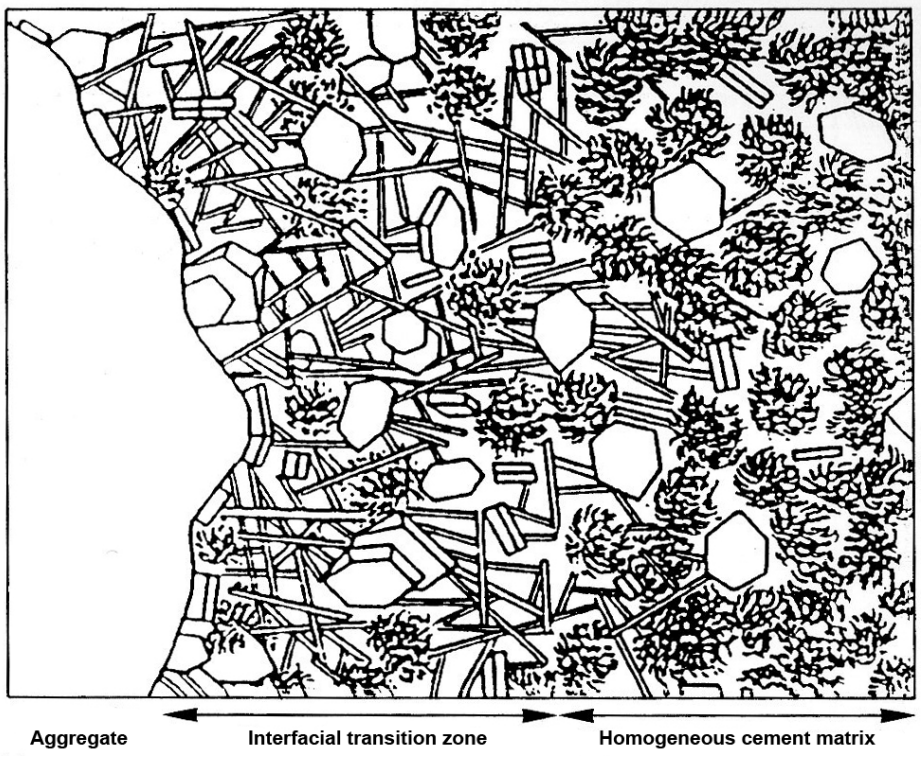

Figure 1.14. Schematic representation of the microstructural aspect of ITZ

The development of ITZ seriously affect both mechanical and durability properties, reducing matrix-aggregate adhesion and thus tensile strength, and providing preferential channels for fluid penetration and accumulation of aggressive compounds.

1.4 MIX DESIGN

The term “mix design” identifies the procedure of definition and optimization of concrete components to obtain a compact, strong and durable material. Nowadays, the study of concrete proportioning is performed according to well-defined parameters that allow correlation between composition of the mixture and its future properties in terms of workability, shrinkage, mechanical strength, elastic modulus and durability.

Dosage of components, expressed in Kg/m^3, shall be proportioned according to the desired mechanical properties. W/c ratio is the fundamental parameter for the forecast of compressive strength and durability properties, while the choice of the aggregate in terms of typology (natural or from crushed stones), dimensions and granulometric distribution shall be evaluated according to the dimensions of the structural elements to be constructed, the disposition of the reinforcement bars and the desired workability. Furthermore,

aggregate choice directly influences water demand of concrete, together with chemical admixtures, and significantly affects cement dosage. The latter directly influences mechanical resistance of concrete, increasing compressive strength at higher dosages (with constant w/c ratio), but influencing the degree of shrinkage, too.

According to the number of modeled parameters, mix design can be simplified or complex. Simplified mix design considers compressive strength, workability and maximum aggregate diameter only, while complex mix design considers durability parameters also (Maynard & Weller, 1970; Collepardi et al., 2008).

The study of mix design is a quite recent discipline: in the past, concretes were manufactured without particular attention to accurate components proportioning, often with pernicious effects both in terms of mechanical strength and durability. The production on low cost mixes (with low cement dosages and rich in fine aggregate) with locally available and often inadequate raw materials was frequent (Barbisan & Guardini, 2007). For these reasons, the study of historic concretes cannot disregard an accurate reconstruction of the original mix designs, which is the key for a thorough understanding of the causes of bad mechanical properties and degradation phenomena.

1.5 REINFORCED CONCRETE

The formulation of reinforced concrete was conceived to supply to the low tensile strength of the material, generally about ten times lower than compressive strength. To withstand this mechanical deficiency, structural steels (commonly abbreviated to “rebars”), characterized by excellent tensile strengths, are cast into fresh conglomerate in areas subjected to tensile stresses. Despite the heterogeneity of materials, their adhesion enables the transmission of tensile stresses acting on concrete to the steel bars, while compressive stresses are absorbed by the conglomerate itself (Barbisan & Guardini, 2007). This collaborative behavior is favored by the fact that materials are characterized by similar thermal expansion coefficients at room temperature. Given that the interfacial adhesion between steel and conglomerate is fundamental for a full collaboration between the two main components of concrete, the use of steel bars, adequately shaped on the surfaces to improve adhesion, is now common. Even if the introduction of ridged rebars in the construction technology field dates back to the 1940s, their large-scale utilization only started during the 1960s.

During the history of concrete technology, various concrete reinforcement systems were developed. Some of the most successful historic systems are reported in the following images.

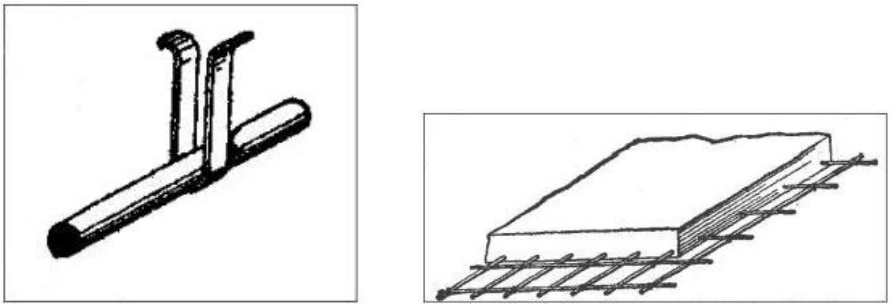

Figure 1.15. To the left: typical disposition of rebars and stirrups according to Hennebique system (1892). To the right: Monier system (1872), typical net of rebars, connected by steel wires (Traettino, 2005)

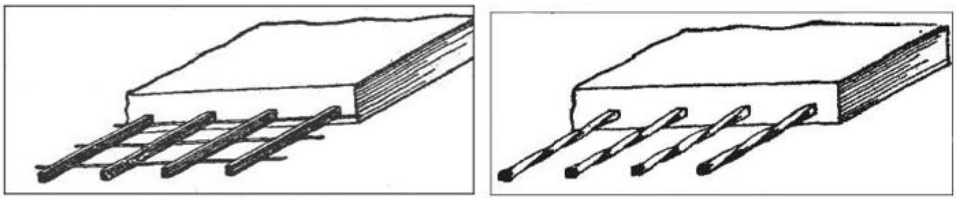

Figure 1.16. To the left: Hyatt system (1878), constituted by main reinforcement rebars connected by steel wires passing through holes. To the right: Ransome system (1884), with helicoidal rebars (Traettino, 2005)

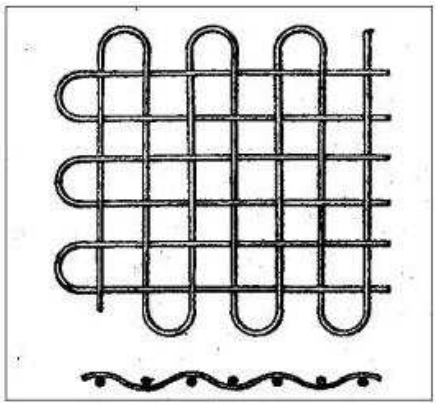

Figure 1.17. Cottancin system (1889), characterized by a regular weave of two separated rebars **(**Traettino, 2005**)**

Rebars are characterized by variable diameters, usually between 4 and 32 mm, and they are used both as longitudinal reinforcements and as stirrups, to keep the longitudinal bars and withstand shear. Nowadays, the use of arc-welded steel nets with spacing between 10 and 20 cm is frequent, mainly for the reinforcement of slabs and walls (Traettino, 2005).
Reinforced concrete production can be both cast *in situ* and prefabricated.

On site, production is performed by casting the conglomerate inside formworks, where rebars were previously placed. To ensure concrete homogenization, it is subjected to vibration procedures, both vibrating the formworks and through vibrating probes inserted in the fresh conglomerate. Formworks must be removed only after an adequate period of curing of concrete in humid conditions, to prevent rapid superficial water evaporation and consequent cracking development. Generally, curing is performed through the deposition of a film of water on concrete surfaces and subsequent covering of the structural elements with tissues.

On the other hand, prefabrication of concrete leads to the production of modular structural elements, both at the production site or in dedicated production plants, and subsequent assembly (figure 1.18). This technique, even if it implies logistical difficulties due to materials transportation and placing, allows a better control of the production process.

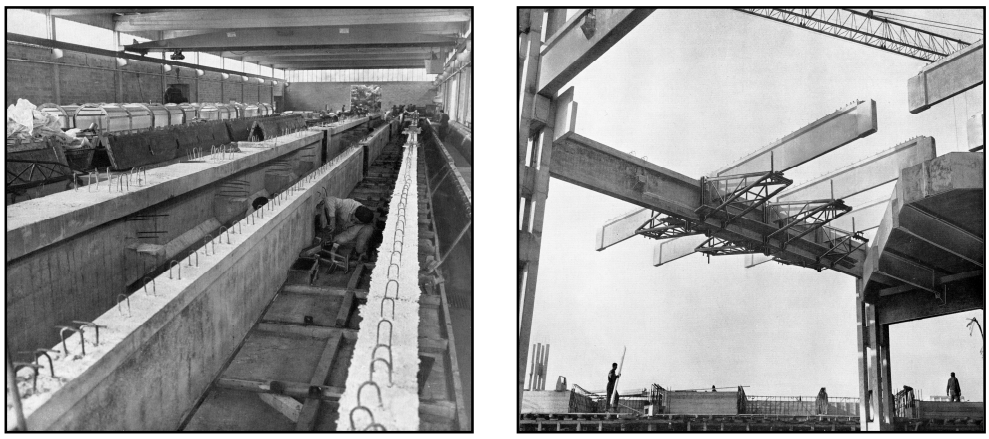

Figure 1.18. Prefabrication of reinforced concrete modular elements and subsequent placing at the construction site, ex Foro Boario (PD) (Saccomani, 1970)

A fundamental component of reinforced concrete is the so-called concrete cover, defined as the volume of conglomerate between rebars and external atmosphere. This element plays a fundamental role in the conservation of steel rebars from oxidation (as it will be thoroughly discussed in the following paragraphs), and thus it must be sufficiently thick and characterized by low permeability. The inadequacy of concrete covers is one of the main causes for historic concretes degradation. Nowadays, stainless steel rebars are produced, but high production costs limit their capillary diffusion in reinforced concrete production technology (Traettino, 2005).

1.6 CONCRETE DEGRADATION

Concrete degradation can be related to chemical, physical or mechanical degrading agents and is favored both by external and intrinsic factors. The main external factors which influence concrete degradation are temperature, relative humidity, water percolations, exposure to polluted environments, waters and soils, and construction in seismic areas. Intrinsic factors are mainly related to the nature of concrete constituents and production technology. Nowadays, the knowledge of the influence of mix design on durability of concrete allows obtaining high performance materials through optimization of concrete proportioning. As previously seen, the adoption of adequate w/c ratios and correct selection of aggregate in terms of both minero-petrographic composition and grain size distribution are factors that influence markedly concrete durability properties. Also, accurate casting is crucial for the resistance of concrete to external degrading agents. For instance, inadequate vibration can cause segregation of the inert fraction, with consequent development of anomalous porosity that leads both to low mechanical properties and reduced durability (Taylor, 1990 St John et al., 1998). Correct structural planning of concrete buildings is equally important for the improvement of mechanical resistance and durability. Incorrect load calculations could lead to overloading tensile stresses on structural elements, causing deformation and fissuration and subsequent chemical, physical and mechanical deterioration.

In order to perform an accurate analysis of concrete degradation, it must be taken into account that alteration factors and phenomena are strictly interrelated. For instance, a chemical alteration can cause a mechanical stress which favors a physical attack (Taylor, 1990; Walker, 1992). The following paragraphs present an overview of the main concrete degradation phenomena, taking into consideration triggering factors and consequences on material durability.

1.6.1 Acidic attack

Cement conglomerates are subject to acidic attack due to their natural alkalinity. Acidic attack can be related to the action of both organic and inorganic acids derived from atmospheric pollutants like carbon, nitrogen and sulfur oxides (Zivica & Bajza, 2001).

These acidic compounds can derive from industrial processes and urban multi-pollutants, but also from natural processes such as bacterial and vegetal activities. The main effects of acidic attack on concrete are dissolution and leaching phenomena on the cement matrix which cause loss of cohesion, worsen mechanical properties and trigger other alteration processes. The intensity of acidic attack is related to the permeability of materials and concentration of acids in pore solution (Zivica & Bajza, 2001; 2002). Acids dissolve hydrated phases of cement (CSH, CH, AFm, AFt) and form salts. These compounds can be insoluble, forming passivating layers that protect concrete from further alteration (as in the case of calcium oxalates), or they can react with other components of cement matrix and form expansive reaction products that cause cracking due to the development of tensile stresses on conglomerates, as in the case of sulfuric acid, that leads to the formation of gypsum and ettringite (Zivica & Bajza, 2001):

$$H_2SO_4 + Ca(OH)_2 \rightarrow CaSO_4 \cdot 2H_2O \quad (1.10)$$

$$3CaSO_4 \cdot 2H_2O + 3CaO\ Al_2O_3 \cdot 6\ H_2O + 24\ H_2O \rightarrow 3CaO \cdot Al_2O_3 \cdot 3CaSO_4 \cdot 32\ H_2O \quad (1.11)$$

Waters rich in carbon dioxide, characterized by pH values below 8.5, can be highly aggressive for concretes. CO_2 can derive from biochemical processes such as decomposition, bacterial activities and decomposition of carbonate compounds in soils. Carbon dioxide reacts with portlandite according to the following reactions:

$$CO_2 + Ca(OH)_2 \rightarrow CaCO_3 + H_2O \quad (1.12)$$

$$CO_2 + CaCO_3 + H_2O \rightarrow Ca(HCO_3)_2 \quad (1.13)$$

Calcium bicarbonate has higher solubility than calcium carbonate, thus it easily hydrolyzes in water solution, with consequent loss of hydration products in the cement matrix (Zivica & Bajza, 2001; Harris, 2001; Soler, 2007).

Amongst organic acids, the most dangerous ones are acetic acid and phenols. These compounds react with cement matrices causing decalcification of hydrated products (both CH, CSH, AFm and AFt) and forming highly water-soluble calcium salts (calcium acetates and calcium phenolates), thus hindering the formation of passivating layers that stop alteration process. Consequently, a continuous progression of degradation occurs, which leaves decalcified matrices constituted by amorphous silicates only, highly fractured and subjected to dusting (Zivica & Bajza, 2001).

As previously stated, concretes are always subject to acidic attack due to their alkalinity. Nevertheless, their resistance can be improved by optimizing mix designs. Conglomerates

with high cement dosages and w/c ratios under 0.5 result to be more resistant due to their low permeability (Zivica & Bajza, 2002).

1.6.2 Carbonation

Carbonation is the main cause of the chemical degradation of reinforced concretes. Carbonation process causes the transformation of portlandite (present in cement matrices as a secondary product of cement hydration) into calcium carbonate due to the diffusion of atmospheric CO_2 into concrete pore network, according to the following reaction (Taylor, 1990; Walker, 1992; St John et al., 1998):

$$Ca(OH)_2 + CO_2 \rightarrow CaCO_3 + H_2O \quad (1.14)$$

(in water solution)

Portlandite consumption and calcium carbonate formation lower concrete pH from values of about 12.5 to values lower than 9. Calcite is not the only carbonation product. Frequently, a high degree of carbonation causes the formation of aragonite and metastable calcium carbonates like vaterite (Zivica & Bajza, 2001). The carbonation degree is inversely proportional to the saturation degree of concrete, as CO_2 penetration is hindered by high water saturation levels in the pores. Nevertheless, low degrees of saturation tend to curb the reaction, as the carbonation process develops in water solution. Thus, the ideal relative humidity interval for the development of the process is between 50 and 70 % (Taylor, 1990; Walker, 1992; St John et al., 1998). Carbonation is an interfacial process which develops from the external to the inner portions of concrete. The progression of the carbonation front in time is expressed by the following equation (Bertolini & Pedeferri, 2000):

$$s = K\sqrt[n]{t} \quad (1.6)$$

where *s* is the carbonation depth, *t* is the time of exposure, *n* is a coefficient related to concrete porosity (n = 2 for porous concretes, n > 2 for compact concretes) and K is a coefficient related to environmental and compositional factors (relative humidity, temperature, CO_2 concentration, concrete alkalinity, w/c ratio and degree of curing of conglomerate).

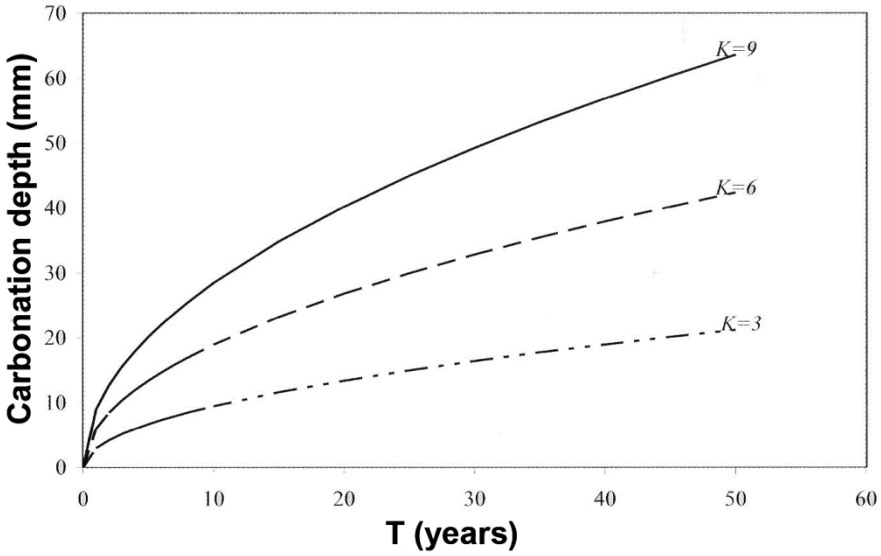

Figure 1.19. Progression of the carbonation front at different K values

As it is crucial for the degree of connected porosity of concrete, w/c ratio plays a fundamental role in determining the extent of carbonation. Similarly, appropriate concrete curing helps in the reduction of this alteration phenomenon.

$CaCO_3$ formation from portlandite determines an increase in molecular volume of approximately 11%, with consequent filling of capillary pores, better compaction of the concrete components and overall improvement of the mechanical properties. On the other hand, pH lowering is deleterious for the conservation of rebars. If the carbonation depth exceeds the concrete cover, rebars are subjected to oxidation, with consequent corrosion and triggering of expansion and fracturing phenomena of the conglomerate (Taylor, 1990; Walker, 1992; St John et al., 1998; Bertolini & Pedeferri, 2000).

1.6.3 Corrosion of reinforcement bars

Carbonation is the main cause of rebars corrosion, due to pH lowering at unfavorable values for the permanence of iron at metallic state. At a pH above 12, typical of unaltered concrete, a thin layer of stable iron oxides and hydroxides develops around the rebars, hindering the penetration of oxygen and water and thus passivating metallic iron from further oxidation. To favor passivation, rebars are frequently covered by magnetite and ferric oxide layers prior to casting.

Passivating oxides become unstable and dissolve at pH lower than 9, allowing oxidation to develop according to the following reactions (Taylor, 1990; Walker, 1992; St John et al., 1998; Bertolini & Pedeferri, 2000; Collepardi et al., 2005; Massidda, 2005; Berke, 2006):

$$4Fe + 8H_2O \rightarrow 4FeOOH + 12\ H^+ + 12e^- \quad (1.15)$$

$$3O_2 + 6\ H_2O + 12e^- \rightarrow 12OH^- \quad (1.16)$$

These electrochemical reactions take place in the presence of an electrolyte, represented by the aqueous solution saturating concrete's pore network. Depassivated iron acts as anode and oxidizes, while still passivated areas act as cathode, attracting electrons released from the anode and releasing hydroxyl groups that migrate from cathode to anode through the electrolyte. The corrosion of rebars causes the formation of hydrated iron oxides, commonly called rust, mainly amorphous and with a molecular volume markedly higher than metallic iron. For this reason corrosion, apart from causing the progressive consumption of rebars with consequent reduction of the tensile strength of reinforced concrete, provokes phenomena of spalling, cracking and corrosion of concrete, with possible detachment of concrete cover and further exposure of the uncorroded steel to the action of degrading agents (Taylor, 1990; Walker, 1992; St John et al., 1998; Bertolini & Pedeferri, 2000; Collepardi et al., 2005; Massidda, 2005; Berke, 2006).

1.6.4 Chloride attack

Presence of dissolved chlorides in pore solution is a significant cause for corrosion of reinforcement bars. Chlorides in pore solution can derive from the raw materials themselves (water, aggregates, admixtures) or from the external environment, mainly capillary rise of saltwater and water saturated by deicing salts (sodium chloride and calcium chloride). Chloride action on rebars causes a localized removal of passivating layers, forming soluble and unstable iron chlorides. The exposure of metallic iron to oxidizing agents triggers oxidation and consequent localized and radial corrosion of rebars, the so called pitting corrosion (Taylor, 1990; Walker, 1992; St John et al., 1998; Bertolini & Pedeferri, 2000; Collepardi et al., 2005; Massidda, 2005; Berke, 2006). This type of oxidation is particularly dangerous, as it does not provoke massive expulsions of iron hydroxides and detachment of concrete cover during the first phases of alteration, consequently making the degradation phenomenon difficult to recognize.

Electrochemical reactions are similar to the ones developed by carbonation, with the exception that the triggering factor is the chloride concentration in solution and not the pH decrease: this allows the start of the oxidation phenomena in alkaline systems too, typical of sound concretes. The critical concentration value for triggering chloride attack is strongly pH-dependent: the lower the pH, the lower the threshold concentration.

Chloride attack does not cause oxidation of rebars only. The phenomenon causes pH decrease to values under 5, with consequent development of acidic attack phenomena on the hydrated phases. Chloride ions can interact with hydrated phases in several ways. Calcium chloride reacts with portlandite to form hydrated calcium oxychloride according to reaction 1.17, while chloride ions interact with sulfate AFm phases to form, by anions exchange, a chloride-containing AFm called Friedel's salt, according to reaction 1.18 (Taylor, 1990).

$$3Ca(OH)_2 + CaCl_2 + 12H_2O \rightarrow 3CaO\cdot CaCl_2\cdot 15H_2O \quad (1.17)$$

$$2\ Cl^- + 3CaO\cdot Al_2O_3\cdot CaSO_4\cdot 10H_2O \rightarrow 3CaO\cdot Al_2O_3\cdot CaCl_2\cdot 10H_2O + SO_4^{2-} \quad (1.18)$$

The resulting expansive compounds can cause both cracking of concrete and formation of superficial efflorescence.

Finally, the saturation of portions of concrete pore network by chloride-rich solutions causes the decrease of the freezing temperature of water, with possible freezing of pore water in adjacent volumes not saturated by chloride salts due to heat subtraction, with consequent triggering of degradation due to freeze-thaw cycles (St John et al., 1998).

1.6.5 Sulfate attack

Amongst the various concrete degradation phenomena, sulfate attack is one of the most dangerous, due to the combined action of tensile stresses generated after the formation of secondary expansive phases, and hydrated phases consumption, with consequent loss of cohesion of the cement matrix (Taylor, 1990; St John et al., 1998). Sulfates may derive from the external environment or from the concrete itself: the former is the case of external sulfate attack (ESA), the latter of internal sulfate attack (ISA).

ISA occurs when sulfate-rich solutions saturate the concrete pore network. This phenomenon is frequent in areas near the coastline, due to the capillary rise of saltwater rich in sulfates, or in polluted areas, both domestic and industrial, due to the capillary rise of polluted fluids and dissolution in pore solution of atmospheric sulfates. Generally,

sulfate attack develops from the external to the inner portions of conglomerate, causing differential tensile stresses between the attacked cortex and the sound inner volume, with consequent occurrence of fracturing phenomena and spalling (Collepardi et al., 2005).

ISA may also be caused by the presence of contaminating gypsum in concrete, both from aggregate and by thermo-decomposition on primary ettringite during vapor curing at temperatures above 70°C. Contaminating gypsum is characterized by lower reactivity with respect to calcium sulfates added to prevent flash set. Also, it is generally characterized by higher crystal size, thus it hydrolyzes slowly.

In both types of sulfate attack, the formation of expansive delayed reaction products in an hardened cement matrix causes mechanical stresses which lead to the development of internal cracking and loss of cohesion (Collepardi et al., 2005).

The main primary and hydrated phases interested by sulfate attack are portlandite, monosulfate and C_3A. Firstly, portlandite is converted into gypsum according to reaction 1.19. Then, sulfates in solution and secondary gypsum produced by reaction 1.19 convert monosulfate and unhydrated C_3A into AFt phase ettringite (delayed ettringite formation, DEF), according to reactions 1.20 and 1.21 (Taylor, 1990; St John et al., 1998).

$$Ca(OH)_2 + SO_4^{2-} + 2H_2O \rightarrow CaSO_4 \cdot 2H_2O + 2OH^- \quad (1.19)$$

$$3CaO \cdot Al_2O_3 \cdot CaSO_4 \cdot 12H_2O + 2(CaSO_4 \cdot 2H_2O) + 16\ H_2O \rightarrow 3CaO \cdot Al_2O_3 \cdot 3CaSO_4 \cdot 32\ H_2O \quad (1.20)$$

$$3CaO \cdot Al_2O_3 + 3(CaSO_4 \cdot 2H_2O) + 26\ H_2O \rightarrow 3CaO \cdot Al_2O_3 \cdot 3CaSO_4 \cdot 32\ H_2O \quad (1.21)$$

C4AF and its hydrated phases can equally be interested by sulfate attack, thus generally sulfate-resistant cements do not contain interstitial phase in concentrations higher than 3%.

Portlandite easily reacts with several sulfate salts (reactions 1.22, 1.23, 1.24, 1.25), forming secondary gypsum and consequently triggering DEF (Taylor, 1990; St John et al., 1998).

$$(NH_4)_2SO_4 + Ca(OH)_2 \rightarrow CaSO_4 \cdot 2H_2O + 2NH_3 \quad (1.22)$$

$$MgSO_4 + Ca(OH)_2 + 2H_2O \rightarrow CaSO_4 \cdot 2H_2O + Mg(OH)_2 \quad (1.23)$$

$$Na_2SO_4 + Ca(OH)_2 + 2H_2O \rightarrow CaSO_4 \cdot 2H_2O + 2NaOH \quad (1.24)$$

$$K_2SO_4 + Ca(OH)_2 + 2H_2O \rightarrow CaSO_4 \cdot 2H_2O + 2KOH \quad (1.25)$$

Also magnesium sulfate reacts with CSH, according to the following reaction:

$$x MgSO_4 + x CSH + x H_2O \rightarrow x CaSO_4 \cdot 2H_2O + x Mg(OH)_2 + x SH \quad (1.26)$$

The formation of secondary brucite causes pH decrease to values of about 10.5. To buffer the phenomenon, CSH dissolves to form portlandite. Newly-formed portlandite reacts again with magnesium sulfate, with further formation of secondary gypsum and brucite, with a cyclic progression of the degradation phenomenon that causes progressive

consumption of hydrated calcium silicates. Moreover, gypsum triggers delayed ettringite formation, and brucite reacts with the amorphous silica gel deriving from magnesium sulfate attack, producing hydrated magnesium silicate according to the following reaction:

$$4Mg(OH)_2 + S\text{-}H_n \rightarrow 4MgO \cdot SiO_2 \cdot 8.5H_2O + (n - 4.5)\, H_2O \quad (1.27)$$

This compound does not have cementing properties, thus concrete results to be poorly coherent and subjected to dusting (Al-Amoudi et al. 1995; Tulliani et al., 2002; Irassar et al., 2003; Neville, 2004).

A further alteration product produced by sulfate attack is thaumasite. This phase is produced by the reaction among CSH, sulfates and secondary gypsum derived from the reaction of portlandite, in climates characterized by low temperature (0-5°C), high relative humidity (UR > 95%) and rich in carbon dioxide:

$$CaSO_4 \cdot 2H_2O + CaCO_3 + CaO \cdot SiO_2 \cdot H_2O + 12H_2O \rightarrow CaO \cdot SiO_2 \cdot CaSO_4 \cdot CaCO_3 \cdot 15H_2O \quad (1.28)$$

The deleterious effects of thaumasite are related both to the tensile stress caused by its high crystallization pressure, and CSH consumption, with consequent disaggregation of the cement matrix (Taylor, 1990; St John et al., 1998).

1.6.6 Alkali-related attacks

Alkalis are frequently present in concrete pore solution in form of soluble salts, mainly alkaline chlorides and sulfates. Sources of alkalis are both external, by capillary rise of saturated solutions, and internal, by leaching from cement matrix and aggregate. Alkaline salts diffuse into concrete by capillarity and can cause four different types of attack: volume increase for hydration reaction, development of hydration pressure, development of crystallization pressure and alkali-aggregate reactions (St John et al., 1998; Thaulow & Sahu, 2004). The first three attacks cause a physical alteration due to development of mechanical stresses on the cement matrix, while the latter causes a combined physical-chemical attack by synergic alteration of concrete constituents and development of tensile stresses due to the formation of hydrated phases.

Volume increase of salts due to hydration is determined by the incorporation of water molecules into their lattice, and causes the application of a hydration pressure on the pore walls. Alkaline sulfates, in particular sodium sulfate thenardite, are easily subjected to hydration, with formation of phases characterized by various water content (e.g. for thenardite: dihydrated eugsterite, decahydrated mirabilite). Crystallization pressure

develops during the precipitation of a salt from a supersaturated solution. It is not necessarily related to hydration processes, and it is exerted by any salt during precipitation. Factors that most influence salt crystallization are solubility, concentration, temperature and relative humidity (Thaulow & Sahu, 2004). These three forms of attack generate tensile stresses on cement matrices that cause cracking, exfoliation and spalling of wide areas of concrete, with consequent exposure of sound portions to the action of external degrading agents (Al-Amoudi et al., 1995; St John et al., 1998; Tsui et al., 2003; Thaulow & Sahu, 2004). The phenomena usually occur in the external portions of concrete structural elements, characterized by significant temperature and relative humidity variations, which favor water evaporation and thus salt crystallization.

Alkali-aggregate reactions (AAR) occur between alkalis in pore solution and various types of aggregate, causing dissolution of the inert fraction and production of secondary phases, often amorphous and characterized by expansive behavior after hydration processes. AAR are divided into two main categories: the alkali-silica reactions (ASR) which interest aggregates partially or totally constituted by amorphous silica like opal, chalcedony, chert, quartzite, ignimbrites and tuffs, and the rarer alkali-carbonate reactions, which interest microcrystalline dolostone and magnesian limestone (Taylor, 1990; Rear et al., 1994; St John et al., 1998; Pecchioni et al., 2008).

As previously seen, alkaline salts dissociate in pore solution, and their anions react with cement matrix constituents to form secondary phases like gypsum, ettringite, calcium oxychloride and Friedel's salt. Moreover, cations react with water to form alkaline hydroxides. These compounds dissociate and hydroxyls cause the break-up of Si-O-Si bonds of amorphous siliceous matrices, releasing in solution silicate anions that react with alkalis to form amorphous silica gels, subject to hydration processes and thus highly expansive (Taylor, 1990; Rear et al., 1994; St John et al., 1998; López-Buendía et al., 2006; Peterson et al., 2006). Hence, ASR are deleterious both for the progressive break-up of aggregate, and for the tensile stresses caused by secondary compounds formation, with consequent development of cracking and loss of overall mechanical strength.

ACR are related to the de-dolomitization phenomenon caused by the reaction between the hydroxyl groups released by the dissociation of alkaline hydroxides and dolomite, with formation of secondary calcite and magnesite according to the following reactions:

$$CaMg(CO_3)_2 + 2OH^- \rightarrow Mg(OH)_2 + CaCO_3 + CO_3^{2-} \quad (1.29)$$

$$CO_3^{2-} + Ca(OH)_2 \rightarrow CaCO_3 + 2OH^- \quad (1.30)$$

$$CO_3^{2-} + Mg(OH)_2 \rightarrow MgCO_3 + 2OH^- \quad (1.31)$$

Secondary carbonates are not expansive, therefore the only alteration contribute of this form of alteration is related to the progressive dissolution of aggregate (Taylor, 1990; Rear et al., 1994; St John et al., 1998; Ozol, 2006; Stark, 2006).

1.6.7 Freeze-thaw cycles

The physical damage of concrete due to freeze-thaw cycles is a crucial topic for the conservation of reinforced concrete structures exposed to cold climates. The deterioration is related to a progressive cracking development due to the tensile stresses caused by cyclic phase transitions of water saturating concrete pore network (St John et al., 1998). At temperatures below $0^{\circ}C$, water freezes, with an increase in volume of about 9% during the transition from liquid to solid state. This process causes the development of tensile stresses on pore walls, which accumulate during a series of subsequent cycles, opening cracks progressively larger, with consequent loss of mechanic strength on attacked concrete. The phenomenon is particularly effective on small water saturated pores like many capillary pores, characterized by the lack of free space to absorb the volume change. On the other hand, entrained air voids, generally connected with capillary pores, can absorb tensional states constituting large reservoir spaces for pore water during phase transition.

A common procedure to prevent the development of this alteration process is the use of deicing salts during cold seasons, with negative consequences related as regards chloride attack. A more effective way to improve concrete resistance to freeze-thaw cycles is the use of air entraining agents during the production of concrete. These admixtures develop a net of entrained air voids on the hardened paste, which are able to absorb tensional stresses during phase transition of pore water.

1.6.8 Physical-mechanical alterations related to environmental causes

Reinforced concrete structures built in marine environments are particularly subject to erosion due to the mechanical action of waves. Intertidal areas are most exposed to degradation. In these portions, continuous variations in the saturation degree of pore

network cause degradation phenomena due to chloride attack and soluble salts crystallization.

Fire damage on reinforced concrete is another significant factor which influences the conservation state of modern structures. Despite its good reactions to thermal events, concrete is not a refractory material. According to the temperature, the time of exposure and the intensity of thermal gradients, concrete undergoes a series of chemical, mineralogical and textural changes. The main events are the evaporation of saturating water between 100°C and 200°C, the loss of structural water on the hydrated phases over 250°C, the decomposition of portlandite at 550°C and the deterioration of the aggregate over this value. Macroscopically, it is possible to observe massive cracking development, exfoliation phenomena, loss of adhesion between components and spalling. Also, the higher thermal expansion coefficient of steel with respect to concrete at high temperatures causes the development of further tension in the material, with dramatic loss in compressive and tensile strength and consequent structural failure (St John et al., 1998; Georgali & Tsakiridis, 2005; Szoke, 2006).

Seismic action can determine irreparable static damages on concrete structures. The release of seismic energies, which causes intense horizontal and vertical motions transferred to the structural elements, can cause the insurgence of macro-cracking, with consequent partial and total collapse of the interested structures (St John et al., 1998).

CHAPTER 2

The studied structures

2.1 INTRODUCTION

This work was aimed at the characterization of cement conglomerates of five historic buildings made of reinforced concrete structural elements. The structures are all located in north-eastern Italy, and they are all protected by national laws concerning the conservation of cultural heritage, being important historic monuments, building of industrial archaeological interest, or both. Moreover, four out of the five buildings studied are currently interested by restoration and rehabilitation, thus the characterization of construction materials has been of crucial importance to reach a proper level of knowledge for the continuation of the works.

The construction time of the five buildings spans over a wide chronological period, comprised between the last decade of the 19th century and the 1960s. They all belong to the first era of reinforced concrete production, characterized by the lack of plasticizers and water-reducing admixtures in the mixes, consistency of the pastes below S4, project of the mixes according to prescribed dosages and not to performance criteria and prevalence of the *in situ* construction of the reinforced concrete structural elements over the use of prefabricated modules. In the following paragraphs, the history of construction and fruition of the studied buildings is briefly reported, together with concise reports on their main structural and architectural features.

2.2 NORTHERN WING OF THE CARRARESI CASTLE

2.2.1 Historical background

The castle is located on the south-west side of the city of Padova, near the Bacchiglione river. The first written accounts regarding the construction of fortified structures in the area dates back to 899. Probably, the fortifications consisted in two separated structures: a tower called Torlonga, and a series of smaller buildings.

The construction of an organic structure dates back to 1242, during the rule of Ezzelino III da Romano. The tyrant patronized the reconstruction of the Torlonga tower and the construction of a second tower, linking the two structures with smaller fortifications. The complex served mainly as a prison. Starting from 1374, under the rule of the Carraresi family, a radical restoration and reconstruction of the structure was performed. The two towers were incorporated into an organic complex, constituted by four wings developed around a central court with an irregular rectangular shape (Bressan, 1986).

In 1405, during the Republic of Venice, a total restoration of the defense system of Padova started. The project planned the construction of a new castle, but it was never carried out. The structure was almost totally abandoned for the following four centuries, apart from occasional uses as warehouse, which caused massive damage to the structures, with numerous structural collapses (figure 2.1). Only the Torlonga tower and the surrounding buildings were preserved from decay, after their final transformation into an astronomical observatory in 1767 (Bressan, 1986). Due to its function, the Torlonga tower was renamed Specola.

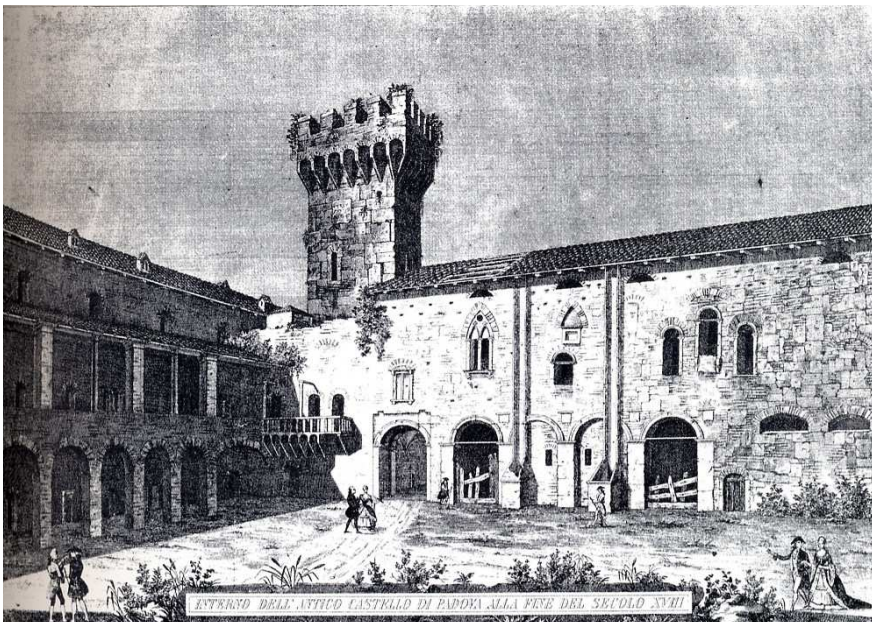

Figure 2.1. Conservation state of the Castle of Padova at the end of 18th century, view from the internal court (Bressan, 1986)

At the beginning of 1800, under French rule, massive restoration works were performed, planned by Daniele Danieletti, to convert the building into a prison. From this moment on, no precise information is available as its use as a prison markedly restricted details on new constructive works. Great help is given by the data reported on the various land registries drafted under French and Austrian rule and under the Italian reign, which showed limited planimetric changes and construction of new buildings during the 19th century (Bressan, 1986) (figure 2.2).

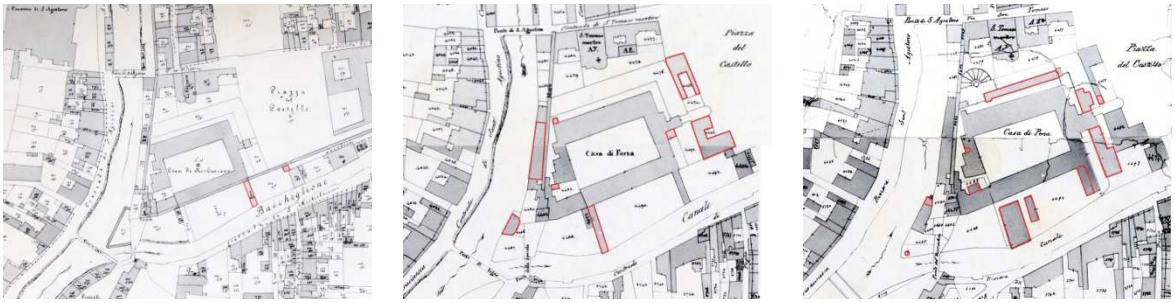

Figure 2.2. Constructive evolution of the Castle of Padova between 19th and 20th century, as indicated by land registries (new buildings indicated in red. Left: 1811 French registry; center: 1845 Austrian registry; right: 1869 Italian registry)

Over the course of the 20th century, the needs of the prison kept growing (also due to the presence of a bicycle production laboratory in the southern wing and a furniture production

laboratory on the ground floor of the northern wing) and, as shown by the Italian land registry of 1956, new volumes were built in the remaining areas (Bressan, 1986).

Pre-existing structures also were interested by noteworthy changes over the last two centuries. The original arched open gallery of the northern wing, limited to the first two floor only (figure 2.1), was raised to the third floor at the beginning of 20th century, maintaining the masonry constructive technique (figure 2.3). Damaged by bombings during World War I, it was reconstructed with a configuration similar to the pre-existing one. Damaged again by World War II bombings, it was substituted during the 1950s by a new open gallery entirely made of reinforced concrete (figure 2.4).

Figure 2.3. Image of the castle at the beginning of the 20th century. The new configuration of Northern wing's open galley is visible (image from Alinari's archive)

Figure 2.4. Northern wing's open gallery, current state

As regards the internal configuration, possibly the majority of modifications were carried out during Danieletti's restoration, with the exception of the substitution of the original timber ceilings with reinforced concrete frames in various constructive phases. In particular, in 1899 hygiene requirements related to the transformation of three dormitory-rooms into infirmary led to the substitution of timber ceilings on three rooms of the first floor with reinforced concrete slabs and beams made by Porcheddu company according to Hennebique construction system. After severe damage caused by World War I bombings, in 1920s the remaining timber ceilings were substituted by reinforced concrete beams and slabs. Moreover, the demolition of some walls on the ground floor to create a unique room, suitable for the establishment of the furniture production laboratory, required the construction of a reinforced concrete structural frame constituted by columns sustaining slabs and beams. Finally, during the restoration works carried out in the 1950s, additional

internal modifications were performed, such as placing a large reinforced concrete beam in the first room of the first floor to better sustain Hennebique slab, and the substitution of the ceilings of both the rooms near the stairs, the first three rooms of the ground floor and some of the rooms of the second floor with reinforced concrete beams sustaining slabs in concrete and masonry.

The castle was finally abandoned in 1990 after the closing of the prison, and it was subject to a rapid and intense degradation. Both the southern and the northern wing roofs were interested by collapse, the first due to a fire, the second due to snow overload.

Since 2003, restoration and rehabilitation of the area has started, first with the demolition of some secondary buildings, and then, in 2008-2009, with the reconstruction of collapsed roofs. Apart from these emergency interventions, a complete restoration of this cultural heritage would return to the city of Padova a fundamental witness of its ancient and recent past.

2.2.2 Structural and architectural features

The actual castle conformation is the result of the heavy modifications which followed one another during time, according to its various uses. Today, the structure cannot be considered a homogeneous building, and it can be subdivided in various sectors, characterized by different uses and construction techniques. The building near the Bacchiglione river, facing the short side of the central court, and the adjacent Specola tower, are property of the University of Padova and of the National Institute of Astrophysics, respectively. On the other side of the structure, the buildings facing the square of the castle are both private and property of the Italian Ministry of Justice. Southern buildings are property of the City of Padova.

The central nucleus, where the former prison was located, is under the protection of the Regional Board of the Italian Ministry of Cultural Heritage. It is organized in three main buildings: a U-shaped structure around the central court, a building looking eastward and a series of small buildings northward, corresponding to the former confinement cells. The U-shaped building corresponds to the ancient medieval castle, as demonstrated by constructive details and by the presence of valuable wall paintings. It can be subdivided in three wings: southern wing, eastern wing and northern wing (figure 2.5).

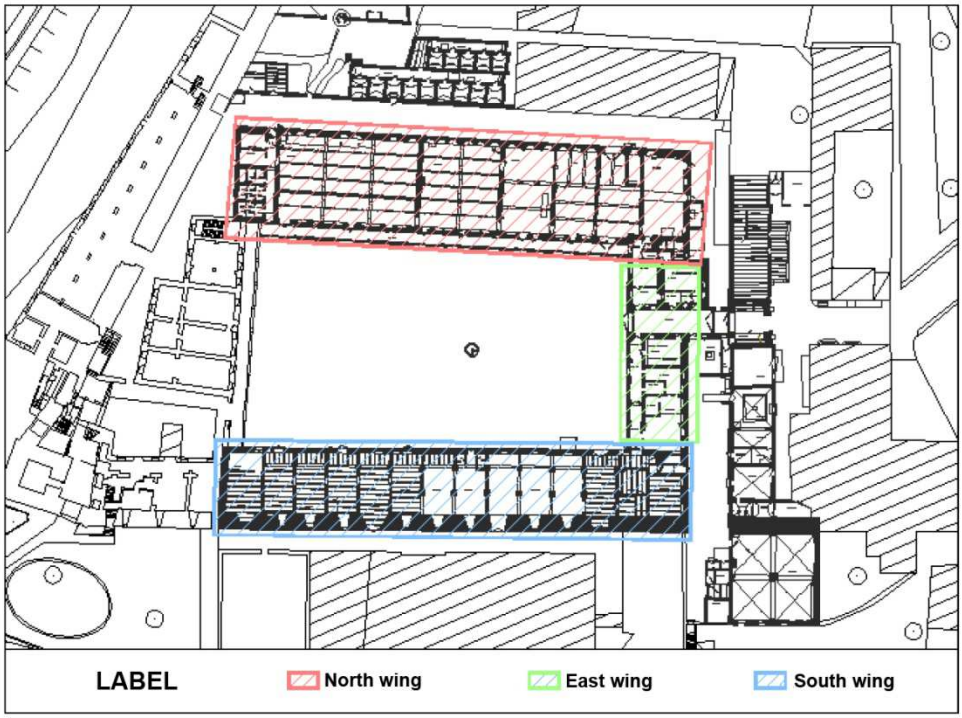

Figure 2.5. Plan of the complex. Wings of the U-shaped buildings are highlighted

The northern wing is a three-storey building: at the ground floor a furniture production laboratory was located, while the upper floors were occupied by cells. The second floor was probably transformed into a series of closed rooms during Danieletti's restoration, as demonstrated by the presence of a series of external arches under the windows, constituting a typical medieval architectural element for the decoration of the terminal portions of masonry walls. Probably, the second floor of the castle was occupied by an open castellated wall. The facade facing the central court is covered by a reinforced concrete open gallery, constructed during the 1950s. The northern facade has a regular series of rectangular windows, probably opened during Danieletti's restoration.

As regards the internal organization of the building, various interventions were performed to unify originally independent rooms. The older interventions, probably executed during Danieletti's restoration, regarded the first three rooms of both ground and first floor, and consisted in the opening of the internal partition walls with three arched apertures (figure 2.6).

The later interventions, probably all executed during the 1920s restoration, consisted in the total demolition of partition walls at the ground floor, substituted by a reinforced concrete structural frame, in order to create a great hall suitable for the productive activities (figure

2.7). Partition walls were also demolished at the upper floors, and were at times substituted by thinner ones, sustaining the new reinforced concrete ceilings and the roof.

Figure 2.6. First floor, opening of partition walls with arched apertures

Figure 2.7. Ground floor, substitution of original partition walls with reinforced concrete frame

As regards the horizontal structural elements, various types of ceilings are observable, pertinent to the various constructive phases. The first three rooms of the ground floor have concrete and masonry ceilings, constructed during the 1950s. On the other rooms of the ground floor reinforced concrete ceilings are present, constructed during the 1920s. All ceilings of the first floor are made of reinforced concrete (1899 and 1920s construction phases), with the exception of the room near the stairs, made in concrete and masonry (1950s construction phase). Some of the rooms of the second floor have ceilings made of concrete and masonry (1950s constructive phase), the others are covered directly by the roof. It is possible to observe two distinct shapes of reinforced concrete beams: beams of the first and third constructive phase are characterized by a regular rectangular section (figure 2.8), while the ones of the second constructive phase are characterized by an enlargement in proximity of the vertical structural elements (figure 2.9).

Figure 2.8. First floor, conformation of Hennebique reinforced concrete beams

Figure 2.9. First floor, conformation of 1920s reinforced concrete beams

The roof is made by timber trusses, sustained by masonry walls. It was interested by a massive collapse during the 1990s, and it has been recently restored according to the original construction technique.

2.3 VICTORY MONUMENT

2.3.1 Historical background

Inaugurated in 1928 and dedicated to the Victory, the monument is located just outside the historical center of the city of Bolzano, along the direction of the main road of the town and after the bridge on the Talvera river.

2.10. Victory monument today

The structure was conceived as a sign of hegemony of the Fascist regime on local German-speaking population. As decided by Fascist dictator Benito Mussolini, the monument was constructed demolishing the remains of a monument dedicated to the German conquest of Bolzano during World War I. The project had already been conceived by the dictator in 1926, and it was commissioned to fascist architect Marcello Piacentini, who gathered the most renowned artists of the time to carry out sculptures and paintings. The monument is nowadays considered one of the maximum expressions of fascist architecture, and it was only the starting point of a radical urban reorganization of the area, which became a monumental square focused on the monument itself (De Rose, 1995; Lupano, 1991; Piacentini, 1929; Soragni, 1993) (figure 2.11). Victory Monument is inspired by Roman triumphal arches, but Piacentini introduced new elements, mainly to simplify the structure architecture and to enhance its modernity and overall symbolic impact.

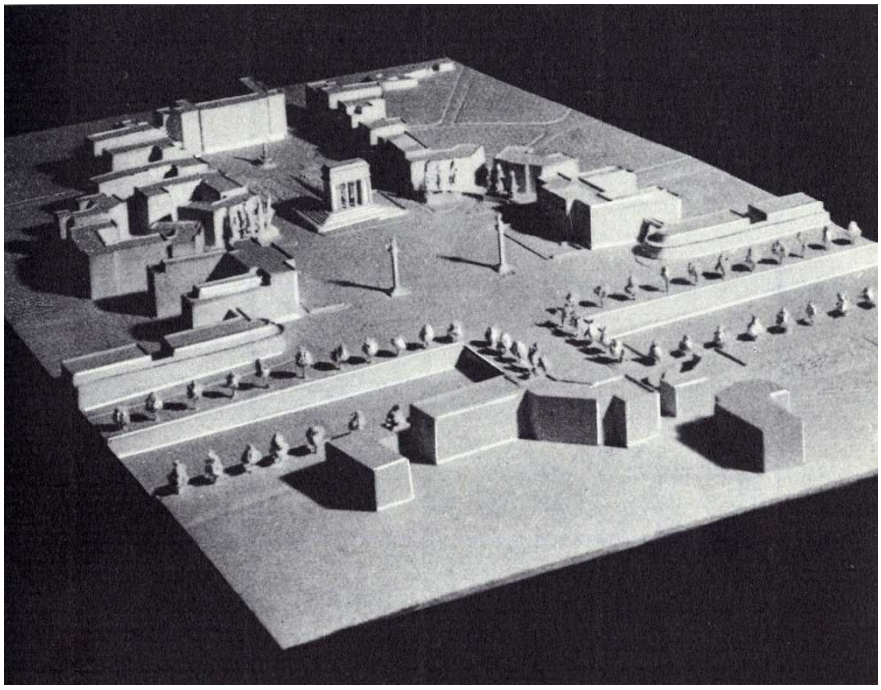

Figure 2.11. Plan of the new monumental square of Bolzano (Soragni, 1993)

Since the end of World War II, the future of the Victory Monument has been intensely debated. Several proposals were presented, including its demolition, a name change, or the creation of a museum against Fascism. The dispute culminated in the 1978 bomb attack, which partially damaged the structure. Today, the dispute is still ongoing, and no compromise has been reached on the future of the monument yet (Gentile, 2007; Nicoloso, 2008; Soragni, 1993).

2.3.2 Structural and architectural features

Inspired by Roman triumphal arches, the structure is 22 meters tall and 10 meters wide. The monument is conceived as a colonnade standing on a large stairway podium (figure 2.12), covering a subterranean crypt constituted by a large central room and sixteen small lateral rooms. The colonnade is constituted by fourteen multiple columns, without capital, sustaining the triumphal arch (figure 2.13).

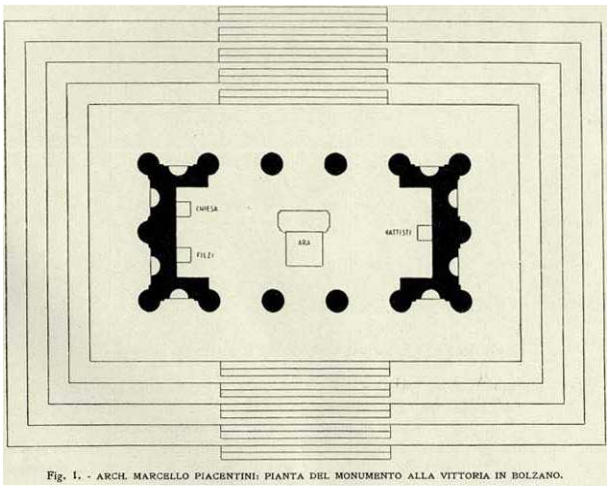

Figure 2.12. Plan of the monument

Figure 2.13. Detail of the multiple columns

The structure stands on a concrete strip foundation, lying on a flattened alluvial ground. The substructure of the podium is constituted by non-reinforced concrete walls, sustaining a series of reinforced concrete slabs forming the stairway and a non-reinforced concrete slab forming a central vault. The slabs of the stairway are limited by reinforced concrete beams (figure 2.14).

Figure 2.14. Detail of the reinforced concrete structural elements forming the stairway from an internal lateral room

The nucleus of the columns is also made of concrete, as well as the ceiling of the monument, sustaining a series of bronze beams. The monument is covered by stone slabs of different lithologic typologies, and decorated by sculptures and paintings made by famous fascist artists, amongst which three marble busts of the Italian irredentists Battisti, Filzi and Chiesa by Adolfo Wildt, a large bronze statue portraying the Risen Christ by Libero Andreotti and the winged Victory on the front facade by Arturo Dazzi (Soragni, 1993) (figure 2.15).

Figure 2.15. Winged Victory sculpture on the front facade

During the construction of the monument, the local representative of the government ordered inspections to verify the rumors on the poor quality of the works. The inspections were carried out too late and could not perform all necessary assessments.

Confirming the above-mentioned rumors, the building has showed clear structural problems since the first few years following its construction: foundation failures caused the breaking of the floor slabs, and massive water infiltrations caused damage not only to the stone coverings, but also to the concrete nucleus, with extensive fissuration of the concrete slab sustaining the colonnade and of the architraves of the columns. Also, the sculptures and the paintings were also heavily damaged by water infiltrations.

A first restoration of the monument was carried out in 1991-1992 by the Department of Cultural Heritage of Verona, and was aimed at consolidating the reinforced concrete nucleus of the colonnade and the bronze ceiling. A new restoration started in November 2009, under the supervision of the Italian Ministry for Cultural Heritage, and was stopped in 2011 as new disputes arose on the future of the monument.

2.4 EX-AGRIMONT AREA, C3 BUILDING

2.4.1 Historical background

Ex-Agrimont area is located in Porto Marghera (VE), and is a fundamental witness of the birth, rise and demise of one of the most important 20th century Italian industrial areas.

At the beginning of the 20th century, Venice hosted the second most important port of Italy, thus its evolution required a further expansion in the mainland, to support oil and carbon industry and better to take advantage of the evolving train transportation system. For the purpose, a free area near the railway, south from the city of Mestre, was chosen, and then called Marghera. Being a marshy area, extensive reclamation works were necessary to make the area fully usable for port activities (Chinello, 1975).

During World War I the construction of the first industrial area of Porto Marghera started, planned and promoted by Giuseppe Volpi, 1st Count of Misurata. The project was approved in 1917, and soon the first productive activities were established in the previously reclaimed areas, together with the first thermoelectric plant. Also, a large canal was drained in the lagoon in 1919 (the Vittorio Emanuele III channel), to connect the area

with the Venice port, and the urban settlement of Marghera was built in 1922 (Chinello, 1975).

The area was interested by a rapid development: in 1925 there were already seventeen industrial and commercial plants, with 1200 employees. At the beginning of World War II, more than one hundred companies were located in the area, with approximately 15000 employees. Due to this exponential increase, the extension of the area southwards began (Chinello, 1975).

The two main companies responsible for the rapid growth of Porto Marghera were Montecatini and Edison, which settled in the area with several chemical and energy production plants. The former built in 1927 the first nucleus of the future Agrimont industry. The production plant was aimed at the production of phosphate- and ammonia-based fertilizers according to the so-called "wet process method", and it was settled in a limited area, constituted by three productive buildings and one administrative building.

The first few years of World War II saw further development of the area, though afterwards it was interested by massive bombings which caused severe damage to the production plants.

After an initial phase of post-war crisis, culminating in the years 1950-51, the industrial area began to grow again: in 1955 all areas were occupied by productive plants, and there were about 18000 employees (Chinello, 1975).

Montecatini fertilizers production plant was significantly enlarged during these years, with the construction of three large buildings, all constituted by arched reinforced concrete frames, two located south from the older productive plant, and one north, the C3 building. The latter was linked to the others through a platform. Moreover, other secondary buildings were built, together with a series of large reservoirs near the navigation canal for the storage of raw materials.

In the mid-1950s, a plan for the construction of a second industrial area was approved, and several petrochemical industries were established and rapidly grew. From then on, the industrial area and the urban settlement knew a fast development, and in 1960 there were about 200 productive plants, working in the fields of chemistry, metallurgy, ceramic production and petrochemical production (Chinello, 1975).

During the years of economic boom other firms were established, and in 1963 the construction of a third industrial area was planned (but never built). The growth continued up until the mid-1970s, when the expansion of Porto Marghera halted and the number of

employees underwent a progressive reduction. The crisis was particularly severe during the 1980s, with a mean annual loss of 1000-1200 workplaces. The crisis forced the firms to carry out important internal reorganizations, and several companies permanently closed. During these years, the two companies responsible of the growth of Porto Marghera , Montecatini and Edison, merged, with the creation of the Montedison group. After the fusion, the fertilizer production plant passed under the administration of Agrimont company, controlled by Montedison itself. The crisis, by then endemic, continued during the 1990s and also hit Agrimont company, which ultimately closed in 1997.

After ten years of neglect, in 2007 the Ex-Agrimont area was included in the restoration plan of Porto Marghera industrial area. A reclamation of polluted soils was performed, together with the removal of the asbestos fiber cement roofing of the industrial buildings, and 7 hectares of the area were sold to Fincantieri S.p.A.. The remaining area was included in a project for the creation of a multi-purpose recreational center called "City of Cinema". The restoration and rehabilitation of the buildings started in 2009. Currently, the demolition of most damaged and less valuable buildings has been performed, and the restoration of the C3 building, which will constitute the gist of the new center, has started.

2.4.2 Structural and architectural features

In the Ex-Agrimont area, the buildings of the 1920s and 1950s constructive phases can be clearly differentiated from one another (figure 2.16).

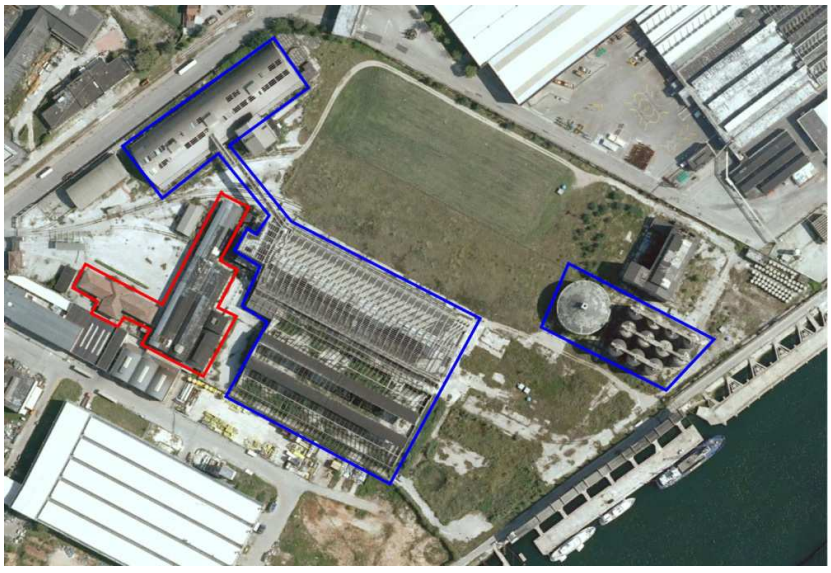

Figure 2.16. Ex-Agrimont area. 1920s buildings in red, 1950s buildings in blue

The buildings of the first construction phase are located approximately at the center of the area. The productive area is constituted by three elongated buildings, parallel to each other. They are all 15 meters large, while the first one develops on a length of 110 meters, the second one on a length of 70 meters, and the third one on a length of 40 meters. They are all made of a structural frame of reinforced concrete, with ceilings sustained by reinforced concrete trusses (figure 2.17). Non-structural walls are made of bricks. Near the productive area and perpendicularly oriented to it, a masonry building is located. This was the administrative base of the firm.

Three main buildings were constructed in the second phase. Two of them are located on the south, near the older productive area and perpendicular to it. Productive activities were established inside them. The last one, C3 building, is located on the north, with an orientation parallel to the near street. It served mainly as storehouse of both end products and by-products, and it was directly connected to the railroad. A platform connected the building with the productive area (figure 2.18).

Figure 2.17. 1920s productive area, ceiling made of reinforced concrete trusses

Figure 2.18. 1950s buildings, platform linking productive buildings and C3 building

The three buildings are made with an extremely innovative construction technique for the time: they are constituted of structural frames of reinforced concrete beams and columns,

covered with prefabricated modular elements made of steel, plastic materials and fiber cement; with several apertures (windows and skylights) which gave great brightness to the internal rooms. The productive building to the west is 60 meters wide and 120 meters long, it has a pyramidal shape and is conceived as a modern cathedral, with a large nave delimited from the two aisles by two series of reinforced concrete columns (figure 2.19). The productive building to the east is 60 meters wide and 150 meters long, while the C3 building is 40 meters wide and 130 meters long. The two buildings, connected by the platform, have a completely different architectural conformation compared to the west productive building. They are both made of a series of reinforced concrete arches forming a barrel-shaped structure, with a single large internal room (figure 2.20).

Figure 2.19. 1950s constructive phase, west productive building

Figure 2.20. 1950s constructive phase, east productive building

The C3 building (figure 2.21) is 20 meters tall, and is constituted by 22 couples of load bearing reinforced concrete semi-arches, all pre-stressed and prefabricated, connected at the top by complementary joints (figure 2.22). The semi-arches are characterized by solid rectangular cross-sections up until 2 meters of height. The dimensions of the rectangular cross-section are 30x110 cm. From this height, the cross-section changes and has the shape of the letter I. The I cross-section is 30 cm wide and 110 cm high. The thickness of the I cross-section flange is equal to 20 cm and the thickness of its web is equal to 10 cm. The I cross-sections continue until the joints on the top. Up until 2 meters of height the structure is enclosed by a reinforced concrete wall produced on-site, while over this height the semi-arches are connected by prefabricated non-structural reinforced concrete beams which constituted the backing for the original fiber-cement roofing (figure 2.23).

Figure 2.21. 1950s constructive phase, C3 building

Figure 2.22. C3 building, semi-arches joint

Figure 2.23. C3 building, reinforced concrete frame

Other secondary buildings were built during the 1950s constructive phase, together with a series of large reservoirs near the canal for the storage of raw materials.

In the following years, probably during the 1980s, a tall structure was built near the C3 building, constituted by a reinforced concrete structural frame and non-structural walls made of bricks.

2.5 EX-ZWEIFEL EMBROIDERY PLANT

2.5.1 Historical background

The structure is located in San Giovanni Lupatoto, near Verona. The embroidery company was founded on April 28 1926 by two embroidery entrepreneurs from Switzerland, Emilio Peter and Cristiano Saxer, together with the latter's sons, Federico and Giusto Zweifel. Next to a pre-existing building, converted into the owner's home and offices, a new industrial structure was rapidly built, and twelve embroidery machines were installed. In mid-November 1926, the embroidery plant started hiring its staff and by mid-December 135 people were working there (Castagnetti, 1998). The company's products, at first destined almost solely to exports, could successfully penetrate the Italian market, until the outbreak of World War II. During the War, activity slowed down due to the lack of raw materials, delays in payments and war events, until it was stopped in 1944. After the war, the company was reorganized under the technical and business point of view. The slow recovery was hindered by Swiss competition, which had entered the Italian market, and by the difficulties in exports. The 1950s marked a strong growth, corresponding to the Italian economic boom. In 1963 the company had to buy two further frames, which required the enlargement of the machine hall. A new floor was also built, creating the room where control, repair and shipping operations were carried out for the whole production (Castagnetti, 1998). The masonry works finished in 1964: the new hall, 22 m large, with a vast vault ceiling, was a marvelous work of art for the time (the idea of a single hall, not interrupted by any centerpieces, had been inspired by engineer Nervi's works). The new frames were the starting point for the renewal of all machines and the purchase of new ones. During the 1970s, the company faced a serious economic crisis, due to growing imports from Switzerland and Austria. In 1980 the company obtained positive results, even though with obsolete machines, but in 1984 a new crisis arose. Half of the stakeholders withdrew, the others followed the path of renewal, which implied the purchase of new machines, the creation of external work centers and a staff reduction. In the first few months of 1990, an Anglo-French group expressed their interest in buying the plant, with the guarantee of renewing the machines and maintaining the whole staff. The experts responsible for the negotiation unexpectedly advised against the sale, proposing a plan to

give new momentum to the production. Yet, the cooperation was a failure and sales plummeted (Castagnetti, 1998). On May 14 1991, after 65 years of activity, the embroidery plant ceased its work. After its closure, the plant remained unused, with few exceptions, and was included in an urban renovation plan. Within such works, on October 8 2008, part of the roof collapsed, probably due to the impact of an excavator against a reinforced concrete beam. Most likely, the collapse of the roof took place because of the detachment of some tie rods, and the consequent collapse of the structure on the floor underneath. Afterwards, due to the load of the debris, increased by the rainfalls, the 1926 floor collapsed too, whereas the 1962 floor was intact. In July 2011, after almost three years of negotiations on the kind of intervention to carry out for the requalification of the area, the remaining non-collapsed portion was pulled down.

2.5.2 Structural and architectural features

Over the years, the structure underwent enlargement and maintenance operations, until its collapse in autumn 2008. In figure 2.24, from a cadastral search of 1986, the buildings belonging to the company are visible and their perimeter is shown by a thick black line. The buildings in red and in yellow were already there in 1926. The area in green is the one of the original plant, whereas the area in blue is the 1962 enlargement. Figure 2.25 shows a global view of the structure, with the offices building in the foreground, followed by the Plant. The different construction phases are visible: the 1926 ground floor, characterized by arched windows, and the 1962 first floor, with wider windows thanks to a reinforced concrete frame.

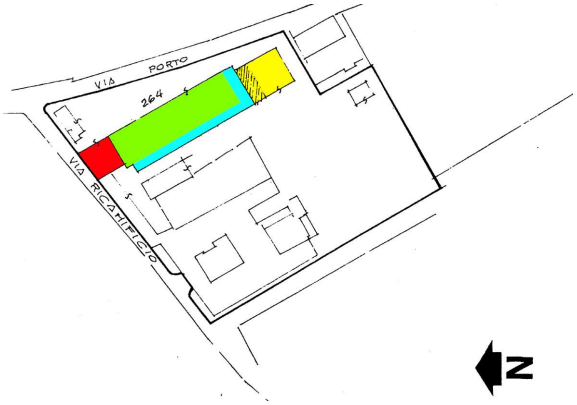

Figure 2.24. Plan of the embroidery plant according to 1986 land registry

Figure 2.25. Ex-Zweifel embroidery plant conservation state in 2009

The original industrial structure was built in 1926, when the company was created. The structure had a rectangular plan of approximately 63x15 m and consisted of masonry walls supporting a floor in iron and concrete. Figure 2.26 shows part of the 1926 structure, between the right wall and the 1962 steel columns. The wall lays on a lean concrete layer, 0.8 to 1.2 m thick and 15-30 cm larger than the wall. The foundations lay on a stable ground, constituted by a gravel bed or a mix of lime mortar and gravel. The eastern perimeter wall was the only one still standing after 1962 enlargement, and it was made of a mixed masonry of bricks and rocks, 40 cm thick. The ceiling was constituted by a hurdle of iron bars, supporting a concrete slab and a hollow tiles layer for weight reduction purposes. The completion slab was covered by a waterproof coating, until the 1962 addition. On the coating there was a layer of earth and grass, similar to modern green roofs.

Given the purchase of new and larger machines, in 1962 an enlargement of the plant was necessary. Instead of building a new structure, the existing one was enlarged and the production continued uninterrupted during construction works. The new hall was approximately 67 m long and 22 m large: the larger dimensions, compared to the 1926 structure, were due to the addition of a reinforced concrete frame with a ceiling of concrete and masonry with a 7.20 m span on the eastern side and one with 4.55 m span on the southern side, linking the plant to the nearby building (figure 2.26). The external frame was made of square cross-section columns, 40x25 cm in size, with a spacing ranging from 4.95 to 6.40 m, and by rectangular cross-section beams, 65x40 cm. As for the construction of the internal frame, minimum columns dimensions were required, together with the possibility to continue with the production; such prerequisites implied wider spacings and the use of steel columns bolted to concrete foundation plinths, located at a spacing of 10.70 m, reduced to 5.90 and 9.10 m at the ends. The columns supported a beam parallel to the main axis of the structure and a smaller one, orthogonally oriented, supporting the floor linking the structure to the southern building. Each beam was tapered in correspondence to each pillar. In the part of the structure built in 1962, a common concrete and masonry ceiling was built, with a spacing of 7.20 m. As for the 1926 part of the ceiling, it was reinforced by means of a new concrete casting, 9-10 cm thick, on the existing ceiling. Yet, the casting only increased the load on the floor, as the waterproof coating had not been removed. In the 1962 structure there were no load-bearing walls, as the loads were supported by reinforced concrete frames. The masonry walls present were simply plug walls, 40 cm thick, built with two brick layers and an internal gap.

Figure 2.26. Ground floor of the structure. 1: 1926 outer walls; 2: 1926 ceiling; 3: 1963 ceiling; 4: 1963 structural frame; 5: 1963 main beam; 6: 1963 secondary beam

The covering of the upper floor lay on a reinforced concrete frame, continuing from the bottom one, with a perimeter riddle, beams and columns with the same features of the ground floor ones. The covering had a 22 m spacing and a 18.33 m radius of curvature. The resulting arch was thus divided in 16 parts, corresponding to the rhombi constituting the vault, each 1.47 m long (figure 2.27). The great barrel vault was divided into two parts by a joint constituted by two large reinforced concrete arches (figure 2.28), close together.

Figure 2.27. First floor of the structure

Figure 2.28. Joint between column and arch

The two parts had different lengths along the main axis of the structure; the remaining one after 2008 collapse was 36.65 m long. The covering was made of pre-fabricated beams assembled on site, 90 cm long. The covering was built in subsequent zones, 4 m large, the same size as the metal rib on which the pre-fabricated parts were joined, by welding the rebars from the beams. They were then covered by a layer of tiles, a layer of cement mortar, approximately 1 cm thick, a layer of polystyrene and an external bituminous coating. This kind of covering, which may now seem somewhat expensive due to the low degree of prefabrication, was instead a good alternative to other building typologies for spacing of this sort; it was chosen because it matched aesthetic value and costs which were similar to those of other coverings for the same spacing.

2.6 EX-FORO BOARIO

2.6.1 Historical background

The structure is located immediately outside the historical center of Padova, in an area between the railway line to Bologna and the SR 47 road (Australia beltway). In 1964 the Municipality of Padova published a call for tender to build the new cattle market (Foro Boario) of the town. The tender was awarded to the construction company Guaraldo from Treviso, with a project drafted by architect Giuseppe Davanzo in collaboration with engineer Giandomenico Cocco and Pio Guaraldo. The building was inaugurated on June 10 1968 (Saccomani, 1970). The project was preceded by a statistical study to quantify the number of animals annually conducted to the market. The results were the basis to plan an adequate structure for the expected number of animals. The Foro Boario is constituted by different areas: market, parkings, lairage, isolation stall, over a 120,000 m^2 area (Saccomani, 1970).

Architect Davanzo's project is still an ideal solution for a market and its proper functioning. The architectural structure draws inspiration from the ancient cattle markets, but also from fairs and circus, usually held under big tops which covered but did not close the areas. Thus, the architect created a unique structure, made of concrete big tops, sloping down from two pointed central towers, recalling the poles supporting the circus tents

(figure 2.29). One of the most interesting features is the space between the staggered coverings, which ensured air change and light in the central areas of the market as well.
The Foro Boario was not modified after its construction in the 1960s. Despite its value, its modernity and its great potential, the structure has never been used neither as a market, nor to host any other service. Building the new Foro Boario witnessed the need to equip the town with an adequate structure for the arrival of cattle from the whole Veneto region and surrounding regions, but, over time, Verona took on a leading role in the sector, marginalizing Padova. The building has never been used by the Municipality, also given its location outside the historical center. The interest for the recovery of the former Foro Boario has involved the Municipality, architects, engineers and entrepreneurs, but a solution has not been found yet.

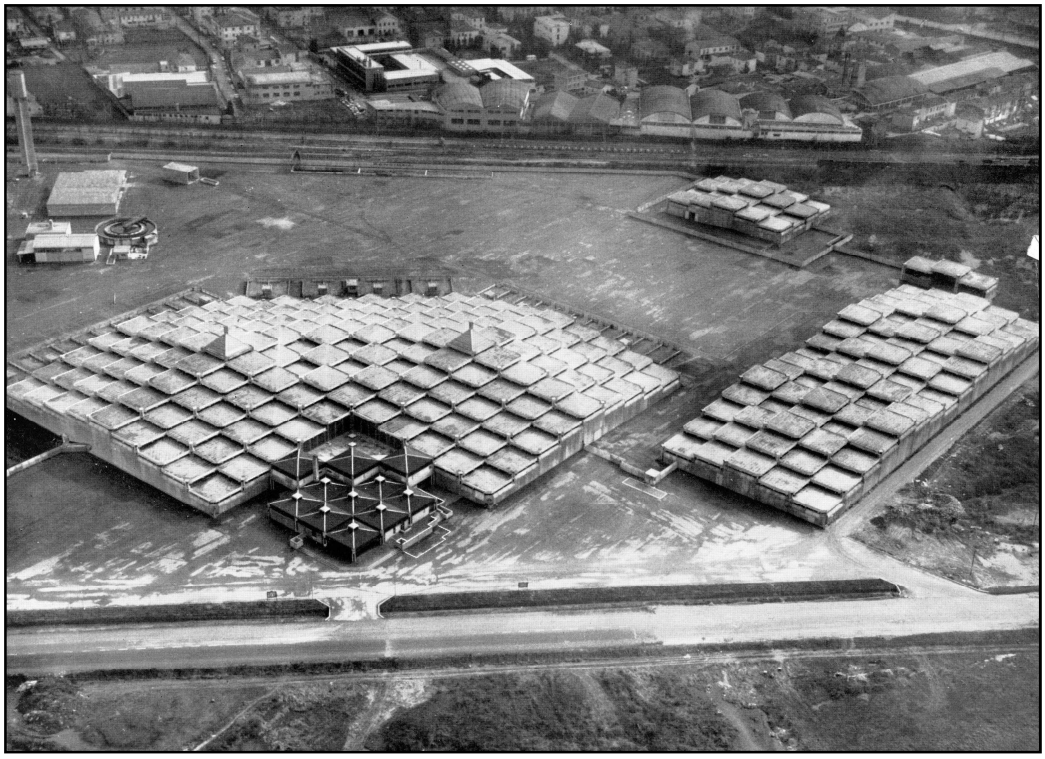

Figure 2.29. Aerial view of the Ex-Foro Boario (Saccomani, 1970)

2.6.2 Structural and architectural features

The market plan consists of two large overlapping squares (figures 2.29, 2.30). Each square is subdivided in square “tents” constituting the basic unit, with a 10x10 m size. The

overall covering system is composed by four square slabs, partially overlapping, 10x10 m each (figure 2.31).

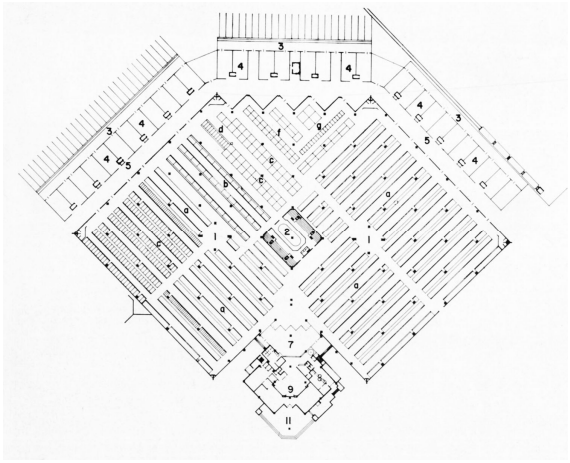

Figure 2.30. Plan of the main building (Saccomani, 1970)

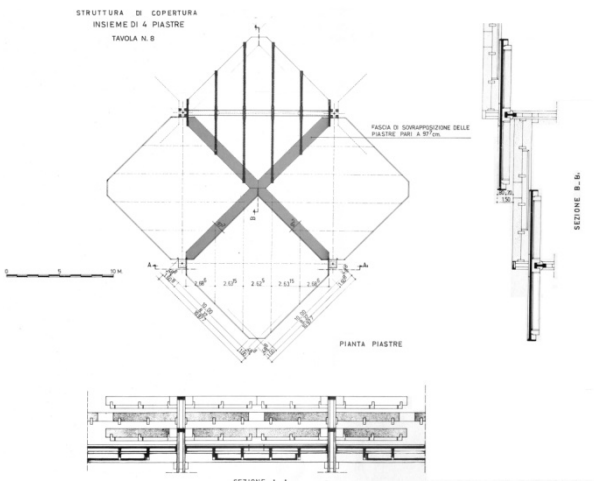

Figure 2.31. Plan and sections of the basic module constituting the roofing (Saccomani, 1970)

Each slab is constituted by a 14 m load-bearing beam in prestressed reinforced concrete, lying on the square's diagonal, on its pillars (Saccomani, 1970). The beam has four double pedestals where the orthogonal secondary beams lie; on such beams there are 10 small beams in reinforced concrete covering the square slab (Saccomani, 1970) (figure 2.32).

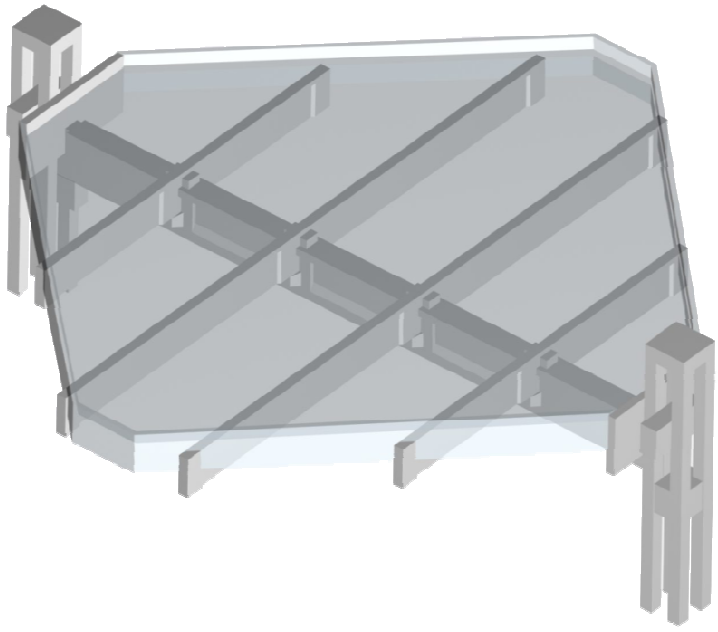

Figure 2.32. Axonometric projection of one modular element, mounted on two columns (Crosato, 2010)

Finally, the covering floor is 12 cm thick and constituted by 23 prefabricated elements, which are rectangular, trapezoidal or triangular and lie on the beams and the slabs. The covering slab covers an area approximately 11x11 m wide: as the bottom square is 10x10 m wide, the upper slabs guarantee a 1 m open covering, from rain too. The columns supporting the covering slabs are made of 4 poles, 25x25 cm, linked by tie plates where the main beams lie (Saccomani, 1970). Wall plugs for side coverings are made of expanded clay concrete, 22 cm thick and 2 m large, their height varies according to the height of the structure. Some parts of the structure were made with reinforced concrete casted on site, such as foundations, pointed towers, Auction hall, General Services hall and others. Even though the original project provided for the columns to be prefabricated, they were built onsite. The prefabricated elements were built in two workshops: one onsite and one in Paese (Treviso), in the prefabrication workshop of the company Guaraldo Precompressi (Saccomani, 1970).

CHAPTER 3

Multi-analytical characterization of the conglomerates

3.1 INTRODUCTION

A full characterization of the cement conglomerates constituting the reinforced concrete structural elements of the studied buildings was performed according to a custom formulated multi-analytical approach, elaborated on purpose in order to reach a full level of knowledge of the materials characteristics. The characterization was of crucial importance to crosscheck the results obtained by newly-developed quantitative methodology for the reconstruction of the mix design, which will be thoroughly described in the following chapter.

In the following paragraphs, the methodologies of sampling and analysis of the materials will be described in detail, highlighting the strategies elaborated to improve the level of knowledge on the structures, minimizing the obtrusiveness and favoring the crosschecking of results among tests at different levels of invasiveness.

Investigations were carried out with two different complementary aims: obtaining information about the mechanical properties of materials and studying their chemical and physical characteristics. The results of the analyses, which allowed to discern the materials of each building according to their characteristics, will be reported in detail. They provided the opportunity to check constructive details, allowing to intervene with more confidence with suitable restoration techniques, if needed, but also to prevent the execution of intrusive repair works, when not justified by an experimentally demonstrated worsening of the structural conditions.

3.2 THE SAMPLING CAMPAIGNS

3.2.1 Preliminary surveys

Sampling operations have been preceded by preliminary surveys performed on site to verify the conservation state of the structural elements and to choose the most suitable areas for the extraction of cores, both in terms of representativeness and preservation of the structural integrity of the buildings. In particular, the positions of the structural elements with low bending moment, shear and axial force values were selected for the performing of the sampling procedures.

The compressive strengths of the selected concrete elements were non destructively evaluated on site through a Schmidt Hammer (figure 3.1). The rebound indexes were measured following the prescriptions indicated by European Standard UNI EN 12504-2, and the compression strength values were obtained by means of correlation curves, provided with the instrument. These tests allowed defining possible local non-homogeneities of the conglomerates, with consequent accurate planning of the destructive sampling operations.

Furthermore, an accurate characterization of the geometric characteristics of the internal steel reinforcements of the concrete resulted to be of crucial importance, to avoid damage to the rebars during coring. Presence, distribution and diameter of the reinforcement bars inside the cement conglomerates were reconstructed through a non-destructive analytical approach, using a Hilti Ferroscan magnetic scanner (figure 3.2). The acquisition of the magnetic signal was performed using a 60x60 cm reference grid, with an internal 150x150 mm net, as indicated by the European Standard UNI EN 12504-2. Data were stored on the internal memory of the instrument and then elaborated through the dedicated Ferroscan software. Data were then crosschecked performing localized scarifications of the concrete covers by means of a hammer drill.

Figure 3.1. Schmidt hammer test on a concrete arch of the C3 building of the Ex-Agrimont Area

Figure 3.2. Magnetic scanner test on the stairway concrete of the Victory Monument

A brief summary of the rebars placement on the main structural elements of the studied buildings, as determined by magnetic scanner tests and scarifications, is hereby reported;

- **Northern Wing of the Carraresi Castle**. As regards the beams, clear differences in the placement of the rebars can be observed according to the construction phase (figure 3.3). The beams of the first construction phase are reinforced with two pairs of plain longitudinal bars, each with a diameter of 23 mm. The pairs are placed at the bottom of the structural elements and covered by a concrete cover, 35 mm thick. At about one third of the length of the structural element, the upper bars bend upwards, with an angle of approximately 10°, reaching the top of the beam at its end. Each couple of bars is held together by a series of plain stirrups, constituted by steel plates 40 mm wide and placed with variable spacing, smaller in proximity to the end of the structural elements. The beams of the second construction phase are reinforced with three pairs of plain longitudinal bars, each with a diameter of 20 mm. The pairs are placed at the bottom of the structural elements and covered by a concrete cover 10 mm thick. At the end of the length of the structural element, in correspondence to the enlargement of the section, the lower bars bend downwards, with an angle of approximately 45°, reaching the bottom of the beam at its end. Each couple of bars is held together by a series of stirrups, constituted by plain rods with a diameter of 7 mm and placed with variable spacing, smaller in proximity to the end of the structural elements. The beams of the third construction phase are reinforced with 8 plain longitudinal bars, of which those at the two ends have an 18 mm diameter, whereas the others have a diameter of 16 mm. Some of the rebars

bend upwards at the end of the structural elements, and they are all held together by plain rods with a 7 mm diameter, acting as stirrups and placed with a constant spacing.

As regards the reinforcement of the slabs, differences between the first and second construction phase are recognizable. Hennebique slabs are reinforced with plain longitudinal bars with a diameter of 9 mm, placed at the bottom of the structural elements with a spacing of 30 cm and enclosed by stirrups constituted by plain steel plates 20 mm wide. The concrete cover is about 20 mm. The slabs of the second phase are reinforced with plain longitudinal bars with a diameter of 9 mm, placed at the bottom of the structural elements with a spacing of 10 cm. The stirrups are absent, and the concrete cover is about 10 mm.

Finally, columns built at the ground floor during the second constructive phase are totally non reinforced.

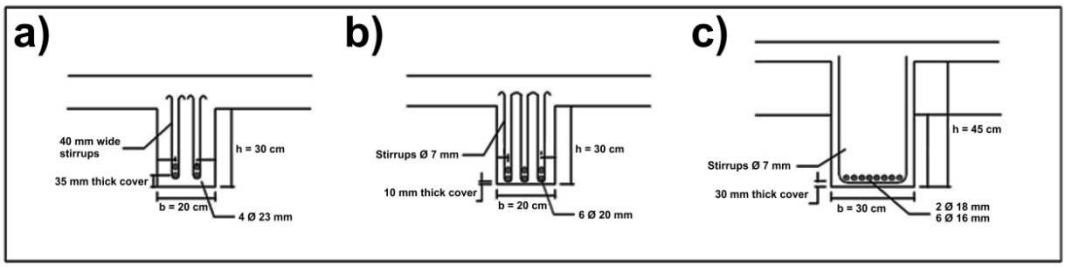

Figure 3.3. Northern Wing of the Carraresi Castle, reconstruction of the rebars placement on the beams for the three construction phases (a: first phase, b: second phase, c: third phase)

- **Victory Monument**. The stairway slabs are reinforced with a steel net of a 30x30 cm spacing, constituted by plain bars with a diameter of 8 mm. Stirrups are absent, and the concrete cover is about 50 mm.

  The stairway beams are reinforced at the bottom of the section by 6 plain bars with a 14 mm diameter, while stirrups have a diameter of 8 mm and are placed with a spacing of 50 cm, not always regular. The concrete cover is about 20 mm.

  Finally, all the walls of the substructure and the central vaulted slab are totally non reinforced.
- **Ex-Agrimont Area, C3 building**. The arches are reinforced with longitudinal plain bars with an 8 mm diameter. 5 bars are placed at the front side of the arches, while at the lateral side they are placed with a spacing of 20 cm. The longitudinal bars are

held together by a series of plain stirrups with an 8 mm diameter, placed with a spacing of 20 mm. The concrete cover is about 20 mm.

As regards the lateral wall, it is reinforced with an arc-welded steel net with a 20 mm spacing. The concrete cover is about 20 mm.

- **Ex-Zweifel Embroidery Plant**. Only the placement of the rebars of the concrete elements constituting the external frame of the 1963 enlargement is hereby described, as they are the sole elements cast on site, on which the study was focused.

  The columns are reinforced with six longitudinal plain bars with a 15 mm diameter, four placed at the corners of the rectangular section and two halfway on the longer sides. The longitudinal bars are held together by a series of plain stirrups with a 5 mm diameter, placed with a spacing of 15 mm. The concrete cover is about 30 mm.

  The beams and the riddle are reinforced with 7 longitudinal plain bars, four placed at the corners of the rectangular section and three further rebars at the bottom of the structural elements. The former have a 10 mm diameter, while the latter have an 18 mm diameter. The longitudinal bars are held together by a series of plain stirrups with a 5 mm diameter, placed with a variable spacing, more reduced in proximity to the end of the structural elements. The concrete cover is about 25 mm.

  The same type of reinforcement has been used for the arches, with the exception that longitudinal-shaped bars were utilized to improve the adhesion between concrete and steel.

- **Ex-Foro Boario**. Only the disposition of the rebars of the columns, the linkage blocks and the beam segments is hereby described, as they are the main structural elements cast on site, on which the study was focused.

  Each of the four poles constituting the columns is reinforced with 4 longitudinal-shaped bars with a 14 mm diameter, placed at the corners of the square section, and a series of shaped stirrups with a 6 mm diameter, placed with a variable spacing (12.5 cm at the margins of the structural elements, 50 cm in the intermediate portions). The concrete cover is about 30 mm.

  Besides the reinforcement of the columns, linkage blocks are additionally reinforced with 8 longitudinal shaped bars with a 14 mm diameter, placed both at the corners and the middle points of the square section, and three shaped stirrups with a 16 mm diameter. The concrete cover is about 30 mm.

Beam segments are reinforced with longitudinal shaped bars and shaped stirrups both with an 8 mm diameter and placed with a 10 cm spacing. The concrete cover of these elements is extremely reduced, with a mean thickness of 4 mm and in some cases it is absent altogether.

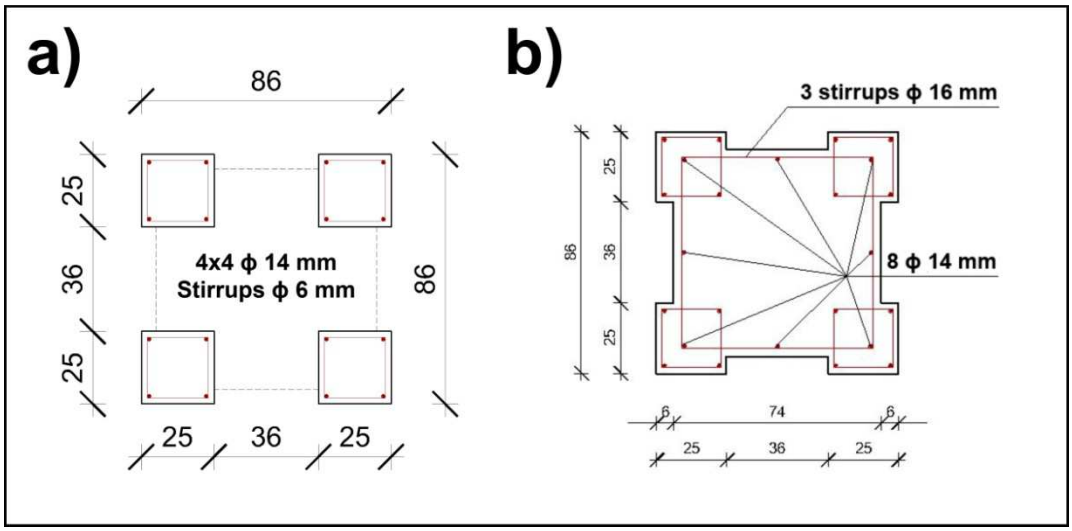

Figure 3.4. Ex-Foro Boario, reconstruction of the rebars disposition on a) the columns and b) the linkage blocks

3.2.2 Sampling operations

After the identification of the proper sampling areas through preliminary surveys, the main sampling operations were performed by means of coring.

Concrete samples were extracted following the prescriptions indicated by the European Standards UNI EN 12390-1 and UNI EN 12504-1 through a Hilti DD 130 water lubricated diamond coring system, equipped with diamond core bits of variable diameters and mounted on a vertical stage. Prior to the perforation, the vertical stage was fixed by means of security screws on the structural element to be sampled, in horizontal or vertical position according to the chosen direction of sampling (figure 3.5). On the basis of the dimensions of the structural elements, core bits with different diameters were used, to limit the invasiveness of the sampling. A 100 mm core bit (diameter of the resulting cores: 95 mm) was used for most of the cores, while an 80 mm core bit (diameter of the resulting cores: 75 mm) was used for thinner structural elements, namely the beams of the Northern Wing of the Carraresi Castle, the stairway concrete of the Victory Monument and the columns of

the Ex-Foro Boario. Apart from thin horizontal structural elements, cores with a minimum length twice their diameter were extracted (figure 3.6).

Figure 3.5. Coring on a stairway beam of the Victory Monument

Figure 3.6. Cores extracted from several structural elements of the Ex-Zweifel Embroidery Plant

Considering the invasiveness of the sampling operations by means of extraction of large cores, a series of integrative stratigraphic samples were extracted for each structure by means of micro-coring (figures 3.7, 3.8), performed through a Millers Falls water lubricated hollow tip drill equipped with 25 mm diamond core bits (diameter of the resulting cores: 20 mm). Furthermore, large portions of concrete cover from scarification residuals were collected from areas near to the ones where the micro-cores were extracted, to integrate the volume of sampled concrete.

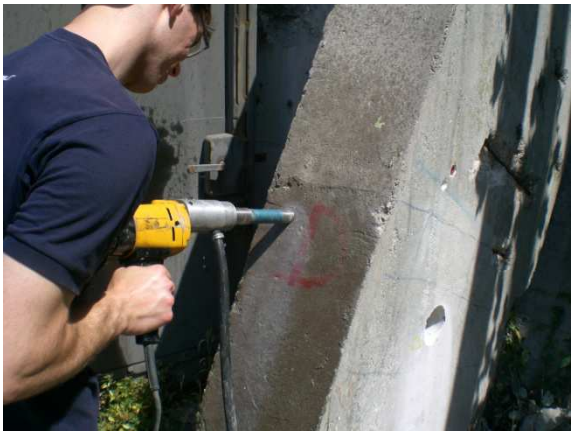

Figure 3.7. Extraction of a micro-core from an arch of the C3 Building of the Ex-Agrimont Area

Figure 3.8. Micro-core extracted from a slab of the Northern Wing of the Carraresi Castle

3.3 EXPERIMENTAL

3.3.1 Materials

The study was focused only on the characterization of the structural concrete elements of the buildings, and mainly on the elements cast on site, being the most susceptible ones to problems related to non standardized production protocols. The arches of the C3 building of the Ex-Agrimont Area were the only prefabricated elements studied, being the main constituents of the load-bearing frame of the building. According to the structural nature of the buildings, different elements were sampled, namely slabs, walls, columns, arches, beams and riddles. A detailed description of the concrete structural elements sampled for each structure is hereby reported.

- **Northern Wing of the Carraresi Castle**. 13 samples representative of all the concrete structural elements built during the three construction phases were taken, with the exception of the structural constituents of the external concrete open gallery. 7 cores were performed, integrated with 6 micro-cores and scarification residuals. All the characteristics of the samples and their areas of sampling are reported in table 3.1 and figure 3.9.

Sample	Element	Construction phase	Location	Type of sample
CC1	Slab	2	First floor	Core
CC2	Slab	1	Second floor	Core
CC3	Slab	2	Second floor	Core
CC4	Slab	1	Second floor	Micro-core + scarification
CP1	Column	2	Ground floor	Core
CP2	Column	2	Ground floor	Micro-core + scarification
CT1	Beam	1	Ground floor	Core
CT2	Beam	3	First floor	Core
CT3	Beam	2	First floor	Core
CT4	Beam	2	Ground floor	Micro-core + scarification
CT5	Beam	3	First floor	Micro-core + scarification
CT6	Beam	2	First floor	Micro-core + scarification
CT7	Beam	1	First floor	Micro-core + scarification

Table 3.1. Northern Wing of the Carraresi Castle, denominations and characteristics of the samples

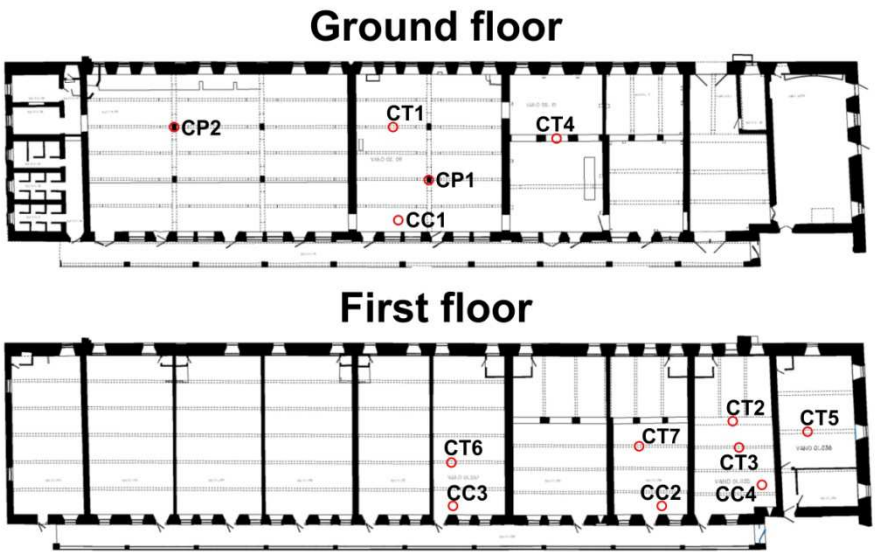

Figure 3.9. Northern Wing of the Carraresi Castle, sampling locations

- **Victory Monument**. 14 samples representative of the concrete structural elements constituting the substructure and the stairway were taken. 7 cores were performed, integrated with 7 micro-cores and scarification residuals. All the characteristics of the samples and their areas of sampling are reported in table 3.2 and figure 3.10.

Sample	Element	Location	Type of sample
BS1	Lateral wall	Northern crypt, height 150 cm	Core
BS2	Lateral wall	Northern crypt, height 80 cm	Core
BS3	Central wall	Northern wall, height 150 cm	Core
BS4	Central wall	Northern wall, height 80 cm	Core
BS5	Lateral wall	Eastern crypt	Micro-core + scarification
BS6	Central wall	Southern wall	Micro-core + scarification
BV1	Vaulted slab	Centre of the colonnade	Core
BV2	Vaulted slab	Centre of the colonnade	Micro-core + scarification
BG1	Stairway slab	Northern stairway	Core
BT1	Stairway beam	Northern stairway	Core
BT2	Stairway beam	Northern stairway	Micro-core + scarification
BT3	Stairway beam	Northern stairway	Micro-core + scarification
BT4	Stairway beam	Western stairway	Micro-core + scarification
BT5	Stairway beam	Southern stairway	Micro-core + scarification

Table 3.2. Victory Monument, denominations and characteristics of the samples

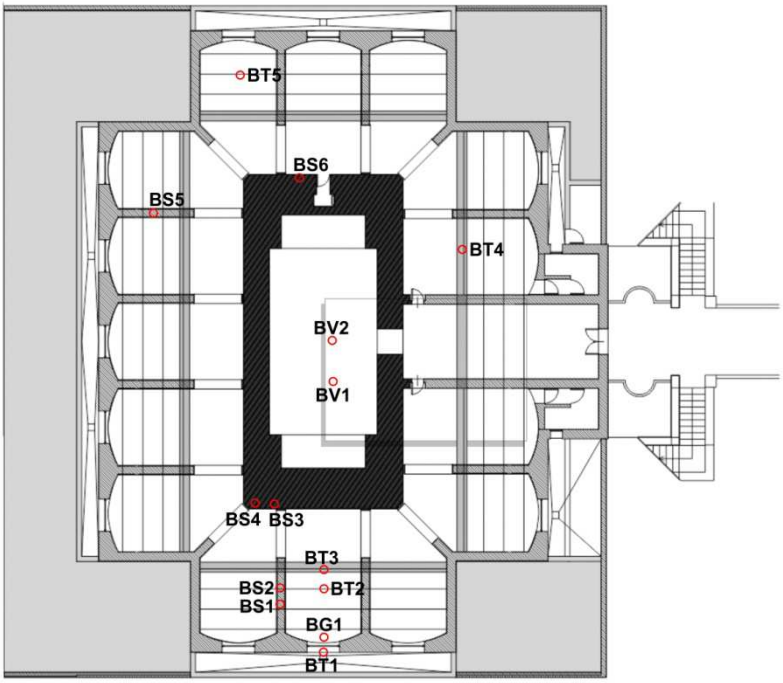

Figure 3.10. Victory Monument, sampling locations

- **Ex-Agrimont Area, C3 building**. 7 samples were taken from the concrete arches constituting the structural frame of the building. 3 cores were performed, integrated with 4 micro-cores and scarification residuals. The characteristics of the samples and their areas of sampling are reported in table 3.3 and figure 3.11.

Sample	Element	Location	Type of sample
MC1	Arch	South-western side	Core
MC2	Arch	South-western side	Core
MC3	Arch	North-eastern corner	Core
MC4	Arch	South-western side	Micro-core + scarification
MC5	Arch	North-eastern side	Micro-core + scarification
MC6	Arch	South-eastern side	Micro-core + scarification
MC7	Arch	South-eastern corner	Micro-core + scarification

Table 3.3. C3 building of the Ex-Agrimont Area, denominations and characteristics of the samples

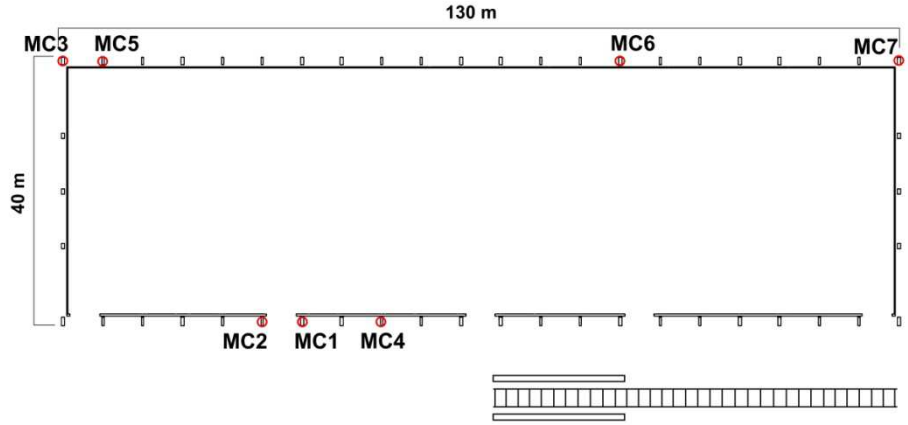

Figure 3.11. C3 building of the Ex-Agrimont Area, sampling locations

- **Ex-Zweifel Embroidery Plant**. 10 samples from the external concrete frame built during the 1963 enlargement were taken. For security reasons, no sampling operation was performed on the non-collapsed portion of the building, so the materials were sampled from collapsed structural elements. 7 cores were performed, integrated with 3 micro-cores and scarification residuals. The characteristics of the samples and their areas of sampling are reported in table 3.4 and figure 3.12.

Sample	Element	Location	Type of sample
RP1	Column	North-eastern side	Core
RP2	Column	North-eastern side	Core
RP3	Column	North-eastern side	Core
RC1	Riddle	North-eastern side	Core
RC2	Riddle	North-eastern side	Micro-core + scarification
RT1	Beam	North-eastern side	Core
RT2	Beam	North-eastern side	Core
RA1	Arch	-	Core
RA2	Arch	-	Micro-core + scarification
RA3	Arch	-	Micro-core + scarification

Table 3.4. Ex-Zweifel Embroidery Plant, denominations and characteristics of the samples

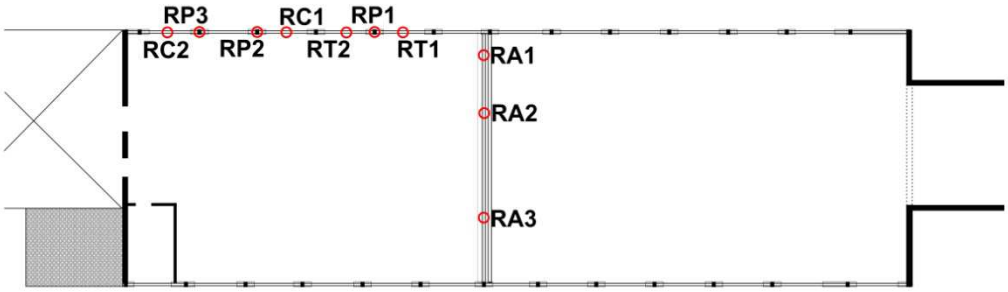

Figure 3.12. Ex Zweifel Embroidery Plant, sampling locations

- **Ex-Foro Boario**. 10 samples from the concrete columns and beam segments cast on site were taken. 2 cores have been performed, integrated with 7 micro-cores and scarification residuals. The characteristics of the samples and their areas of sampling are reported in table 3.5 and figure 3.13.

Sample	Element	Location	Type of sample
FP1	Column	South-east side	Core
FP2	Column	South-east side	Core
FP3	Column	South-east side	Micro-core + scarification
FP4	Column	South-east side	Micro-core + scarification
FP5	Column	Central area	Micro-core + scarification
FP6	Column	Central area	Micro-core + scarification
FP7	Column	Central area	Micro-core + scarification
FT4	Beam segment	South-east side	Micro-core + scarification
FT5	Beam segment	Central area	Micro-core + scarification
FT6	Beam segment	Central area	Micro-core + scarification

Table 3.5. Ex-Foro Boario, denominations and characteristics of the samples

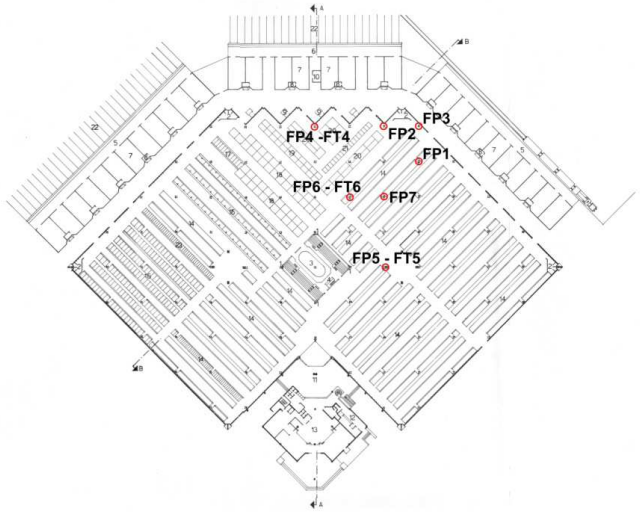

Figure 3.13. Ex-Foro Boario, sampling locations

3.3.2 Methods

The concrete samples were studied through a multi-scale and multi-analytical approach comprising compression tests and petrographic, mineralogical, microchemical and microstructural analyses, in order to fully characterize the mechanical, chemical, mineralogical and textural characteristics of the conglomerates and their constituents.

Compressive strength tests were performed on the sampled cores, with a Galdabini 300 t monoaxial press, following the European Standard UNI EN 12390/3. Then, a petrographic characterization of all concrete samples was performed following the American standard ASTM C856 (Standard Practice for Petrographic Examination of Hardened Concrete), modified on purpose and integrated considering the Italian Standard UNI 11176 (Petrographic description of a mortar). The study was performed both on massive samples, through macroscopic and stereomicroscope observations, and on 30 μm thin sections, obtained by vacuum impregnating portions of the materials with epoxy resin and sectioning them transversally. In order to perform a statistically significant microscopic examination, 3 thin sections were prepared for each core, two from internal portions and one from the external portion. Moreover, a thin section was prepared for each core and for each scarification residual. Chromatic determinations of the concretes were performed by comparison with the National Research Council Rock Color Chart (1963).

To determine the mineralogical profiles of the fine aggregate and the hardened binder, XRPD analyses were performed on the fractions under 500 μm and under 63 μm of the

samples, dry disaggregated and sieved, with a Philips X'Change diffractometer in Bragg-Brentano geometry equipped with a Cu X-ray tube operating at 40 kV and 40 mA (CuKα radiation), and an X'Celerator detector, both mounted on a PW1050/37 theta-2theta vertical goniometer. Data acquisition was performed by operating a continuous scansion from 3.01° [2θ] to 79.99° [2θ], at an acquisition rate of 0.02° [2θ] per second. Diffraction patterns were interpreted with X'Pert HighScore Plus 3.0 software by PANalytical, reconstructing mineral profiles of the compounds by comparison with ICDD and ICSD databases.

The mineralogical and petrographic studies were integrated by performing microchemical and microstructural analyses on thin sections samples using a Camscan MX 2500 scanning electron microscope (SEM), equipped with a LaB_6 electron source and an EDAX energy dispersive X-ray detector (EDS). Qualitative interpretation of spectra and semiquantitative estimation of chemical profiles were performed through SEMQuant Phizaf software. Moreover, chemical maps were acquired, in order to obtain spatial distributions of the mineral phases of both the binder and the aggregate.

3.4 RESULTS

3.4.1 Northern Wing of the Carraresi Castle

3.4.1.1 Compressive strength values

The compressive strength values for the sampled cores, expressed in terms of cylindrical strength (f_c), are reported in table 3.6.

Sample	**F_c (MPa)**
CC1	24.6
CC2	33.4
CC3	29.5
CP1	27.3
CT1	22.1
CT2	48.1
CT3	43.3

Table 3.6. Northern Wing of the Carraresi Castle, compressive strength values for the sampled cores

The results indicate differences in the mechanical behavior of the concrete elements according to the phase of construction. The Hennebique concrete is characterized by the highest compressive strengths, despite being the oldest. The beam gave a particularly high compressive strength value, typical of modern concretes. It is possible to hypothesize that the strict, even though still empirical, mix design and casting prescriptions of the Hennebique patent were thoroughly followed during the building of the structural element, with consequent improvement of the overall quality of the materials.

The concrete of the second constructive phase is characterized by lower compressive strength values, probably related to a general lack of accuracy in the project of the mix and in the casting procedure. The lower quality of the material can be justified by the emergency nature of the construction work, in a post-war period with low availability of raw materials and specialized workmanship.

Finally, the concrete of the third constructive phase is characterized by high compressive strength values, comparable to those of the Hennebique concrete, indicating an overall quality of both mix design and casting procedures.

The discrimination of the materials according to the construction phase is confirmed by their mineral-petrographic features, which are hereby described.

3.4.1.2 Concrete of the first constructive phase

The materials are characterized by proper volumetric proportions between inert fraction and cement matrix, typical of lean structural concretes. The aggregate is homogeneously distributed in the hardened conglomerate for most of the samples. Only sample CC2 is interested by slight segregation phenomena, showing an enrichment in coarse aggregate in the lower portion, associated to the presence of a layer depleted in gravel along the middle of the section (figure 3.14).

The granulometric distribution of the aggregate has a clear bimodal shape and is comparable to an ideal Bolomey curve, with discrepancies related to limited enrichments in fine gravel and coarse/fine sand in the original mix. Generally, slabs are slightly richer in coarse aggregate than the beams.

Figure 3.14. Sample CC2, slight coarse aggregate segregation in the lower portion of the section

The coarse aggregate is constituted by rounded natural gravel characterized by poor grading and variable, generally from medium to low, sphericity (figures 3.15, 3.16). Concrete of both the slabs and the beams is manufactured with gravels maximum dimension within the class of the coarse gravels, slightly greater for the former (30 and 27 mm, respectively). For all the analyzed concrete samples, the peak of granulometric distribution of the coarse aggregate is within the class of the fine gravels. Petrographically, carbonate rocks are predominant, constituting approximately the 60% of the total volumetric fraction (figures 3.15, 3,16, 3.17). Amongst the various carbonate species, sparry dolostones and micritic limestones are predominant, with associated bioclast mudstones and grainstones and rare marls and micritic limestones with chert nodules. The remaining fraction is constituted by a heterogeneous assemblage of siliceous rocks, amongst which metamorphic lithologies like quartzites, schists and granitic gneisses are predominant. Moreover, small chert fractions are present, together with a subordinate fraction of felsic igneous rocks, with predominant trachytes and granites. The coarse aggregate is characterized by high compactness, with almost total absence of meso- and macroporosity and a reduced microporosity for the sparry carbonates only (figures 3.15, 3.16). No signs of secondary cracking of the clasts are observable.

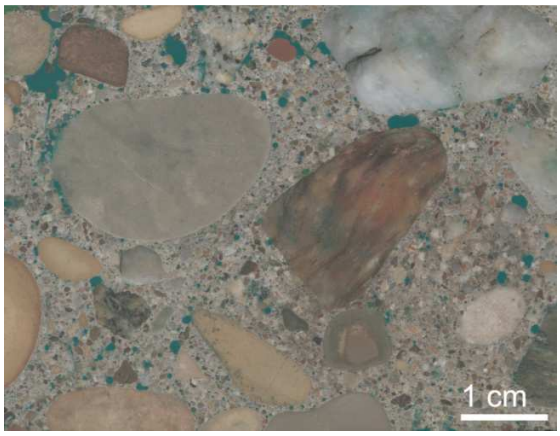

Figure 3.15. Sample CT3, polished cross section. The pore network is impregnated by green epoxy

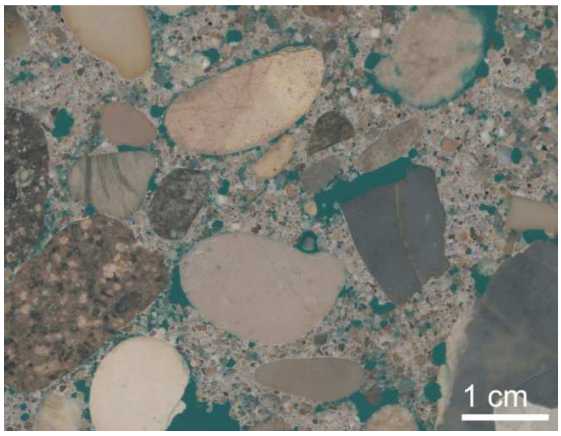

Figure 3.16. Sample CC2, polished cross section

The fine aggregate is constituted by sub-angular to sub-rounded natural sand characterized by poor grading, with peaks of distribution in the classes of the coarse and medium sands, and generally high sphericity (figures 3.17, 3.18). Petrographically, a predominance of carbonate rocks of the same nature of those constituting the coarse aggregate is observable for the granulometric class of the very coarse sands only (figure 3.17). A progressive enrichment in siliceous clasts occurs at decreasing granulometries, becoming predominant in the classes of the medium and fine sands (figure 3.18). Amongst them, only rare rock fragments are present, while the most relevant volumetric fraction is constituted by quartz grains, also in microcrystalline and metamorphic form (figures 3.17, 3.18). Associated k-feldspar, highly altered plagioclase and rare mica flakes are also present. The petrographic observations are fully consistent with the mineralogical assemblages determined by XRPD (figure 3.19). The fine aggregate is characterized by high compactness, with almost total absence of internal porosity. No signs of secondary cracking of the clasts are observable.

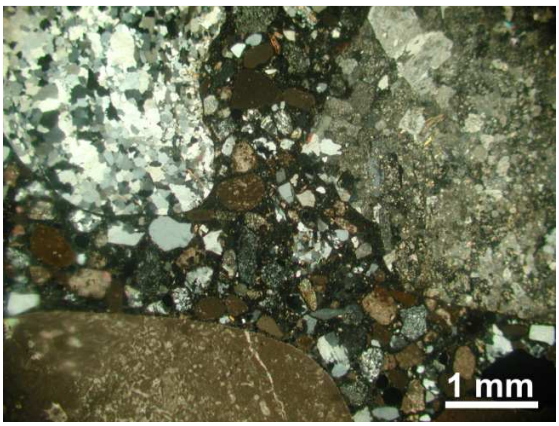

Figure 3.17. Sample CT7, crossed polars microphotograph

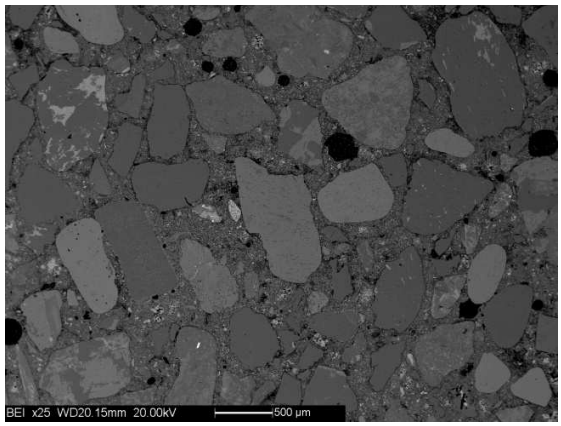

Figure 3.18. Sample CC4, SEM-BSE image. Quartz grains appear darker

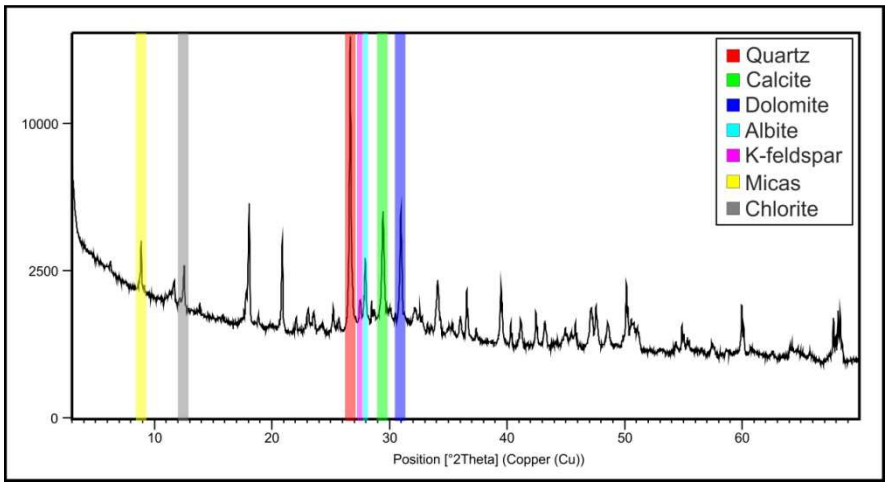

Figure 3.19. Sample CT3, diffraction pattern of the fraction under 500 µm, with highlighted the main reflexes of the crystalline phases constituting the fine aggregate fraction

The cement matrix is characterized by a light gray color and generally shows high adhesion to the aggregate, with a reduced presence of interfacial voids on the most elongated coarse grains of the slabs only. Anomalous cracking patterns related to inadequate curing procedures are totally absent; the volumetric degree of capillary porosity is extremely reduced (figure 3.20), suggesting the adoption of low w/c ratios for the manufacturing of the conglomerates.

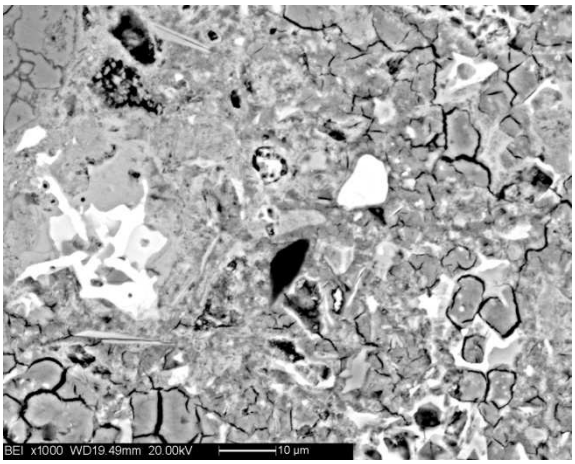

Figure 3.20. Sample CC2, high magnification SEM-BSE image. Capillary porosity is visible

The overall macro- and mesoporosity is low for the concrete of the beams, generally around 3% over the total volume of the samples and homogeneously distributed with a volumetric equivalence between spherical submillimetric entrained air voids and irregular entrapped air voids/water voids with maximum dimensions of 4-5 mm and medium dimensions of 1-2 mm (figure 3.15). These features confirm the reduced w/c ratios adopted

and indicate proper compaction and vibration procedures of the fresh conglomerates during casting operations. As regards the concrete of the slabs, higher macro- and mesoporosity values may be observed, being generally comprised between 5 and 7% over the total volume of the samples. Irregular and elongated entrapped air voids/water voids, with maximum dimensions of 10-11 mm and medium dimensions of 2-4 mm, are predominant over spherical submillimetric entrained air voids (figure 3.16). These features indicates less accurate compaction and vibration procedures of the fresh conglomerates during casting operations, probably related to logistic difficulties related to the great superficial extension of these structural elements.

3.4.1.3 Concrete of the second constructive phase

The materials are characterized by a greater volumetric fraction of hardened matrix with respect to the concrete of the first constructive phase, indicating the utilization of higher cement dosages in the original mix design. The aggregate is homogeneously distributed in the hardened conglomerate for all samples. Differences in the granulometric distribution according to the type of structural element are observable, though they all have bimodal distributions distant from the ideal Bolomey curves: slabs are enriched in fine gravel and medium sand, columns are enriched in fine sand and beams are strongly enriched in fine gravel.

The coarse aggregate is constituted by rounded natural gravel characterized by poor grading and generally medium sphericity, highly variable for the slabs (figures 3.21, 3.22). The concrete is manufactured with gravels with variable maximum dimensions according to the type of structural element, similar for the slabs and the beams (32 mm) and lower for the columns (17 mm). The peak of granulometric distribution of the coarse aggregate is for all samples within the class of the fine gravels. Petrographically, carbonate rocks are predominant, constituting approximately the 60% of the total volumetric fraction (figures 3.21, 3.22). Amongst the various carbonate species, sparry dolostones and micritic limestones are predominant, with associated bioclast mudstones and grainstones and rare marls and micritic limestones with chert nodules. The remaining fraction is constituted by a heterogeneous assemblage of siliceous rocks, equally distributed between metamorphic lithologies (quartzites, schists and granitic gneisses) and felsic igneous rocks (trachytes, rhyolites and granites). The coarse aggregate is characterized by high compactness, with almost total absence of meso- and macroporosity and a reduced microporosity for the

sparry carbonates only (figures 3.21, 3.22). No signs of secondary cracking of the clasts are observable.

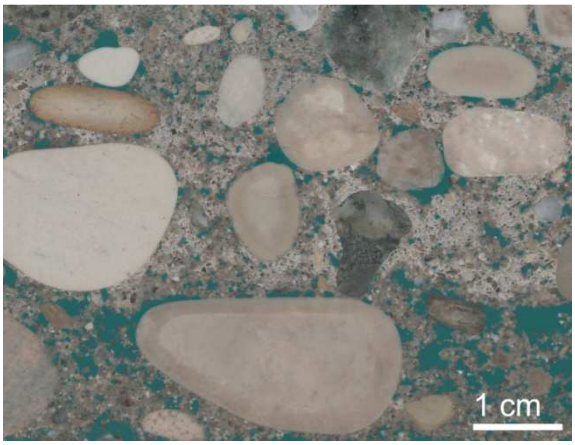

Figure 3.21. Sample CC1, polished cross section

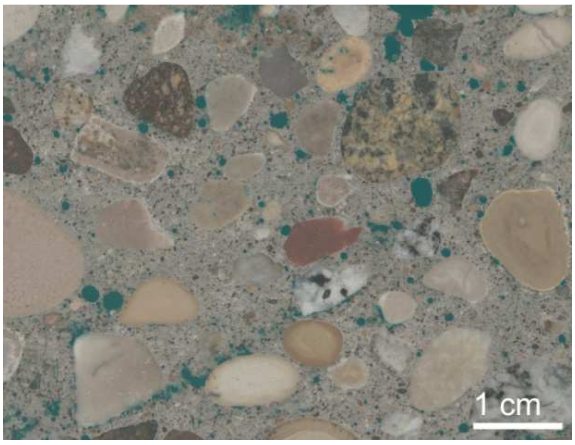

Figure 3.22. Sample CP1, polished cross section

The fine aggregate is constituted by sub-angular to sub-rounded natural sand characterized by medium-high grading and generally high sphericity (figures 3.23, 3.24). The granulometric distributions show maximum frequency in the class of the medium sands for the concrete of the slabs and the beams, and in the class of the fine sands for the concrete of the columns. As observed for the concrete of the first constructive phase, a petrographic predominance of carbonate rocks of the same nature of those constituting the coarse aggregate is observable for the granulometric class of the very coarse sands only (figure 3.24). A progressive enrichment in siliceous clasts occurs at decreasing granulometries, becoming highly predominant in the classes of the medium and fine sands (figures 3.24, 3.25, 3.26). Amongst them, only rare rock fragments are present, while the most relevant volumetric fraction is constituted by quartz grains, also in microcrystalline and metamorphic form (figure 3.23). Associated k-feldspar, highly altered plagioclase and rare mica flakes are also present. The petrographic observations are fully consistent with the mineralogical assemblages determined by XRPD (figure 3.27). The fine aggregate is characterized by high compactness, with almost total absence of internal porosity. No signs of secondary cracking of the clasts are observable.

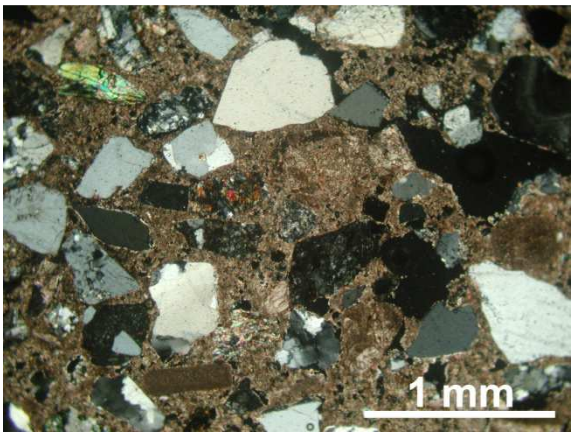

Figure 3.23. Sample CT1, crossed polars microphotograph

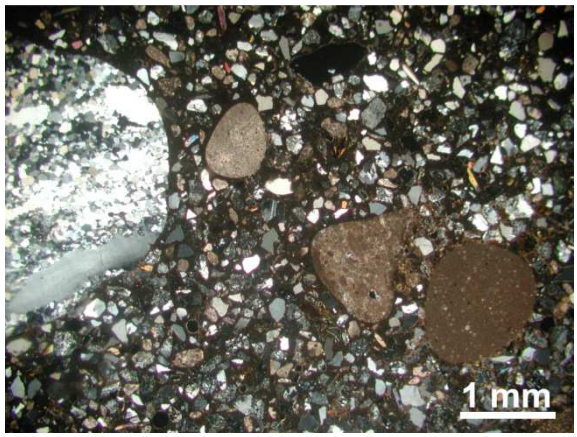

Figure 3.24. Sample CP2, crossed polars microphotograph

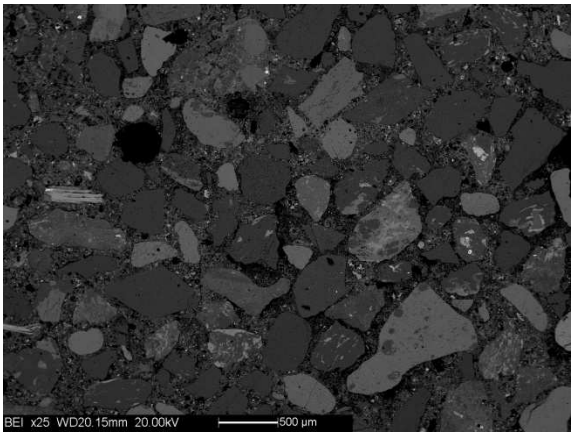

Figure 3.25. Sample CC3, SEM-BSE image. Quartz grains appear darker

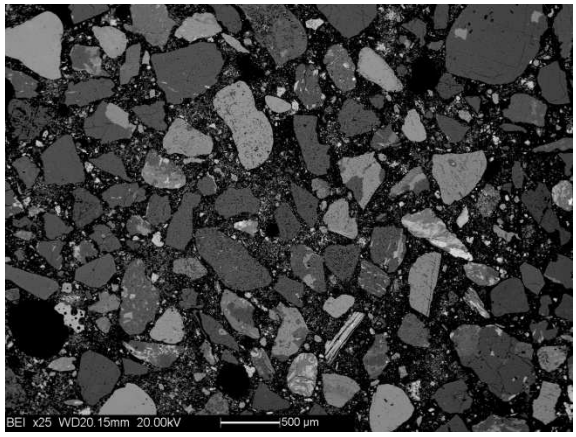

Figure 3.26. Sample CP1, SEM-BSE image. Quartz grains appear darker

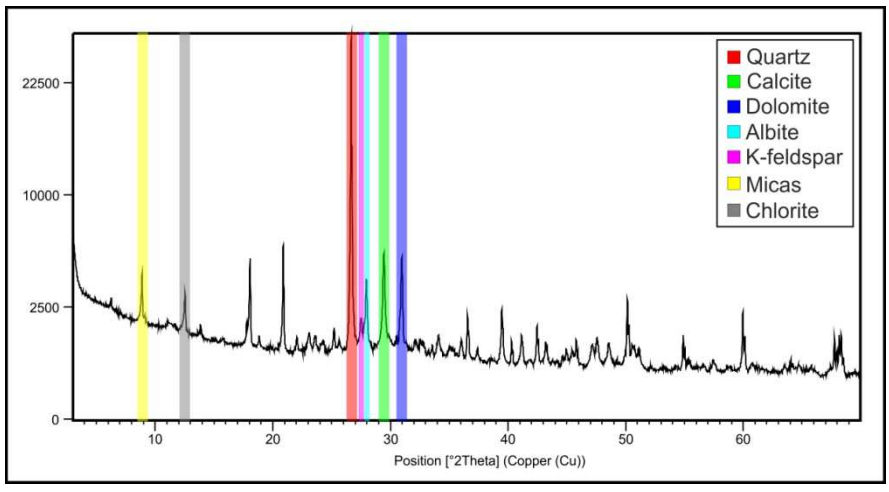

Figure 3.27. Sample CT6, diffraction pattern of the fraction under 500 µm, with highlighted the main reflexes of the crystalline phases constituting the fine aggregate fraction

The cement matrix is characterized by a light gray color and shows a differentiated adhesion to the aggregate according to the structural elements, being high for the concrete of the columns and lower for the concrete of the other elements, with significant occurrence of interfacial voids on the coarser grains, especially for the beams. Anomalous cracking patterns related to inadequate curing procedures are totally absent. The volumetric degree of capillary porosity is reduced, even though higher than the one observed for the concrete of the first constructive phase (figure 3.28), suggesting the adoption of higher w/c ratios for the manufacturing of the conglomerates.

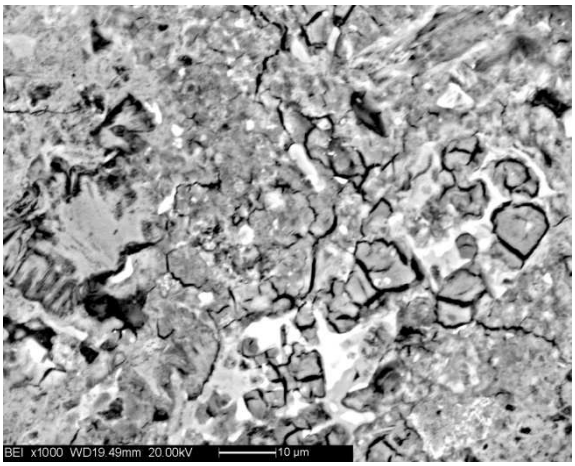

Figure 3.28. Sample CP1, high magnification SEM-BSE image. Capillary porosity is visible

Differentiated degrees of macro- and mesoporosity are observable according to the type of structural element. As for the columns, voids percentages are comparable to the ones observed for the concrete of the first constructive phase (figure 3.22). Voids are homogeneously distributed in the conglomerates and irregular entrapped air voids/water voids with maximum dimensions of 7-8 mm and medium dimensions of 1-3 mm prevail over spherical submillimetric entrained air voids. As for the other structural elements, voids percentages are higher, between 9% and 11% over the total volume of the samples. Irregular and elongated entrapped air voids/water voids, with maximum dimensions of 7-8 mm and medium dimensions of 1-3 mm, are highly predominant over spherical submillimetric entrained air voids (figure 3.21). Moreover, the former are disposed preferentially in the proximity of the coarse aggregate particles.

The textural features of the samples indicate a more accurate mix design formulation for the concrete of the columns, associated with better casting and compaction procedures. This may be related to the lack of reinforcement on these elements, which required an

improvement of the quality of the materials. On the contrary, the reinforced concrete of the horizontal structural elements suffers from excessive macro- and mesoporosity, related both to excessive dosages of coarse aggregate and to bad compaction and vibration procedures during the casting of fresh conglomerate.

3.4.1.4 Concrete of the third constructive phase

The materials are characterized by a greater volumetric fraction of hardened matrix with respect to the concrete of the other constructive phases, indicating the utilization of higher cement dosages in the original mix design. The aggregate is homogeneously distributed in the hardened conglomerate for all samples. The granulometric distribution of the aggregate has a bimodal shape and is far from the ideal Bolomey curve, with discrepancies related mainly to a marked enrichment in fine gravel in the original mix.

The coarse aggregate is constituted by rounded natural gravel characterized by medium-high grading and generally medium sphericity (figure 3.29). The maximum dimensions are within the class of the coarse gravels (32 mm). For all analyzed concrete samples, the peak of granulometric distribution of the coarse aggregate is within the class of the fine gravels. Petrographically, carbonate rocks are dominant, constituting approximately 50% of the total volumetric fraction (figures 3.29, 3.30). Amongst the various carbonate species, sparry dolostones and micritic limestones are predominant, with associated bioclast mudstones and grainstones and rare marls and micritic limestones with chert nodules. The remaining fraction is constituted by a heterogeneous assemblage of siliceous rocks, amongst which felsic volcanic lithologies are predominant (rhyolites and trachytes). Clasts of metamorphic rocks are common, mainly quartzites with associated schists and gneisses, while felsic plutonic rocks, mainly granites, are rare. The coarse aggregate is characterized by high compactness, with almost total absence of meso- and macroporosity and a reduced microporosity for the sparry carbonates only (figure 3.29). No signs of secondary cracking of the clasts are observable.

The fine aggregate is constituted by sub-angular to sub-rounded natural sand characterized by poor grading, with peaks of distribution in the classes of the coarse and medium sands, and generally high sphericity (figures 3.30, 3.31).

Figure 3.29. Sample CT2, polished cross section

In these materials, a predominance of carbonate rocks of the same nature of those constituting the coarse aggregate is observable for the granulometric class of the very coarse sands only. A progressive enrichment in siliceous clasts occurs at decreasing granulometries, becoming highly predominant in the classes of the medium and fine sands (figures 3.30, 3.31). Amongst them, only rare rock fragments are present, while the most relevant volumetric fraction is constituted by quartz grains, also in microcrystalline and metamorphic form. Associated k-feldspar, highly altered plagioclase and rare mica flakes are also present. The petrographic observations are fully consistent with the mineralogical assemblages determined by XRPD (figure 3.32). The fine aggregate is characterized by high compactness, with almost total absence of internal porosity. No signs of secondary cracking of the clasts are observable.

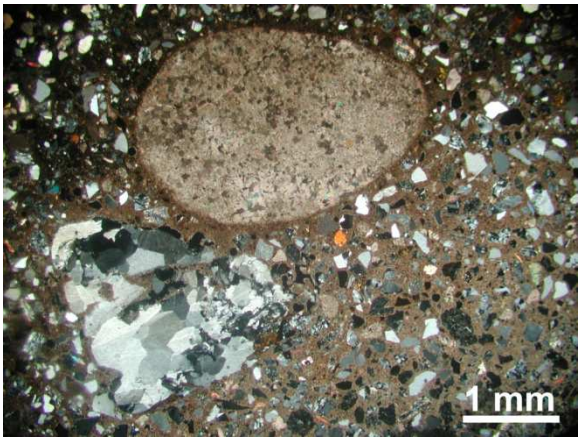

Figure 3.30. Sample CT5, crossed polars microphotograph

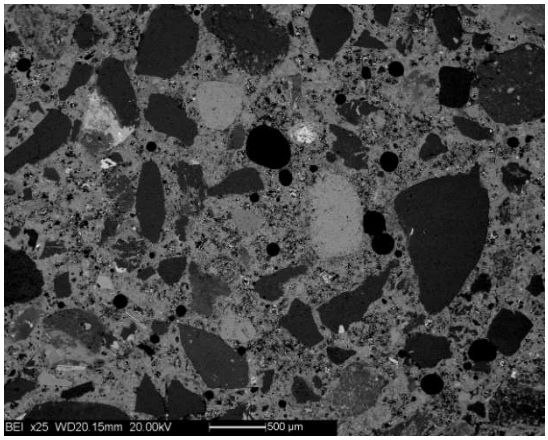

Figure 3.31. Sample CT2, SEM-BSE image. Quartz grains appear darker

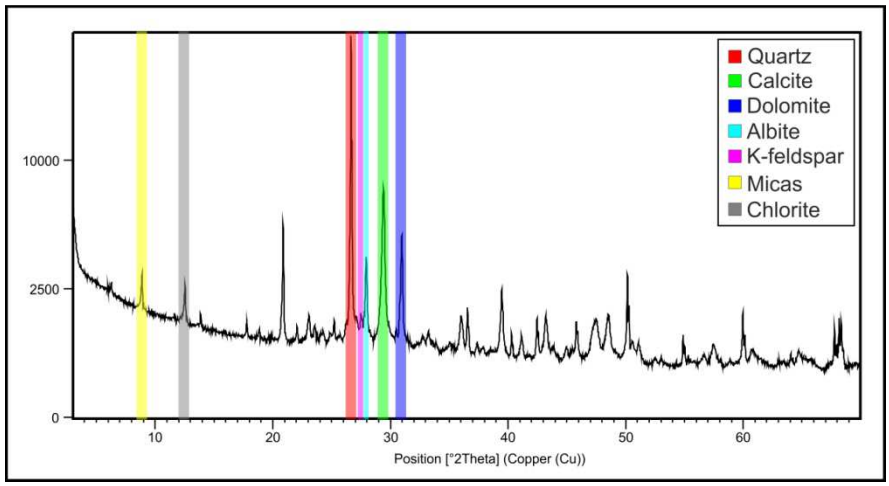

Figure 3.32. Sample CT5, diffraction pattern of the fraction under 500 µm, with highlighted the main reflexes of the crystalline phases constituting the fine aggregate fraction

The cement matrix is characterized by a light gray color and generally shows high adhesion to the aggregate, with scanty interfacial voids on the coarser grains only. Anomalous cracking patterns related to inadequate curing procedures are totally absent; moreover, the volumetric degree of capillary porosity is extremely reduced (figure 3.33), suggesting the adoption of low w/c ratios for the manufacturing of the conglomerates.

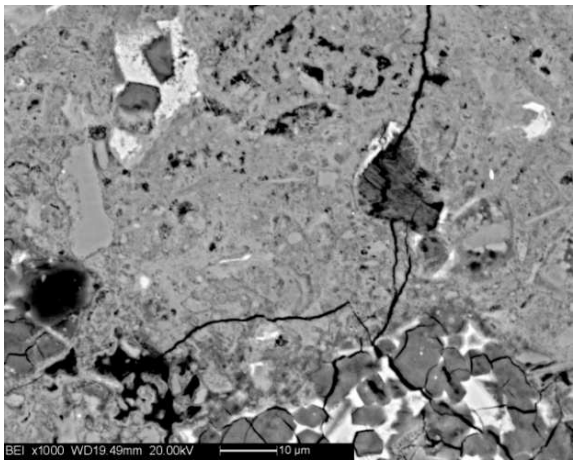

Figure 3.33. Sample CT2, high magnification SEM-BSE image. Capillary porosity is visible

The overall macro- and mesoporosity is extremely low, between 1% and 2% over the total volume of the samples, homogeneously distributed in the conglomerates and with a prevalence of spherical submillimetric entrained air voids over irregular entrapped air voids/water voids with maximum dimensions of 3-4 mm and medium dimensions of 1-2 mm (figure 3.29). These features both confirm the reduced w/c ratios adopted and indicate

proper compaction and vibration procedures of the fresh conglomerates during casting operations.

3.4.2 Victory Monument

3.4.2.1 Compressive strength values

The compressive strength values for the sampled cores, expressed in terms of cylindrical strength (f_c), are reported in table 3.7.

Sample	F_c (MPa)
BS1	6.6
BS2	8.3
BS3	15.5
BS4	5.2
BV1	9.7
BG1	32.2
BT1	40.8

Table 3.7. Victory Monument, compressive strength values for the sampled cores

The results indicate strong differences in the mechanical behavior of concrete according to the type of structural element.

The concrete of the walls and the vaulted slab are characterized by low and highly heterogeneous compressive strength values. The bad mechanical properties suggest both the adoption of incorrect mix design and inaccurate casting procedures. The heterogeneous values, particularly evident for the couples of cores taken from the same walls at different heights, suggest significant macroscopic segregation phenomena due to the lack of fresh concrete compaction and homogenization.

The stairway concrete is characterized by markedly higher compressive strength values, indicating the adoption of better mix design and a manufacture according to more accurate casting and homogenization procedures.

The discrimination of the materials according to the structural element is confirmed by their minero-petrographic features, which are hereby described.

3.4.2.2 Concrete of the walls

The materials are characterized by inadequate volumetric proportions between inert fraction and cement matrix, with a clear deficit of binder associated to the presence of excessive amounts of fine aggregate and, for the concrete of the lower portions of the walls, of the coarser fractions of gravel. A homogeneous distribution of the aggregate is observable only at the millimetric and centimetric scale, thus identifying the concrete as highly incongruent along the vertical sections of the walls.

The granulometric distributions of the aggregate have a clear bimodal shape distant from the ideal Bolomey curves, with strong enrichment in coarse sand for all samples, and in coarse gravel for the concrete of the lower portions.

The coarse aggregate is constituted by rounded natural gravel characterized by poor grading and highly variable sphericity, generally medium-low. The maximum dimensions are within the class of the coarse gravels (28 mm) for the concrete of the higher portions, and within the class of the very coarse gravels (40 mm) for the concrete of the lower portions. The peaks of granulometric distribution of the coarse aggregate are variable, being within the classes of the fine and medium gravels for the concrete of the higher portions, and within the classes of the coarse and very coarse gravels for the concrete of the lower portions (figures 3.34, 3.35).

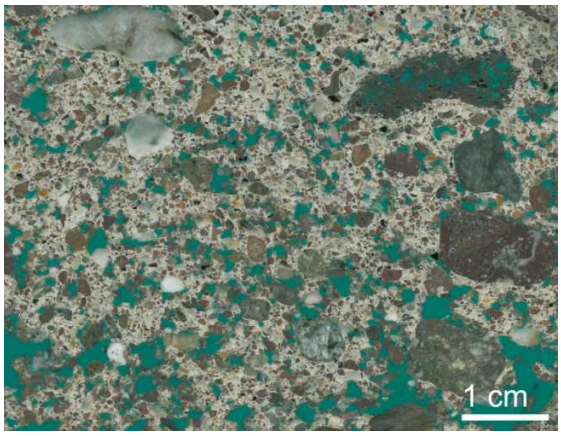

Figure 3.34. Sample BS1, polished cross section

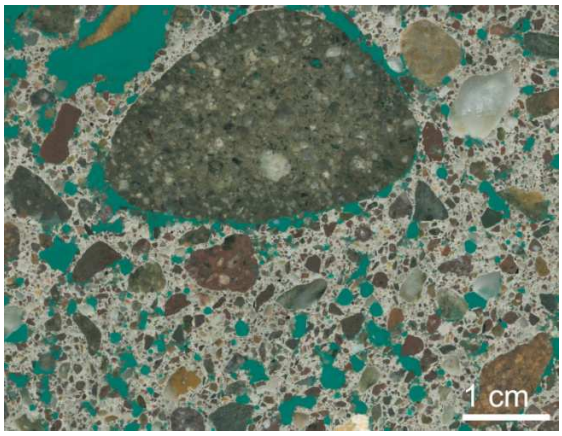

Figure 3.35. Sample BS2, polished cross section

Petrographically, felsic volcanic species are highly predominant, in particular ignimbrites and rhyolites. A subordinate metamorphic fraction is also present, constituted by quartzites, schists and very rare amphibolites. Furthermore, chert fragments and very rare felsic plutonic rocks are present. The aggregate is often highly fractured, in particular

ignimbrite and quartzite pebbles. Ignimbrites are the main constituents of the coarse aggregate, and they are characterized by colors variable between grayish-green and dark red. As highlighted by petrographic analyses in thin section (figure 3.36), they are constituted by an amorphous siliceous groundmass where phenocrysts of quartz, feldspars, mica and highly altered clinopyroxene are dispersed. EDS microanalyses on the glassy matrices showed their siliceous-aluminous nature (figure 3.37), with mean weight percentages of SiO_2 and Al_2O_3 of 59.50% and 17.00%, respectively. Furthermore, the groundmass is rich in sodium, potassium and calcium, with the following mean percentages of oxides: Na_2O 4.10%, K_2O 5.30%, CaO 14.00%.

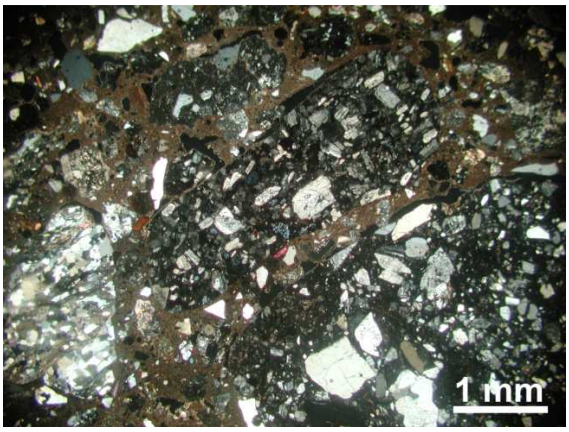

Figure 3.36. Sample BS4, ignimbrite rock fragments (crossed polars microphotograph)

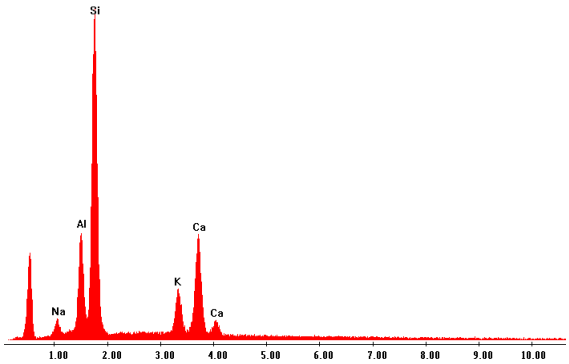

Figure 3.37. Typical EDS spectrum of the glassy groundmass of the ignimbrites

The fine aggregate is constituted by sub-angular to sub-rounded natural sand characterized by poor grading, with peaks of distribution in the class of the coarse sand, and medium-high sphericity (figures 3.38, 3.39, 3.40, 3.41). The petrographic nature of the sand is similar to the one of the coarse aggregate, with an enrichment in silicate minerals, mainly quartz and subordinately mica, chlorite, clinopyroxene and amphibole.

The petrographic observations are fully consistent with the mineralogical assemblages determined by XRPD (figure 3.42). A diffuse fracturing of ignimbrite and metamorphic quartz grains is observable for the fine aggregate, too.

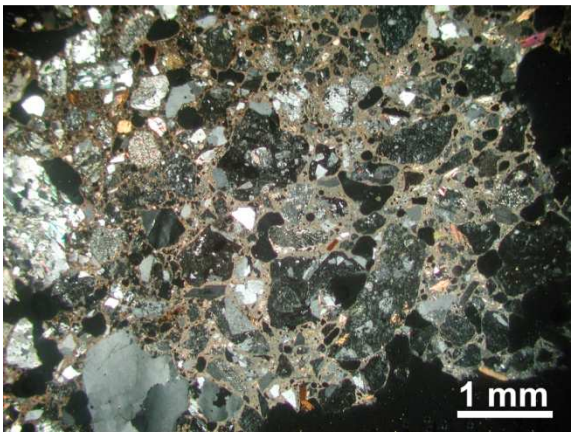

Figure 3.38. Sample BS1, crossed polars microphotograph

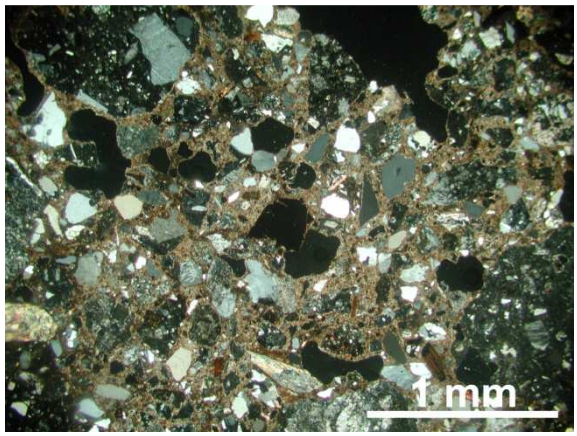

Figure 3.39. Sample BS3, crossed polars microphotograph

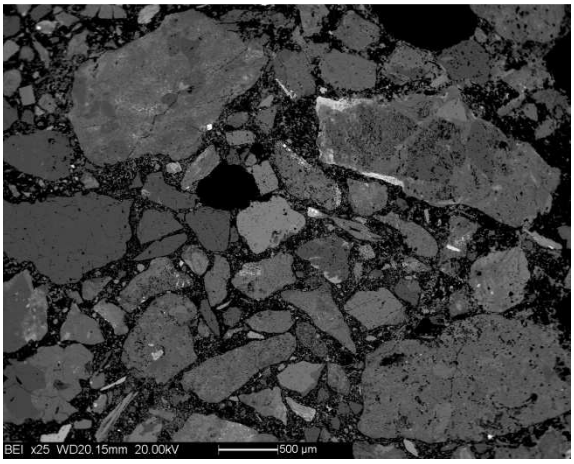

Figure 3.40. Sample BS5, SEM-BSE image

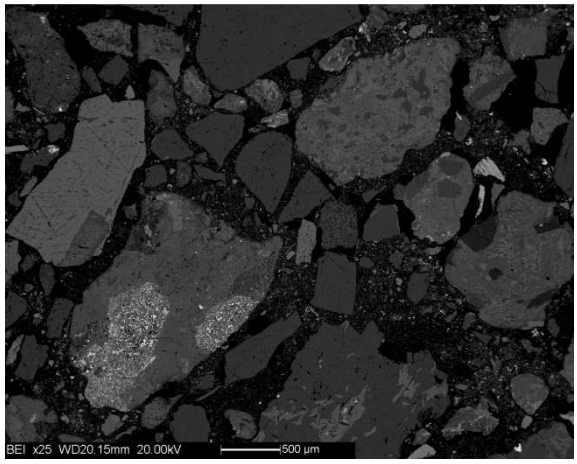

Figure 3.41. Sample BS6, SEM-BSE image

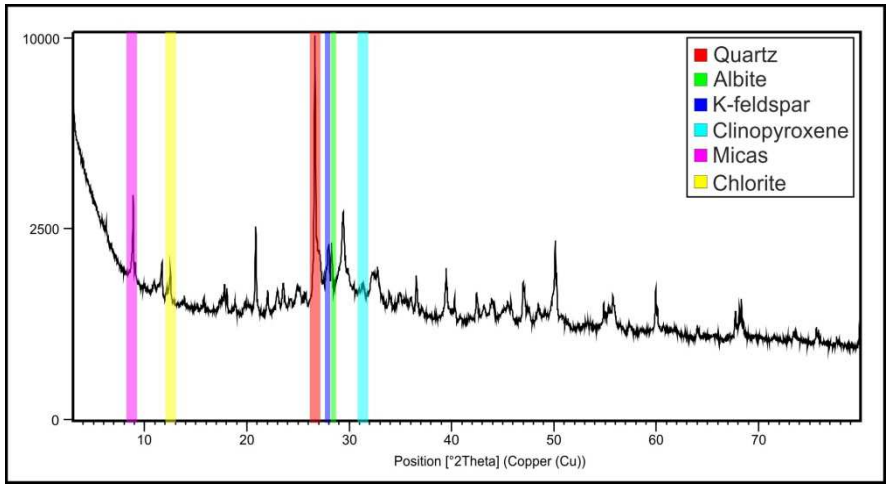

Figure 3.42. Sample BS2, diffraction pattern of the fraction under 500 µm, with highlighted the main reflexes of the crystalline phases constituting the fine aggregate fraction

The cement matrix is characterized by a white color and generally shows poor adhesion to the aggregate, with diffused presence of interfacial voids in the proximity to the coarser grains. The volumetric degree of capillary porosity is reduced, but it is higher for the concrete of the lateral walls (figures 3.43, 3.44), suggesting the adoption of generally low w/c ratios, lower for the conglomerates of the central walls.

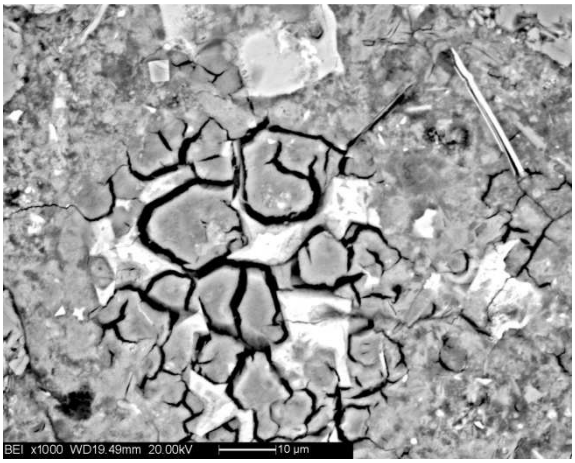

Figure 3.43. Sample BS1, high magnification SEM-BSE image. Capillary porosity is visible

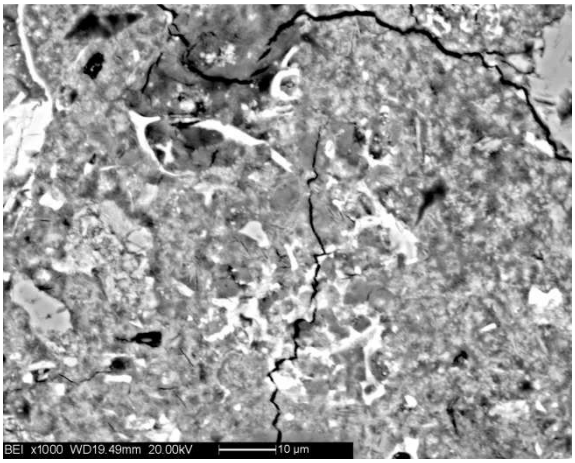

Figure 3.44. Sample BS3, high magnification SEM-BSE image. Capillary porosity is visible

The overall macro- and mesoporosity is high, generally between 10% and 15%, with a preponderance of irregular entrapped air voids/water voids with maximum dimensions of 3-5 mm and medium dimensions of 1-3 mm over spherical submillimetric entrained air voids (figures 3.34, 3.35). These features are due to both wrong mix design and bad compaction and homogenization procedures during the casting of the conglomerates.

3.4.2.3 Concrete of the vaulted slab

The materials are characterized by greater volumetric fraction of hardened matrix with respect to the concrete of the other structural elements, indicating the utilization of higher cement dosages in the original mix design. Despite this, the overall proportioning of the constituent is incorrect, being the materials depleted in coarse aggregate.

The aggregate is homogeneously distributed in the hardened conglomerate for all samples, and the granulometric distribution displays a unimodal pattern distant from the ideal Bolomey curve, with strong enrichment in coarse sand.

The coarse aggregate is constituted by rounded natural gravel characterized by poor grading and variable, generally low, sphericity (figure 3.45). The concrete is manufactured

with gravels with maximum dimension within the class of the coarse gravel (18 mm). The peak of granulometric distribution of the coarse aggregate is for all samples within the class of the fine gravel. The petrographic nature of the inert fraction is similar to the one observed for the aggregate of the other structural elements. The aggregate is often highly fractured, in particular ignimbrite and quartzite pebbles.

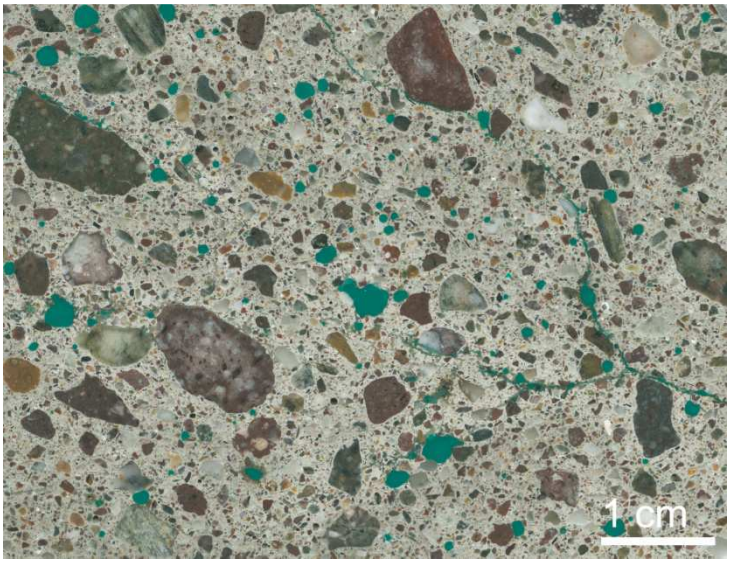

Figure 3.45. Sample BV1, polished cross section

The fine aggregate is constituted by sub-angular to sub-rounded natural sand characterized by poor grading, with peaks of distribution in the class of the coarse sands, and generally high sphericity (figures 3.46, 3.47). The petrographic nature of the sand is similar to that of the concrete walls, with diffuse fracturing of ignimbrite and metamorphic quartz.

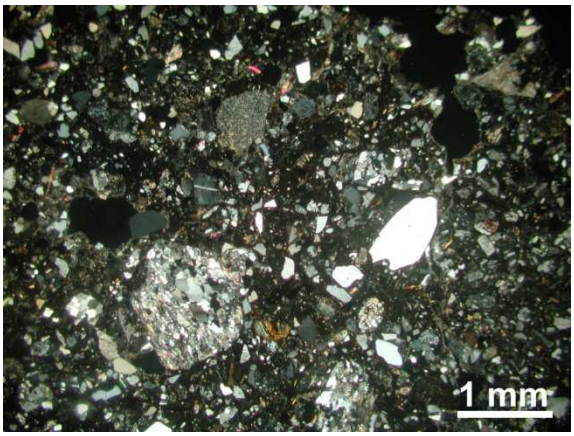

Figure 3.46. Sample BV2, crossed polars microphotograph

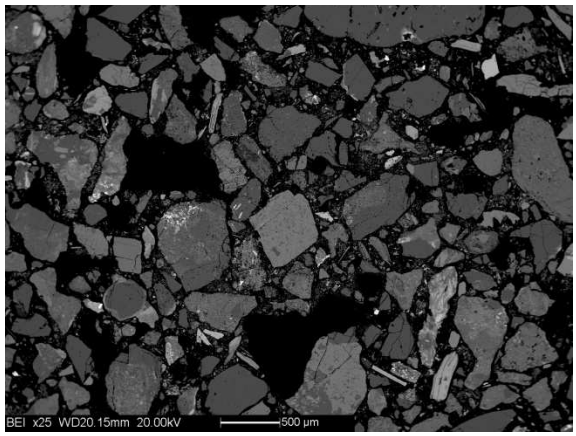

Figure 3.47. Sample BV1, SEM-BSE image

The cement matrix is characterized by a white color and generally shows good adhesion to the aggregate, with absence of interfacial voids in the proximity of the coarser grains. The volumetric degree of capillary porosity is high (figure 3.48), suggesting the adoption of high w/c ratios for the manufacturing of the conglomerates. Moreover, macro-cracking patterns are observable in the cement matrices, probably related both to the excessive w/c ratios and to inadequate curing procedures of the fresh conglomerates.

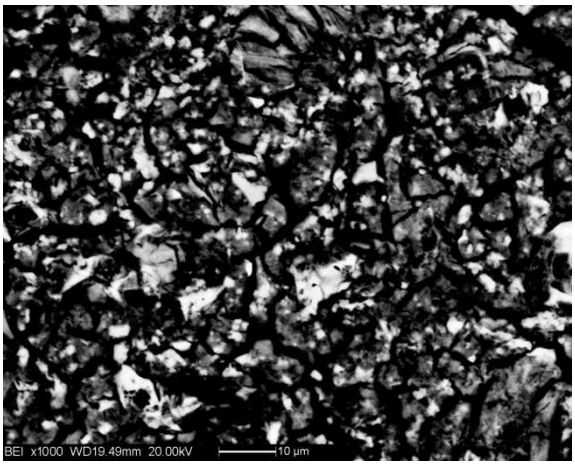

Figure 3.48. Sample BV2, high magnification SEM-BSE image. Capillary porosity is visible

The overall macro- and mesoporosity is generally low, between 2% and 5%, with a preponderance of irregular entrapped air voids/water voids with maximum dimensions of 4-5 mm and medium dimensions of 1-3 mm over spherical submillimetric entrained air voids (figure 3.45), indicating a good compaction of the fresh conglomerates, surely related to the high fluidity of the mixture due to the high w/c ratio.

3.4.2.4 Concrete of the stairway beams and slabs

The materials are characterized by a greater volumetric fraction of hardened matrix with respect to the concrete of the walls, indicating the utilization of higher cement dosages in the original mix design. Despite this, the overall proportioning of the constituent is incorrect, being the materials strongly depleted in coarse aggregate.

The aggregate is homogeneously distributed in the hardened conglomerate for all the samples, and the granulometric distribution has a unimodal shape distant from the ideal Bolomey curve, with strong enrichment in medium sand.

The coarse aggregate is constituted by rounded natural gravel characterized by poor grading and highly variable sphericity, generally medium-low (figure 3.49). The concrete

is manufactured with gravels with maximum dimensions within the class of the medium gravels (14 mm). The peak of granulometric distribution of the coarse aggregate is for all the samples within the class of the very fine gravels. The petrographic nature of the inert fraction is similar to the one observed for the aggregate of the concrete walls. The aggregate is often highly fractured, in particular ignimbrite and quartzite pebbles.

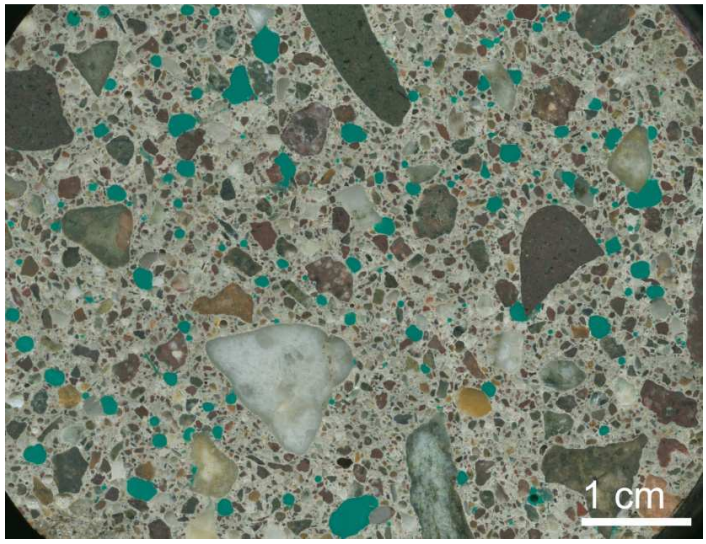

Figure 3.49. Sample BT1, polished cross section. The pore network is impregnated by green epoxy

The fine aggregate is constituted by sub-angular to sub-rounded natural sand characterized by poor grading, with peaks of distribution in the class of the medium sands, and generally high sphericity (figures 3.50, 3.51). The petrographic nature of the sand is similar to the one of the concrete walls, with diffuse fracturing of ignimbrite and metamorphic quartz also in these samples.

Figure 3.50. Sample BT2, crossed polars microphotograph

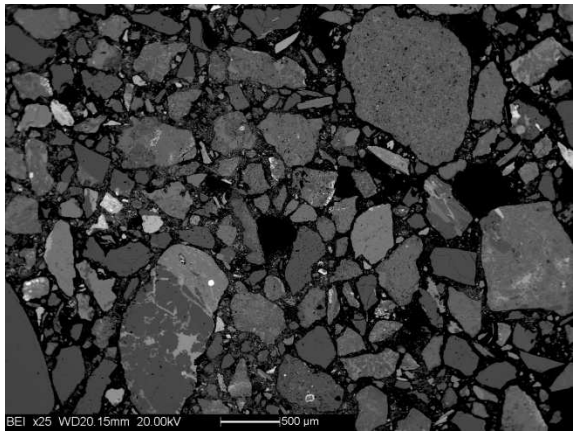

Figure 3.51. Sample BT1, SEM-BSE image

The cement matrix is characterized by a bluish-white color and generally shows good adhesion to the aggregate, with absence of interfacial voids in the proximity to the coarser grains. Anomalous cracking patterns related to inadequate curing procedures are totally absent; the volumetric degree of capillary porosity is low (figure 3.52), suggesting the adoption of low w/c ratios for the manufacturing of the conglomerates.

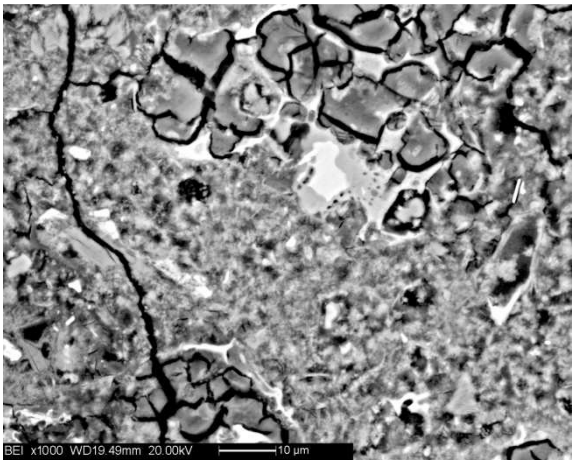

Figure 3.52. Sample BT5, high magnification SEM-BSE image. Capillary porosity is visible

The overall macro- and mesoporosity is generally low, between 4% and 5%, with a preponderance of irregular entrapped air voids/water voids with maximum dimensions of 5-6 mm and medium dimensions of 1-3 mm over spherical submillimetric entrained air voids (figure 3.49). These features indicate proper compaction and vibration procedures of the fresh conglomerates during casting operations.

3.4.3 Ex-Agrimont Area, C3 building

3.4.3.1 Compressive strength values

The compressive strength values for the sampled cores, expressed in terms of cylindrical strength (f_c), are reported in table 3.8.

Sample	**F_c (MPa)**
MC1	53.7
MC2	65.3
MC3	42.4

Table 3.8. C3 building of the Ex-Agrimont Area, compressive strength values for the sampled cores

As shown by test results, the concrete samples are characterized by quite dispersed, but rather high, compressive strength values, typical of modern high performance concretes. Surely, the prefabrication of the structural elements favored a deeper control of the production process, guaranteeing a high quality standard of the concrete. Furthermore, the prestressing procedure contributed to reaching higher compressive strength values. On the other hand, the fluctuations of the mechanical strengths suggest the adoption of rather accurate mix design, but not strictly uniform, with consequences on the overall performances of the materials.

These hypotheses are confirmed by the mineral-petrographic features of the concrete samples, which are hereby described.

3.4.3.2 Mineral-petrographic features

The materials are characterized by proper volumetric proportions between inert fraction and cement matrix, typical of ordinary structural concretes. Slightly greater volumetric fraction of hardened matrix are observable in MC3 and MC5 samples with respect to the other concrete samples, indicating the utilization of higher cement dosages in the original mix design. The aggregate is homogeneously distributed in the hardened conglomerate for all samples.

The granulometric distributions of the aggregate of all concrete samples have a bimodal shape, with a marked predominance of the coarse aggregate distribution maximum over the sand fraction distribution maximum. Furthermore, granulometric curves are comparable to the ideal Bolomey curves, with discrepancies related to enrichments in fine gravel in the original mixes. Generally, limited enrichments are observable. MC3 and MC5 samples only showed more marked enrichments (figure 3.54).

The coarse aggregate is constituted by sub-rounded to rounded natural gravel characterized by medium grading and variable sphericity, from medium to high (figures 3.53, 3.54). The maximum dimensions of the gravels are homogeneous, always within the class of the coarse gravels and comprised between 17 and 20 mm. The peaks of granulometric distribution of the coarse aggregate are markedly constant, always within the class of the fine gravels. A marked petrographic homogeneity of the gravels is observable, being carbonate rocks highly predominant (more than 80% over the total volumetric fraction, figures 3.53, 3.54). Amongst the various carbonate species, sparry and micritic limestones are dominant, with minor sparry dolostones, bioclast grainstones and micritic limestones

with chert nodules. The remaining fraction is constituted by a heterogeneous assemblage of siliceous rocks, amongst which cherts, felsic volcanic rocks and quartzites are predominant. Rare granite and serpentinite fragments are also present. The coarse aggregate is characterized by high compactness, with almost total absence of meso- and macroporosity and a reduced microporosity for the sparry carbonates only (figures 3.53, 3.54). No signs of secondary cracking of the clasts are observable.

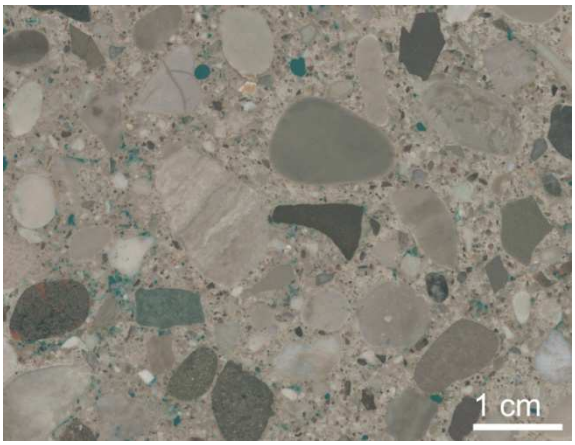

Figure 3.53. Sample MC1, polished cross section

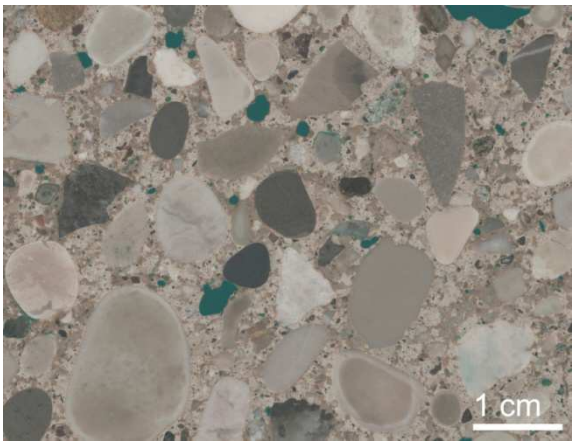

Figure 3.54. Sample MC3, polished cross section

The fine aggregate is constituted by sub-angular to sub-rounded natural sand characterized by poor grading, with peaks of distribution in the classes of the coarse and medium sands, and medium-high sphericity (figures 3.57, 3.58). Petrographically, it is mainly constituted by an association of carbonate rock fragments of the same nature of the ones constituting the coarse aggregate and quartz grains, also in microcrystalline and metamorphic form (figures 3.55, 3.56). Associated highly altered plagioclase crystals and rare mica flakes are also present, together with rare felsic rock fragments, both volcanic and plutonic, and very rare clastic sedimentary rock fragments. A progressive enrichment in siliceous clasts is observable at decreasing granulometry (figure 3.55).

The petrographic observations are fully consistent with the mineralogical assemblages determined by XRPD (figure 3.59). The fine aggregate is characterized by high compactness, with almost total absence of internal porosity. No signs of secondary cracking of the clasts are observable.

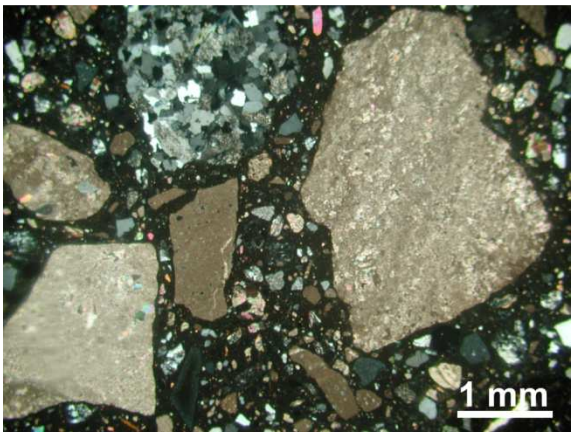

Figure 3.55. Sample MC6, crossed polars microphotograph

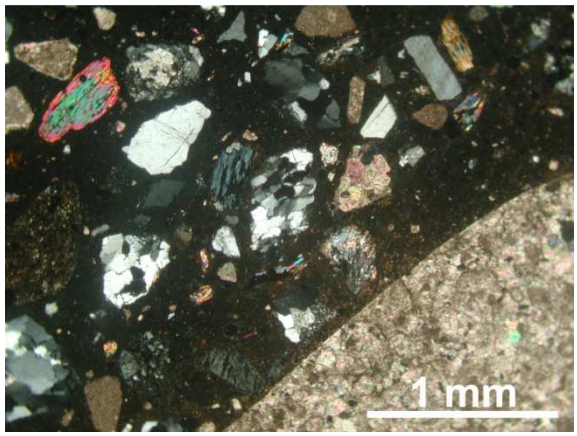

Figure 3.56. Sample MC4, crossed polars microphotograph

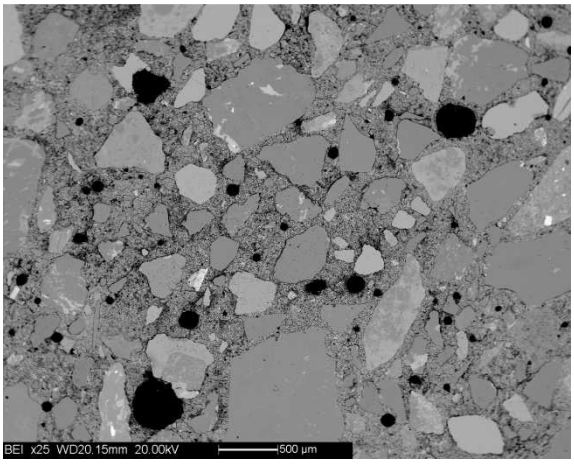

Figure 3.57. Sample MC7, SEM-BSE image

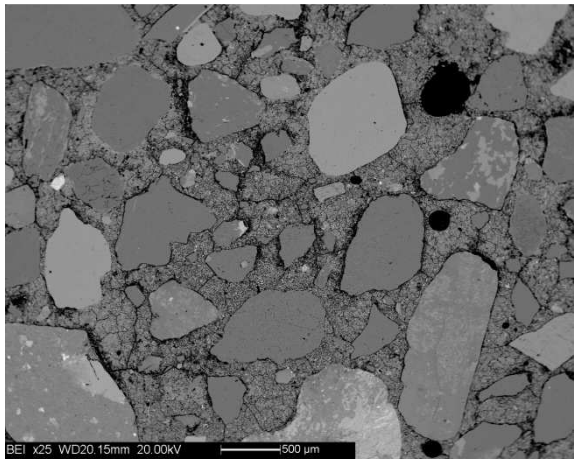

Figure 3.58. Sample MC5, SEM-BSE image

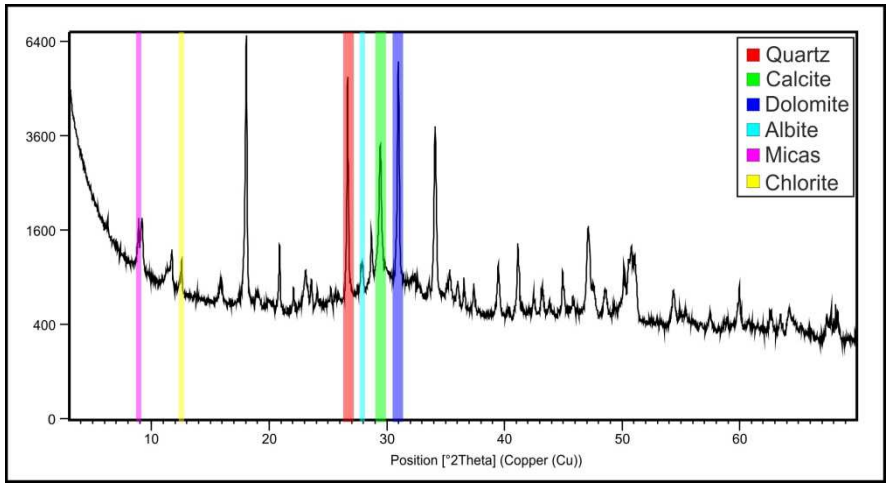

Figure 3.59. Sample MC2, diffraction pattern of the fraction under 500 µm, the main reflexes of the crystalline phases constituting the fine aggregate fraction are highlighted

The cement matrix is characterized by a yellowish gray color and generally shows high adhesion to the aggregate, with reduced presence of interfacial voids on MC3 and MC5 samples only. Anomalous cracking patterns related to inadequate curing procedures are totally absent. The volumetric degree of capillary porosity is low for most of the samples (figure 3.60), suggesting the adoption of proper w/c ratios for the manufacturing of the conglomerates. For MC3 and MC5 samples only, a greater capillary porosity is observable (figure 3.61), indicating the manufacturing of the concrete elements with greater w/c ratios with respect to the other structural modules.

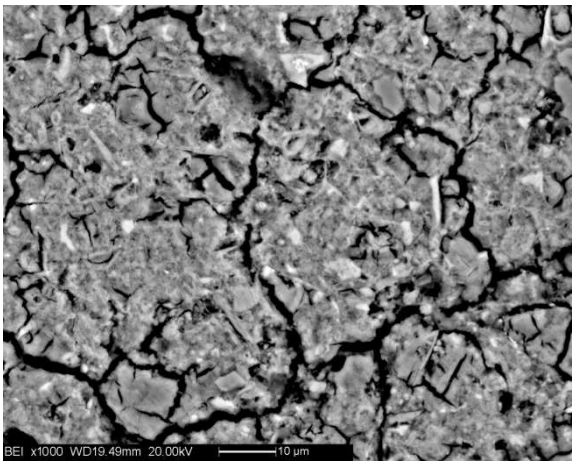

Figure 3.60. Sample MC1, high magnification SEM-BSE image. Capillary porosity is visible

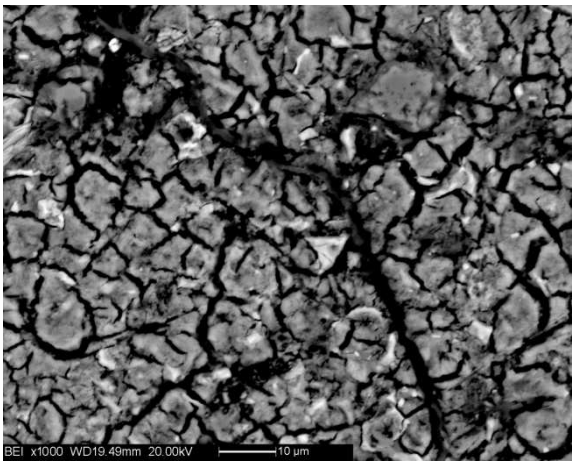

Figure 3.61. Sample MC3, high magnification SEM-BSE image. Capillary porosity is visible

The overall macro- and mesoporosity is extremely low for all the concrete samples, always below 2% over the total volume of the samples, and homogeneously distributed with a volumetric equivalence between spherical submillimetric entrained air voids and irregular entrapped air voids/water voids with maximum dimensions of 4-5 mm and medium dimensions of 1-2 mm (figures 3.53, 3.54). Again, a slightly greater degree of porosity is observable in MC3 and MC5 samples, with greater amounts of entrapped air voids/water voids, occasionally over-centimetric, and a lower occurrence of submillimetric entrained air voids with respect to the other samples (figures 3.57, 3.58).

These features indicate, for all samples, proper compaction and vibration procedures of the fresh conglomerates during casting operations. On the other hand, the greater degree of macro- and mesoporosity on MC3 and MC5 samples confirms the adoption of higher w/c ratios for the manufacturing of these structural elements.

3.4.4 Ex-Zweifel Embroidery Plant

3.4.4.1 Compressive strength values

The compressive strength values for the sampled cores, expressed in terms of cylindrical strength (f_c), are reported in table 3.9.

Sample	F_c (MPa)
RP1	20.3
RP2	21.7
RP3	21.9
RC1	27.6
RT1	26.8
RT2	27.3
RA1	4.5

Table 3.9. Ex-Zweifel Embroidery Plant, compressive strength values for the sampled cores

The results indicate strong differences in the mechanical behavior of the concrete according to the type of structural element.

The concrete of the column is characterized by similar compressive strength values, indicating a substantial homogeneity in the mix design of the conglomerates.

The concrete of the beams and the riddle is characterized by similar mechanical properties, indicating an homogeneous mix design. The higher compressive strength values with respect to the concrete of the columns indicate a better formulation of the conglomerates, according to a more accurate mix design.

Finally, the concrete of the arches is characterized by dramatically low compressive strength values, significantly lower than the minimum compressive strengths required by structural concretes. These features indicate both an extremely reduced quality in the mix design of the concrete and inadequate casting procedures of the structural elements.

The discrimination of the materials according to the structural element is confirmed by their mineral-petrographic features, which are hereby described.

3.4.4.2 Concrete of the columns

The materials are characterized by proper volumetric proportions between inert fraction and cement matrix, typical of lean structural concretes. The aggregate is homogeneously

distributed in the hardened conglomerate for all samples and the granulometric distributions have a bimodal pattern distant from the ideal Bolomey curve, with relevant enrichment in coarse and medium sand.

The coarse aggregate is constituted by rounded natural gravel characterized by poor grading and variable sphericity, from medium to high (figures 3.53, 3.54). The maximum dimension of the gravels is strictly homogeneous, always within the class of the coarse gravels and comprised between 28 and 30 mm. Moreover, the peaks of granulometric distribution of the coarse aggregate are markedly constant, always within the class of the fine gravels. A marked petrographic homogeneity of the gravels is observable, being carbonate rocks highly predominant (more than 75% over the total volumetric fraction, figure 3.62). Amongst the various carbonate species, sparry dolostones and micritic limestones are dominant, and are associated to minor quantity of bioclast-, intraclast- and ooid-bearing wackestones and packstones. The remaining fraction is constituted by a heterogeneous assemblage of siliceous rocks, amongst which cherts, quartzites and felsic volcanic rocks are predominant. Rare schist and gneiss fragments are also present. The coarse aggregate is characterized by high compactness, with almost total absence of meso- and macroporosity and a reduced microporosity for the sparry carbonates only (figure 3.62). No signs of secondary cracking of the clasts are observable.

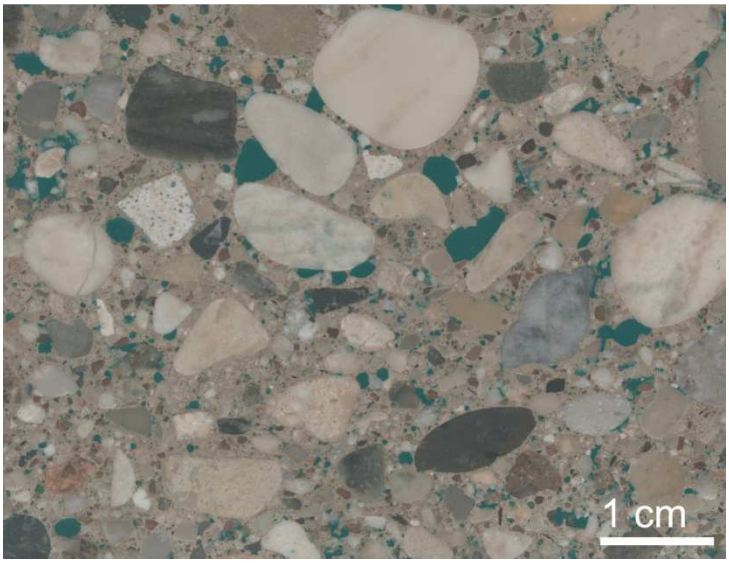

Figure 3.62. Sample RP1, polished cross section

The fine aggregate is constituted by sub-angular to sub-rounded natural sand characterized by poor grading, with peaks of distribution in the classes of the coarse and medium sands, and medium-high sphericity, even though quite variable (figures 3.63, 3.64).

Petrographically, it is mainly constituted by carbonate rock fragments of the same nature of the ones constituting the coarse aggregate, with associated quartz grains, also in microcrystalline and metamorphic form (figures 3.63, 3.64). Lower amounts of k-feldspar, highly altered plagioclase and rare mica flakes are also present. A progressive enrichment in siliceous clasts is observable at decreasing granulometry.

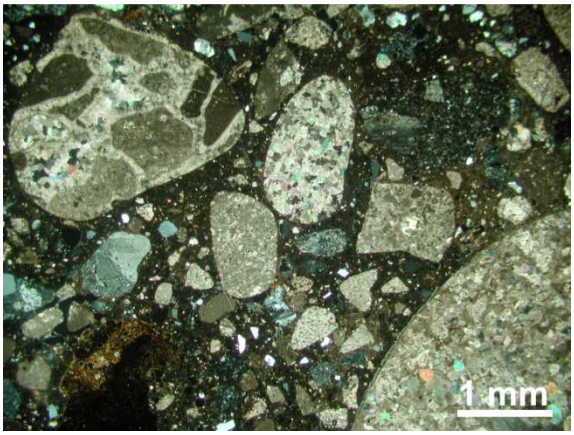

Figure 3.63. Sample RP3, crossed polars microphotograph

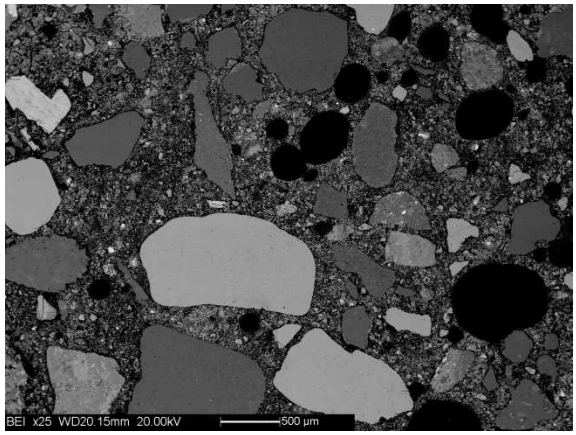

Figure 3.64. Sample RP2, SEM-BSE image

The petrographic observations are fully consistent with the mineralogical assemblages determined by XRPD (figure 3.65). The fine aggregate is characterized by high compactness, with a reduced degree of internal microporosity, mainly in the sparry carbonates. No signs of secondary cracking of the clasts are observable.

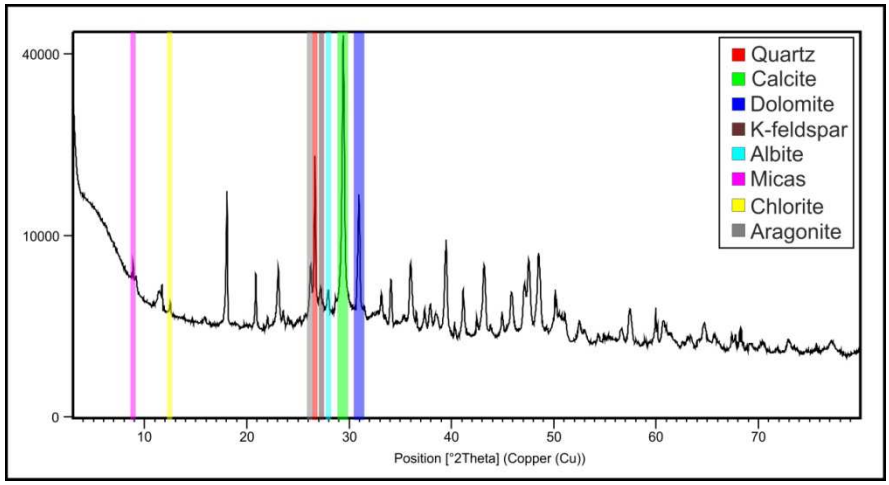

Figure 3.65. Sample RP1, diffraction pattern of the fraction under 500 µm, the main reflexes of the crystalline phases constituting the fine aggregate fraction are highlighted

The cement matrix is characterized by a yellowish gray color and generally shows high adhesion to the aggregate, with a reduced presence of interfacial voids on the coarser grains only. Anomalous cracking patterns related to inadequate curing procedures are totally absent. The volumetric degree of capillary porosity is high for all the samples (figure 3.66), suggesting the adoption of high w/c ratios for the manufacturing of the conglomerates.

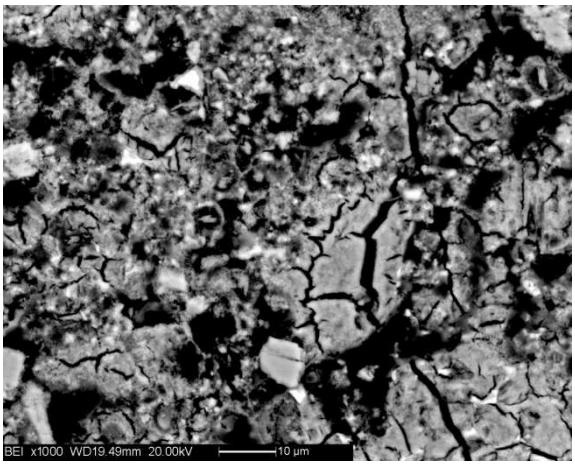

Figure 3.66. Sample RP2, high magnification SEM-BSE image. Capillary porosity is visible

The overall macro- and mesoporosity is low for all concrete samples, around 4% over the total volume of the samples, and homogeneously distributed with a substantial volumetric equivalence between spherical submillimetric entrained air voids and irregular entrapped air voids/water voids with maximum dimensions of 9-10 mm and medium dimensions of 1-3 mm (figure 3.62). These features indicate adequate compaction and vibration procedures of the fresh conglomerates during casting operations.

3.4.4.3 Concrete of the beams and the riddle

The materials are characterized by a greater volumetric fraction of hardened matrix with respect to the concrete of the columns, indicating the utilization of higher cement dosages in the original mix design. The aggregate is homogeneously distributed in the hardened conglomerate for all samples. Differences in granulometric distributions according to the type of structural element are observable, though they all have bimodal distributions comparable to the ideal Bolomey curves: beams are enriched in medium sand, while the riddle is markedly enriched in fine gravel.

The coarse aggregate is constituted by rounded natural gravel characterized by variable grading, poor for the beams and higher for the riddle. The sphericity is medium-high, lower for the riddle (figures 3.67, 3.68). The concrete is manufactured with gravels with variable maximum dimensions according to the type of structural element, greater for the beams (30 mm) than for the riddle (22 mm). The peak of granulometric distribution of the coarse aggregate is for all samples within the class of the fine gravels. The petrographic nature of the inert fraction is similar to the one observed for the aggregate of the concrete columns. The coarse aggregate is characterized by high compactness, with almost total absence of meso- and macroporosity and a reduced microporosity for the sparry carbonates only (figures 3.67, 3.68). No signs of secondary cracking of the clasts are observable.

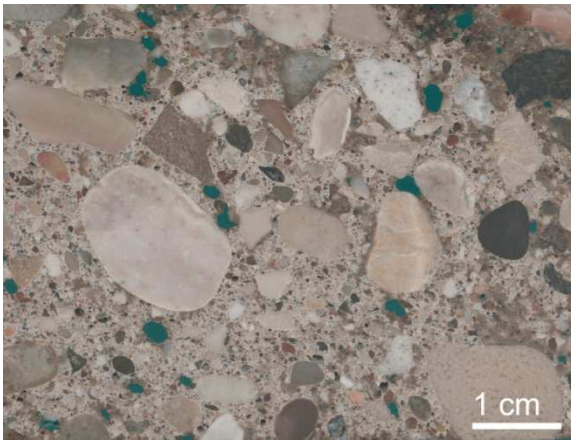

Figure 3.67. Sample RT2, polished cross section

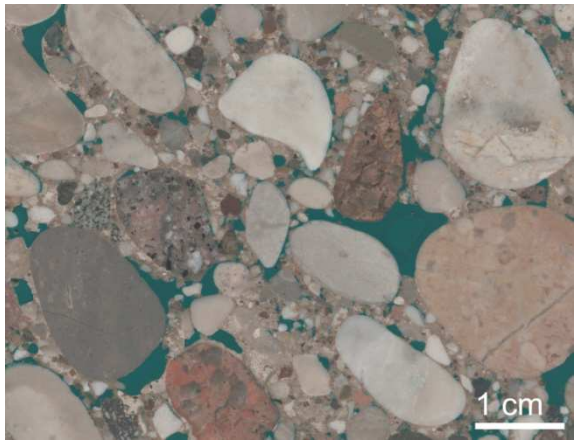

Figure 3.68. Sample RC1, polished cross section

The fine aggregate is constituted by sub-angular to sub-rounded natural sand characterized by poor grading and medium-high sphericity (figures 3.69, 3.70). The granulometric distribution displays maximum frequency in the class of the medium sands for the concrete of the beams (figure 3.71), and in the class of the coarse sands for the concrete of the riddle (figure 3.72). The mineral-petrographic nature of the sand and its textural appearance is similar to the one of the concrete columns.

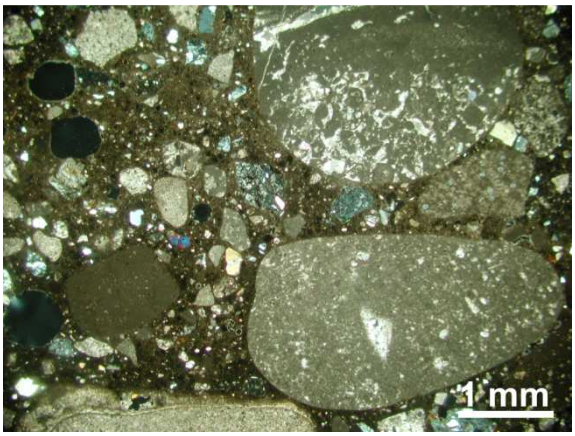

Figure 3.69. Sample RT1, crossed polars microphotograph

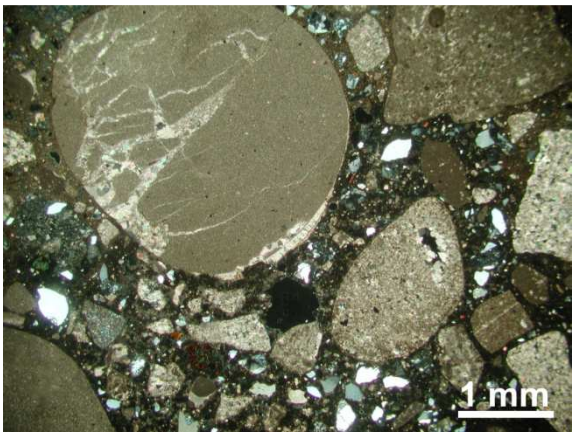

Figure 3.70. Sample RC2, crossed polars microphotograph

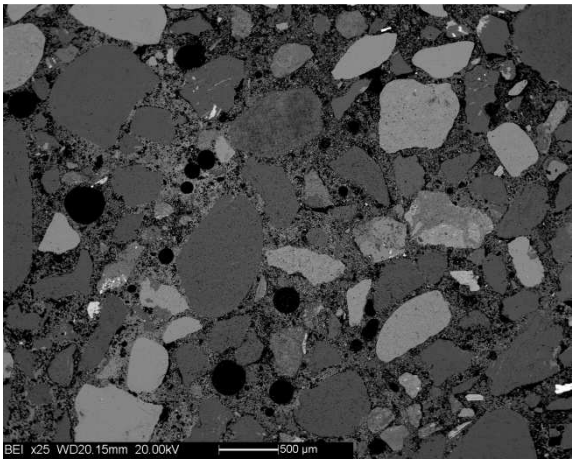

Figure 3.71. Sample RT3, SEM-BSE image

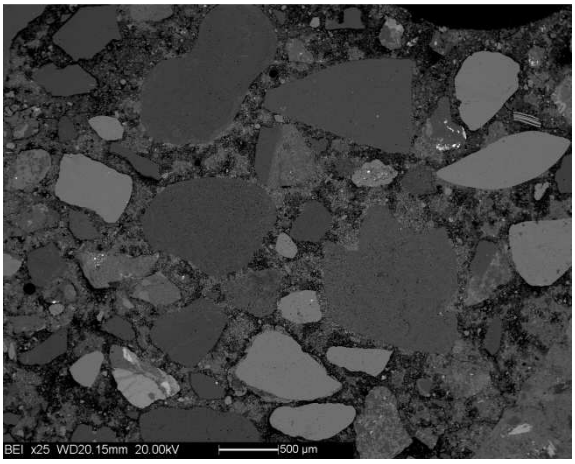

Figure 3.72. Sample RC1, SEM-BSE image

The cement matrix is characterized by a yellowish gray color and shows a differentiated adhesion to the aggregate according to the structural elements, being high for the concrete of the beams and lower for the concrete of the riddle, with a limited occurrence of interfacial voids on the coarser grains. Anomalous cracking patterns related to inadequate curing procedures are totally absent. The volumetric degree of capillary porosity is reduced (figure 3.73), suggesting the adoption of medium-low w/c ratios for the manufacturing of the conglomerates.

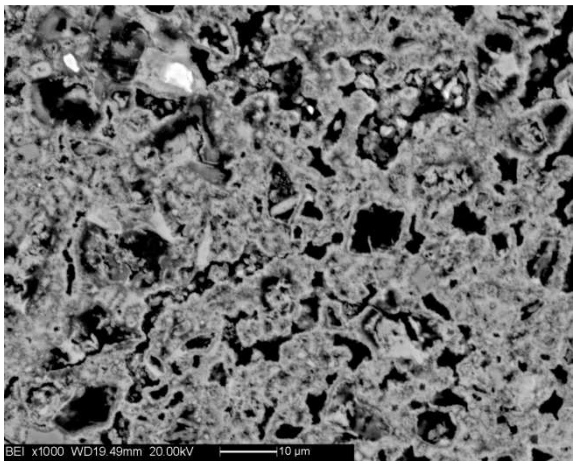

Figure 3.73. Sample RT3, high magnification SEM-BSE image. Capillary porosity is visible

Differentiated degrees of macro- and mesoporosity are observable according to the type of structural element. As for the riddle, voids percentages are comparable to the ones observed for the concrete of the columns (figure 3.22), while the degree of porosity for the concrete of the beams is slightly lower. Porosity is homogeneously distributed in the samples, with a substantial volumetric equivalence between spherical submillimetric entrained air voids and irregular entrapped air voids/water voids with maximum dimensions of 4-6 mm and medium dimensions of 1-2 mm for the concrete of the beams (figure 3.67), while a prevalence of irregular entrapped air voids/water voids, occasionally over-centimetric, is observable in the concrete of the riddle (figure 3.68), due to the already cited limited presence of interfacial voids on the coarser aggregate grains. These features indicate overall adequate compaction and vibration procedures of the fresh conglomerates during casting operations; the different typology of porosity in the concrete of the riddle may be related to the higher gravel content with respect to the other structural elements.

3.4.4.4 Concrete of the arches

The extremely poor mechanical properties of these structural elements are justified by the strongly incorrect mix design which characterize the conglomerates. The materials are characterized by significantly lower volumetric fraction of hardened matrix with respect to the concrete of the columns, indicating the utilization of insufficient cement dosages in the original mix design. A marked deficit in coarse aggregate is observable, associated to an enrichment in fine aggregate. The inert fraction is homogeneously distributed in the hardened conglomerate for all samples, and its granulometric distributions have a clear

bimodal pattern significantly differing from the ideal Bolomey curves, with strong enrichments in medium gravel and, particularly, in medium sand.

The coarse aggregate is constituted by rounded natural gravel characterized by high grading and variable sphericity, from medium to low (figure 3.74). The maximum dimensions of the gravels are within the class of the coarse gravels (24 mm), while the peaks of granulometric distribution are within the class of the medium gravels. The petrographic nature of the inert fraction is similar to the one observed for the aggregate of the other concrete elements. The coarse aggregate is characterized by high compactness, with almost total absence of meso- and macroporosity and a reduced microporosity for the sparry carbonates only (figure 3.74). No signs of secondary cracking of the clasts are observable.

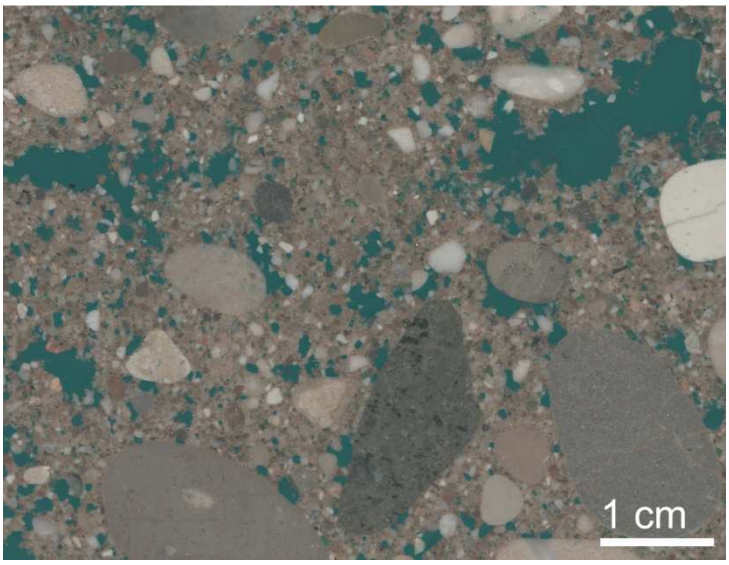

Figure 3.74. Sample RA1, polished cross section

The fine aggregate is constituted by sub-angular to sub-rounded natural sand characterized by high grading and variable generally medium-high sphericity (figures 3.75). The peak of granulometric distribution is within the class of the medium sands (figure 3.76). The mineral-petrographic nature of the sand and its textural appearance is similar to the one of the concrete columns.

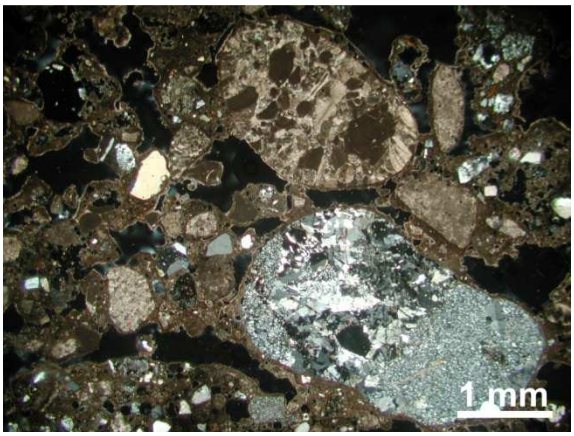

Figure 3.75. Sample RA2, crossed polars microphotograph

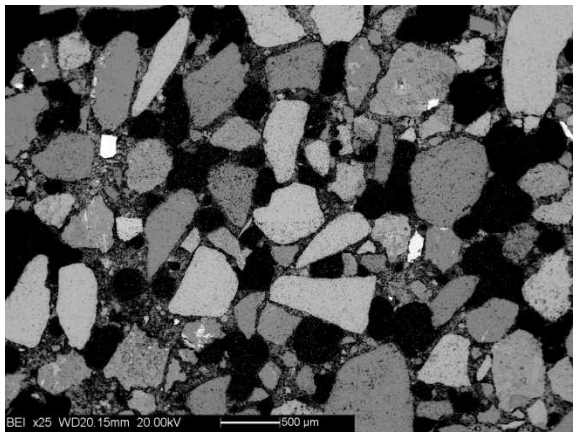

Figure 3.76. Sample RA1, SEM-BSE image

The cement matrix is characterized by a grayish-orange color and shows poor adhesion to the aggregate, with diffused presence of interfacial voids in the proximity to the coarser grains. The volumetric degree of capillary porosity is high (figure 3.77), suggesting the adoption of high w/c ratios for the manufacturing of the conglomerates. Macro-cracking patterns are observable in the cement matrices, probably related both to the excessive w/c ratios and to inadequate curing procedures of the fresh conglomerates.

Figure 3.77. Sample RA2, high magnification SEM-BSE image. Capillary porosity is visible

The overall macro- and mesoporosity is extremely high for all concrete samples, around 15% over the total volume of the samples, homogeneously distributed in the materials. A marked prevalence of irregular entrapped air voids/water voids over spherical submillimetric entrained air voids is observable. The voids have medium dimensions of 7-9 mm, but they are often interested by coalescence phenomena, with formation of diffuse

interconnected pore networks characterized by over-centimetric dimensions and dendritic shapes (figure 3.74). These features are mainly due to incorrect mix design of the conglomerates, but also indicate bad compaction and homogenization procedures during the casting of the concrete elements.

3.4.5 Ex-Foro Boario

3.4.5.1 Compressive strength values

The compressive strength values for the sampled cores, expressed in terms of cylindrical strength (f_c), are reported in table 3.10.

Sample	F_c (MPa)
FP1	57.0
FP2	55.4

Table 3.10. C3 building of the Ex-Foro Boario, compressive strength values for the sampled cores

As shown by tests results, the concrete samples are characterized by high compressive strength values, typical of modern high performance concretes. The evidences indicate an accurate manufacturing of the structural elements cast onsite, using concrete with optimized mix design, well homogenized and properly cured.

These hypotheses are confirmed by the mineral-petrographic features of the concrete samples, which are hereby described.

3.4.5.2 Mineral-petrographic features

The materials are characterized by proper volumetric proportions between inert fraction and cement matrix, typical of ordinary structural concretes. Slightly greater volumetric fraction of hardened matrix are observable in FP2 and FP3 samples with respect to the other concrete samples, indicating the utilization of higher cement dosages in the original mix design. The proportioning of components is homogeneous for all structural elements, indicating both a standardized casting procedure and the simultaneous casting of columns, linkage blocks and beam segments. The aggregate is homogeneously distributed in the hardened conglomerate for the samples.

The granulometric distributions of the aggregate of all concrete samples have a unimodal shape, with maximum of distribution in the coarse aggregate. Furthermore, granulometric curves are strictly comparable to the ideal Bolomey curves, with limited discrepancies related to slight enrichments in medium and fine sand in the original mixes. The coarse aggregate is constituted by rounded natural gravel characterized by poor grading and medium-high sphericity (figures 3.78, 3.79). The maximum dimensions of the gravels are strictly homogeneous, always within the class of the coarse gravels and comprised between 15 and 16 mm. The peaks of granulometric distribution of the coarse aggregate are markedly constant, always within the class of the fine gravels. Petrographically, carbonate rocks are predominant, constituting approximately 60% of the total volumetric fraction (figures 3.78, 3.79, 3.80). Amongst the various carbonate species, sparry dolostones and micritic limestones are predominant, with minor bioclast- and ooid-bearing mudstones and grainstones, and rare marls and micritic limestones with chert nodules. The remaining fraction is constituted by a heterogeneous assemblage of siliceous rocks, equally distributed between metamorphic lithologies (quartzites, schists and granitic gneisses) and felsic igneous rocks (trachytes, rhyolites and granites). Relevant amounts of chert are present, too. The coarse aggregate is characterized by generally high compactness, with almost total absence of meso- and macroporosity and a reduced microporosity for the sparry carbonates only (figures 3.78, 3.79). Nevertheless, secondary reaction rims occasionally occur on carbonate clasts, and several chert grains show secondary interfacial cracking patterns. These features clearly indicate alteration phenomena affecting the inert fraction, and they will be thoroughly described in chapter 5.

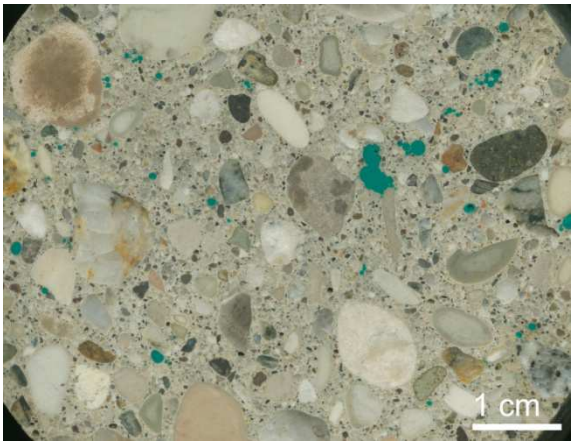

Figure 3.78. Sample FP1, polished cross section

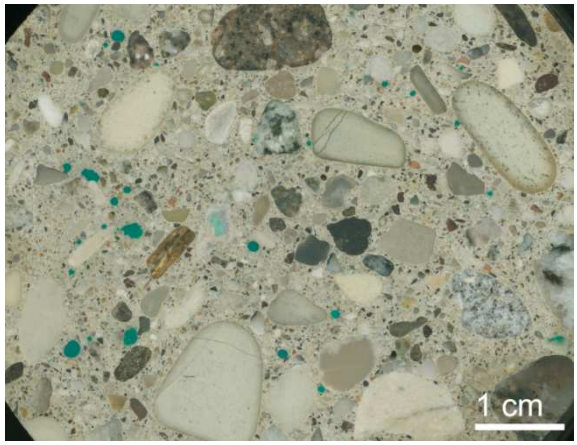

Figure 3.79. Sample FP2, polished cross section

The fine aggregate is constituted by sub-angular to sub-rounded natural sand characterized by poor grading, with peaks of distribution in the class of the coarse sands, and medium-high sphericity (figures 3.82, 3.83). Petrographically, a predominance of carbonate rocks of the same nature of the ones constituting the coarse aggregate is observable for the granulometric class of the very coarse sands (figure 3.80). A progressive enrichment in siliceous clasts occurs at decreasing granulometries, becoming predominant in the classes of the medium and fine sands (figure 3.81). Amongst them, only rare rock fragments are present, while the most relevant volumetric fraction is constituted by quartz grains, frequently in microcrystalline and metamorphic form (figure 3.81). Associated highly altered plagioclase crystals and rare mica flakes are also present.

The petrographic observations are fully consistent with the mineralogical assemblages determined by XRPD (figure 3.84). The fine aggregate is characterized by generally high compactness, with reduced internal microporosity. Nevertheless, the same alteration features observed for the coarse aggregate occur in the sand fraction.

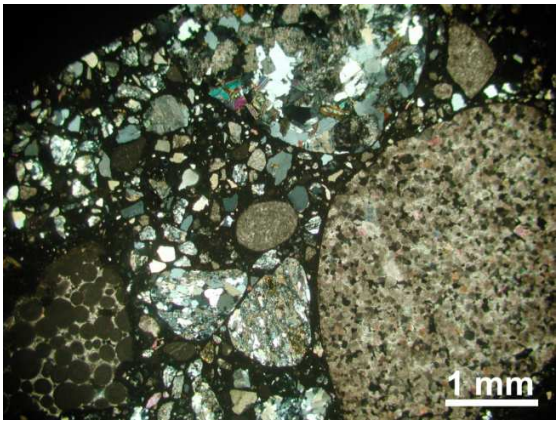

Figure 3.80. Sample FP1, crossed polars microphotograph

Figure 3.81. Sample FP3, crossed polars microphotograph

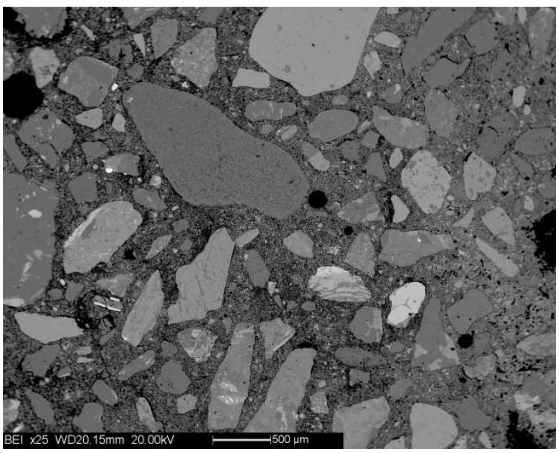

Figure 3.82. Sample FP7, SEM-BSE image

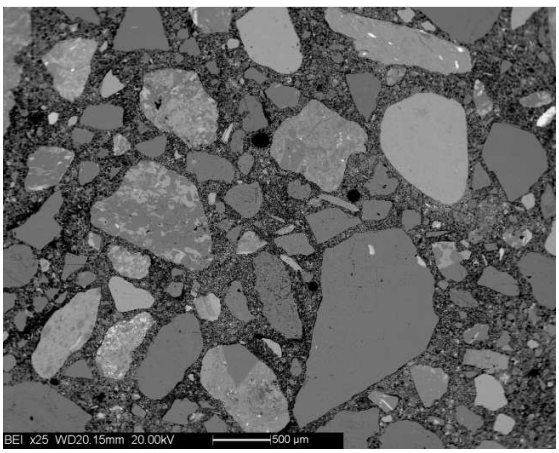

Figure 3.83. Sample FP2, SEM-BSE image

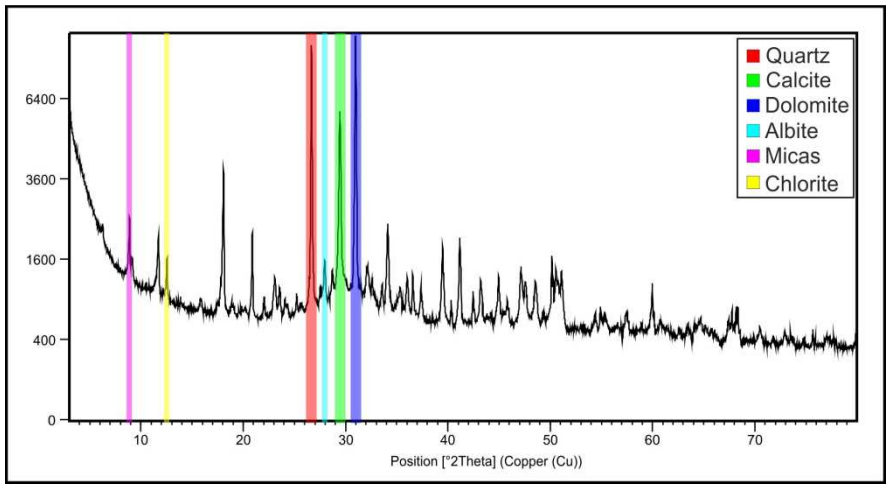

Figure 3.84. Sample FT6, diffraction pattern of the fraction under 500 µm, the main reflexes of the crystalline phases constituting the fine aggregate fraction are highlighted

The cement matrix is characterized by a pale greenish-yellow color and generally shows high adhesion to the aggregate, with an almost total absence of interfacial voids. Anomalous cracking patterns related to inadequate curing procedures are totally absent. The volumetric degree of capillary porosity is low for most of the samples (figure 3.85), suggesting the adoption of proper w/c ratios for the manufacturing of the conglomerates. In FP2 and FP3 samples only, a greater capillary porosity is observable (figure 3.86), indicating the manufacturing of the concrete elements with greater w/c ratios with respect to the other structural modules.

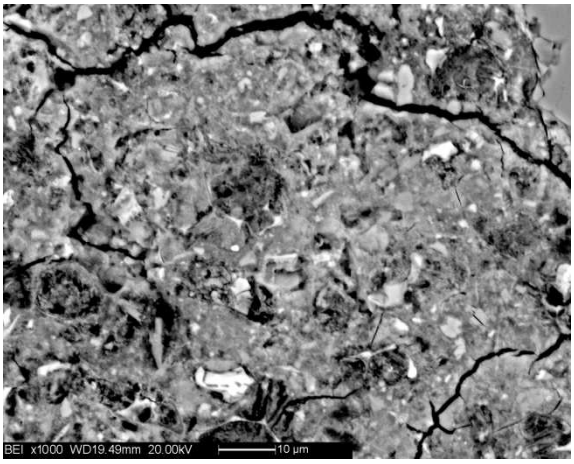

Figure 3.85. Sample FP4, high magnification SEM-BSE image. Capillary porosity is visible

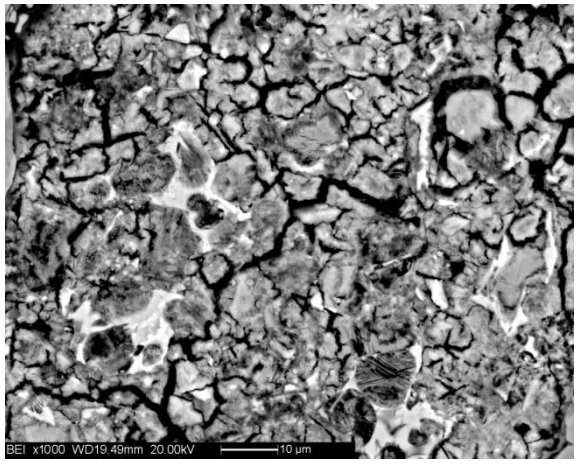

Figure 3.86. Sample FP3, high magnification SEM-BSE image. Capillary porosity is visible

The overall macro- and mesoporosity is extremely low for all concrete samples, always around 1% over the total volume of the samples, and homogeneously distributed with a

slight prevalence of spherical submillimetric entrained air voids over irregular entrapped air voids/water voids with maximum dimensions of 5-6 mm and medium dimensions of 1-3 mm (figures 3.78, 3.79).

These features indicate, for all samples, proper compaction and vibration procedures of the fresh conglomerates during casting operations.

3.4.6 Binder hydration

The degree of hydration is high on all concrete samples of the analyzed structures, with a presence of relict clinker grains always below 10% over the total hardened paste volume. Generally, only sporadic and partially reacted clinker grains, often characterized by large dimensions (figure 3.87), can be observed in the materials. Local accumulations of relict clinker grains can be observed in the concretes manufactured with low w/c ratios only (figure 3.88).

Figure 3.87. Sample BV1, large relict clinker grain in the hardened paste (crossed polars microphotograph)

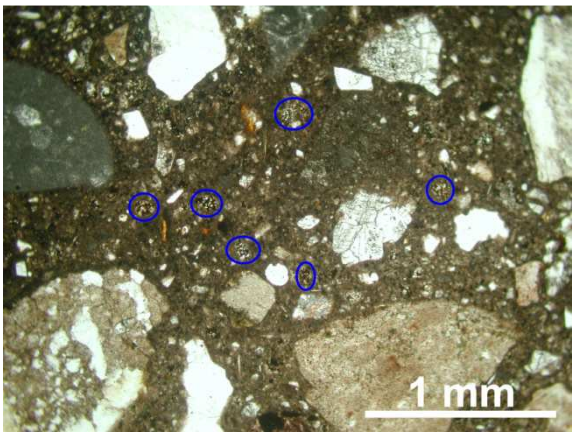

Figure 3.88. Sample CT2, local accumulation of relict clinker grains (plane polars microphotograph)

XPRD analyses on the finer fractions of the materials (figures 3.89, 3.90) showed no traces of C_3S and minor amounts of C_2S, indicating a high degree of hydration of the calcium silicates. A reduced but significant occurrence of C_3A and C_4AF is common for all materials. Considering the reduced amounts of interstitial phase in the original, unhydrated binder, the identification of C_3A and C_4AF peaks in the diffraction patterns of the analyzed concrete samples indicates degrees of hydration significantly lower for these phases with respect to calcium silicates.

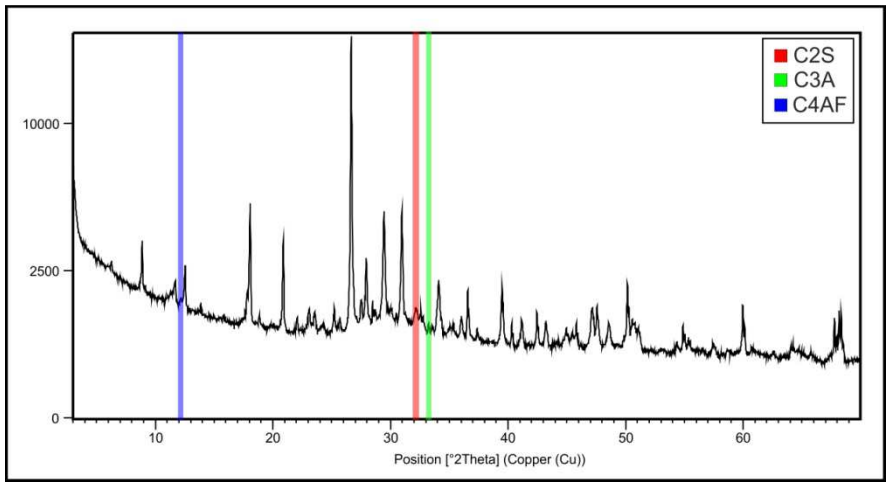

Figure 3.89. Sample CT2, diffraction pattern of the fraction under 63 µm, the main reflexes of the main crystalline phases constituting the cement clinker are highlighted

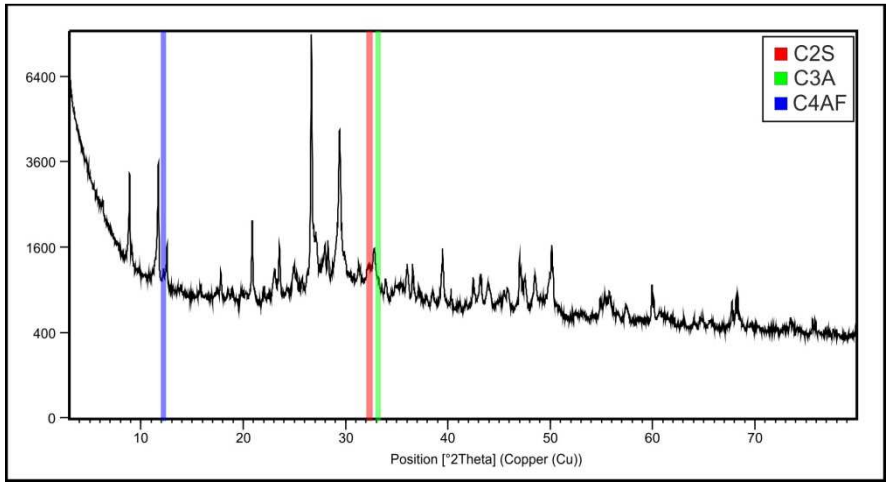

Figure 3.90. Sample BG1, diffraction pattern of the fraction under 63 µm, the main reflexes of the main crystalline phases constituting the cement clinker are highlighted

As shown by SEM analyses, relict clinker grains have medium dimensions comprised between 30 and 60 µm (figures 3.91, 3.92), with a limited occurrence of particles above 100 µm in the older concretes only (figure 3.93). As shown by the morphology of calcium silicates relicts and phantoms, a marked prevalence of euhedral C_3S crystals over subedral C_2S crystals occurred in the older clinkers too, indicating production processes of the cements at temperatures comparable to modern ones.

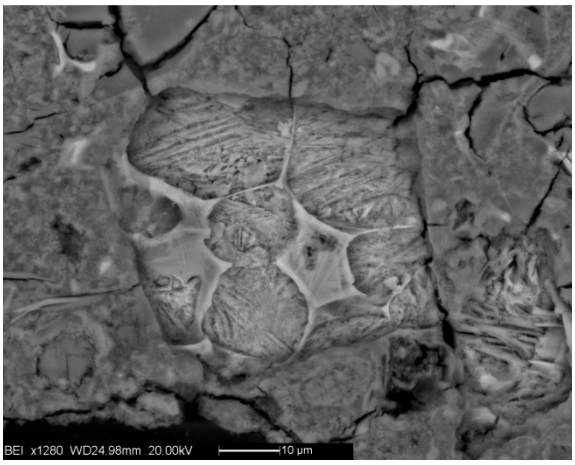

Figure 3.91. Sample RC1, SEM-BSE image of a relict clinker grain

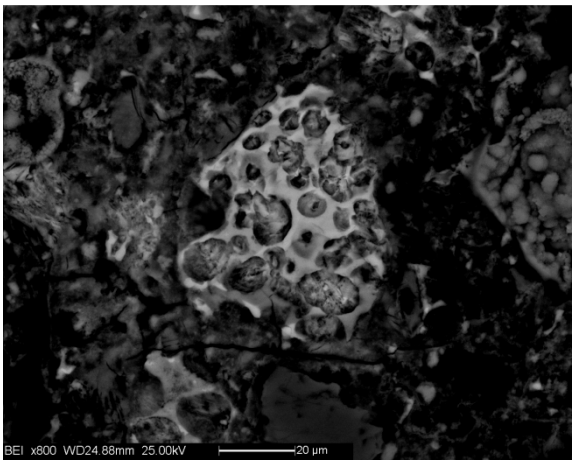

Figure 3.92. Sample FP1, SEM-BSE image of a relict clinker grain

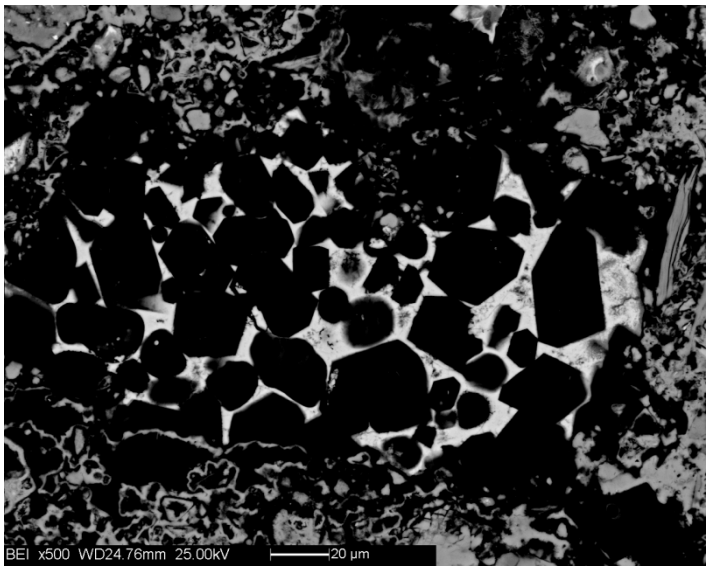

Figure 3.93. Sample BS4, SEM-BSE image of a relict clinker grain

SEM-EDS analyses confirmed the hypothesis of a lower degree of hydration of C_3A and C_4AF with respect to calcium silicates: relict clinker grains are frequently constituted by a skeleton of totally unhydrated interstitial phase (figures 3.94, 3.95), while calcium silicates are widely and in some case totally reacted. These features are particularly discernible by EDS maps of the grains, with the anhydrous frame of the interstitial phase clearly highlighted by Al and Fe maps (figures 3.96, 3.97).

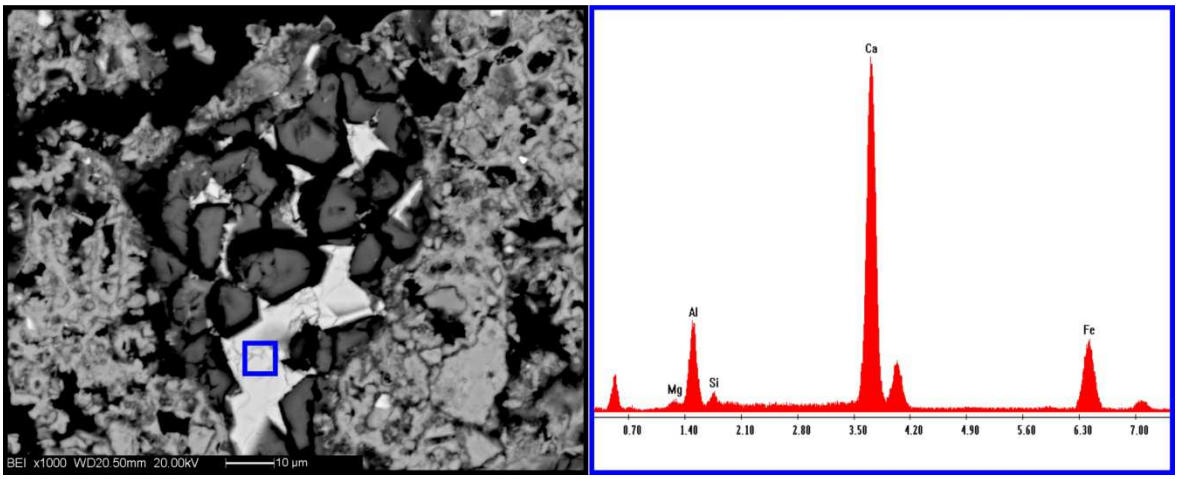

Figure 3.94. Sample CT1, SEM-BSE image of a relict clinker grain and EDS analysis of the interstitial phase

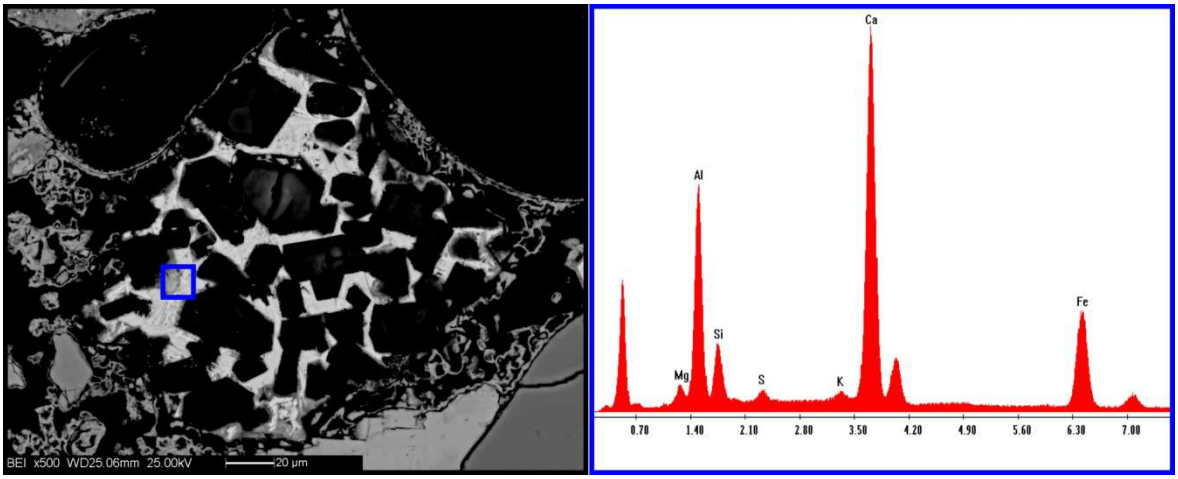

Figure 3.95. Sample BS1, SEM-BSE image of a relict clinker grain and EDS analysis of the interstitial phase

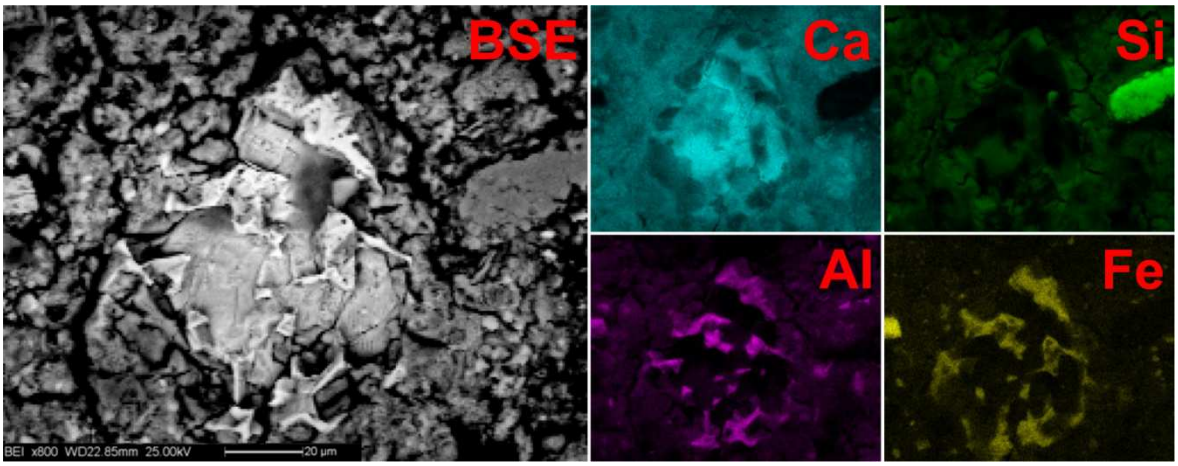

Figure 3.96. Sample MC3, SEM-BSE image of a relict clinker grain and EDS maps of Ca, Si, Al and Fe

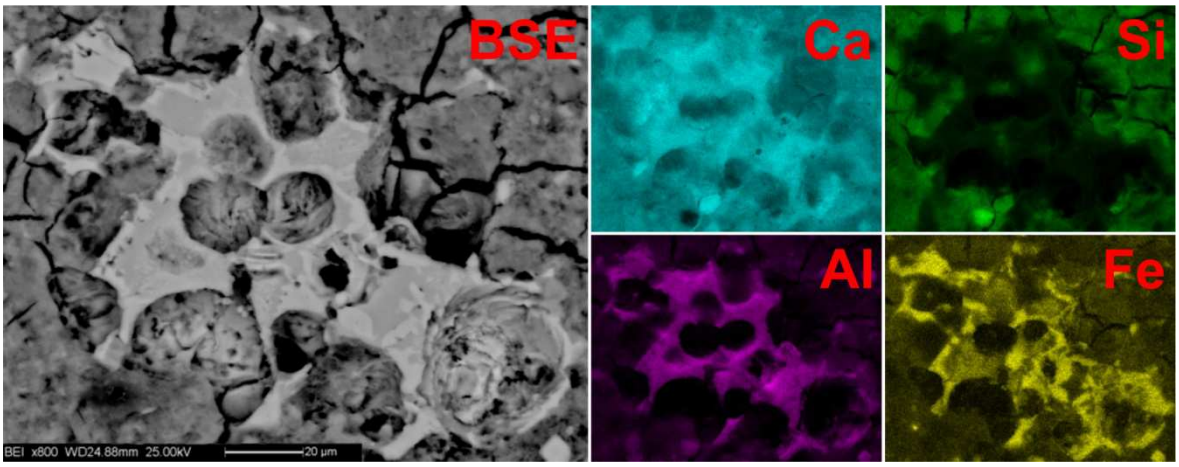

Figure 3.97. Sample FP3, SEM-BSE image of a relict clinker grain and EDS maps of Ca, Si, Al and Fe

3.5 CONCLUSIONS

The multi-analytical characterization of the concretes of the studied structures led to a thorough understanding of the materials, allowing the determination of the main characteristics of the constituents, together with an accurate, even though still qualitative, determination of the mix design of the conglomerates. Moreover, strong correlation between these parameters and the mechanical properties of the concretes were observed.

As regards the characteristics of the raw materials, the mineral-petrographic nature of the inert fractions suggests a local supply from alluvial deposits and river beds for the concretes of all structures. As regards the four structures located in the Veneto region, the prevalence of carbonate constituents in the aggregate, with enrichment in siliceous clasts towards the finer granulometry, indicates a supply from gravel quarries of the great rivers of the north-eastern Po valley, namely the Adige, Brenta and Piave rivers. Extensive aggregate quarrying activity is widespread in the Veneto region, with wide reservoirs of materials suitable for the manufacturing of standard and high performance concretes (Dal Cin, 1967; Fontanive, 1974; Stefanini, 1977; Bozzo et al., 2005). The high compactness of the aggregates used for the manufacturing of the concretes indicates an accurate discrimination of the clasts characterized by better mechanical properties and textural characteristics, in order to improve the performances of the resulting structural elements.

As regards the Victory Monument in Bolzano, mineral-petrographic characteristics of the inert fraction indicate local supply of raw materials, from the bed of the adjacent Talvera river, constituted mainly by clasts of felsic volcanic rocks, in particular ignimbrites

(Brondi, 1973). Such materials are hardly suitable for the utilization in the construction fields, due both to their chemical-mineralogical nature and their poor mechanical properties (Brondi, 1973). Furthermore, they were used as aggregate for the concretes of the building without proper selection procedures, as demonstrated by the diffuse presence of fractured clasts. These features indicate an approach to the building of the structure mainly focused on a rapid construction, limiting production costs as much as possible.

As regards the binder, a common use of Portland Cement with chemical and mineralogical characteristics similar to the ones of modern Ordinary Portland Cement was observed. This indicates a production of the binder in plants equipped with rotary kilns, capable of reaching properly the temperatures necessary for the occurrence of the clinkering process. Slight morphological differences are observable in the older concrete elements, i.e. the concretes of the first two constructive phases of the Northern Wing of the Carraresi Castle and the concretes of the Victory Monument, with a limited occurrence of relict clinker grains with dimensions above 100 µm. Textural and mineralogical features demonstrated the high reactivity of the binders, with the reaching of an advanced degree of hydration in all the materials, even though manufactured with low w/c ratio. Despite this, clear evidences of lower degrees of hydration of the interstitial phase with respect to the calcium silicates were observed, with a common occurrence of completely unreacted skeletons of C_3A and C_4AF aggregates.

As regards the mix design of the conglomerates, strong differences in the original mixtures according to the analyzed structure, the construction phase and the type of structural element were observed, with direct consequences on the mechanical properties of the concretes.

Mix design of the concretes used for the Northern Wing of the Carraresi Castle is differentiated according to the construction phase, with Hennebique elements characterized by the use of well proportioned aggregates, with proper amounts of cement in the mixes and low w/c ratios. Casting and homogenization procedures were optimal. Consequently, the materials have low permeability and excellent mechanical properties. 1920s concretes were prepared with a poorer mix design, despite the use of higher cement dosages, as shown by the adoption of aggregate granulometric curves far from the ideal Bolomey curves and higher w/c ratios. Textural features suggest less accurate casting and homogenization procedures for the horizontal elements, in particular for the concrete of the beams, while the columns were cast properly, probably due to the fact that they are not

reinforced. All these features reflected in the overall permeability and mechanical resistance of the structural elements. Finally, 1950s concretes are characterized by proper mix design as regards cement dosages and w/c ratios, while aggregates are still not well proportioned. Despite this, the materials are characterized by low permeability and high compressive strength values, probably due to proper casting and compaction procedures of the conglomerates.

Mix design of the concretes of the Victory Monument is differentiated according to the type of structural elements. Concrete walls are characterized by bad proportioning of the constituents, with low cement dosages and granulometric distribution of the aggregates strongly enriched in sand fraction and in some cases in coarse gravel. Casting and homogenization procedures were inadequate, certainly owing to the low workability of the pastes, due to the adoption of low w/c ratios. Consequently, materials are highly permeable, strongly segregated and of poor mechanical characteristics. The concrete of the vaulted slab, despite being produced with higher cement dosages, displays poor mechanical properties and high permeability due to the strongly incorrect grading of the aggregate, highly enriched in sand fraction, and to the excessive w/c ratios. Only stairway concrete was produced according to a better mix design, with higher cement dosages and lower w/c ratios. On the contrary, aggregate grading strongly differs from the ideal Bolomey curves, as it is enriched in sand fraction. These characteristics, together with accurate casting and homogenization procedures, allowed the reaching of proper mechanical resistances and permeability properties. These characteristics, together with the lack of reinforcement, suggest a structural conception of the walls and the vaulted slab to withstand compressive stresses only, while a more accurate structural plan was conceived for the realization of the reinforced concrete of the stairway elements, in order to optimize their flexural behavior.

Mix design of the concretes of the C3 building is substantially homogeneous and well optimized, with proper cement dosages and granulometric distributions comparable to the ideal Bolomey curves. Differences can be found in some cases in the adopted w/c ratios: despite being generally adequate, the adoption of higher values have been hypothesized for some structural elements, also characterized by higher cement dosages. Probably, additional aliquots of water were added to reach proper workability properties, varied by the increments in viscosity caused by the introduction of higher quantities of cement in the conglomerates. These features affected the overall permeability and compressive strength

values of the materials, despite being still significantly high, thanks to both the standardized casting and homogenization processes related to the prefabrication of the structural elements and the prestressing procedure adopted during the manufacturing of the arches.

Mix design of the concretes of the Ex-Zweifel Embroidery Plant is markedly differentiated according to the type of structural elements. Notwithstanding adequate proportioning between cement and aggregate amounts and proper casting and homogenization procedures, the concrete of the columns shows granulometric distribution differing from the ideal Bolomey curves mainly due to enrichments in sand fraction. Moreover, w/c ratios are excessive. These features affect the overall mechanical properties of the materials. Concrete of the beams and the riddle is characterized by better mix design, with higher cement dosages, low w/c ratios and granulometric curves comparable to the ideal Bolomey curves. Consequently, compressive strength values are higher. On the contrary, concrete of the arches is characterized by extremely poor mix design, with insufficient cement dosages, excessive w/c ratio and granulometric curves strongly differing from the ideal Bolomey curves, mainly due to marked enrichments in sand fraction. These features caused high permeability of the materials and extremely low mechanical resistance, and are to be considered the main cause of the severe structural collapse of the building.

Finally, mix design of the concrete of the Ex-Foro Boario is markedly homogeneous and well optimized, with proper cement dosages and granulometric distributions strongly comparable to the ideal Bolomey curves. In this case too, some structural elements are characterized by simultaneous higher w/c ratios and cement dosages, related to processes of optimization of concrete workability. Textural characteristics suggest accurate casting and homogenization procedures for the manufacturing of all the structural elements. All these features allowed obtaining a reduced permeability of the materials, together with high mechanical properties.

As previously stated, the determined characteristics of the mix design of concretes, even if accurate, are merely qualitative. In order to quantitatively reconstruct the characteristics of the original mixtures of the conglomerates, the materials were analyzed according to innovative protocols of multiscale image analysis, which will be described in the following chapter, together with the main analytical results obtained.

CHAPTER 4

Mix designs reconstruction by multiscale image analysis

4.1 INTRODUCTION

The reconstruction of mix designs of concrete elements of pre-existing structures is nowadays of crucial importance, considering the rising interest for the conservation and rehabilitation of the reinforced concrete contemporary architecture. In a process of characterization of a reinforced concrete building, the study of the chemical, mineralogical and textural properties of the materials and their constituents is fundamental to reach a full degree of knowledge propaedeutic to the planning and execution of proper restoration procedures, overcoming the mere characterization of the mechanical properties of concretes by means of classic compressive strength tests.

At the state of the art, concrete petrography is the most diffuse analytical approach for the study of material characteristics of concrete. As seen in the previous chapter, several international standards and procedural recommendations are available in the scientific and technological community for the petrographic analysis of concrete, making it a well established, fully reliable and widely used analytical technique. Furthermore, it was previously demonstrated that an integrated approach, extending the analysis of the materials also to the mineralogical, microchemical and microstructural fields, is able to dramatically improve the level of knowledge of concrete properties and characteristics, from the macro- to the micro- nanoscale.

These analytical procedures, even though highly effective, are still strictly qualitative, in particular as regards the determination of several parameters, which are fundamental for the reconstruction of the original mix designs (e.g. water/cement ratio, cement/aggregate ratio, granulometric distribution curve of the inert fraction). At the state of the art, considering the multiscale nature of concrete, these characteristics are studied trough manual point-count methodologies, such as those explained in ASTM C 457 standard. The

main limitations of the manual point-counting techniques applied to the study of concrete lie in the subjectivity of the analyses and in the fact that they are extremely time-consuming.

In this respect, several studies (Soroushian et al., 2003; Jakobsen et al., 2006; Peterson, 2008) proved the efficacy of 2D digital image analysis to obtain an objective and unbiased volumetric and morphological estimation of entrained air voids system, without extending the technique to the characterization of the other concrete constituents (cement matrix, aggregate, entrapped air voids/water voids, capillary porosity). The limitation on the use of the technique to the sole study of air voids lies in the fact that all other concrete constituents are highly polydisperse, so an accurate analysis requires a multiscale approach, from the nanometric to the centimetric scale. Consequently, it is necessary to deal with relatively large samples, digitalized at a resolution capable to extend the analytical dimensional span as much as possible, integrating the results with the ones obtained by micro- and nanoscale image analysis for the study of the concrete constituents of lower dimensions. Such theoretical analytical protocol requires high computational properties, due to the large dimensions of the images to analyze, so it was never systematically adopted for the study of concrete.

Moreover, the digital discrimination of concrete constituents is highly problematic due both to a marked overlapping in their RGB values and the lack of clear colorimetric tracers. Consequently, the elaboration of accurate protocols of materials treatment is crucial to reach adequate enhancements of every single constituent.

Despite these problems, 2D digital image analysis is the only analytical technique theoretically able to give reliable, rapid and unbiased results on a such polydisperse material. Consequently, one of the main objectives of this research project consisted in the development of a valid and multiscale protocol of sample preparation, image acquisition, and analysis in order to fully and quantitatively reconstruct mix designs of the studied historical concretes. In the following paragraph, an accurate description of the elaborated protocol of analysis will be reported, together with the main analytical results obtained on the concrete samples taken from the five studied historic buildings.

4.2 EXPERIMENTAL

4.2.1 Materials

The study was performed on the 26 structural elements from which at least a large core for compression tests had been extracted.

From each core, three types of samples were prepared: a series of samples to perform the image analysis of all constituents from the macroscale to the microscale, a series of samples to integrate the image analysis of the fine aggregate at the microscale and a series of samples to perform the image analysis of the capillary porosity system at the microscale and the nanoscale.

As regards the first series of samples, they were constituted by concrete slabs with a planar unperturbed surface to be digitalized and subjected to 2D image analysis. The slabs were cut from the cores prior to the compression tests by means of a water lubricated Struers Unitom-2 manual cutting machine equipped with a 350 mm diamond cut-off wheel. Care was taken not to sample the most external portions of the materials, in order to avoid areas possibly altered by external degrading agents. The cut of the samples was as rapid as possible, to limit the invasiveness of the operation on the surfaces to be analyzed. Also, the surfaces were subjected to a preliminary lapping procedure through a water lubricated Struers Labopol-5 lapping machine equipped with no. 100 and no. 500 silicon carbide abrasive papers, to eliminate asperities and cracking patterns caused by the sawing procedures. Depending on the dimensions of the cores, both orthogonal circular slabs and longitudinal polygonal slabs were sampled (figures 4.1, 4.2). On the basis of the maximum dimensions of the coarse aggregate, variable numbers of slabs were sampled in order to reach a statistically significant area of analysis; generally, a single slab was sampled for concretes manufactured with gravels characterized by maximum dimensions under 16 mm (medium gravel and lower), two slabs for concretes with gravels of maximum dimensions between 16 and 24 mm, three slabs for concretes with gravels of maximum dimensions over 24 mm.

After the cutting and preliminary lapping procedures, a rapid and accurate drying of the samples by spraying compressed air and thermal treatment in oven at 60°C for 24 hours

was performed, to avoid the triggering of alteration phenomena due to the presence of excess water on the surfaces.

Figure 4.1. Sample FP2, concrete slab cut orthogonally to the main axis of the core

Figure 4.2. Sample CC1, concrete slab cut parallel to the main axis of the core

To perform the microscale image analysis of the fine aggregate, two further thin sections were prepared for each core from portions of concrete sampled from the nuclei, in addition to the two internal thin sections already prepared for the petrographic study.
Finally, to perform the micro-nanoscale image analysis of the capillary porosity, a tablet of epoxy resin containing five separate microsamples of hardened cement matrix with exposed and polished surfaces was prepared for each core.

4.2.2 Samples treatment and images acquisition

To simplify the digital discrimination of the three main constituents of the hardened concretes (cement matrix, aggregate and pore network), a custom formulated protocol of sample treatment preliminary to the acquisition of the digital images was elaborated for the concrete slabs.
In order to enhance the visibility of the pore network on the surfaces to be analyzed, a protocol of impregnation of the porosity by dyed epoxy resin was developed. Optimum results were obtained with a mixture of Struers EpoFix resin, white dye and emerald green Phthalocyanine-based dye, both dispersed in an inert solvent. The three components, mixed

with a 30:2:1 ratio, were able to give a homogeneous opaque deep green color. The freshly-cut surfaces were vacuum-impregnated with the mixture on a Struers CitoVac impregnation unit. To ensure optimum results, five cycles of impregnation at a pressure of 0.90 bar, followed by rapid evacuation, were executed for each sample. After an appropriate period of curing, the resin in excess was removed from the surfaces of the slabs on a water lubricated Struers Labopol-5 lapping machine equipped with a no. 100 silicon carbide abrasive paper until the concrete surfaces were exposed, with the pore network filled by the green resin. Then, the samples were polished with a series of progressively finer aluminum oxide abrasives (no. 500, 800, 1200) through a Depiereux automatic polishing machine, until smooth reflective surfaces were obtained.

The lapping and polishing procedure caused an inevitable removal of a submillimetric layer of material on the treated slabs. This process, even though optimal for the further removal of superficial layers possibly damaged by the cutting procedure, caused the removal of the green epoxy which impregnated the entrained air voids of lower dimensions (figure 4.3). To overcome this problem, newly exposed micro-voids were again highlighted by filling them with a powder of synthetic eskolaite (Cr_2O_3), characterized by a green colour similar to the one of the resin (figure 4.4). Prior to the aspersion on the concrete surfaces, the powder was finely micronized on a McCrone Micronizing Mill.

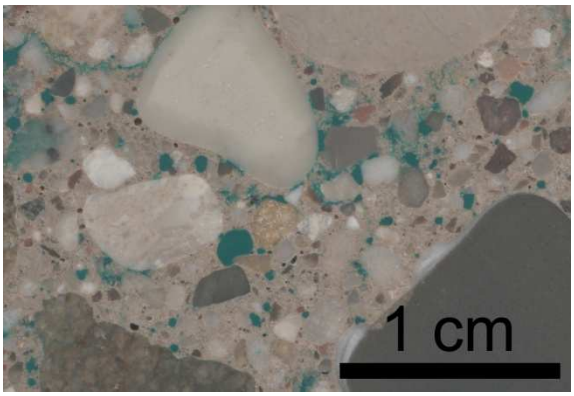

Figure 4.3. Sample RP1, detail of an area after vacuum impregnation of dyed epoxy and polishing. The larger voids are still impregnated, while the finer voids are still exposed

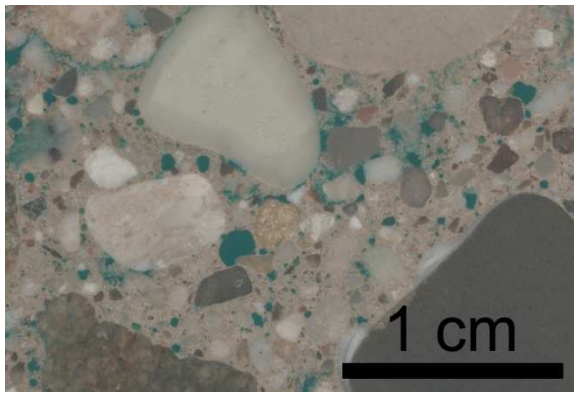

Figure 4.4. Sample RP1, detail of the same area reported in figure 5.3 after the superficial aspersion of micronized eskolaite. The visibility of the whole pore network is now enhanced

The treated surfaces were then scanned in 24-bit RGB color through a high-end Epson V750 PRO flatbed scanner at a 4.0 DMax optical density and a 3600x3600 dpi (8x8 µm)

optical resolution. Prior to the acquisition of the images, a calibration of the color palette of the input system was performed creating a standard ICC profile through an IT8 target.

Then, to enhance the visibility of cement matrices, a strategy of selective staining of the hardened binder by means of chemical treatment was adopted (Chinchón et al., 2004; Fernandez, 2008; Linares et al., 2009). The selective staining were performed by means of immersion of the surfaces to be analyzed in a solution of 3% tartaric acid-3% tannic acid in deionized water. The organic acids form organometallic complexes with the iron of the Fe-containing AFm phases, causing a diffuse reddish coloration of the cement matrices due to changes in Fe oxidation state (figures 4.5, 4.6). Due to the low pH of the solution (about 1.50), the polished slabs were immersed for 2 minutes only, sufficient to stain the matrices without causing significant dissolution of CH and CSH of the cement matrices and carbonates of the inert fraction.

After the selective stain, the surfaces were re-scanned at the same resolution and with the same orientation adopted for the first scanning. Moreover, to enhance both the adhesion between the sample and the plate of the scanner and the image quality due to the different refractive index, slabs were scanned with a fluid mount technique, using deionized water as scanning medium.

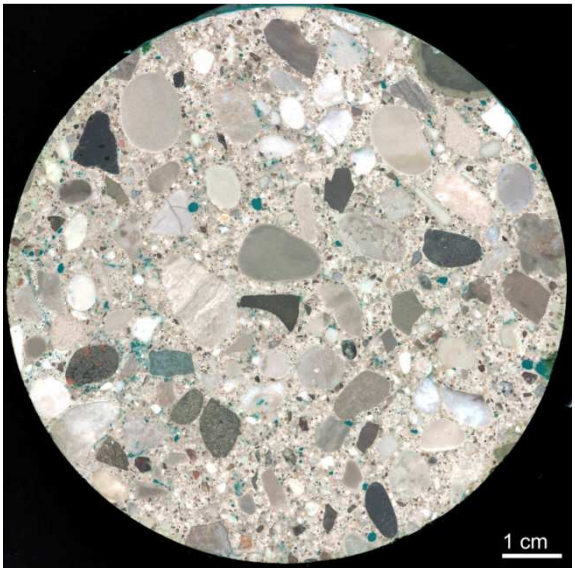

Figure 4.5. Sample MC1, RGB scansions of a polished slab prior to the selective staining process

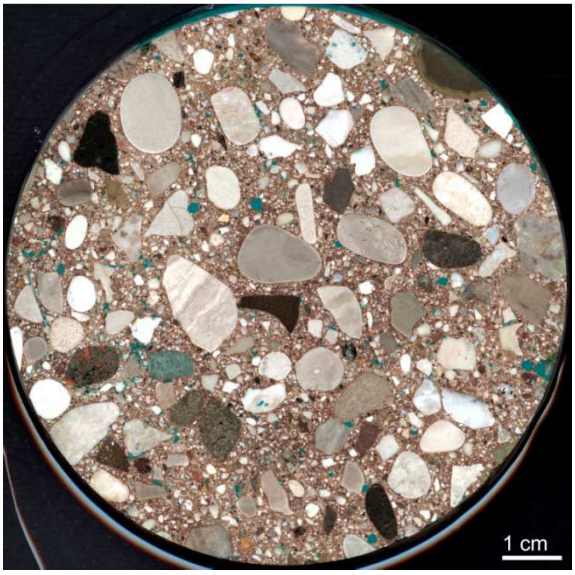

Figure 4.6. Sample MC1, RGB scansion of the same polished slab after the selective staining process

As regards the samples for the microscale image analysis of the fine aggregate, no samples pre-treatments were adopted, apart from the metallization procedures necessary for the

SEM analysis. Ten couples of images were acquired at the electron microscope for each core, using a Camscan MX 2500 scanning electron microscope (SEM) equipped with a LaB_6 electron source and an EDAX energy dispersive X-ray detector (EDS). For each selected area, both a BSE and SE image were acquired, at a standard magnification of 25x (field of view: 4.7 mm, maximum resolution: 2 µm), operating at an electric potential difference of 20 kV with a working distance of 20 mm. BSE images were taken at maximum contrast, optimizing the brightness of the detector in order to reach an optimum discrimination of the inert fraction with respect to the other concrete constituents (figure 4.7). As regards the SE images, they were acquired at maximum contrast values, adjusting the brightness to a value of saturation for the cement matrices only, characterized by lower density with respect to the aggregate particles and the voids filled by epoxy. Consequently, cement matrices resulted mainly white, while the pore network and the sand grains resulted uniformly black (figure 4.8).

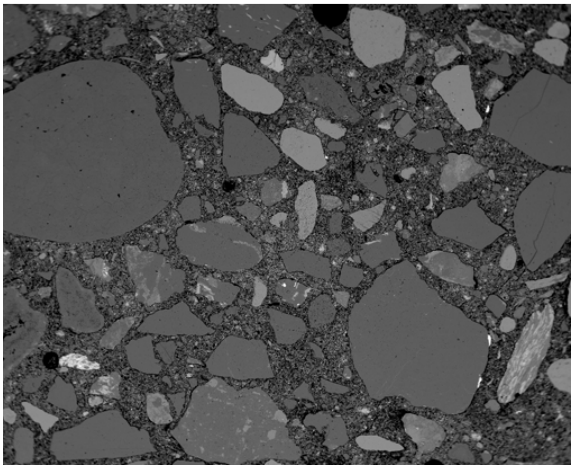

Figure 4.7. Sample FP1, BSE image acquired for the microscale image analysis of the fine aggregate

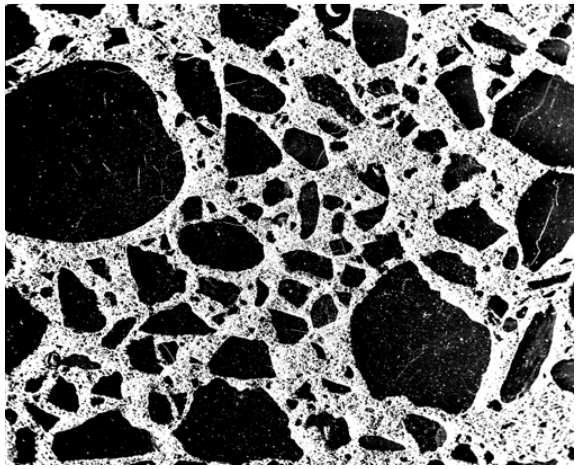

Figure 4.8. Sample FP1, SE image acquired for the microscale image analysis of the fine aggregate

Furthermore, two series of chemical maps were acquired for each core, at the same magnification, field of view, resolution and instrumental parameters adopted for the acquisition of the BSE-SE images. 11 elements were mapped (Ca, Si, Al, Fe, Na, K, Mg, S, Ti, C, O), acquiring a BSE image of the analyzed area prior the mapping (figure 4.9).

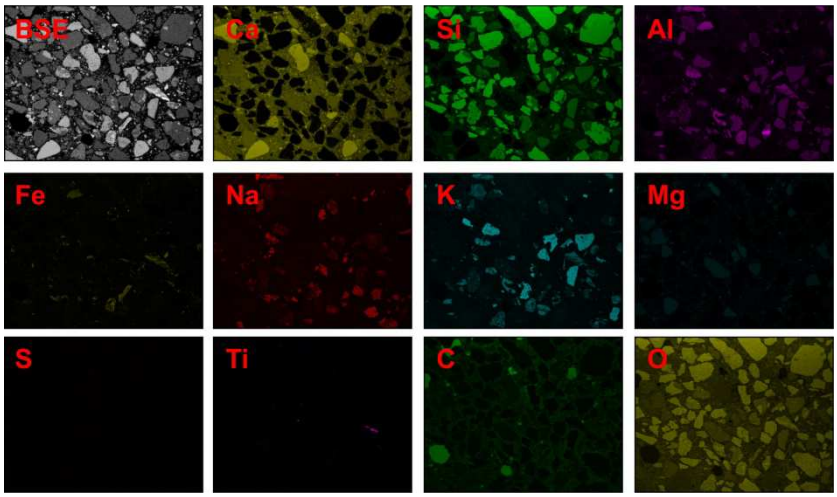

Figure 4.9. Sample CP1, BSE image and chemical maps acquired for the microscale image analysis of the fine aggregate

No pre-treatment procedures were adopted for the micro-nanoscale image analysis of the capillary porosity samples either, apart from the metallization procedures necessary for the SEM analysis. A series of 20 high resolution BSE images of the cement matrices were acquired for each core, 4 for each microsample, using a FEI Quanta 200 scanning electron microscope (SEM) equipped with a tungsten electron source and an EDAX energy dispersive X-ray detector (EDS). Images were acquired at a standard magnification of 1000x (field of view: 150 µm, maximum resolution: 100 nm), operating at an electric potential difference of 20 kV with a working distance of 4 mm. Furthermore, brightness and density values of the BSE detector were maintained strictly controlled at standard values during the acquisition of all the images for all the 26 series of samples, in order to obtain fully comparable images (figure 4.10, 4.11).

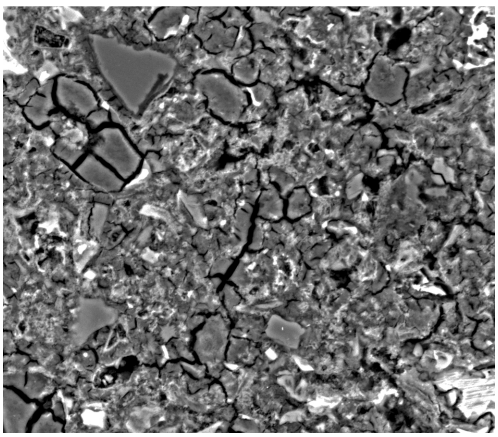

Figure 4.10. Sample CC2, BSE image acquired for the image analysis of capillary porosity

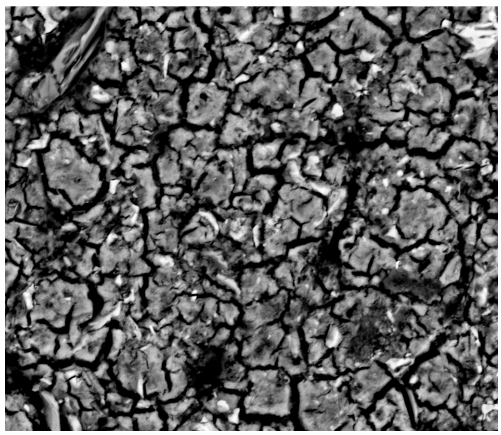

Figure 4.11. Sample MC3, BSE image acquired for the image analysis of capillary porosity

4.2.3 Images segmentation

A series of preliminary operations were performed on the RGB images of the polished slabs prior to the segmentation of the main concrete components. First of all, the two images acquired before and after the selective staining process were accurately registered in order to obtain a precise correspondence between each pixel of the raster matrix. The registration process was performed through ENVI 4.7 software, defining 40 ground control points (GCP) for each image, with an RMS error at least lower than 2. After the definition of GCP matrices, images were warped according to the rotation, scaling and translation (RST) method, using a Cubic Convolution resampling algorithm (AA. VV., 2011). After the registration, each RGB image were decomposed in three 8-bit grayscale images corresponding to each single channel of the original image, obtaining 6 grayscale images for each polished slab. Then, the 6 images were merged through ENVI 4.7 software, obtaining a 6-band composite image. A comparative analysis of each single band before and after the selective staining process clearly evidenced the effect of the chemical treatment on the overall grayscale gamma of each image, highlighting a significant change in grayscale values for the areas corresponding to the cement matrix, while the grayscale values of the inert fraction and the enhanced pores remained substantially constant, with only minor variations in the worst cases (figures 4.12, 4.13, 4.14).

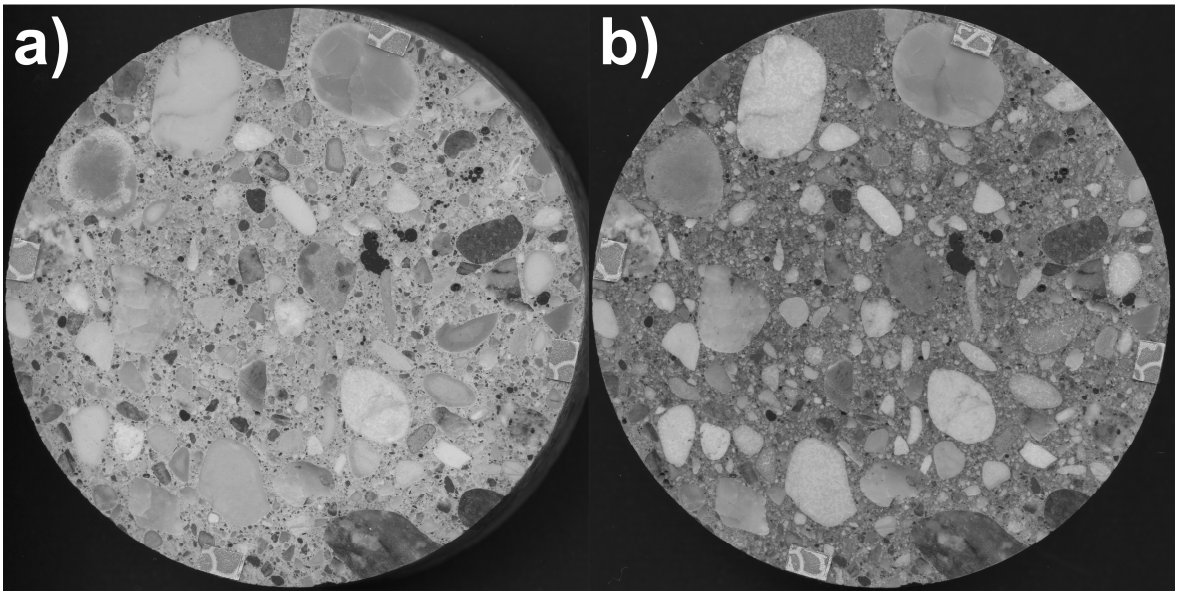

Figure 4.12. Sample FP1, R band before (a) and after (b) the selective staining process

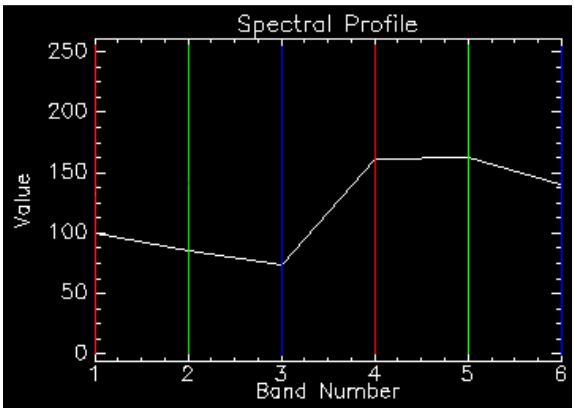

Figure 4.13. Sample FP1, typical spectral profile of the cement matrix (1, 2, 3: R, G, B bands of the stained surface; 4, 5, 6: R, G, B bands of the original surface). A clear lowering of RGB values is observable after the staining process

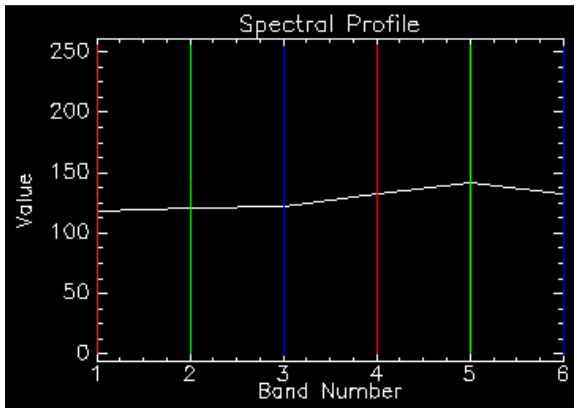

Figure 4.14. Sample FP1, typical spectral profile of an aggregate particle (1, 2, 3: R, G, B bands of the stained surface; 4, 5, 6: R, G, B bands of the original surface). RGB values remain substantially constant before and after the staining process

The selective stain allows the elaboration of false-color images through the recombination of RGB bands of both images, with the cement matrices assuming colorations corresponding to the primary RGB and CMYK colors (figure 4.15).

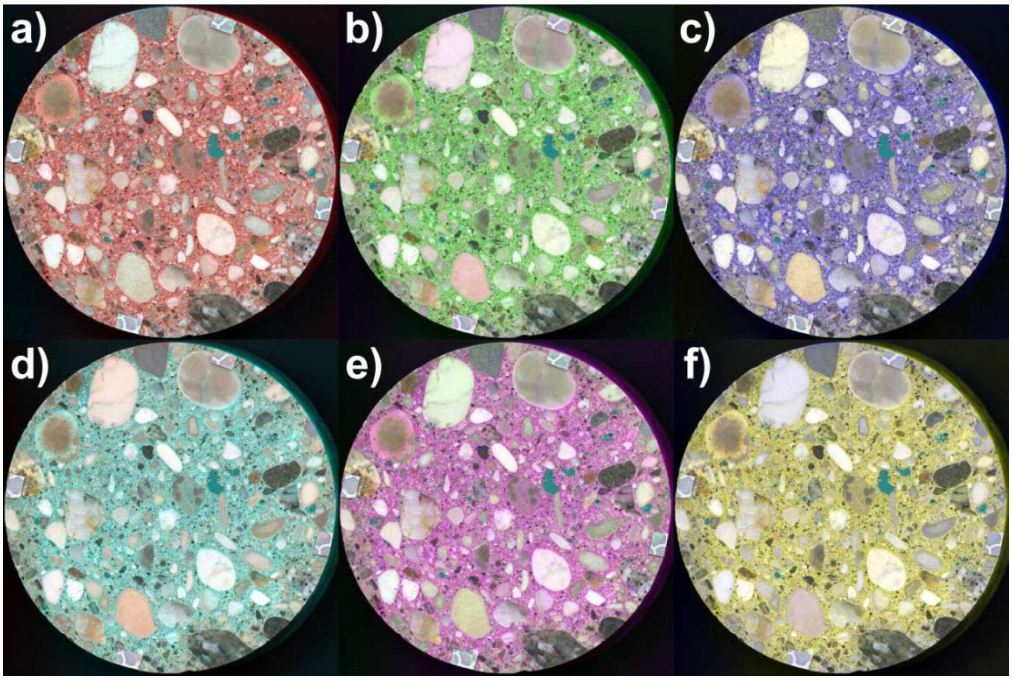

Figure 4.15. Sample FP1, false-color images obtained by the combination of the RGB bands of the two images: a) R from the original surface, GB from the stained surface; b) G from the original surface, RB from the stained surface; c) B from the original surface, RG from the stained surface; d) GB from the original surface, R from the stained surface; e) RB from the original surface, G from the stained surface; f) RG from the original surface, B from the stained surface

The segmentation of the three main volumetric components of the concretes was performed applying a maximum likelihood classification to a series of defined classes described by an adequate number of training pixels. Maximum likelihood classification assumes that the statistics for each class in each band are normally distributed and calculates the probability that a given pixel belongs to a specific class (Richards, 1999). Three main classes were defined for each image: a class for the cement matrix, a class for the voids filled by epoxy resin and a class for the voids filled by synthetic eskolaite powder. No probability thresholds were defined for the second class, while a probability threshold of 0.9 and 0.95 was defined for the first and third class, respectively. The maximum likelihood algorithm resulted to be extremely effective in the discrimination of the cement matrices and the voids (figures 4.16, 4.17), while the aggregate particles were left unclassified and segmented for difference (figure 4.18).

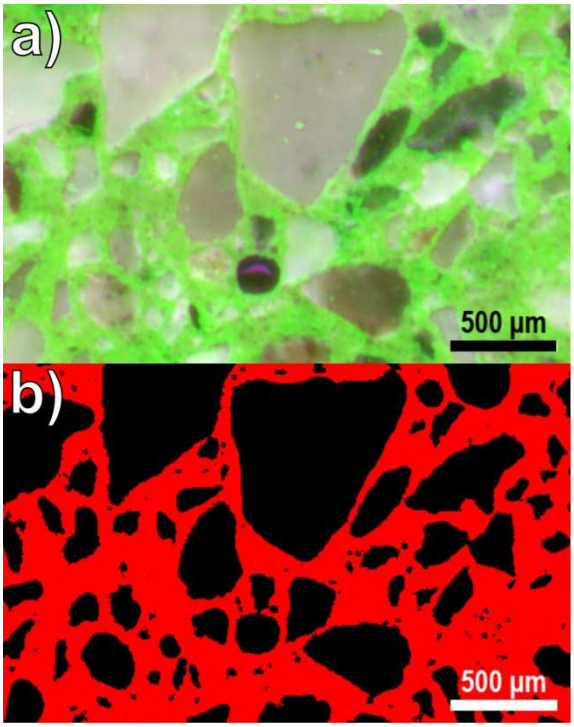

Figure 4.16. Sample FP2, original false-color image (a) and cement matrix classification image (b, in red). All other concrete constituents are left unclassified

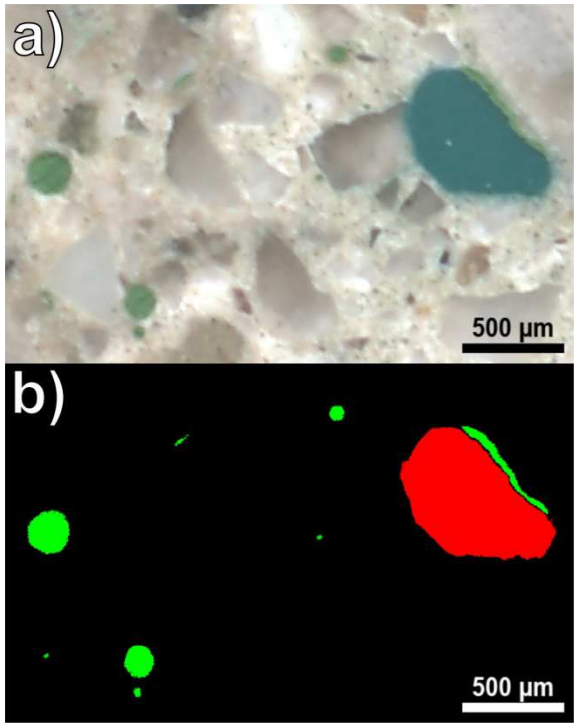

Figure 4.17. Sample MC1, original image (a) and voids classification image (b, voids filled by epoxy in red, voids filled by synthetic eskolaite in green). Cement matrix and aggregate are left unclassified

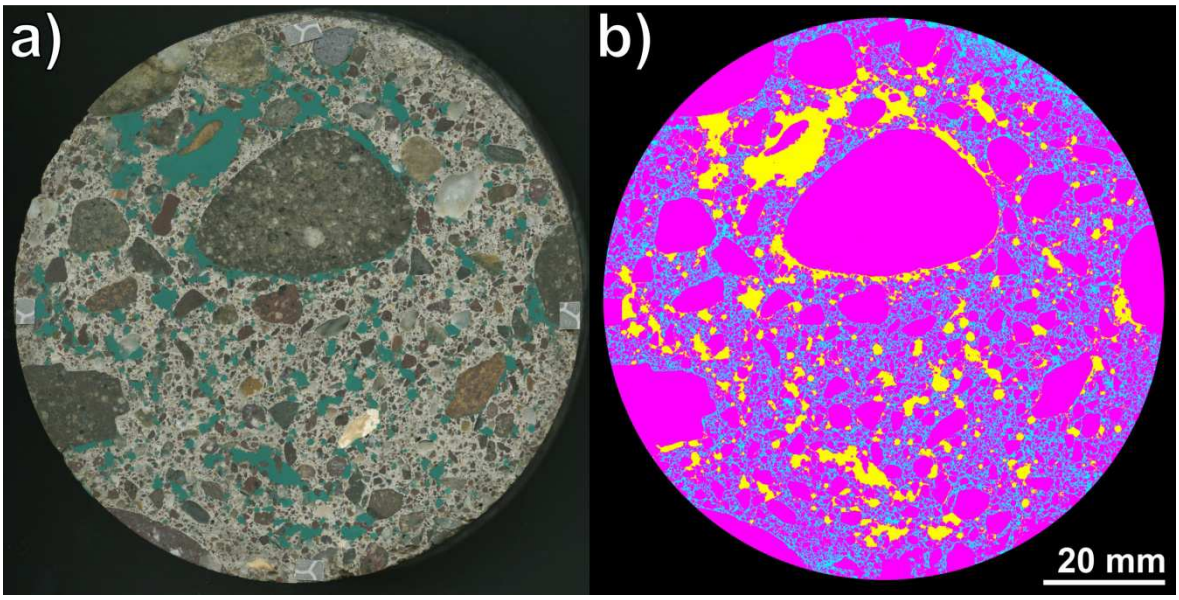

Figure 4.18. Sample BS2, original polished surface (a) and segmented image after the classification process with the maximum likelihood algorithm (b). Cement matrix in cyan, aggregate in magenta, voids in yellow

The procedure of segmentation of the BSE-SE images taken for the microscale analysis of the fine aggregate was preceded by a series of custom formulated images treatments. First of all, a removal of background noise artifacts was performed on the SE image through ImageJ 1.44p software, applying sequentially a remove outliers filter with a radius of 2 pixels and a median filter with a radius of 1 pixel (figure 4.19).

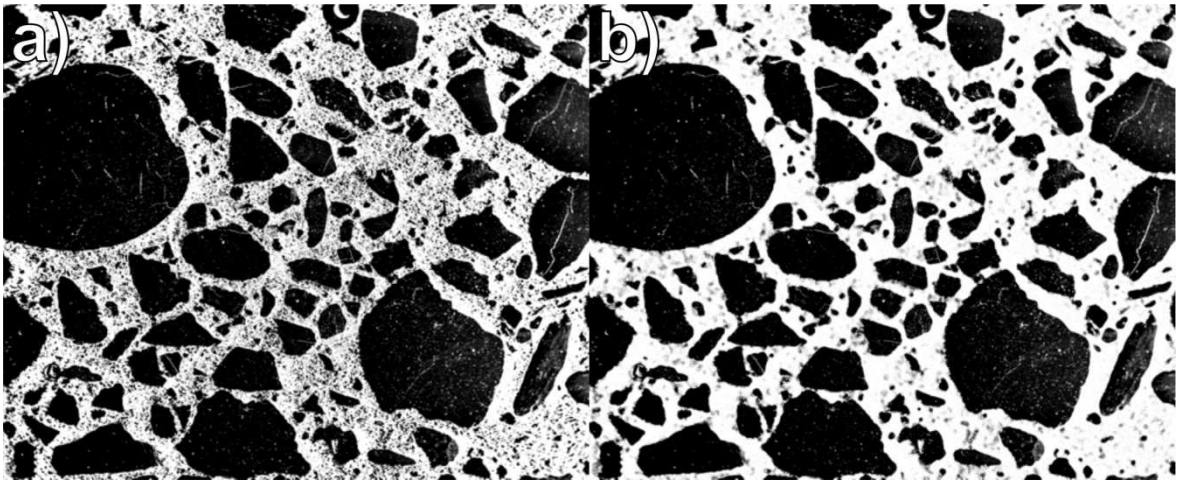

Figure 4.19. Sample FP1, SE image reported in figure 4.8 before (a) and after (b) the protocol of removal of the background noise artifacts

Then, the treated SE image and the BSE image were merged in a unique composite image through ENVI 4.7 software. The procedure favored the definition of particle shapes on the

BSE images, at the same time allowing a clear discrimination between cement matrix, aggregate and voids, characterized by well defined color ranges (figure 4.20 a). An accurate segmentation of the aggregate particles was subsequently performed defining threshold values on the RGB channels of the image through the Threshold Color plugin of ImageJ (Landini, 2011), binarizing the obtained image and performing sample post-treatments applying a median filter to the segmented image in case of permanence of background noise artifacts (figure 4.20 b).

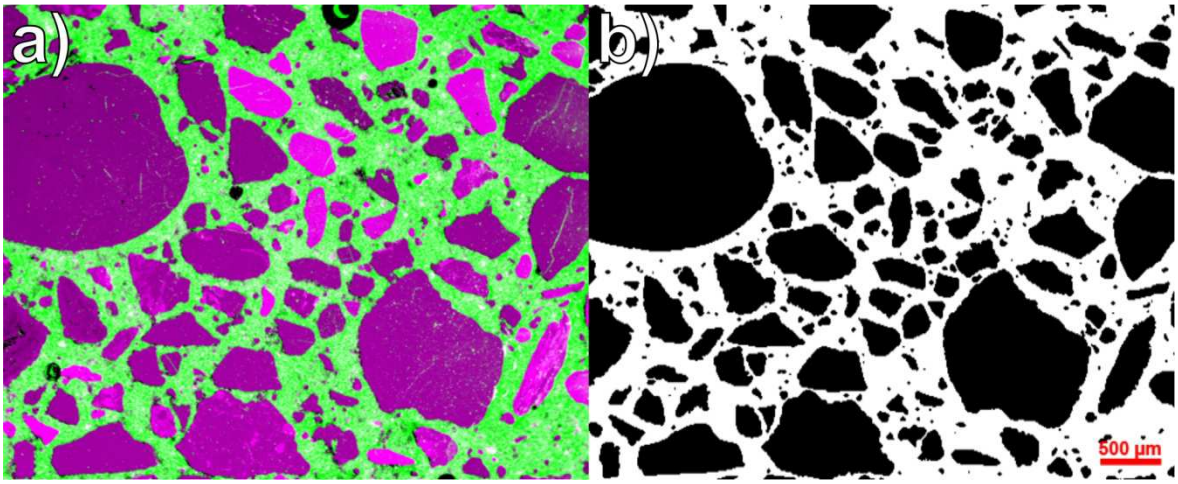

Figure 4.20. Sample FP1, composite image obtained by merging the BSE and SE images (a) and segmentation of the aggregate particles (b)

The EDS chemical maps acquired were used to perform a multi-elemental image analysis, modification of the procedure elaborated by Stutzman (2004) for the quantitative image analysis of Ordinary Portland Cement. The procedure allowed not only the segmentation of the fine aggregate particles, but also the obtaining of a quantitative mineralogical profile of the inert fraction. Before performing the image analysis, all the acquired maps were subjected to an enhancement procedure through ImageJ software, consisting in an optimization of the brightness/contrast values and in the removal of background noise artifacts applying a median filter with a radius of 0.2 pixels (figure 4.21).

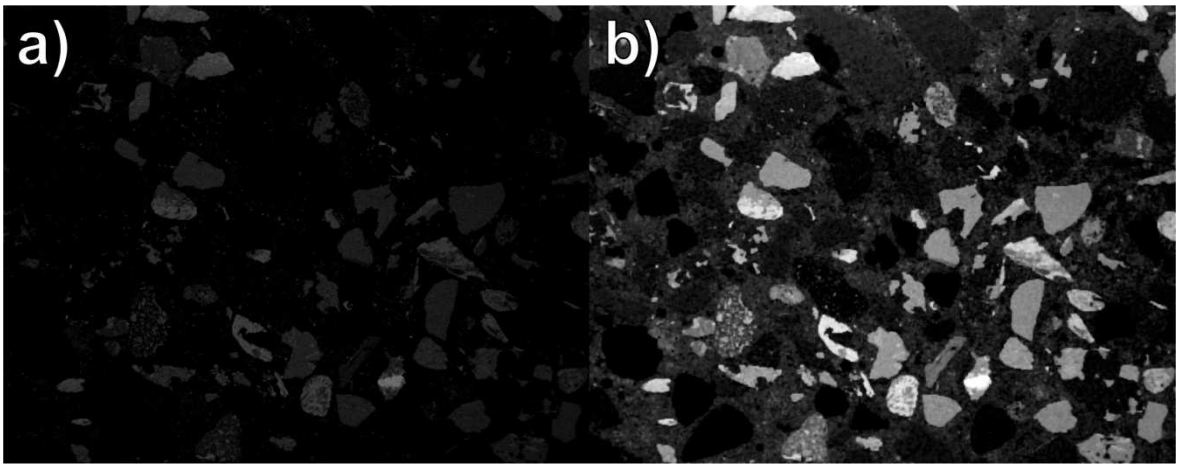

Figure 4.21. Sample CP1, Al map before (a) and after (b) the image optimization protocol

Then, the 11 chemical maps plus the corresponding BSE image were merged through ENVI 4.7 software, obtaining a 12-band composite image. The principle of discrimination of the mineral phases constituting the aggregate fraction of the concrete samples is based on the creation of composite RGB images constituted by three maps of the main chemical constituents of the minerals to enhance (figure 4.22).

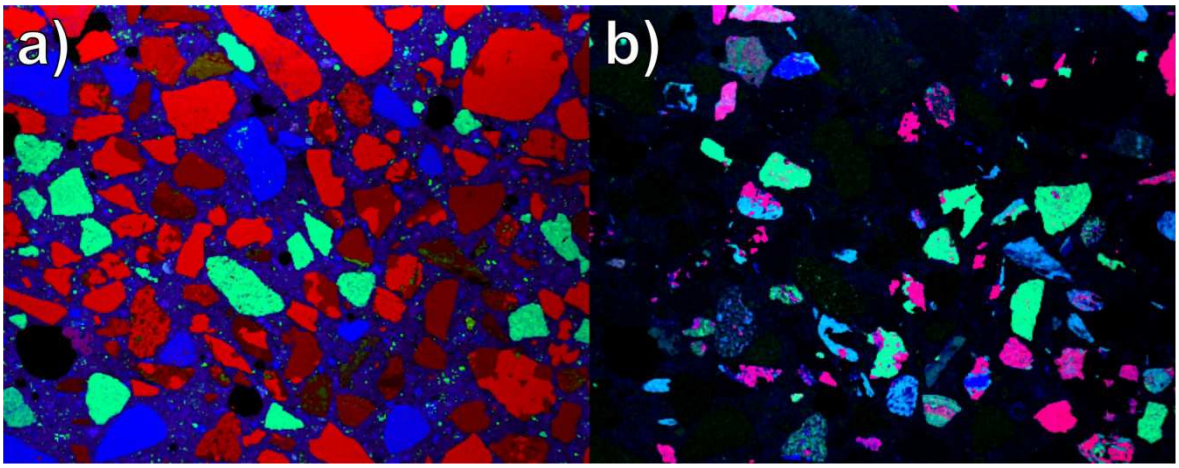

Figure 4.22. Sample CP1, RGB images obtained by merging different chemical maps on the three bands. a) R: Si map, G: Mg map, B: Ca map. Quarz, calcite and dolomite are clearly recognizable (in red, blue and cyan, respectively). b) R: Na map, G: K map, B: Al map. K-feldspar and albite are clearly recognizable (in cyan and magenta, respectively)

Through adequate combinations of the chemical maps, each mineral constituent of the aggregate fraction was defined by a class described by an adequate number of training pixels. The cement matrix and the voids were assigned to specified classes, not to leave unclassified pixels. Then, the multiband images were classified through a maximum

likelihood algorithm, obtaining a mineralogical map of the analyzed areas (figure 4.23 a). An accurate segmentation of the aggregate particles was subsequently performed defining threshold values on the RGB channels of the mineralogical maps through the Threshold Color plugin of ImageJ, binarizing the obtained images and performing sample post-treatments applying a median filter to the segmented images in case of permanence of background noise artifacts (figure 4.23 b).

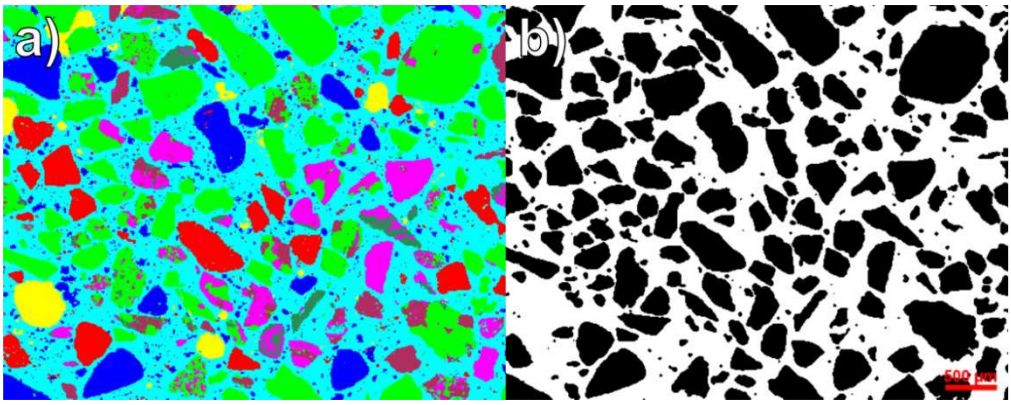

Figure 4.23. Sample CP1, results of the multi-elemental image analysis. a) mineralogical map obtained through the multi-elemental image analysis procedure (quartz in green, calcite in blue, dolomite in red, K-feldspar in magenta, albite in maroon, biotite in dark green, cement matrix in cyan, voids in yellow). b) segmentation of the aggregate particles

Finally, the procedure of segmentation of the BSE images taken for the micro-nanoscale analysis of the capillary porosity consisted on a preliminary enhancement of the images through ImageJ software by optimization of their brightness/contrast values, followed by a simple imposition of a threshold value to grayscale images, to segment the pore network from the hardened paste (figure 4.24).

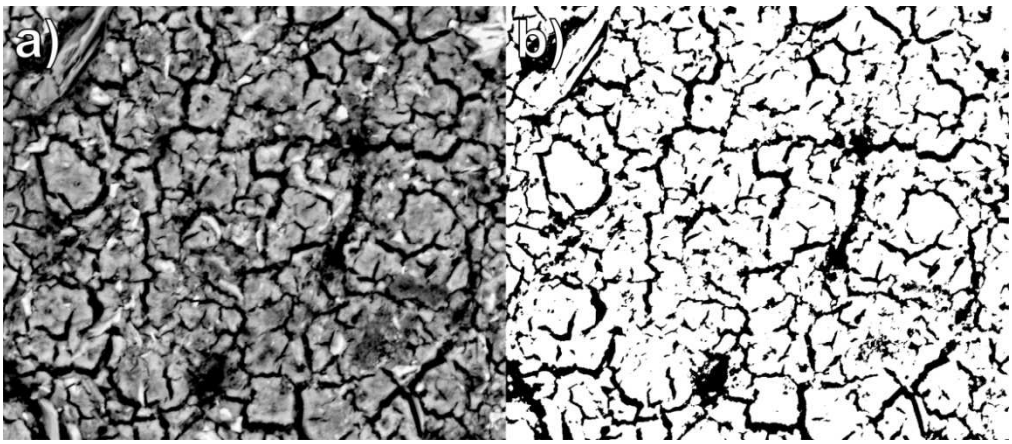

Figure 4.24. Sample MC3, enhanced image of the cement matrix (a) and segmented capillary porosity (b)

4.2.4 Mix designs reconstructions

The volumetric percentages of the three main constituents of the concrete samples were extrapolated segmenting and analyzing the classified images of the polished slabs through the Threshold Color plugin and the Analyze Particles function of ImageJ and considering a direct correlation between the areal percentage of each single constituents and its volumetric percentage. To check the accuracy of the results obtained through the image analysis protocol, a manual point count of the percentages of voids, cement matrix and aggregate in the analyzed samples was performed on the acquired images according to ASTM C 457 standard, using the Bubble Counter v2007.0 script for Adobe Photoshop (Sutter, 2007).

Considering the direct linear correlation between w/c ratio and capillary porosity of concretes (Ingham, 2011), the w/c ratio of the concrete samples was extrapolated by the volumetric percentages of pores on the high resolution images of the hardened pastes. Volumetric percentages were calculated through the Analyze Particles function of ImageJ, considering a direct correlation with the areal values.

To calculate the regression function between the experimental capillary porosity percentages and the w/c ratio of the materials, a series of standard samples of hardened cement pastes characterized by progressively increasing w/c ratio (from 0.40 to 0.85 at steps of 0.05) were prepared. Considering that the composition of clinkers of all studied concretes can be considered similar to modern Ordinary Portland Cements, as highlighted by the textural and mineralogical features described in chapter 3 and demonstrated by the common reaching of high compressive strength values in the analyzed samples, A CEM I 42.5 R (EN 197-1 classification) Ordinary Portland cement was selected for the preparation of all the samples. Each sample was prepared mixing 10 grams of cement with an appropriate amount of tap water utilizing and IKA Eurostar Digital Stirrer, set at a fixed speed of 400 rpm and following the mixing protocol developed by GRACE (2009), organized as follows:

- 30 s of mixing;
- stopping the mixer for 15 s, necessary to clean the stirrer from the paste;
- 75 s of mixing;
- stopping the mixer for 60 s, necessary to clean the stirrer from the paste;
- 60 s of final mixing.

After the mixing, the pastes were poured in polypropylene test tubes, which were hermetically sealed with both a polypropylene top and Parafilm. The samples were cured for six months at controlled temperature and relative humidity values, then they were sectioned with a water lubricated Buehler Isomet 1000 high precision cutting machine, accurately dried by spraying compressed air and thermal treatment in oven at 60°C for 24 hours, englobed in tablets of epoxy resin with an exposed surface and polished. Then, a series of 20 high resolution BSE images of the cement matrices was acquired for each sample, using a FEI Quanta 200 environmental scanning electron microscope (ESEM) operating in high vacuum, equipped with a tungsten electron source and an EDAX energy dispersive X-ray detector (EDS). Images were acquired at a standard magnification of 1000x (field of view: 150 µm, maximum resolution: 100 nm), operating at an electric potential difference of 20 kV with a working distance of 4 mm. Furthermore, brightness and density values of the BSE detector were maintained strictly controlled at standard values during the acquisition of all images for all samples, in order to obtain fully comparable images. Then, after a preliminary improvement of the images through ImageJ software by an optimization of their brightness/contrast values, the capillary porosities were segmented imposing a threshold value to the grayscale images and their volumetric percentages was calculated through the Analyze Particles function of ImageJ, considering a direct correlation with the areal values. The progressive volumetric increase of the capillary porosity at increasing w/c ratios is clearly recognizable from the segmented images (figure 4.25).

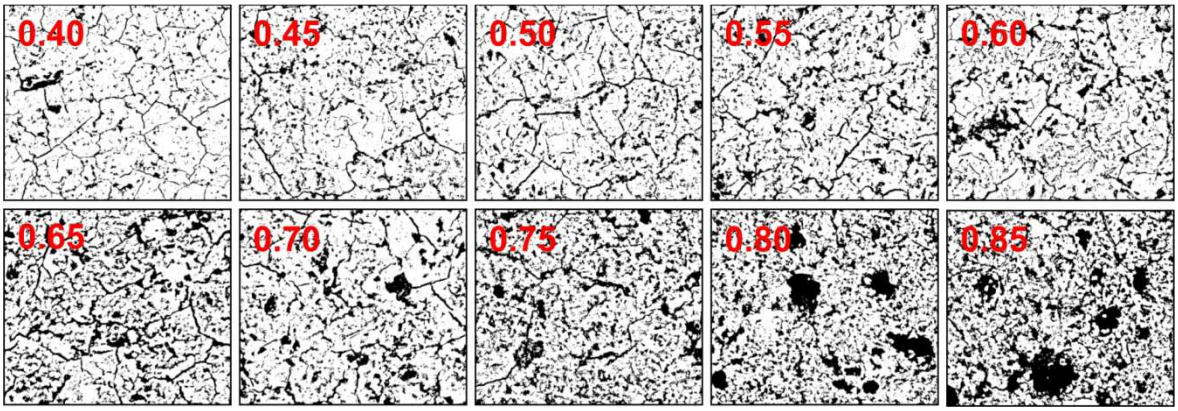

Figure 4.25. Segmented capillary porosity from 10 BSE images of hardened cement pastes prepared with progressively increasing w/c ratio

Starting from the extrapolated volumetric percentages of capillary porosity of the standard samples, a linear regression model was elaborated through Minitab 16 software (figure 4.26).

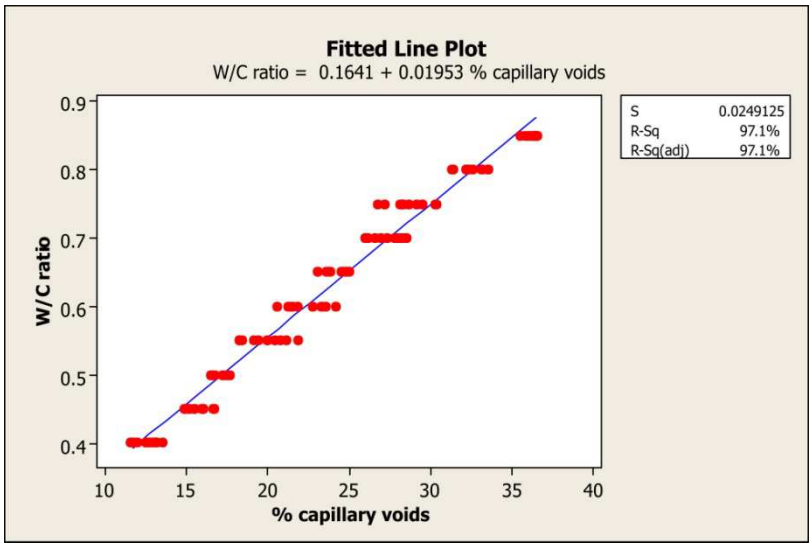

Figure 4.26. Linear regression model between w/c ratio and percentage of capillary porosity

The model is characterized by a high R^2 value (0.97) and a low standard error (0.02), so it can be considered highly reliable. The extrapolated regression function, used for the calculation of the w/c ratios of the analyzed concretes, is the following:

$$\text{w/c ratio} = 0.1641 + 0.01953(\%\ \text{capillary voids}) \quad (4.1)$$

The conversion of the volumetric percentages of aggregate and cement matrix into absolute weight fractions was performed by estimating the densities of the solid components of concretes.

Sand densities were determined by the quantitative determination of their mineralogical profiles obtained by multi-elemental image analysis. Considering the similarities in the mineral-petrographic nature of the fine aggregate for all concretes of each structure, a unique reference density value of the sand fraction was calculated for each studied building. For the Northern Wing of the Carraresi Castle only, three different density values were calculated, one for each constructive phase. After the determination of the absolute volumetric proportions of the main mineral phases constituting the fine aggregate for each structure, the overall density values of the fine aggregates were calculated considering the literature density values of each single mineral constituent (Carmichael, 1984; Schön,

1996). The volumetric percentages of the mineral phases of the fine aggregates, together with the calculated density values, are reported in table 4.1.

Structure	**Cc**	**Dol**	**Qtz**	**Al**	**An**	**Fld**	**Bt**	**Mus**	**Chl**	**Hem**	**Vgl**	**ρ (g/cm^3)**
Carraresi Castle, ph. 1	15.6	18.5	36.8	12.5	3.7	10.5	2.4	-	-	-	-	2.64
Carraresi Castle, ph. 2	17.7	11.3	42.1	12.9	-	10.5	3.7	1.8	-	-	-	2.64
Carraresi Castle, ph. 3	12.3	7.3	53.6	14.3	-	9.2	3.4	-	-	-	-	2.64
Victory Monument	1.4	1.0	29.1	12.5	-	9.8	2.8	10.7	4.1	0.5	28.1	2.62
Ex-Agrimont Area	27.8	9.9	37.4	8.5	2.3	7.9	5.7	-	-	0.5	-	2.66
Ex-Zweifel Plant	29.4	29.3	21.1	5.7	0.2	11.8	1.9	0.6	-	-	-	2.61
Ex-Foro Boario	12.4	35.7	33.8	8.9	-	5.7	3.5	-	-	-	-	2.64

Table 4.1. Volumetric percentages of the main mineral phases constituting the fine aggregate of the studied structures and calculated densities values. For the Northern Wing of the Carraresi Castle three datasets were reported, according to the different construction phases. Abbreviations: Cc = calcite, Dol = dolomite, Qtz = quartz, Al = albite, An = anorthite, Fld = K-feldspar, Bt = biotite, Mus = muscovite, Chl = chlorite, Hem = hematite, Vgl = volcanic glass

As for the estimation of the gravel densities, a manual digital petrographic discrimination of the clasts according to their petrographic nature was performed on the polished slabs, creating a multi-layer image with Adobe Photoshop CS5 containing both the original, untreated scansion of the analyzed surface and the image of the segmented coarse aggregate. Subsequently, each petrographic family of gravels was highlighted with a specific RGB color (figure 4.27). Finally, the resulting image was segmented and analyzed through the Threshold Color plugin and Analyze Particles function of ImageJ, obtaining the volumetric percentages of the main. The relative proportions between limestones and dolostones were considered equal to the relative proportions between calcite and dolomite obtained by the multi-elemental image analysis. After the determination of the absolute volumetric proportions of the lithological types constituting the coarse aggregate for each structure, the overall density values of the coarse aggregates were calculated considering the literature density values of each single lithological constituent (Carmichael, 1984; Schön, 1996). The volumetric percentages of the lithological types of the coarse aggregates, together with the calculated density values, are reported in table 4.2.

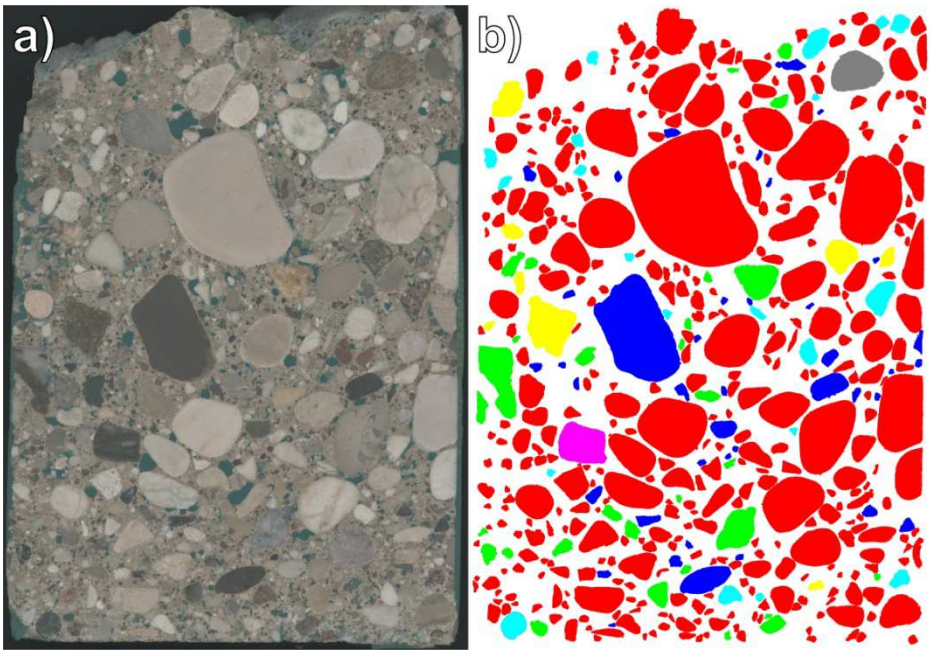

Figure 4.27. Sample RP1, RGB scansion of a polished slab (a) and discrimination of the gravel particles according to their petrographic nature (b). Carbonates are colored in red, quartzite in green, chert in blue, rhyolite in cyan, gneiss in magenta, trachite in yellow, schist in gray

Structure	**Lim**	**Dls**	**Qrt**	**Chr**	**Rhy**	**Tr**	**Sch**	**Gn**	**Srp**	**Gr**	**Ign**	**ρ (g/cm^3)**
Carraresi Castle, ph. 1	29.6	30.1	19.0	1.2	0.4	7.6	7.7	2.3	-	2.1	-	2.62
Carraresi Castle, ph. 2	37.8	23.7	11.5	1.8	4.3	7.7	2.1	3.3	-	7.8	-	2.60
Carraresi Castle, ph. 3	31.9	19.0	13.4	0.5	20.9	4.0	2.0	6.6	-	1.7	-	2.60
Victory Monument	-	-	18.2	1.3	20.2	2.4	2.4	-	-	-	55.5	2.59
Ex-Agrimont Area	61.4	22.1	2.5	6.9	5.8	-	-	-	0.9	0.4	-	2.59
Ex-Zweifel Plant	38.9	38.8	7.0	7.9	2.6	3.2	1.2	0.4	-	-	-	2.60
Ex-Foro Boario	16.0	45.8	10.5	7.0	1.3	7.9	2.6	4.1	-	4.8	-	2.62

Table 4.2. Volumetric percentages of the main lithological constituents of the coarse aggregate of the studied structures and calculated densities values. For the Northern Wing of the Carraresi Castle three datasets were reported, according to the different construction phases. Abbreviations: Lim = limestone, Dls = dolostone, Qrt = quartzite, Chr = chert, Rhy = rhyolite, Tr = trachite, Sch = schist, Gn = gneiss, Srp = serpentinite, Gr = granite, Ign = ignimbrite

To determine the densities of the hardened cement matrices, the regression function between their values and w/c ratios was extrapolated. For the purpose, a series of standard samples of hardened cement pastes characterized by progressively increasing w/c ratios

(from 0.35 to 0.85 at steps of 0.10) were prepared with the same OPC used for the preparation of the samples for the w/c ratios extrapolation, following the same mixing and curing procedure. Seven replicas were prepared for each of the six target w/c ratios. After the curing period, the samples were accurately dried by thermal treatment in oven at 60°C for 48 hours and subsequent permanence in desiccator for 7 days, and the densities of five replicas for each w/c ratio were determined without further treatments through a Quantachrome Ultrapyc 1000 helium stereopycnometer. The mean density values obtained at the six target w/c ratios are reported in table 4.3, together with the standard deviation values.

w/c ratio	**Mean ρ (g/cm^3)**	**Standard deviation**
0.35	2.3021	0.0020
0.45	2.2393	0.0024
0.55	2.2264	0.0033
0.65	2.2159	0.0023
0.75	2.2157	0.0031
0.85	2.2155	0.0026

Table 4.3. Mean density and standard deviation values for each series of hardened paste samples at increasing w/c ratios

The measurements indicate solid concordances between the replicas, as indicated by the low standard deviation values. Furthermore, it is possible to observe a rapid and exponential decrease of density values in the w/c ratio interval comprised between 0.35 and 0.55. Over this value, the density variations are extremely limited, indicating the reaching of an asymptotic point. This may be explained by the fact that at low w/c ratios the progressive incorporation of water molecules in the crystalline structure of the hydrated phases causes a lowering of the overall density of the hardened pastes, while at higher w/c ratios further water additions to the fresh mix only cause greater development of capillary porosity.

Considering the trend of the experimental measurements, they cannot be fitted adequately by a linear regression model. Consequently, a nonlinear regression model was elaborated through Minitab 16 software, fitting the data with a convex asymptotic regression function (figure 4.28).

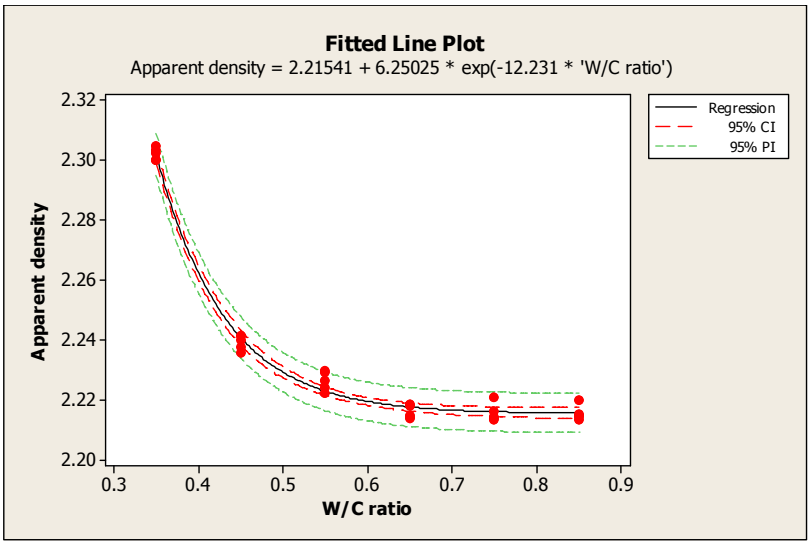

Figure 4.28. Nonlinear regression model between w/c ratio and density of the hardened cement matrix. 95% confidence and prediction intervals are reported

The regression model fits properly the experimental data, as demonstrated by the low sum of the squared residuals (SSE, 0.00026) and by the fact that all measurements are comprised within the 95% prediction interval. The extrapolated regression function, used for the calculation of the hardened paste densities of the analyzed concretes, is the following:

$$\text{Density} = 2.21541 + 6.25025e^{(-12.231 \text{w/c ratio})} \qquad (4.2)$$

The determined densities cannot be considered as absolute densities of the hardened cement pastes, as the gas flow of the measurement cannot reach the non-connected porosity of the materials, essentially constituted by the CSH gel pores.

Thus, the absolute density of the two replicas for each target w/c ratio not analyzed by helium pycnometry has been determined indirectly by thermogravimetric analysis (TGA). After being finely powdered, the samples were analyzed through a custom-built thermal analyzer, with a heating ramp rate of 10°C/min (from 20 to 1000°C) in static air. Furthermore, a sample of anhydrous cement was analyzed with the same instrumental parameters. The results of the TG analyses are reported in table 4.4, indicating the relative weight losses, in percentage of the initial mass, for the intervals 20-456°C, 457-621°C and 622-1000°C.

Sample	Wt. loss 20-456°C (%)	Wt. loss 457-621°C (%)	Wt. loss 622-1000°C (%)
CEM	0.415	0.087	0.637
0.35a	16.581	3.777	1.079
0.35b	17.372	3.972	1.101
0.45a	21.460	4.882	1.594
0.45b	21.230	4.837	1.532
0.55a	22.058	4.869	2.039
0.55b	22.253	5.023	1.801
0.65a	22.548	5.250	1.646
0.65b	22.590	5.186	1.697
0.75a	22.538	5.526	1.408
0.75b	22.553	5.532	1.431
0.85a	22.559	5.233	2.097
0.85b	22.548	5.402	1.998

Table 4.4. Results of the thermogravimetric analyses for the analyzed samples, with indicated the relative weight losses at three temperature intervals

The weight losses at the 20-456°C interval were considered due to the loss of structural water from the CSH and AFm phases for the samples of hardened cement pastes. As for the sample of anhydrous cement, it was ascribed to the loss of structural water from the calcium sulphates. The weight losses at the 457-621°C interval were ascribed to the dehydroxylation of portlandite, while the weight losses in the 622-1000°C interval were considered due to the decarbonation of calcium carbonates. The presence of carbonates in the samples were considered due to carbonation phenomena of the portlandite, so their weight losses were opportunely converted into additional weight losses of the calcium hydroxides, considering the differences in molecular mass between portlandite and calcium carbonates.

Starting from the relative weight losses, the percentages of CH and CSH-AFm phases in the samples of hardened cement paste were calculated. The amount of residual unhydrated cement was calculated, assuming its total hydration at a w/c ratio of 0.85 (as indicated by microstructural evidences obtained by SEM analysis of the samples) and considering a constant CH/(CSH + AFm) ratio of 0.16 for all the samples, calculated on the samples at w/c ratio of 0.85 and coherent with literature data (Bensted & Barnes, 2002). The absolute densities of the hardened pastes were calculated considering the calculated relative concentrations of the constituents and densities values of 2.500, 2.392, 2.242 and 3.130 for CSH gels, AFm phases, portlandite and anhydrous cement, respectively (Taylor, 1990;

Bensted & Barnes, 2002; Korpa & Trettin, 2006). Furthermore, a constant CSH/AFm ratio of 3.852 was considered (Bensted & Barnes, 2002). The calculated relative percentages of the constituents of the hardened pastes are reported in table 4.5, together with the calculated absolute density values.

Sample	CSH, AFm (% wt.)	CH (% wt.)	Cement (% wt.)	ρ (g/cm^3)
0.35a	58.78	9.56	31.66	2.6617
0.35b	60.32	10.01	29.66	2.6476
0.45a	77.49	12.60	9.91	2.5126
0.45b	74.88	12.43	12.69	2.5312
0.55a	80.70	13.12	6.18	2.4871
0.55b	79.33	13.16	7.51	2.4957
0.65a	82.82	13.47	3.72	2.4702
0.65b	80.69	13.39	5.92	2.4847
0.75a	84.70	13.77	1.52	2.4551
0.75b	83.25	13.82	2.93	2.4642
0.85a	86.01	13.99	0	2.4447
0.85b	85.77	14.23	0	2.4442

Table 4.5. Calculated relative percentages of the constituents of the hardened pastes and calculated absolute density values

Again, it is possible to observe a rapid and exponential decrease of the calculated density values in the w/c ratio interval comprised between 0.35 and 0.55. Over this value, the density variations progressively decrease, reaching an asymptotic point. This confirms the hypothesis of reduction of the overall density of the hardened pastes at low w/c ratios due to the progressive incorporation of water molecules in the crystalline structure of the hydrated phases, while at higher w/c ratios further water additions to the fresh mix only cause a larger development of capillary porosity.

Considering the trend of the experimental measurements, in this case too, they cannot be fitted adequately by a linear regression model. An accurate fit of the data was obtained by elaborating two nonlinear regression models based on convex asymptotic regression functions through Minitab 16 software, one comprising all data (figure 4.29), the other excluding the calculated absolute densities for the samples prepared with w/c ratio of 0.35 (figure 4.30).

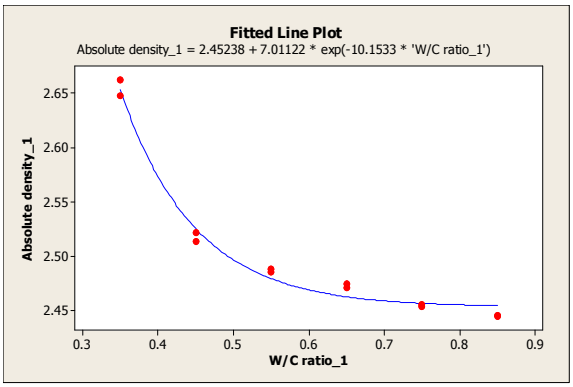

Figure 4.29. Nonlinear regression model between w/c ratio and calculated absolute density of the hardened cement matrix, all samples

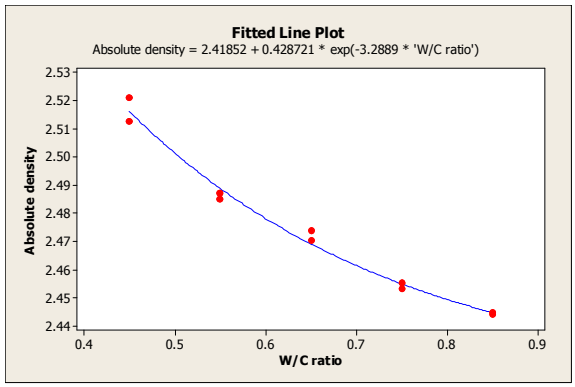

Figure 4.30. Nonlinear regression model between w/c ratio and calculated absolute density of the hardened cement matrix, 0.35 samples excluded

The regression models fit properly the experimental data, as demonstrated by the low sum of the squared residuals, lower for the one with the partial dataset (0.00008) than the one with the full dataset (0.00077). The extrapolated regression functions are the following:

$$\text{Absolute density} = 2.45238 + 7.01122e^{(-10.1533\text{w/c ratio})} \quad (4.3)$$

$$\text{Absolute density} = 2.41852 + 0.428721e^{(-3.2889\text{w/c ratio})} \quad (4.4)$$

Equation 4.3, which describes the model elaborated for the full dataset, was used for the calculation of the absolute hardened paste densities of the concretes with w/c ratios lower than 0.45, while equation 4.4 was used for all other samples.

For each concrete sample, both the apparent density and the absolute density of the cement matrices were calculated. The difference in the two values was used for the calculation of the total porosity of the CSH gel pores in the materials.

Furthermore, the relative amounts of portlandite according to the w/c ratio calculated by the TG measurements were utilized to elaborate a regression function for the extrapolation of the w/c ratio from totally carbonated cement matrices. The linear regression function, calculated considering an increase in the molecular volume of the former CH equal to 11.75% due to the carbonation process, is the following:

$$\text{w/c ratio} = 0.1863 + 0.01987(\%\text{ capillary voids}) \quad (4.5)$$

Finally, the weight quantities of anhydrous cement in the original mixes according to their w/c ratios were estimated calculating the mass ratio between anhydrous cement and hardened cement pastes of the standard samples and elaborating a regression function between the extrapolated values and w/c ratios. The ratios were calculated from the net weight losses of the samples determined by TGA, considering them directly related to the amount of structural water in the hydrated phases. The elaborated nonlinear regression

model, obtained through Minitab 16 software fitting the data with a convex asymptotic regression function, is reported in figure 4.31.

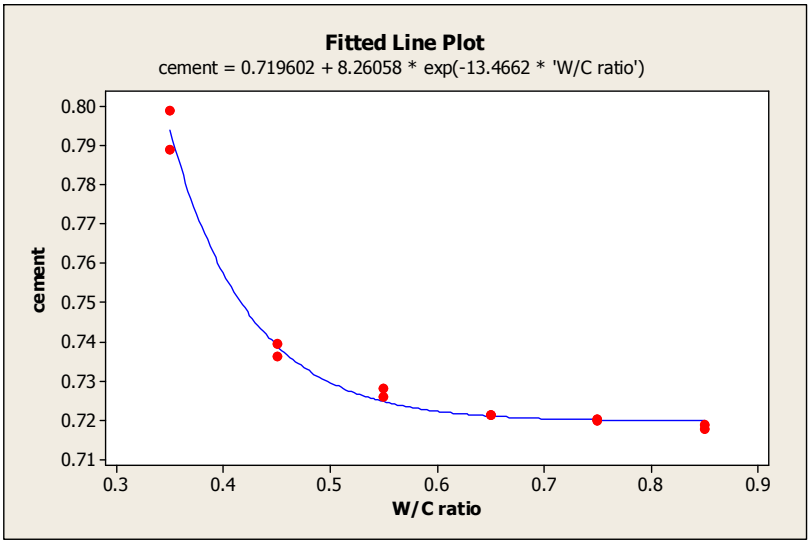

Figure 4.31. Nonlinear regression model between w/c ratio and anhydrous cement/hardened cement pastes ratio

The regression model fits properly the experimental data, as demonstrated by the low sum of the squared residuals (0.00007). The extrapolated regression function is the following:

$$\text{Anhydrous cement ratio} = 0.719602 + 8.26058e^{(-13.4662 \text{w/c ratio})} \quad (4.6)$$

4.2.5 Reconstruction of the aggregate granulometric curves and pore network characterization

Before performing the image analysis for the reconstruction of the granulometric curves, a series of enhancement operations was performed on the images of the segmented aggregate extrapolated from the polished slabs. A common problem, especially in the leanest concretes, was related to the fact that the aggregate particles were in some cases in contact, being thus interpreted as a unique particle by the image analysis software. To overcome this problem, the regions of images presenting diffuse contacts between particles were selected with the Region of Interest (ROI) tool of ImageJ, and then the ROIs were processed through the Watershed Algorithm (Mei, 2003). The filter calculates the Euclidian distance map (EDM) for a group of pixels, finding the ultimate eroded points (UEPs), the last pixels that should be eliminated in case of erosion of the particle. It then

dilates each UEP as much as possible, either until the edge of the particle or the edge of the region of another (growing) UEP is reached. In the contact points, the separation of the particles is performed. After applying the algorithm, a check of its accuracy was performed, making the adequate corrections in case of wrong particles cutting. Finally, the images were post-treated with a median filter to remove imperfections and background noises (figure 4.32).

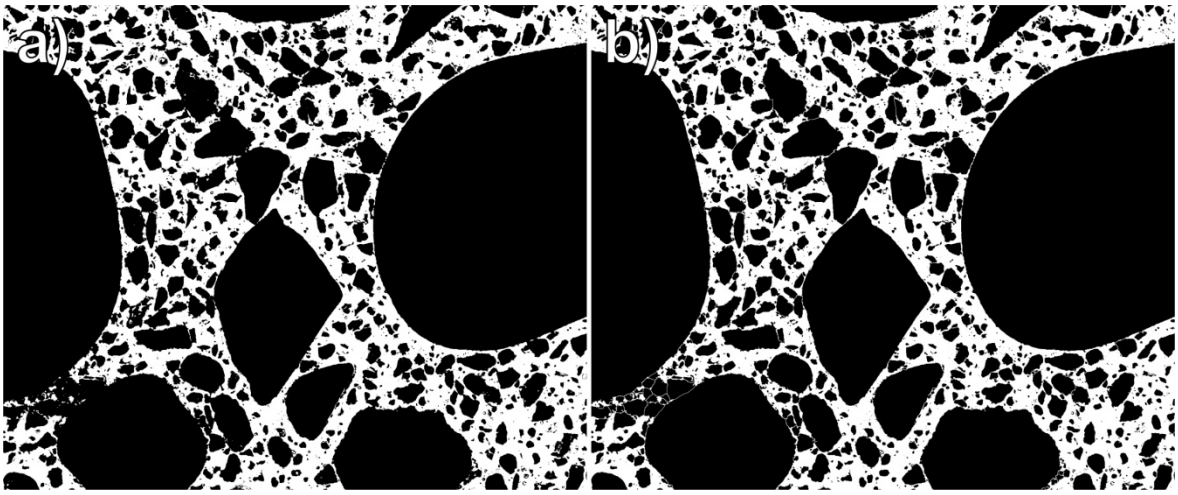

Figure 4.32. Sample MC2, detail of an area of segmented aggregate before (a) and after (b) the procedure of image enhancement

After the image enhancement procedures, the segmented images of both the polished slabs and the samples prepared for the microscale image analysis of the fine aggregate were analyzed through the Analyze Particles function of ImageJ. For each aggregate particle, its area, perimeter, Feret's Diameters and circularity were calculated.

Feret's Diameters were used as size descriptors for the reconstruction of the granulometric curves of the analyzed concrete samples. In general, Feret's Diameter is defined as the distance between two parallel tangents of the particle at an arbitrary angle. In practice, the Minimum $x_{F,min}$ and Maximum Feret Diameter $x_{F,max}$, the Mean Feret Diameter and the Feret Diameters obtained at 90° to direction of the Minimum and Maximum Feret Diameters $x_{F,max90}$ are used (Andronico & Lo Castro, 2008). The Minimum Feret Diameter is often considered as the diameter equivalent to a sieve analysis, so it was used as reference parameter to determine the characteristic sieve aperture for each aggregate particle.

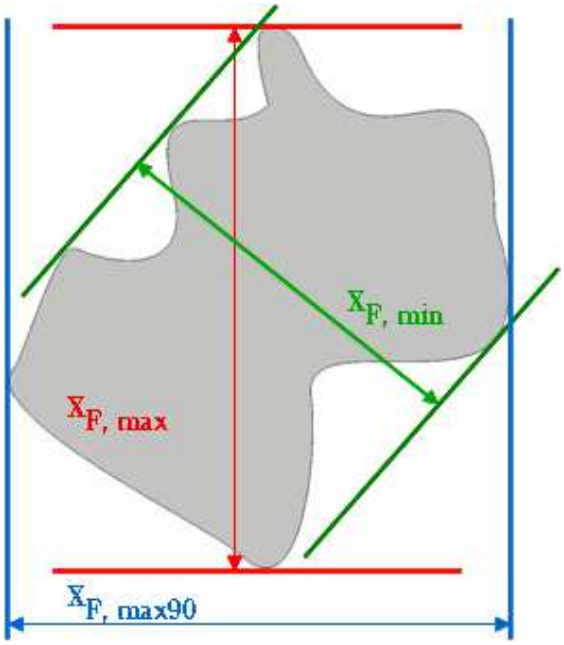

Figure 4.33. Feret's Diameters

To reconstruct the granulometric curves, the retained and passing fractions of the aggregate particles at the standard ASTM sieves were calculated taking into account the Minimum Feret diameter and the area of each grain. The adopted standard sequence is the following: 50 mm, 31.5 mm, 19.1 mm, 12.7 mm, 9.52 mm, 4.76 mm, 2.38 mm, 1.19 mm, 0.59 mm, 0.30 mm, 0.15 mm, 0.075 mm, 0.038 mm. The segmented images of the polished slabs were utilized to extract the parameters of the particles retained at the 0.59 mm standard sieve, while the images segmented from the BSE-SE images and the chemical maps were utilized to extract the parameters of the particles passing through the 0.59 mm standard sieve. The experimental granulometric curves were subsequently compared with the reference Füller & Thompson and Bolomey curves. Furthermore, the fineness modulus of the aggregate fractions of the analyzed concretes were calculated. Fineness modulus (FM) is an empirical size descriptor obtained by adding the total percentage of the sample of an aggregate retained on each of a specified series of sieve, and dividing the sum by 100. The sieve sizes are 0.15 mm, 0.30 mm, 0.59 mm, 1.19 mm, 2.38 mm, 4.76 mm, 9.52 mm, 19.1 mm and 38.1 mm (Collepardi et al., 2008).

In addition to the reconstruction of the granulometric curves, a description of the shapes of the aggregate particles was performed calculating the mean circularity values of the fractions retained at each standard sieve. The circularity parameter is defined as $4\pi\cdot[\text{area}/(\text{perimeter})^2]$, and ranges from 0 (infinitely elongated polygon) to 1 (perfect

circle). Furthermore, the relative standard deviations from the mean circularity values were calculated, to define the shape variation of the particles. Then, the weighted mean circularity and the weighted standard deviation from the mean of both gravel and sand fraction were calculated for each concrete sample. The weighted values were extrapolated by the sum of all the values at each standard sieve multiplied for the ratio of aggregate fraction at the target sieve over the total aggregate.

Finally, the size distribution of the voids was calculated from the images of the segmented pore networks of the materials through the Analyze Particles function of ImageJ software, considering the Maximum Feret Diameter of each segmented void and its area. The voids were subdivided in the following size intervals: lower than 0.1 mm, 0.1-0.2 mm, 0.2-0.3 mm, 0.3-0.4 mm, 0.4-0.5 mm, 0.5-0.6 mm, 0.6-0.7 mm, 0.7-0.8 mm, 0.8, 0.9 mm, 0.9-1 mm, 1-2 mm, 2-3 mm, 3-4 mm, 4-5 mm, 5-6 mm, 6-7 mm, 7-8 mm, 8-9 mm, 9-10 mm, larger than 10 mm. Furthermore, an empirical size descriptor was elaborated also for the voids, defined porosity modulus. The descriptor is obtained by adding the total percentage of the porosity comprised on each of the defined size intervals, and dividing the sum by 100.

4.3 RESULTS

4.3.1 Verification of the accuracy of the image analysis protocol

The volumetric percentages of the three main components of the hardened concrete samples, as determined by both the image analysis protocol and the point count procedure, are reported in table 4.6. The regression plots reported in figures 4.34, 4.35 and 4.36 express the relation between the volumetric measurements performed with the two analytical techniques, indicating the relative standard errors and coefficients of determination.

Sample	Matrix IA (% vol.)	Aggregate IA (% vol.)	Voids IA (% vol.)	Matrix PC (% vol.)	Aggregate PC (% vol.)	Voids PC (% vol.)
CC1	23.5	67.2	9.3	23.9	66.5	9.6
CC2	17.5	76.1	6.4	17.2	76.8	6.0
CC3	25.2	65.9	8.9	26.1	64.9	9.0
CP1	23.3	72.1	4.6	24.0	71.8	4.2
CT1	22.2	66.5	11.3	20.9	67.3	11.8
CT2	23.5	75.0	1.5	22.9	75.8	1.3
CT3	18.9	77.7	3.4	19.3	76.8	3.9
BS1	13.2	74.1	12.7	13.6	73.6	12.8
BS2	16.4	71.2	12.4	15.5	72.5	12.0
BS3	20.4	65.6	14.0	20.2	65.5	14.3
BS4	10.6	84.9	4.5	11.4	84.0	4.6
BT1	32.4	63.4	4.2	33.0	62.1	4.9
BG1	26.7	68.0	5.3	26.2	68.7	5.1
BV1	33.1	64.3	2.6	32.7	64.7	2.6
MC1	27.1	72.1	0.8	26.5	72.4	1.1
MC2	24.9	73.8	1.3	26.1	72.4	1.5
MC3	31.1	66.9	2.0	30.3	68.0	1.7
RP1	21.9	74.0	4.1	22.8	73.2	4.0
RP2	21.9	74.2	3.9	22.5	73.4	4.1
RP3	22.1	74.2	3.7	22.4	73.6	4.0
RT1	26.8	69.5	3.7	28.0	68.5	3.5
RT2	27.0	69.8	3.2	27.7	68.9	3.4
RC1	26.5	69.6	3.9	25.6	70.0	4.4
RA1	14.6	71.5	13.9	13.2	72.7	14.1
FP1	26.5	72.4	1.1	27.1	71.5	1.4
FP2	30.0	69.3	0.7	29.1	70.0	0.9

Table 4.6. Volumetric percentages of the main components of the concrete samples, as determined by image analysis and point count

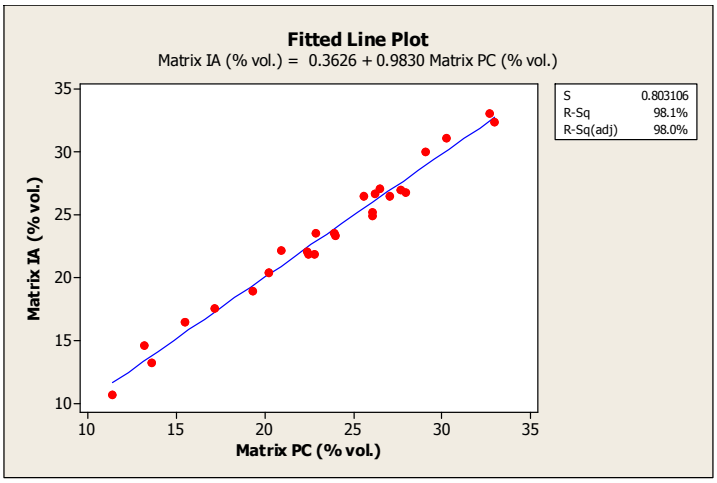

Figure 4.34. Relation between percentages of cement matrix measured by image analysis and point count on the same samples

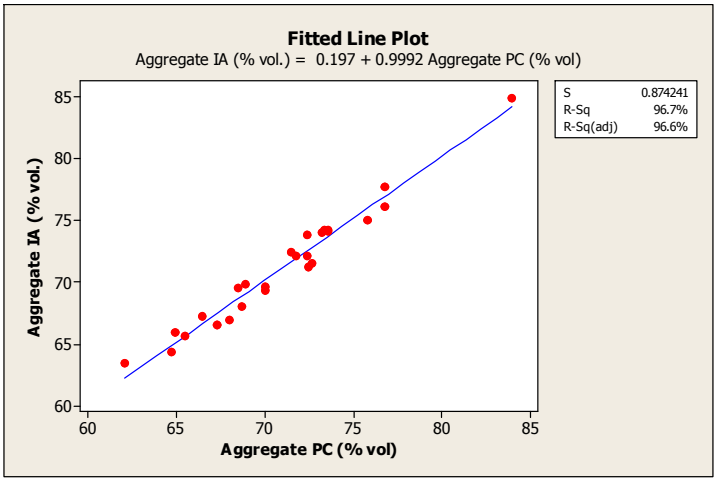

Figure 4.35. Relation between percentages of aggregate measured by image analysis and point count on the same samples

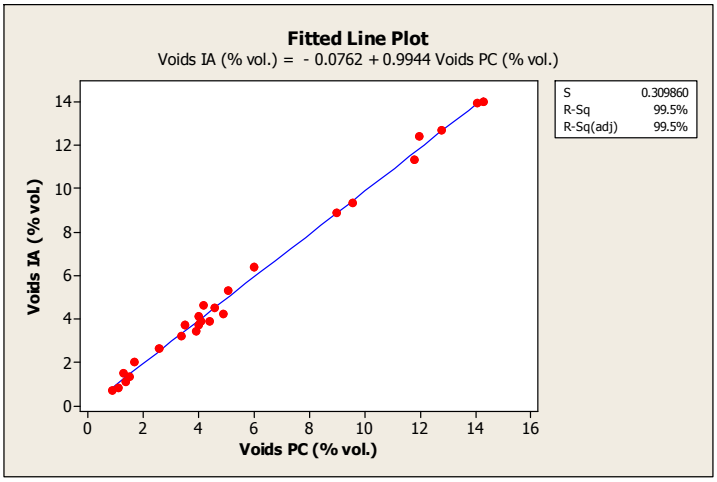

Figure 4.36. Relation between percentages of voids measured by image analysis and point count on the same samples

The comparisons between the analytical results obtained using the two methods show an extremely close linear correlation with each other, with a mean R^2 of 0.981. The linear correlation is particularly high for the determinations of the voids percentages, with an R^2 of 0.995 and a S of 0.310, proving the efficacy of the technique as a valid alternative to the standard point count procedure of the air voids described by ASTM C 457.

Less accurate linear correlations are observable for the determination of the relative percentages of cement matrix and aggregate, with an R^2 of 0.981 and a S of 0.803 for the former, and an R^2 of 0.967 and an S of 0.874 for the latter. Nevertheless, the values indicate an extremely high linear correlation for these measurements also, confirming the reliability of the formulated image analysis protocol.

4.3.2 Northern Wing of the Carraresi Castle

The mix designs characteristics of the analyzed concrete samples, as determined by the image analysis protocol, are reported in table 4.7. The cement and aggregate contents in the original mixes, expressed in Kg/m^3, are reported, together with the water/cement (w/c) ratio, the cement/aggregate (c/a) ratio and the volumetric percentages of voids and pores in the hardened concretes.

Sample	Cement (kg/m^3)	w/c ratio	c/a ratio	Gravel (kg/m^3)	Sand (Kg/m^3)	Voids (% vol.)	Pores (% vol.)
CC1	303.83	0.53	0.17	1248.33	506.75	9.3	6.7
CC2	248.12	0.43	0.12	1501.87	520.51	6.4	4.4
CC3	334.77	0.52	0.19	1232.82	488.20	8.9	6.8
CP1	296.89	0.55	0.16	1226.11	658.44	4.6	6.8
CT1	291.01	0.54	0.17	1210.18	526.95	11.3	6.1
CT2	348.18	0.41	0.18	1481.82	478.62	1.5	5.4
CT3	266.43	0.44	0.13	1364.80	674.24	3.4	4.7

Table 4.7. Mix designs of the Northern Wing of the Carraresi Castle concretes

The characteristics of the mix designs clearly confirm the differences in concretes compositions according to the constructive phase.

The Hennebique concretes are lean, with uniform c/a ratios of 0.12-0.13. Larger cement dosages were adopted for the manufacturing of the beams with respect to the slabs, while both samples are characterized by a marked prevalence of coarse aggregate over fine

aggregate. The most significant characteristic, responsible for the high compressive strengths of the materials, is the low w/c ratios adopted for manufacturing the conglomerates. Considering the lack of utilization of chemical admixtures in the fresh mixes, the casting and homogenization procedure of the fresh conglomerates should have been particularly accurate, to ensure a homogeneous distribution of the materials and a reduced presence of voids in the hardened materials. This justifies the slight segregation phenomena observed on the concretes of the slabs, associated to a greater presence of entrapped air voids, due to the greater difficulties of casting and homogenization of such structural elements characterized by significant areal extensions. On the contrary, the thin slabs are excellently homogenized, with a reduced macroporosity, and consequently show better mechanical properties.

The concretes of the second constructive phase are characterized by higher cement dosages with respect to the Hennebique concretes. The values are homogeneous for CC1, CP1 and CT1 samples, always near 300 Kg/m^3, while they are significantly higher in CC3 sample, the one characterized by higher compressive strength. Conversely, the w/c ratios are higher with respect to the ones of the Hennebique concretes, directly influencing the higher capillary porosity and the lower compressive strength values. As regards the aggregate fraction, gravel is still predominant over sand, but the columns have significantly higher fine aggregate contents with respect to the other structural elements. The overall degree of macroporosity is high for all horizontal elements, indicating a low accuracy in the casting and homogenization processes of the materials. Voids percentages are particularly high in CT1 sample, the one characterized by the lowest compressive strength. On the contrary, macroporosity is lower in CP1 sample, confirming the higher accuracy in the manufacturing of the non-reinforced concrete columns.

Finally, the concretes of the third constructive phase are the ones showing the best overall mix designs. They are manufactured with the highest cement dosages and the lowest w/c ratios. The coarse aggregate is still highly predominant over the fine aggregate, and the overall degree of macroporosity is extremely reduced, indicating excellent casting, compaction and homogenization procedures of the conglomerates. All these features justify the high compressive strength values.

A more detailed analysis of the features of both aggregate fractions and pore networks of the materials is hereby reported.

The main features of the Hennebique concrete's aggregate fractions are reported in table 4.8, while their granulometric curves, compared with the reference Füller & Thompson and Bolomey curves, and the retained fractions at the standard ASTM sieves, compared with the reference Bolomey retained fractions, are reported in figures 4.37 and 4.38.

Sample	D_{max} (mm)	Fineness modulus	WMC gravel	RSD-WMC gravel	WMC sand	RSD-WMC sand
CC2	35.03	5.47	0.333	0.193	0.528	0.239
CT3	27.52	5.05	0.341	0.281	0.554	0.257

Table 4.8. Main features of the aggregate fractions of the Hennebique concretes. WMC stands for weighted mean circularity, RSD-WMC stands for relative standard deviation of the weighted mean circularity

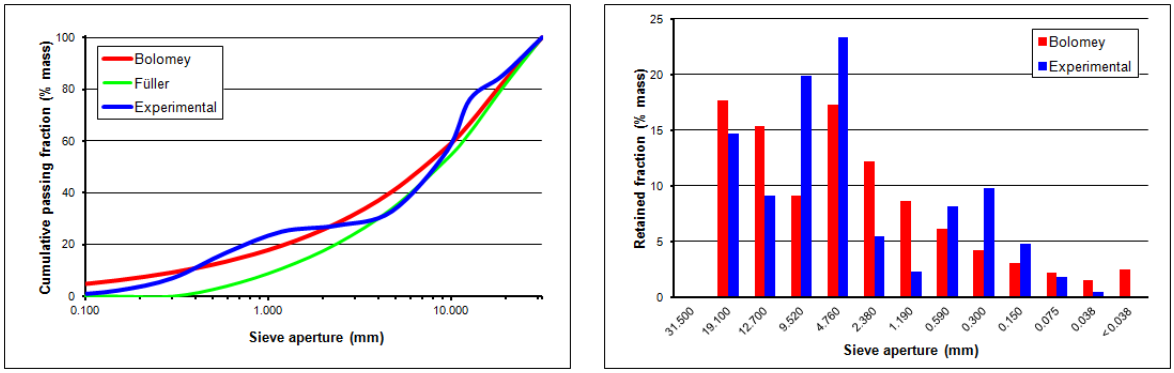

Figure 4.37. Sample CC2: granulometric curve compared with the reference ones (to the left) and retained fractions at the standard ASTM sieves compared with the reference Bolomey ones (to the right)

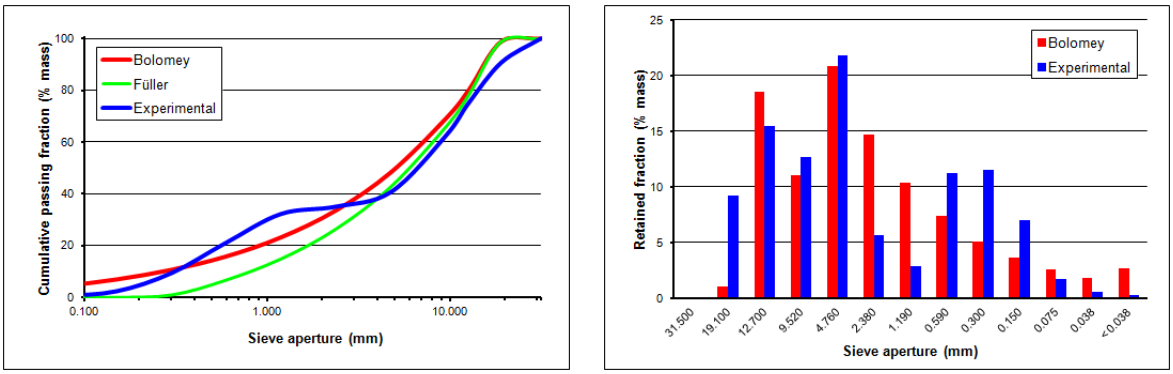

Figure 4.38. Sample CT3: granulometric curve compared with the reference ones (to the left) and retained fractions at the standard ASTM sieves compared with the reference Bolomey ones (to the right)

The concretes of the slabs are characterized by higher D_{max} and fineness modulus values with respect to the concretes of the beams, indicating a formulation of the mixes with coarser aggregate fractions, in terms of both maximum dimensions and gravel quantity. Circularity values are similar for the two samples, indicating the utilization of gravels of

medium-low sphericity and sands of medium-high sphericity. Conversely, the relative standard deviation values indicate greater shape variability for the aggregates of the beams with respect to the aggregates of the slabs. As regards the granulometric distributions, they show affinity with the reference Füller & Thompson curves at greater granulometries only, strongly differing at lower ones. A good resemblance with the reference Bolomey curves is observable. Nevertheless, as indicated by the retained fractions histograms, discrepancies are observable due to enrichments in coarse and medium sands for both samples, and also in medium and fine gravels for the concrete slabs. Despite this, a better overall concordance is observable for CC2 sample, as indicated by the regression plot between experimental and Bolomey cumulative passing fractions (figure 4.39), showing a lower standard error and a higher coefficient of determination (4.56 and 0.985, respectively) with respect to CT3 sample (5.09 and 0.981, figure 4.40). This is mainly due to the more significant enrichment in fine aggregate on the inert fraction of the beam.

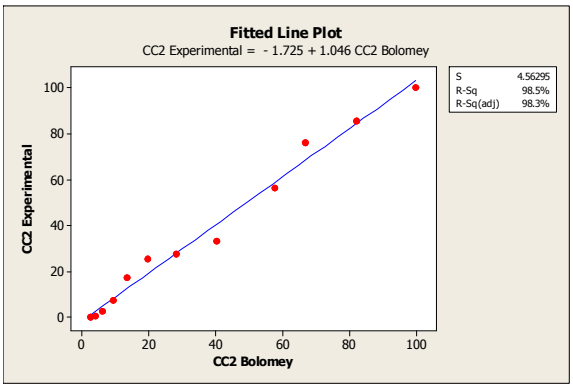

Figure 4.39. Sample CC2, relation between experimental and Bolomey cumulative passing fractions at the standard ASTM sieves

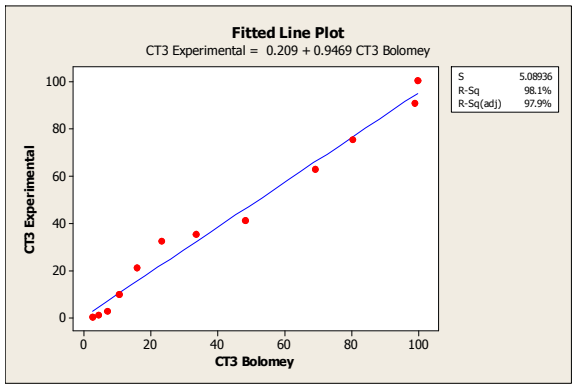

Figure 4.40. Sample CT3, relation between experimental and Bolomey cumulative passing fractions at the standard ASTM sieves

As regards the characteristics of the pore networks, the concretes of the slabs are characterized by the presence of voids characterized by greater maximum dimensions with respect to the ones of the concrete beams, with a strongly polydisperse pore size distribution showing a marked prevalence of over-millimetric voids with maxima of distribution at 1-4 mm and over 10 mm, while the sub-millimetric voids have a Gaussian distribution with maximum at 0.6-0.7 mm (figure 4.41). The concretes of the beams show a narrower pore size distribution, equally subdivided between over- and sub-millimetric voids. The former have a strong peak of distribution at 1 mm, while the latter are more polydisperse, with maximum of distribution at 0.2 mm (figure 4.42).

Consequently, CC2 sample is characterized by a higher value of porosity modulus with respect to CT3 (12.83 *vs.* 8.84).

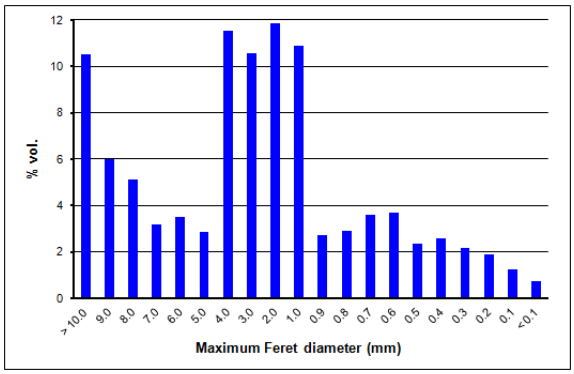

Figure 4.41. Sample CC2, pore size distribution

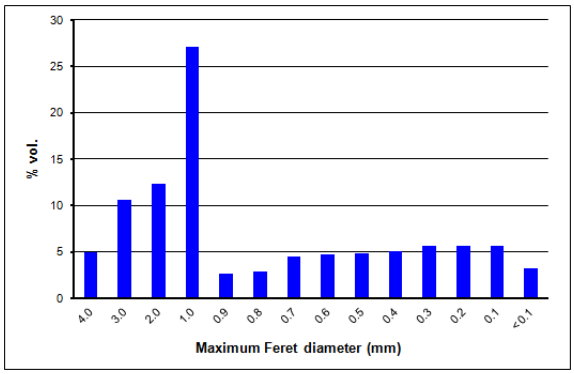

Figure 4.42. Sample CT3, pore size distribution

The main features of the 1920s concrete's aggregate fractions are reported in table 4.9.

Sample	D_{max} (mm)	Fineness modulus	WMC gravel	RSD-WMC gravel	WMC sand	RSD-WMC sand
CC1	30.09	4.93	0.374	0.291	0.613	0.193
CC3	29.76	4.94	0.372	0.269	0.605	0.200
CP1	17.06	4.40	0.327	0.257	0.650	0.172
CT1	32.48	4.91	0.390	0.225	0.619	0.188

Table 4.9. Main features of the aggregate fractions of the Hennebique concretes. WMC stands for weighted mean circularity, RSD-WMC stands for relative standard deviation of the weighted mean circularity

The analytical results confirm significant differences between the concretes of the various structural elements. The horizontal elements are manufactured with aggregates characterized by similar D_{max}, slightly higher for the concretes of the beams. Also, fineness modulus is similar for all samples, as well as shape features of the sand fraction, characterized by higher sphericity and lower variability with respect to the sands of the Hennebique concretes. Differences between the concretes of the beams and the slabs can be found in the shape characteristics of the coarse aggregates; despite the circularity values indicate for all samples a degree of sphericity of the gravel higher than the one of the Hennebique concretes, CT1 sample shows a higher weighted mean circularity of the coarse aggregate with respect to CC1 and CC3, with a significantly lower relative standard deviation, indicating a manufacturing with more rounded and less variable gravels.

The characteristics of the granulometric curves and the histograms of the retained fractions confirm the strong similarities between the aggregates of the two concrete slab samples

(figures 4.43, 4.44): both samples show affinity with the reference Füller & Thompson curves at higher granulometries only, strongly differing from them at lower granulometries. Furthermore, they are always characterized by more significant differences from the reference Bolomey curves with respect to the Hennebique concretes. The discrepancies are mainly related to enrichments in medium and fine sands. Also, enrichments in fine gravels are observable.

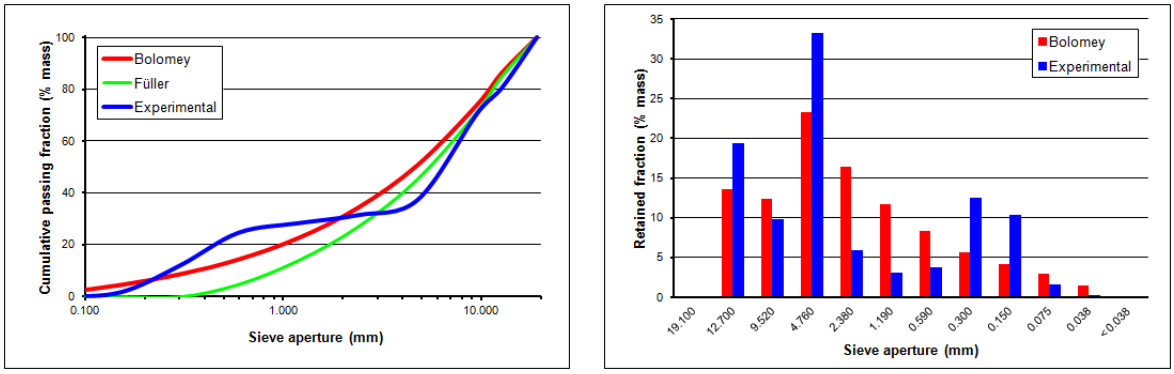

Figure 4.43. Sample CC1: granulometric curve compared with the reference ones (to the left) and retained fractions at the standard ASTM sieves compared with the reference Bolomey ones (to the right)

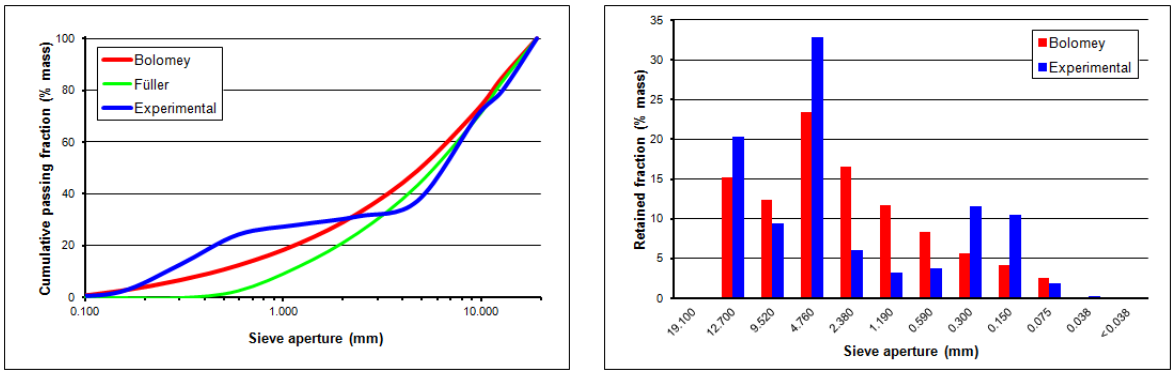

Figure 4.44. Sample CC3: granulometric curve compared with the reference ones (to the left) and retained fractions at the standard ASTM sieves compared with the reference Bolomey ones (to the right)

The lower affinity with the reference Bolomey curves is confirmed by the regression plots between experimental and Bolomey cumulative passing fractions (figures 4.45, 4.46), showing higher standard errors (6.03 for CC1, 5.93 for CC3) and lower coefficients of determination (0.972 for CC1, 0.973 for CC3) with respect to the Hennebique concretes.

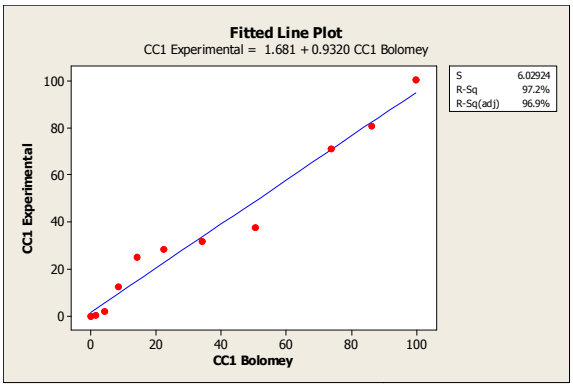

Figure 4.45. Sample CC1, relation between experimental and Bolomey cumulative passing fractions at the standard ASTM sieves

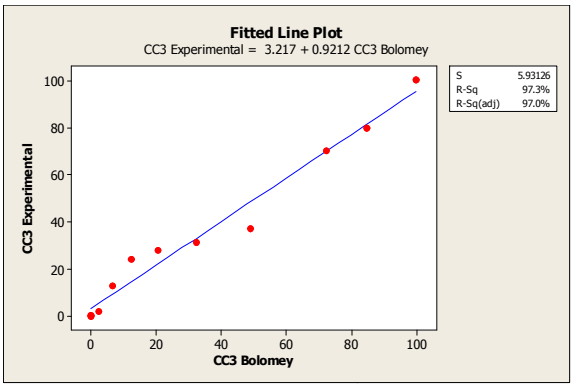

Figure 4.46. Sample CC3, relation between experimental and Bolomey cumulative passing fractions at the standard ASTM sieves

The granulometric curve and the histogram of the retained fractions of CT1 sample (figure 4.47) show similarities with the ones of CC1 and CC3 samples, still being characterized by significant enrichments in medium and fine sands and in fine gravels with respect to the reference distributions. Furthermore, a marked depletion in medium gravels is observable. Consequently, the discrepancies with the Füller & Thompson and Bolomey curves are even more significant than in the concrete slab samples, as indicated by the high standard error (6.96) and by the low coefficient of determination (0.967) of the regression plot between experimental and Bolomey cumulative passing fractions (figure 4.48).

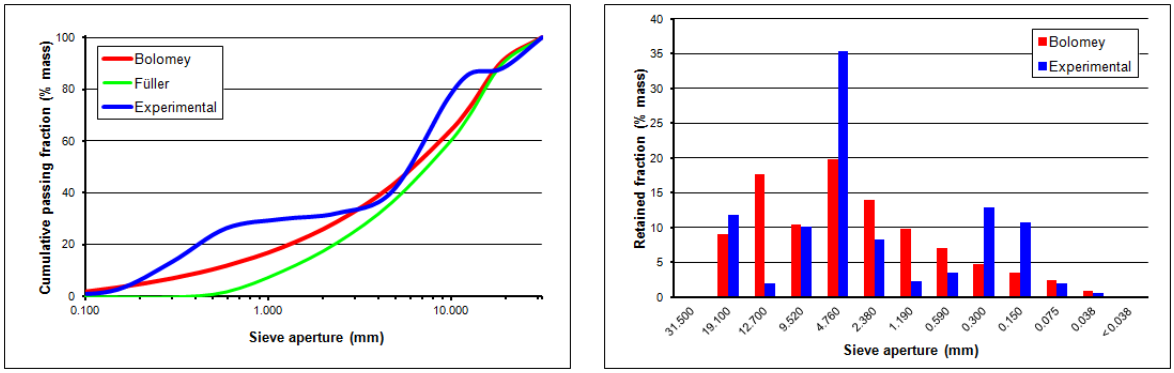

Figure 4.47. Sample CT1: granulometric curve compared with the reference ones (to the left) and retained fractions at the standard ASTM sieves compared with the reference Bolomey ones (to the right)

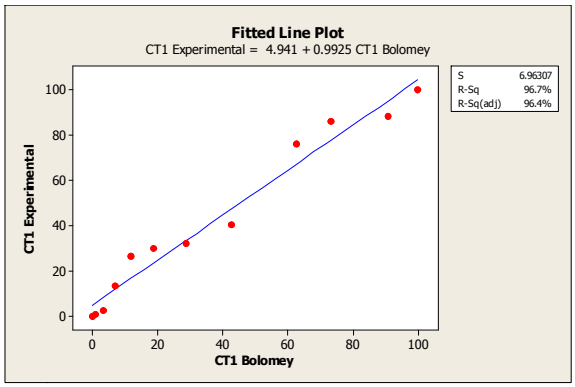

Figure 4.48. Sample CT1, relation between experimental and Bolomey cumulative passing fractions at the standard ASTM sieves

CP1 sample, relative to a concrete column of the second constructive phase, shows significant morphological characteristics of the inert fraction with respect to the concretes of the horizontal structural elements. D_{max} of the aggregate is significantly lower (17.06 mm), together with the fineness modulus (4.40), indicating the utilization of a finer aggregate. Furthermore, the coarse aggregate is characterized by lower sphericity, as indicated by the lower weighted mean circularity, while the overall sphericity of the fine aggregate is higher. As regards the granulometric distribution, a good correspondence with the reference ones is observable at higher granulometries (figure 4.49); in particular, an almost perfect correspondence with the reference Füller & Thompson curve is observable at granulometries higher than 2 mm. Conversely, the granulometric distribution of the sand fraction strongly differs from the reference ones, due to significant enrichments in medium and fine sands.

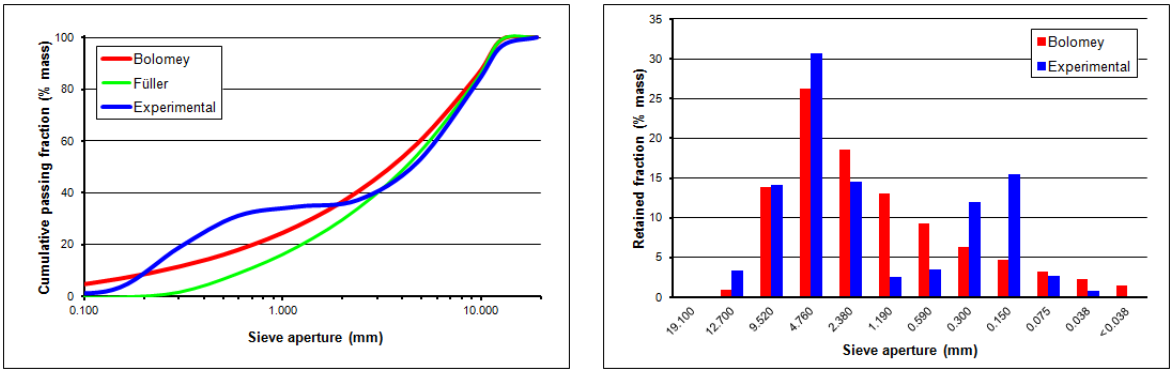

Figure 4.49. Sample CP1: granulometric curve compared with the reference ones (to the left) and retained fractions at the standard ASTM sieves compared with the reference Bolomey ones (to the right)

This feature influences the overall goodness of fit with the reference Bolomey curve, as indicated by the standard error and coefficient of determination of the regression plot between experimental and Bolomey cumulative passing fractions (6.14 and 0.975, respectively, figure 4.50), similar to the ones of the concrete slab samples.

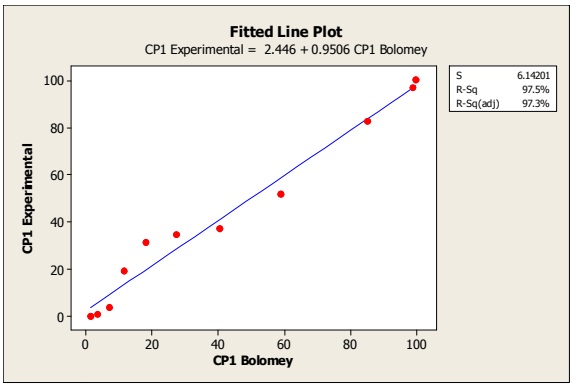

Figure 4.50. Sample CP1, relation between experimental and Bolomey cumulative passing fractions at the standard ASTM sieves

As regards the characteristics of the pore networks, all concrete samples show a marked prevalence of over-millimetric over sub-millimetric voids, as demonstrated by the similar, and rather high porosity modulus values (10.90 for CC1, 11.24 for CC3, 10.39 for CP1, 11.19 for CT1). Such prevalence is particularly significant for the CT1 sample. Furthermore, the voids are highly polydisperse in all samples, and the pore size distributions show comparable features, being all characterized by peaks of distribution of the over-centimetric voids comprised between 1 and 3 mm, and by a homogeneous size distribution of the sub-millimetric ones.

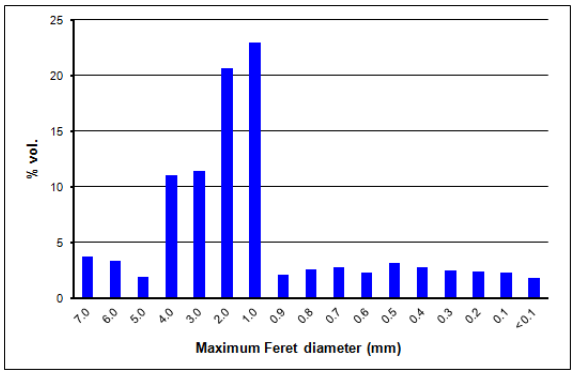

Figure 4.51. Sample CC1, pore size distribution

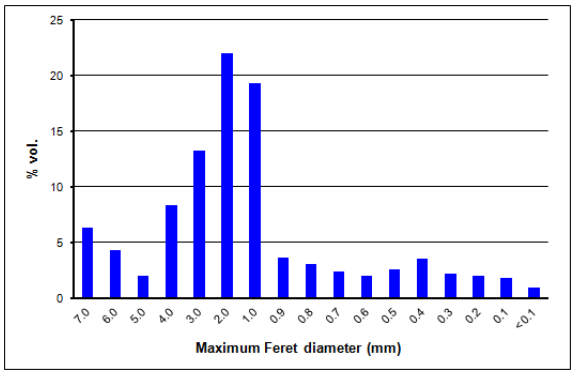

Figure 4.52. Sample CC3, pore size distribution

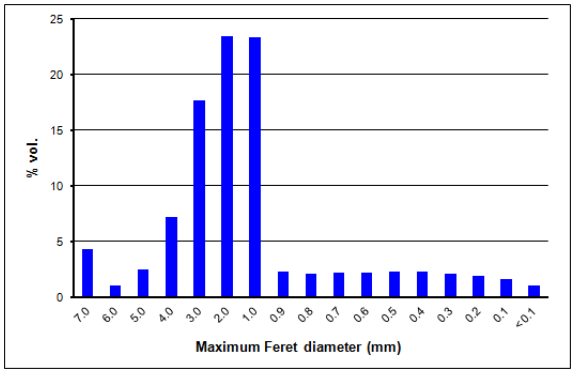

Figure 4.53. Sample CT1, pore size distribution

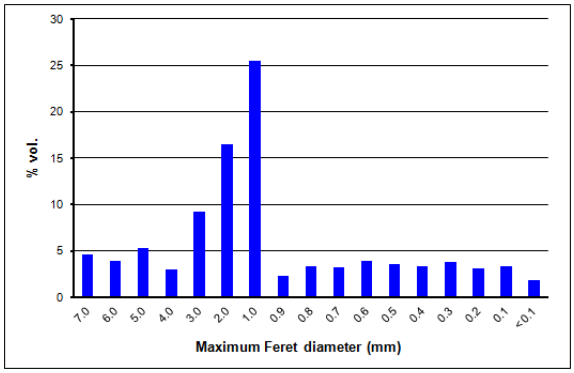

Figure 4.54. Sample CP1, pore size distribution

The main features of CT2 sample's aggregate fraction are reported in table 4.10.

Sample	D_{max} (mm)	Fineness modulus	WMC gravel	RSD-WMC gravel	WMC sand	RSD-WMC sand
CT2	32.49	5.15	0.339	0.216	0.615	0.207

Table 4.10. Main features of the aggregate fraction of CT2 sample. WMC stands for weighted mean circularity, RSD-WMC stands for relative standard deviation of the weighted mean circularity

The sample, relative to a beam of the third constructive phase, is characterized by D_{max} and fineness modulus of the aggregate similar to the ones of the Hennebique beam. Furthermore, sphericity of the gravel is comparable, as indicated by the similar weighted mean circularity. Nevertheless, the weighted mean circularity value of the sand fraction indicates a sphericity akin to the one of the 1920s concrete's fine aggregates. As regards the granulometric distribution, it is akin to the one of CT1 sample, significantly differing from the reference granulometric distributions due to strong enrichments in medium sand and medium gravel and depletions in medium gravel (figure 4.55).

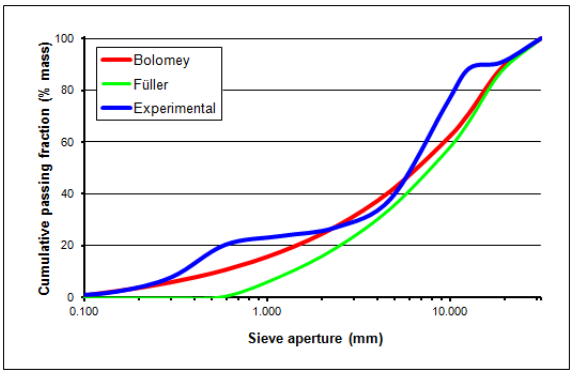

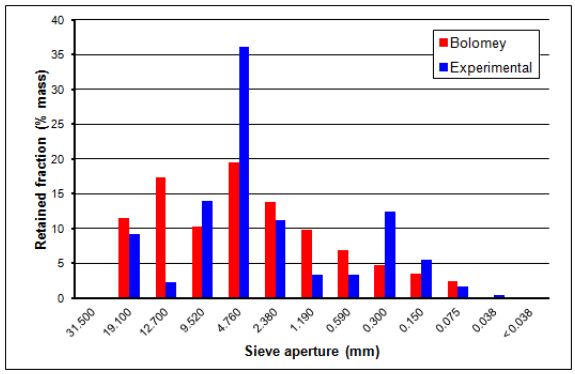

Figure 4.55. Sample CT2: granulometric curve compared with the reference ones (to the left) and retained fractions at the standard ASTM sieves compared with the reference Bolomey ones (to the right)

The discrepancy with the Bolomey curve is clearly highlighted by the high standard error (6.43) and by the low coefficient of determination (0.974) of the regression plot between experimental and Bolomey cumulative passing fractions (figure 4.56).

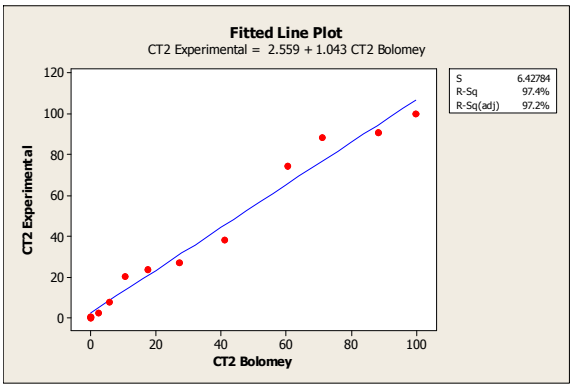

Figure 4.56. Sample CT2, relation between experimental and Bolomey cumulative passing fractions at the standard ASTM sieves

The characteristics of the pore networks significantly differ from the ones of the older concrete samples, confirming the overall higher casting and homogenization accuracy of the 1950s concretes. CT2 sample shows a narrow pore size distribution, as the maximum dimensions of the voids are smaller than 4 mm. Furthermore, sub-millimetric voids are markedly predominant. The pore size distribution is characterized by the presence of two modal peaks, one at 1 mm and the other, more significant, at 0.1 mm (figure 4.57). Consequently, the sample is characterized by a low value of porosity modulus (5.34).

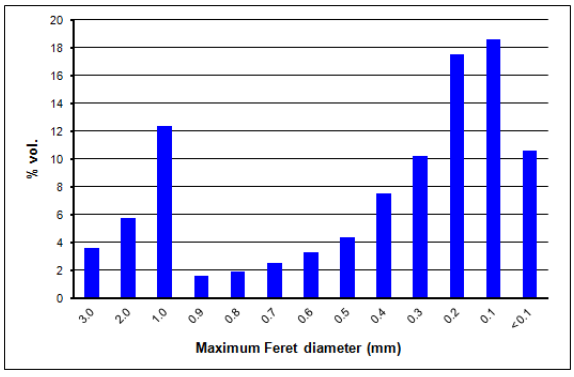

Figure 4.57. Sample CT2, pore size distribution

4.3.3 Victory Monument

The mix designs characteristics of the analyzed concrete samples, as determined by the image analysis protocol, are reported in table 4.11. The cement and aggregate contents in the original mixes, expressed in Kg/m^3, are reported, together with the water/cement (w/c) ratio, the cement/aggregate (c/a) ratio and the volumetric percentages of voids and pores in the hardened concretes.

Sample	**Cement (kg/m^3)**	**w/c ratio**	**c/a ratio**	**Gravel (kg/m^3)**	**Sand (Kg/m^3)**	**Voids (% vol.)**	**Pores (% vol.)**
BS1	170.42	0.56	0.09	630.60	1306.29	12.7	3.7
BS2	211.20	0.56	0.11	995.42	860.64	12.4	4.7
BS3	282.58	0.47	0.17	764.64	947.40	14.0	5.1
BS4	144.06	0.49	0.07	1428.08	781.99	4.5	2.7
BV1	371.22	0.76	0.22	509.88	1171.33	2.6	12.1
BT1	402.42	0.58	0.24	730.12	924.62	4.2	10.0
BG1	330.87	0.59	0.19	747.29	1027.51	5.3	8.2

Table 4.11. Mix designs of the Victory Monument concretes

The characteristics of the mix designs clearly confirm the differences in concretes compositions according to the structural element.

Differences are recognizable also between the mix designs of the lateral and central walls, despite being all characterized by highly incongruent mix designs, indicating clear segregation phenomena of the components due to poor casting procedures and inadequate homogenization of the fresh conglomerates.

The lateral walls concretes are markedly lean, with c/a ratio of 0.09-0.11. The low cement dosage, associated to the medium-low w/c ratio, significantly contributed to lower the consistency class of the conglomerates, increasing their subjectivity to segregation phenomena due to the difficulty to cast and homogenize such viscous pastes. Consequently, the concrete core sampled in the lower portion of the wall is characterized by significantly higher gravel content with respect to the one sampled in the higher portion. Besides these features, the materials are constituted by inert fractions markedly enriched in sand. The poor mix designs directly influenced the development of an anomalous macroporosity in the materials, and consequently influenced negatively their overall mechanical properties.

The segregation phenomena are even more accentuate in the central walls, with the lower portions characterized by an anomalous gravel accumulation, associated to an extremely low cement content. The scarce dosage of hydraulic binder is the main cause for the poor mechanical properties of concretes in these portions of the structural elements. On the contrary, the higher portions show significant enrichments in sand fraction and high cement content, associated to a reduced coarse aggregate content. Despite the inadequate mix design, the high cement content allowed the reaching of satisfactory, even though still low, compressive strength values in these portions of the structural elements. The w/c ratio is lower than the one of the lateral wall for both samples, justifying the subjectivity to segregation of the fresh conglomerates. The degree of macroporosity is high for the concretes of the higher portions, but also for the lower ones, considering the scarce amount of cement matrix due to the low cement content.

The concretes of the vaulted slab are characterized by high cement dosages as indicated by a c/a ratio of 0.22. Despite this, they were manufactured with a significantly high w/c ratio. As regards the aggregate fraction, a marked predominance of fine aggregate over the gravel fraction is observable. All these factors contributed to raise the consistency class of the materials, facilitating the casting and homogenization of the fresh conglomerate. This hypothesis is confirmed by the low volumetric percentage of voids in the hardened materials. Conversely, they caused the development of an anomalous interconnected capillary porosity, which negatively influenced the overall mechanical resistance.

Finally, the stairway concretes are the ones showing the best overall mix designs. They are manufactured with high cement dosages, in particular the concretes of the beams, characterized by a c/a ratio of 0.24 and by the best overall mechanical properties. Furthermore, they were manufactured with medium cement dosages, which favored the workability of the fresh conglomerates without significantly influencing their mechanical resistances. The proper casting and homogenization procedures of the concretes, related to their good workability properties, are confirmed by the medium-low volumetric percentages of macroporosity. Despite these positive characteristics, the materials still show a marked enrichment in fine aggregate, in particular the concretes of the thin slabs, characterized by lower compressive strength values.

The main features of the aggregate fractions of the lateral walls concretes are reported in table 4.12, while their granulometric curves, compared with the reference Füller & Thompson and Bolomey curves, and the retained fractions at the standard ASTM sieves,

compared with the reference Bolomey retained fractions, are reported in figures 4.58 and 4.59.

Sample	D_{max} (mm)	Fineness modulus	WMC gravel	RSD-WMC gravel	WMC sand	RSD-WMC sand
BS1	20.67	3.01	0.297	0.350	0.554	0.214
BS2	36.49	4.17	0.278	0.331	0.513	0.244

Table 4.12. Main features of the aggregate fractions of the lateral walls concretes. WMC stands for weighted mean circularity, RSD-WMC stands for relative standard deviation of the weighted mean circularity

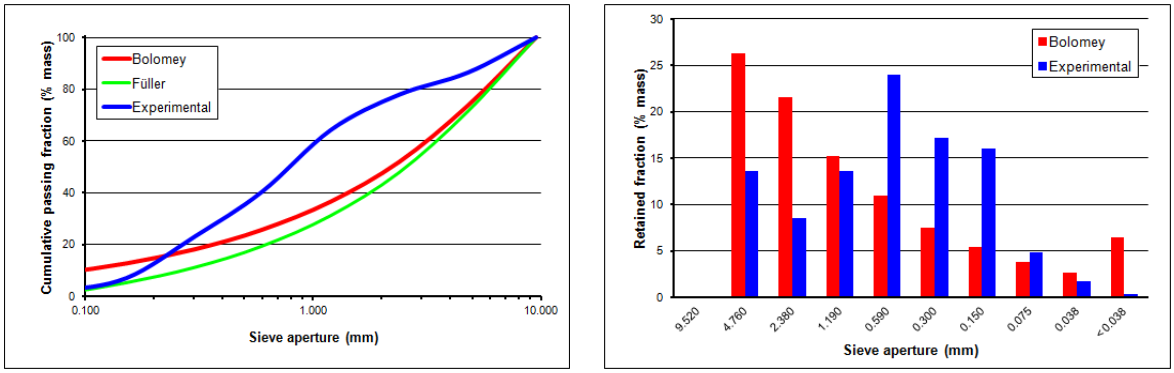

Figure 4.58. Sample BS1: granulometric curve compared with the reference ones (to the left) and retained fractions at the standard ASTM sieves compared with the reference Bolomey ones (to the right)

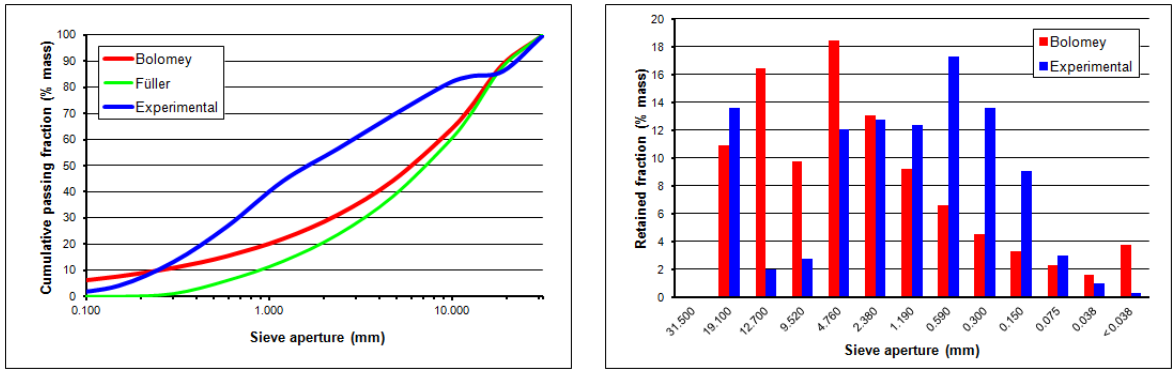

Figure 4.59. Sample BS2: granulometric curve compared with the reference ones (to the left) and retained fractions at the standard ASTM sieves compared with the reference Bolomey ones (to the right)

The characteristics of the aggregate fractions confirm the segregation phenomena on the lateral wall. The lower portions are constituted by an inert fraction with D_{max} of 36.49 mm and fineness modulus of 4.17, while the values are significantly lower in the higher portions (20.67 and 3.01, respectively). Circularity values are similar for the two samples, indicating the utilization of gravels of medium-low sphericity and sands of medium-high sphericity. Moreover, the high values of relative standard deviation from the mean

weighted circularities of the gravels indicate a great shape variability for the coarse aggregate fractions. As regards the granulometric distributions, they strongly differ from the reference ones, due to a strong enrichment in coarse and medium sands associated to a depletion in medium and fine gravels for both samples, and also to a slight enrichment in coarse gravel for the concrete sample of the lower portion of the wall, due to the previously mentioned accumulation of coarse aggregate related to the segregation phenomena. The high discrepancies from the reference Bolomey curves are confirmed by the regression plots between experimental and Bolomey cumulative passing fractions (figures 4.60, 4.61), showing high standard errors (13.64 for BS1, 12.42 for BS2) and low coefficients of determination (0.891 for BS1, 0.898 for BS2).

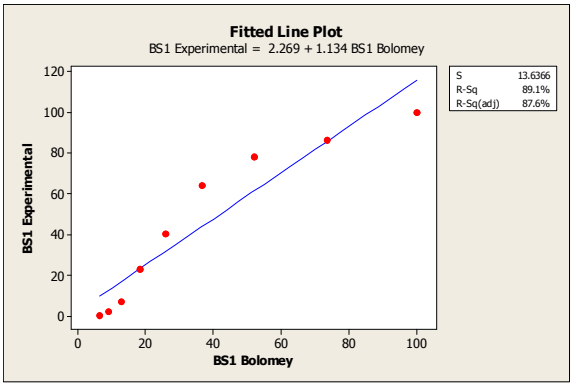

Figure 4.60. Sample BS1, relation between experimental and Bolomey cumulative passing fractions at the standard ASTM sieves

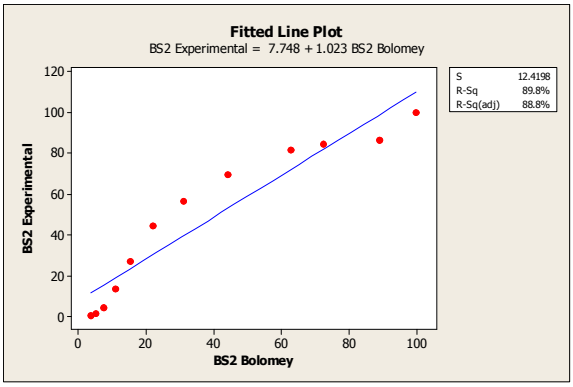

Figure 4.61. Sample BS2, relation between experimental and Bolomey cumulative passing fractions at the standard ASTM sieves

As regards the characteristics of the pore networks, all concrete samples show a marked prevalence of over-millimetric voids, as demonstrated by the high porosity modulus values (13.01 for BS1, 13.44 for BS2). Furthermore, the voids are highly polydisperse in both samples (figures 4.62, 4.63). The pore size distributions of the over-millimetric voids are markedly articulated, with peaks of distribution comprised between 1 and 3 mm associated to the occurrence of relevant volumetric fractions of over-centimetric voids. The sub-millimetric voids show Gaussian distributions, with a single modal peak at 0.7 mm.

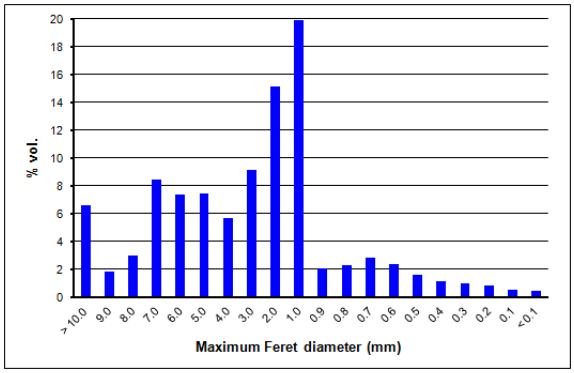

Figure 4.62. Sample BS1, pore size distribution

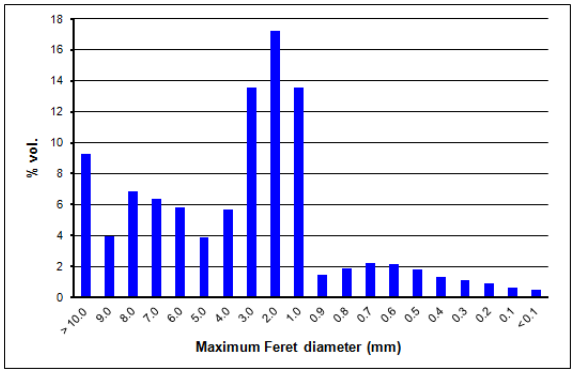

Figure 4.63. Sample BS2, pore size distribution

The main features of the aggregate fractions of the lateral walls concretes are reported in table 4.13, while their granulometric curves, compared with the reference Füller & Thompson and Bolomey curves, and the retained fractions at the standard ASTM sieves, compared with the reference Bolomey retained fractions, are reported in figures 4.64 and 4.65.

Sample	D_{max} (mm)	Fineness modulus	WMC gravel	RSD-WMC gravel	WMC sand	RSD-WMC sand
BS3	29.40	3.78	0.464	0.251	0.585	0.214
BS4	42.27	4.98	0.349	0.208	0.519	0.241

Table 4.13. Main features of the aggregate fractions of the lateral walls concretes. WMC stands for weighted mean circularity, RSD-WMC stands for relative standard deviation of the weighted mean circularity

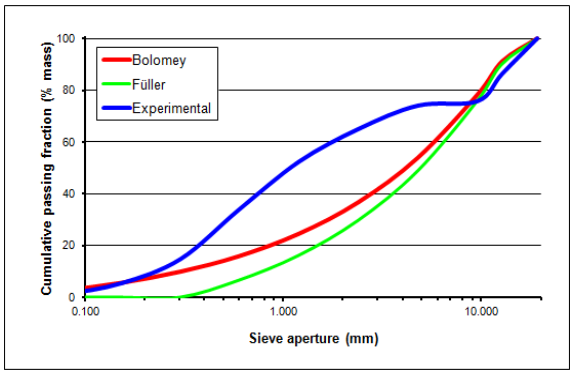

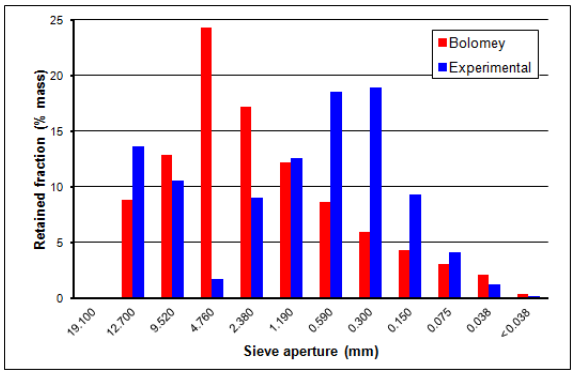

Figure 4.64. Sample BS3: granulometric curve compared with the reference ones (to the left) and retained fractions at the standard ASTM sieves compared with the reference Bolomey ones (to the right)

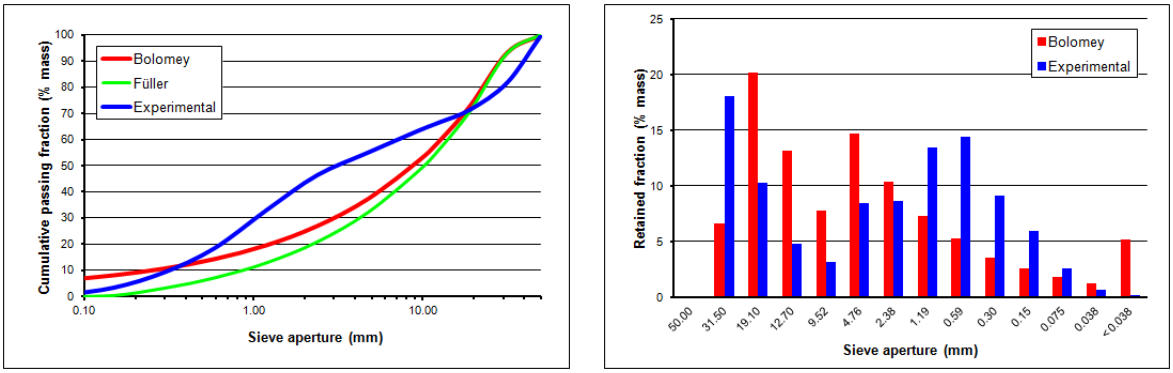

Figure 4.65. Sample BS4: granulometric curve compared with the reference ones (to the left) and retained fractions at the standard ASTM sieves compared with the reference Bolomey ones (to the right)

The characteristics of the aggregate fractions confirm the marked segregation phenomena on the central wall. The lower portions are constituted by an inert fraction with D_{max} of 42.27 mm and fineness modulus of 4.98, while the values are significantly lower in the higher portions (29.40 and 3.78, respectively). Generally, higher ratios of fineness modulus with respect to the concretes of the lateral walls indicate the coarser nature of the inert fraction utilized for the manufacture of the central walls concretes. Furthermore, circularity values are higher than those of the lateral walls concretes, indicating the utilization of more spherical aggregates. As regards the granulometric distributions, they strongly differ from the reference ones, due to a strong enrichment in coarse and medium sands associated to a depletion in medium and fine gravels for both samples, and also to a marked enrichment in coarse gravel for the concrete sample of the lower portion of the wall, due to the previously mentioned accumulation of coarse aggregate related to the segregation phenomena. The high discrepancies from the reference Bolomey curves are confirmed by the regression plots between experimental and Bolomey cumulative passing fractions (figures 4.66, 4.67), showing high standard errors (13.13 for BS3, 10.06 for BS4) and low coefficients of determination (0.885 for BS3, 0.919 for BS4).

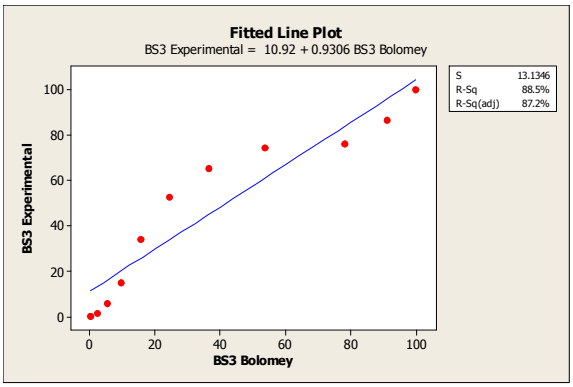

Figure 4.66. Sample BS3, relation between experimental and Bolomey cumulative passing fractions at the standard ASTM sieves

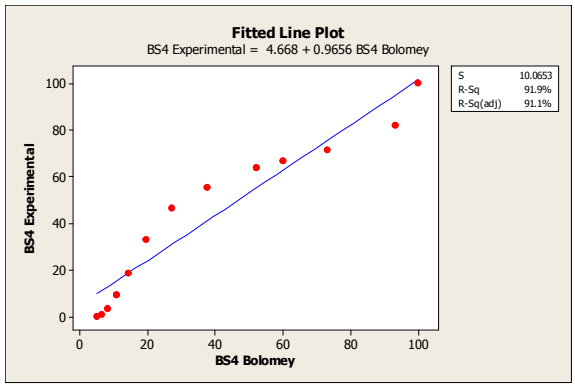

Figure 4.67. Sample BS4, relation between experimental and Bolomey cumulative passing fractions at the standard ASTM sieves

As regards the characteristics of the pore networks, all concrete samples show a marked prevalence of over-millimetric voids, as demonstrated by the high porosity modulus values (13.00 for BS3, 12.33 for BS4). Furthermore, the voids are highly polydisperse in both samples (figures 4.68, 4.69). The pore size distributions of the over-millimetric voids are markedly articulated, with peaks of distribution comprised between 1 and 3 mm associated to the occurrence of relevant volumetric fractions of voids greater than 8 mm. The sub-millimetric voids are more homogeneously distributed, with maxima of distribution at 0.6-0.7 mm.

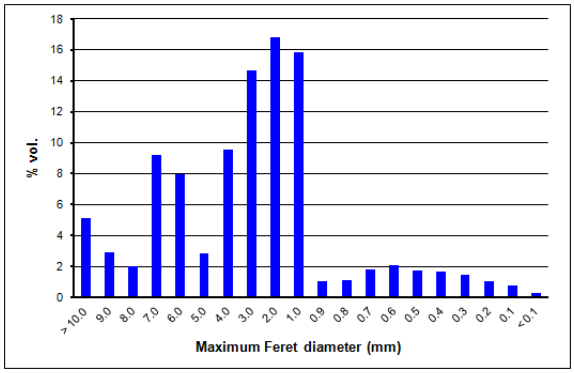

Figure 4.68. Sample BS3, pore size distribution

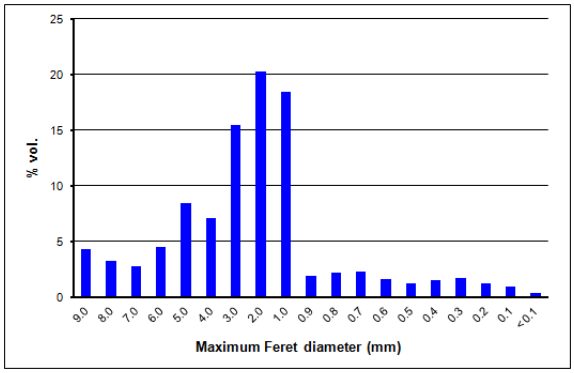

Figure 4.69. Sample BS4, pore size distribution

The main features of the aggregate fraction of BV1 sample, relative to the concrete vaulted slab, are reported in table 4.14, while its granulometric curve, compared with the reference Füller & Thompson and Bolomey curves, and the retained fractions at the standard ASTM sieves, compared with the reference Bolomey retained fractions, are reported in figure 4.70.

Sample	D_{max} (mm)	Fineness modulus	WMC gravel	RSD-WMC gravel	WMC sand	RSD-WMC sand
BV1	13.89	2.68	0.311	0.292	0.578	0.236

Table 4.14. Main features of the aggregate fraction of BV1 sample. WMC stands for weighted mean circularity, RSD-WMC stands for relative standard deviation of the weighted mean circularity

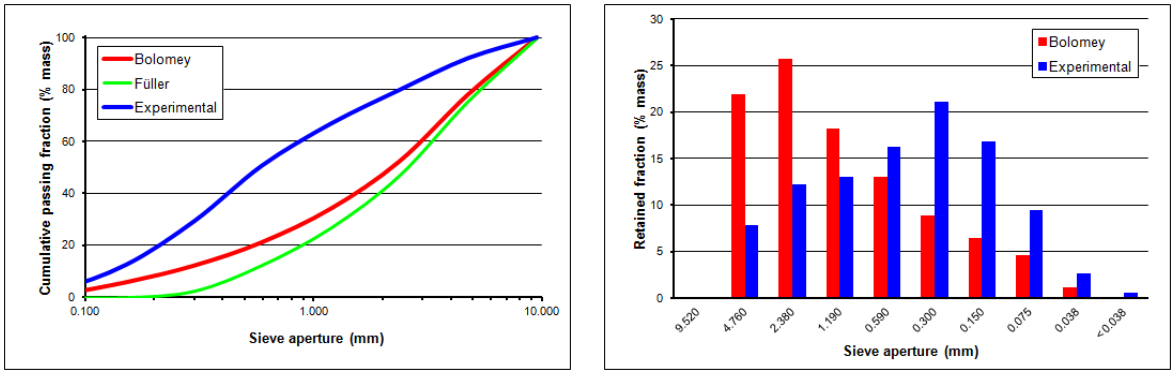

Figure 4.70. Sample BV1: granulometric curve compared with the reference ones (to the left) and retained fractions at the standard ASTM sieves compared with the reference Bolomey ones (to the right)

The inert fraction of the sample is characterized by a marked fineness, as indicated by the low D_{max} of 13.89 and by the fineness modulus value (2.68). Circularity values indicate the utilization of gravels of medium-low sphericity and sands of high sphericity. As regards the granulometric distribution, it strongly differs from the reference ones, being unimodal with peak of distribution in the class of the medium sands, markedly enriched in fine aggregate and significantly depleted in gravel fraction. The high discrepancy from the reference Bolomey curve is confirmed by the regression plot between experimental and Bolomey cumulative passing fractions (figure 4.71), showing a high standard error and a low coefficient of determination (13.91 and 0.886, respectively).

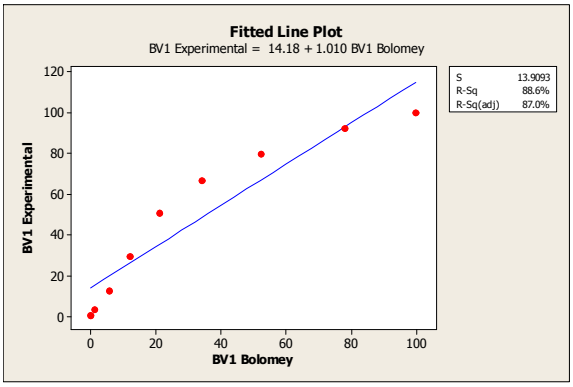

Figure 4.71. Sample BV1, relation between experimental and Bolomey cumulative passing fractions at the standard ASTM sieves

As regards the characteristics of the pore network, the sample shows a marked prevalence of over-millimetric voids, but with a more reduced polydispersity with respect to the concretes of the walls, as demonstrated by the absence of voids with maximum dimensions larger than 5 mm and by the lower value of porosity modulus (10.79). The pore size distribution of the over-millimetric voids is characterized by a peak of distribution at 1 mm (figure 4.72), while the sub-millimetric voids are characterized by a Gaussian distribution with modal peak at 0.5 mm.

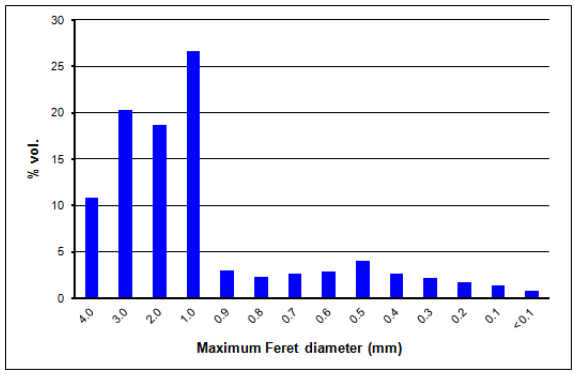

Figure 4.72. Sample BV1, pore size distribution

The main features of the aggregate fractions of the stairway concretes are reported in table 4.15, while their granulometric curves, compared with the reference Füller & Thompson and Bolomey curves, and the retained fractions at the standard ASTM sieves, compared with the reference Bolomey retained fractions, are reported in figures 4.73 and 4.74.

Sample	**D_{max} (mm)**	**Fineness modulus**	**WMC gravel**	**RSD-WMC gravel**	**WMC sand**	**RSD-WMC sand**
BT1	18.58	3.40	0.270	0.299	0.583	0.182
BG1	19.03	3.41	0.276	0.296	0.591	0.188

Table 4.15. Main features of the aggregate fractions of the stairway concretes. WMC stands for weighted mean circularity, RSD-WMC stands for relative standard deviation of the weighted mean circularity

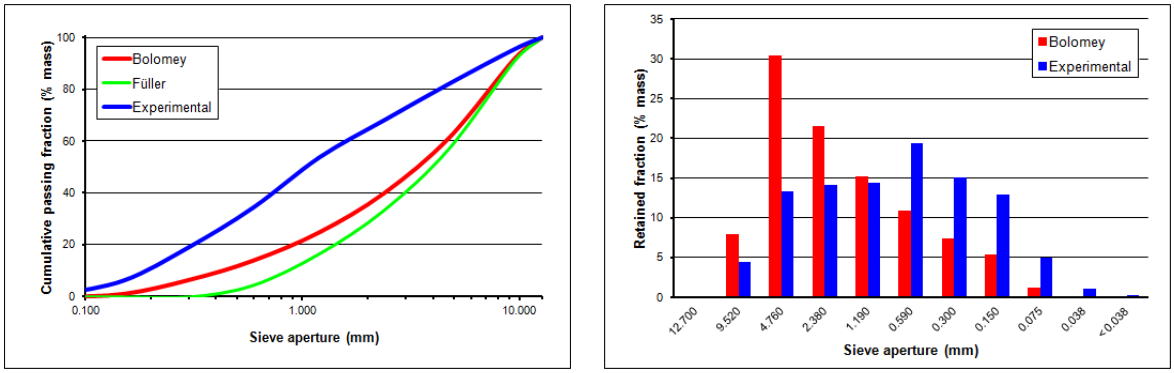

Figure 4.73. Sample BT1: granulometric curve compared with the reference ones (to the left) and retained fractions at the standard ASTM sieves compared with the reference Bolomey ones (to the right)

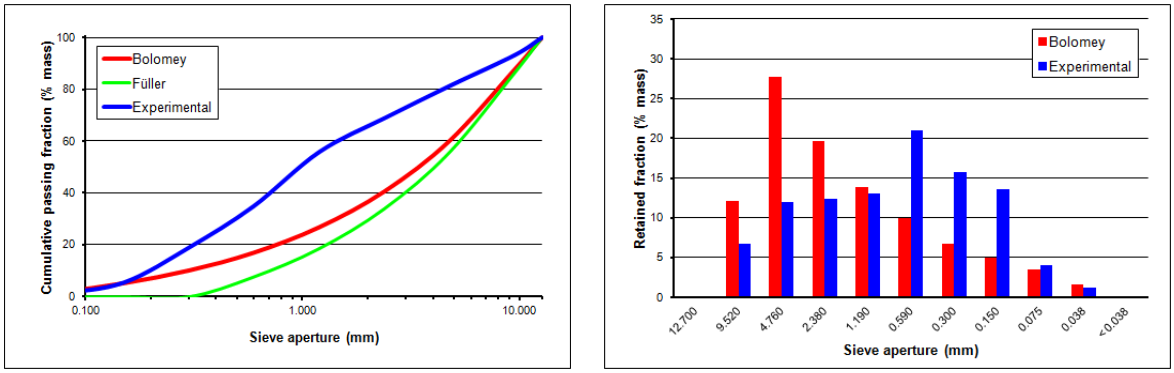

Figure 4.74. Sample BG1: granulometric curve compared with the reference ones (to the left) and retained fractions at the standard ASTM sieves compared with the reference Bolomey ones (to the right)

The inert fraction of the sample is characterized by a fineness in between the ones of the concretes of the walls and the one of the concrete of the vaulted slab, as indicated by the D_{max} of 18.58-19.03 and by the fineness modulus values (3.40-3.41). Circularity values of the coarse aggregates are low and with a high relative standard deviation, indicating a low mean sphericity, even doe significantly variable. Conversely, circularity values of the sand fractions are higher and with a lower relative standard deviation, highlighting the high and uniform sphericity of the fine aggregate. As regards the granulometric distributions, they are significantly akin to the one of the vaulted slab concretes, apart from the occurrence of higher amounts of medium gravels. Nevertheless, they still differ strongly from the reference ones, being unimodal with a peak of distribution in the class of the coarse sands, markedly enriched in fine aggregate and significantly depleted in gravel fraction. The high discrepancies from the reference Bolomey curves are confirmed by the regression plots between experimental and Bolomey cumulative passing fractions (figures 4.75, 4.76),

showing high standard errors (12.23 for BT1, 12.70 for BG1) and low coefficients of determination (0.913 for BT1, 0.905 for BG1).

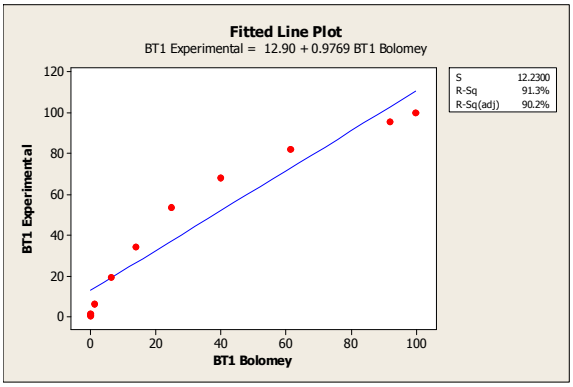

Figure 4.75. Sample BT1, relation between experimental and Bolomey cumulative passing fractions at the standard ASTM sieves

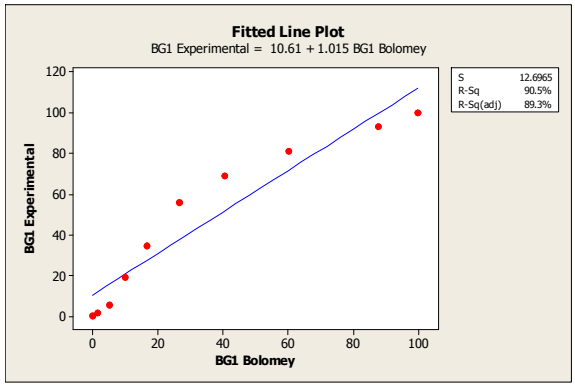

Figure 4.76. Sample BG1, relation between experimental and Bolomey cumulative passing fractions at the standard ASTM sieves

As regards the characteristics of the pore network, the samples show a marked prevalence of over-millimetric voids, with a greater polydispersity with respect to the concretes of the walls, as demonstrated by the presence of voids with maximum dimensions of 5-6 mm and by the higher values of porosity modulus (10.86 for BT1, 10.89 for BG1). The pore size distribution of the over-millimetric voids is characterized by a peak of distribution at 1 mm, but also by significant occurrences of voids with greater maximum dimensions (figures 4.77, 4.78). The sub-millimetric voids are characterized by distributions comparable to Gaussian ones, with a modal peak at 0.3 mm.

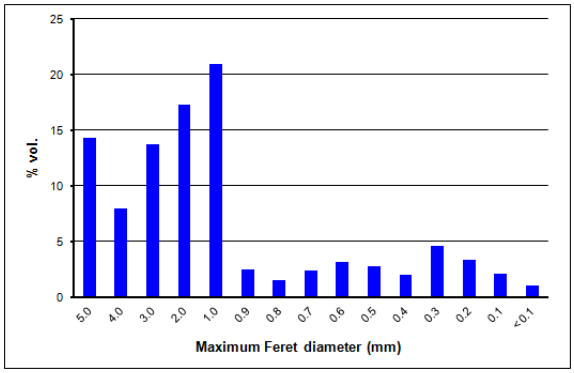

Figure 4.77. Sample BT1, pore size distribution

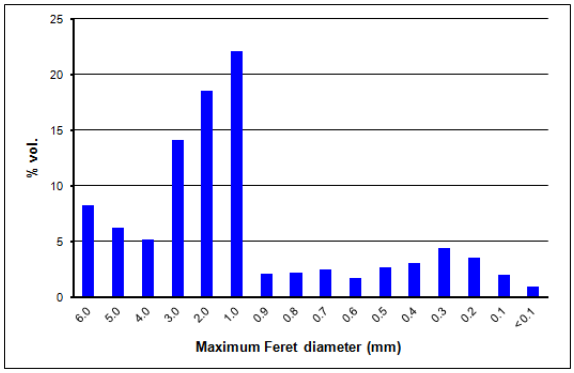

Figure 4.78. Sample BG1, pore size distribution

4.3.4 Ex-Agrimont Area, C3 building

The mix designs characteristics of the analyzed concrete samples, as determined by the image analysis protocol, are reported in table 4.16. The cement and aggregate contents in the original mixes, expressed in Kg/m^3, are reported, together with the water/cement (w/c) ratio, the cement/aggregate (c/a) ratio and the volumetric percentages of voids and pores in the hardened concretes.

Sample	Cement (kg/m^3)	w/c ratio	c/a ratio	Gravel (kg/m^3)	Sand (Kg/m^3)	Voids (% vol.)	Pores (% vol.)
MC1	335.81	0.59	0.18	1221.47	663.84	0.8	8.4
MC2	316.90	0.55	0.16	1376.70	549.80	1.3	7.3
MC3	358.04	0.69	0.21	1384.43	358.41	2	10.9

Table 4.16. Mix designs of the C3 building of the Ex-Agrimont Area concretes

The mix designs, despite being generally accurate and typical of standard and high performance structural concretes, show significant variations, indicating not strictly standardized production processes in the prefabrication plant.

Cement dosages are always higher than 300 kg/m^3, but significantly variable in the three samples. Furthermore, a direct correlation between cement dosage and w/c ratio is observable, confirming the hypothesis of water addition in the mixtures when prepared with higher cement contents, in order to reduce the viscosity of the pastes and to maintain the consistency class of the conglomerate. These variations strongly influenced the overall degree of micro-nanoporosity of the materials, and consequently their mechanical properties: MC2 sample, despite being characterized by the lowest cement dosage, is characterized by the highest compressive strength, owing to the greater overall density of the conglomerate related to the low w/c ratio. On the contrary, MC3 sample shows the lowest compressive strength despite the highest cement dosage, due to the excessive w/c ratio.

A variability in relative proportions between gravel and sand contents is also observable, even though all concretes were manufactured with highly predominant coarse aggregate fractions. In particular, MC3 sample shows a significant gravel over-dosage.

Finally, the volumetric percentages of macroporosity are extremely low in all samples, always below 2%. This indicates proper casting, compaction and homogenization procedures of the fresh conglomerates, surely favored by the prefabrication process. The

slightly higher degree of macroporosity of MC3 sample may be related both to the excessive w/c ratio, and to the gravel over-dosage, which favored the formation of interfacial voids near the coarse aggregate particles.

The main features of the aggregate fractions of the C3 building concretes are reported in table 4.17.

Sample	**D_{max} (mm)**	**Fineness modulus**	**WMC gravel**	**RSD-WMC gravel**	**WMC sand**	**RSD-WMC sand**
MC1	17.94	4.36	0.389	0.308	0.579	0.224
MC2	20.76	4.71	0.405	0.307	0.587	0.209
MC3	18.76	4.85	0.518	0.279	0.589	0.214

Table 4.17. Main features of the aggregate fractions of the C3 building concretes. WMC stands for weighted mean circularity, RSD-WMC stands for relative standard deviation of the weighted mean circularity

The samples are characterized by uniform D_{max} values. The fineness modulus values clearly indicate the prevalence of coarse aggregate over sand fraction, as all are over 4 despite the low maximum dimensions of the inert fraction. Furthermore, all materials are manufactured with sands of medium-high sphericity, as indicated by the similar weighted mean circularity values. Despite these common characteristics, the relative proportions of the aggregate fractions and the shapes of the coarse aggregates differentiate the three concretes. MC1 sample is characterized by a higher amount of fines with respect to the other two samples, as indicated by the lower fineness modulus. Furthermore, MC3 sample is manufactured with gravels characterized by higher and more regular sphericity values with respect to the other samples, as indicated by the weighted mean circularity values and by their relative standard deviation.

As regards the granulometric distributions, the granulometric curve of MC1 sample shows an extremely good correspondence with the reference Bolomey curve, apart from slight discrepancies due to a limited enrichment in gravel at the coarser granulometries (figure 4.79). Nevertheless, the curve at these granulometry values is strictly affine to the reference Füller & Thompson curve. Furthermore, differences from the reference Bolomey curve in the fine aggregate fraction are due to slight enrichments in coarse and medium sand.

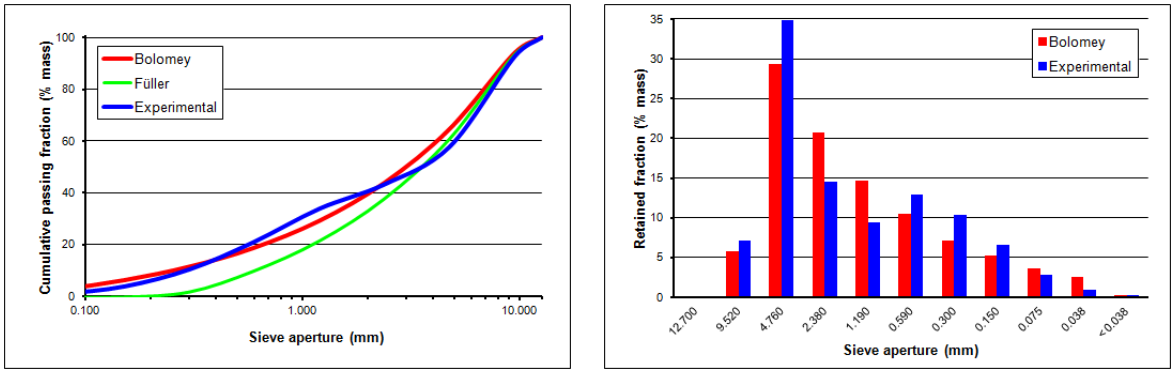

Figure 4.79. Sample MC1: granulometric curve compared with the reference ones (to the left) and retained fractions at the standard ASTM sieves compared with the reference Bolomey ones (to the right)

The good correspondence with the reference Bolomey curve is confirmed by the regression plot between experimental and Bolomey cumulative passing fractions (figure 4.80), showing a low standard error and a high coefficient of determination (3.11 and 0.994, respectively).

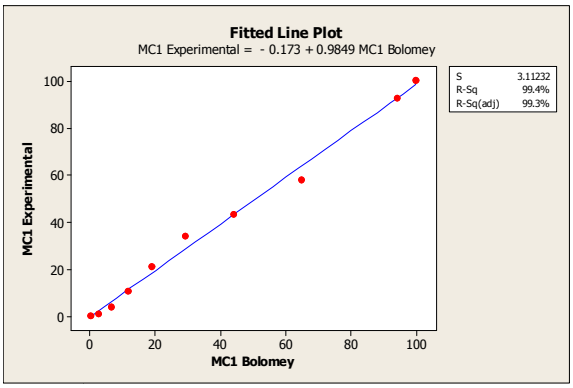

Figure 4.80. Sample MC1, relation between experimental and Bolomey cumulative passing fractions at the standard ASTM sieves

The granulometric distributions of MC2 and MC3 samples are similar to the one observed for MC1 sample, with affinities to the reference Füller & Thompson curves at the coarser granulometries and to the Bolomey curves at the finer ones (figures 4.81, 4.82). The correspondence with the reference Bolomey curve in the fine aggregate is almost perfect for MC3 sample. Nevertheless, higher overall discrepancies are observable, due to more significant enrichments in fine gravel with respect to MC1, in particular for MC3 sample. These experimental evidences are confirmed by the regression plots between experimental and Bolomey cumulative passing fractions (figures 4.83, 4.84), showing higher standard

errors (4.55 for MC2, 5.40 for MC3) and lower coefficients of determination (0.985 for MC2, 0.981 for MC3).

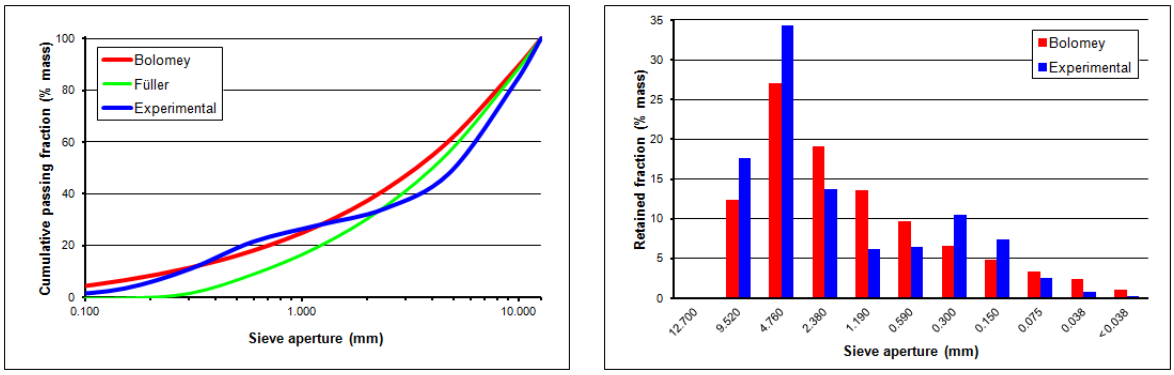

Figure 4.81. Sample MC2: granulometric curve compared with the reference ones (to the left) and retained fractions at the standard ASTM sieves compared with the reference Bolomey ones (to the right)

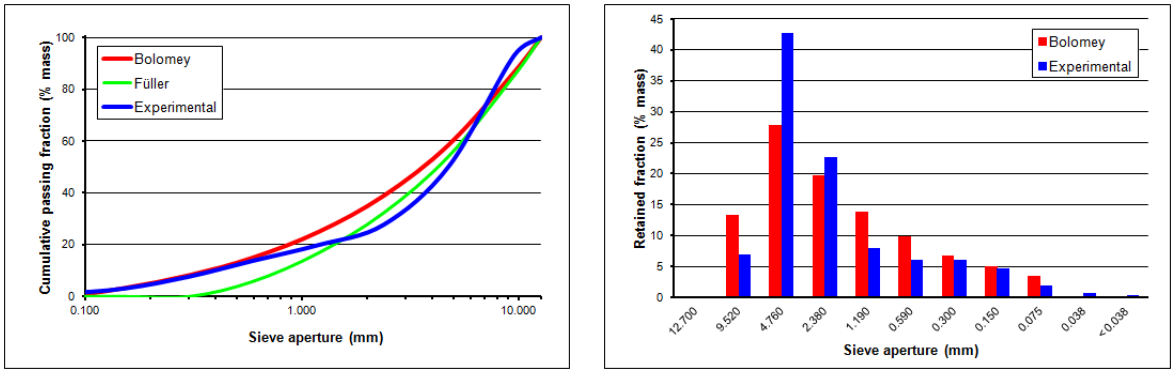

Figure 4.82. Sample MC3: granulometric curve compared with the reference ones (to the left) and retained fractions at the standard ASTM sieves compared with the reference Bolomey ones (to the right)

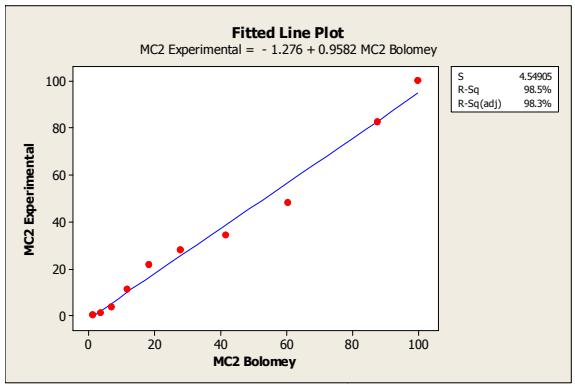

Figure 4.83. Sample MC2, relation between experimental and Bolomey cumulative passing fractions at the standard ASTM sieves

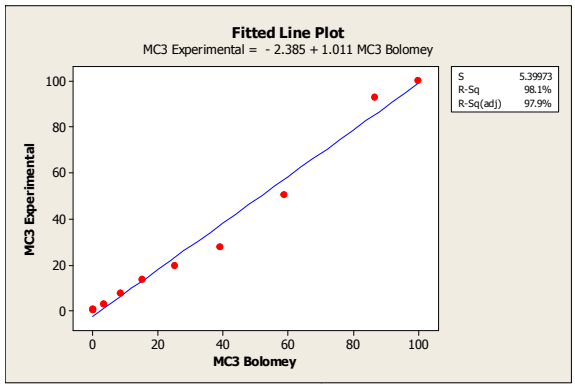

Figure 4.84. Sample MC3, relation between experimental and Bolomey cumulative passing fractions at the standard ASTM sieves

As regards the characteristics of the pore network, MC1 and MC2 samples show a narrow pore size distribution, equally subdivided between over- and sub-millimetric voids, with porosity modulus values of 7.79 for MC2 and of 8.52 for MC2. The over-millimetric voids have a strong peak of distribution at 1 mm, while the sub-millimetric voids are more disperse, with a peak of distribution at 0.1 mm (figures 4.85, 4.86).

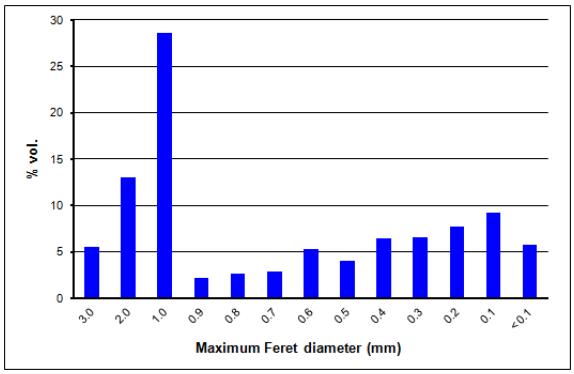

Figure 4.85. Sample MC1, pore size distribution

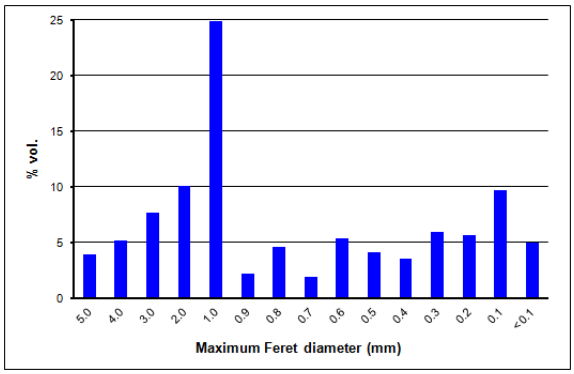

Figure 4.86. Sample MC2, pore size distribution

Higher polydispersity on the dimensions of voids is observable in MC3 sample, with frequent occurrence of over-centimetric voids. Consequently, a volumetric prevalence of over-millimetric voids is observable, as indicated by the higher porosity modulus (11.43). The over-millimetric voids are characterized by an articulated pore size distribution, with peaks of distribution between 2 and 3 mm (figure 4.87). The sub-millimetric voids have a Gaussian distribution, with modal peak at 0.2 mm.

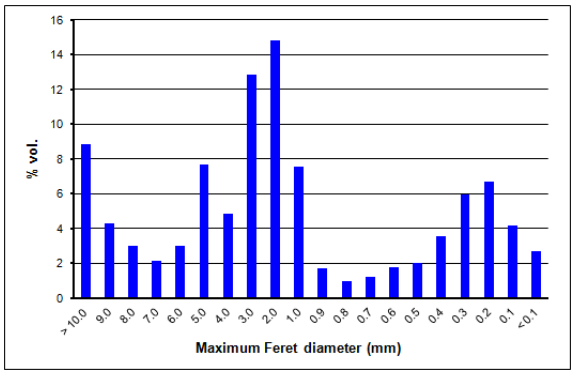

Figure 4.87. Sample MC3, pore size distribution

4.3.5 Ex-Zweifel Embroidery Plant

The mix designs characteristics of the analyzed concrete samples, as determined by the image analysis protocol, are reported in table 4.18. The cement and aggregate contents in the original mixes, expressed in Kg/m^3, are reported, together with the water/cement (w/c) ratio, the cement/aggregate (c/a) ratio and the volumetric percentages of voids and pores in the hardened concretes.

Sample	Cement (kg/m^3)	w/c ratio	c/a ratio	Gravel (kg/m^3)	Sand (Kg/m^3)	Voids (% vol.)	Pores (% vol.)
RP1	240.35	0.76	0.12	1385.37	538.05	4.1	8.3
RP2	240.73	0.76	0.12	1373.84	555.36	3.9	8.2
RP3	243.51	0.75	0.13	1366.37	562.25	3.7	8.4
RT1	332.33	0.59	0.18	1295.47	511.13	3.7	8.3
RT2	336.31	0.58	0.19	1280.74	533.66	3.2	8.3
RC1	325.28	0.60	0.18	1508.45	325.52	3.9	8.3
RA1	147.86	0.86	0.08	929.84	930.96	13.9	6.2

Table 4.18. Mix designs of the Ex-Zweifel Embroidery Plant concretes

The characteristics of the mix designs clearly confirm the differences in concretes compositions according to the structural element.

The columns have homogeneous cement dosages, typical of lean structural concretes. Homogenous and markedly high w/c ratios were adopted, probably to raise the consistency class and thus to facilitate casting and homogenization procedures of the fresh conglomerates, which were performed properly, as demonstrated by the medium-low volumetric percentages of macroporosity. On the other hand, the adoption of high w/c ratios did not allow high mechanical strength values. As regards the relative amounts of coarse and fine aggregate fraction, the former is markedly predominant over the latter for all samples.

The mix designs of the beams and the riddle are characterized by higher cement dosages, and by homogeneous and lower w/c ratios, comprised between 0.58 and 0.60. Cement dosage in the riddle is slightly lower than on the beams. As regards the aggregate fractions, the coarse aggregate is still markedly predominant over the fine aggregate. In particular, MC3 sample shows a significant gravel over-dosage. Volumetric percentages of macroporosity are still medium-low, indicating proper casting and compaction procedures

of the fresh conglomerates. The slightly higher degree of macroporosity of RC1 sample may be related to the gravel over-dosage, which favored the formation of interfacial voids near the coarse aggregate particles.

Finally, the concretes of the arches are characterized by extremely poor mix designs. The cement dosage is lower than 150 kg/m^3, and the w/c ratio is significantly high. Furthermore, the aggregate fraction is characterized by a marked over-dosage of sand, associated to a strong depletion in gravel. Consequently, the materials are extremely permeable, with a diffused macroporosity, around 14% over the total volume of the materials. Such inadequate mix design had pernicious effects on the mechanical properties of the materials, and may be considered the main cause of the diffuse structural failure which interested the structure.

The main features of the aggregate fractions of the concrete columns are reported in table 4.19, while their granulometric curves, compared with the reference Füller & Thompson and Bolomey curves, and the retained fractions at the standard ASTM sieves, compared with the reference Bolomey retained fractions, are reported in figures 4.88, 4.89 and 4.90.

Sample	D_{max} (mm)	Fineness modulus	WMC gravel	RSD-WMC gravel	WMC sand	RSD-WMC sand
RP1	27.78	4.94	0.448	0.269	0.563	0.230
RP2	25.56	4.85	0.447	0.219	0.575	0.207
RP3	24.76	4.86	0.434	0.249	0.574	0.198

Table 4.19. Main features of the aggregate fractions of the concrete columns. WMC stands for weighted mean circularity, RSD-WMC stands for relative standard deviation of the weighted mean circularity

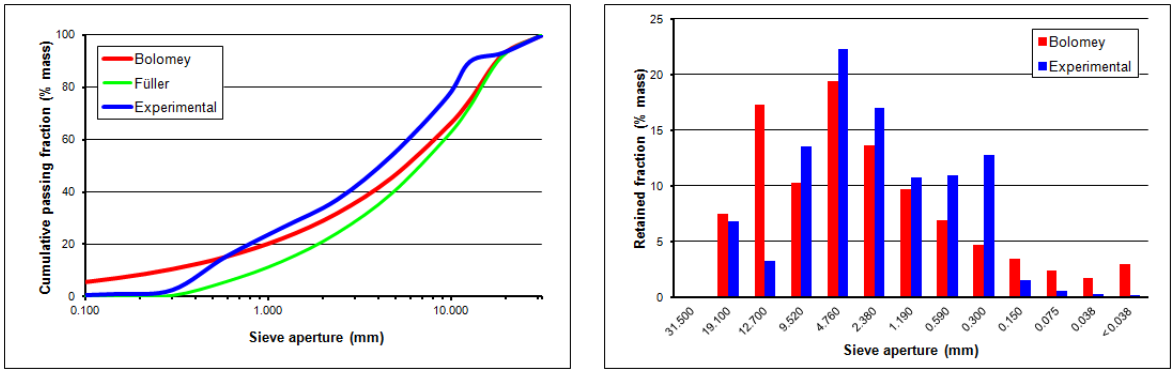

Figure 4.88. Sample RP1: granulometric curve compared with the reference ones (to the left) and retained fractions at the standard ASTM sieves compared with the reference Bolomey ones (to the right)

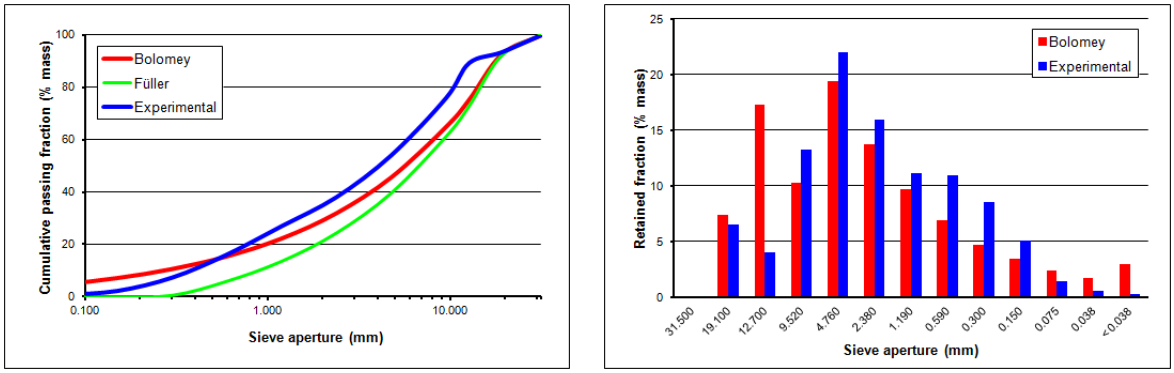

Figure 4.89. Sample RP2: granulometric curve compared with the reference ones (to the left) and retained fractions at the standard ASTM sieves compared with the reference Bolomey ones (to the right)

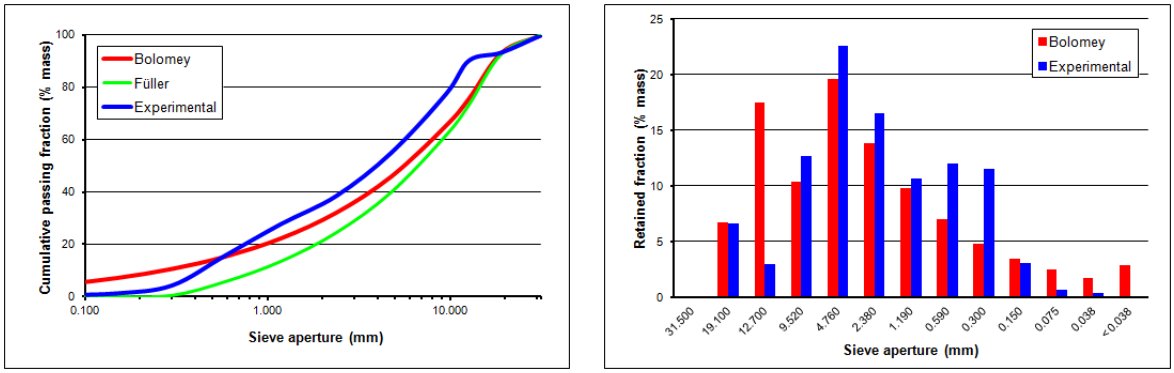

Figure 4.90. Sample RP3: granulometric curve compared with the reference ones (to the left) and retained fractions at the standard ASTM sieves compared with the reference Bolomey ones (to the right)

Experimental data highlighted the similar characteristics of the aggregate fractions of the concrete columns. In the analyzed samples, the prevalence of coarse aggregate over fine aggregate is indicated by the high fineness modulus values, in particular for RP1 sample, also characterized by the highest D_{max} value.

Circularity values of the coarse aggregates confirmed their general medium-high sphericity. The relative standard deviations of the mean circularity values are higher for RP1 and RP3 samples with respect to RP2, indicating a slightly higher shape homogeneity of the coarse aggregates of the latter. Furthermore, all materials are manufactured with sands of medium-high sphericity, as indicated by the similar weighted mean circularity values.

As for the granulometric distributions, they strongly differ from the reference Füller & Thompson curves. On the contrary, resemblance with the reference Bolomey curves is observable. Nevertheless, as indicated by the retained fractions histograms, discrepancies are observable due to enrichments in coarse and medium sands, associated to significant

depletions in medium gravels. The enrichments in fine aggregate are more limited for RP2 sample, thus showing a better resemblance with the reference Bolomey curve with respect to the other samples. This is confirmed by the regression plots between experimental and Bolomey cumulative passing fractions (figures 4.91, 4.92, 4.93): the standard error and coefficient of determination values are differentiated between the two group of samples, similar for RP1 and RP3 (6.23 and 0.978 for RP1, 6.39 and 0.976 for RP3), more accurate for RP2 (5.66 and 0.981, respectively).

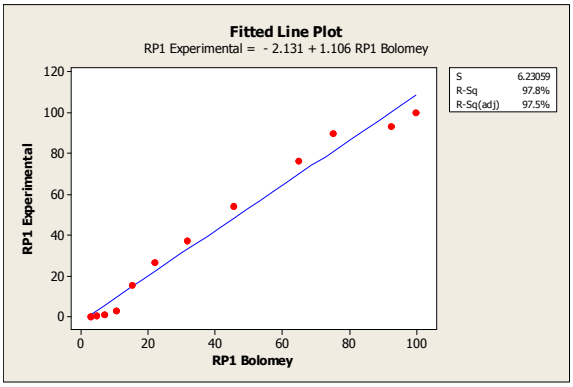

Figure 4.91. Sample RP1, relation between experimental and Bolomey cumulative passing fractions at the standard ASTM sieves

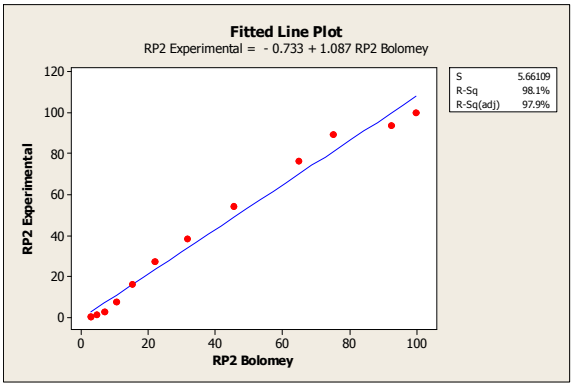

Figure 4.92. Sample RP2, relation between experimental and Bolomey cumulative passing fractions at the standard ASTM sieves

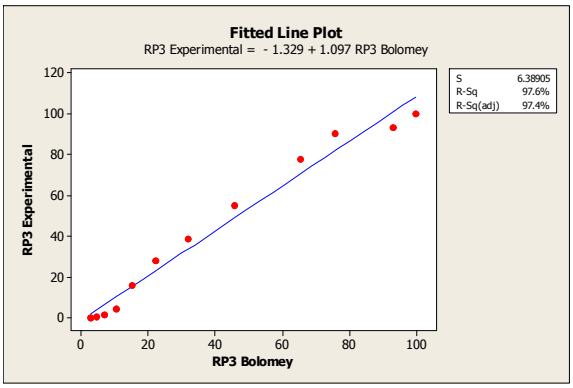

Figure 4.93. Sample RP3, relation between experimental and Bolomey cumulative passing fractions at the standard ASTM sieves

As regards the characteristics of the pore network, slight differences are observable between the samples. RP2 and RP3 are characterized by a volumetric equivalence between over-millimetric and sub-millimetric voids, while the former are slightly prevalent in RP1 sample. Consequently, porosity modulus values are similar for RP2 and RP3 (9.46 and 9.02, respectively), higher for RP1 (10.44). As regards the pore size distributions, they are

markedly polydisperse for RP2 and RP3 sample, as indicated by the presence of voids with maximum dimensions comprised between 9 and 10 mm (figures 4.95, 4.96). The size distribution of the over-millimetric voids is quite articulated, with a maximum of distribution at 1 mm. The sub-millimetric voids have a Gaussian distribution, with modal peak at 0.2 mm. RP1 sample has a narrower pore size distribution, with voids of maximum dimensions comprised between 6 and 7 mm (figure 4.94). The over-millimetric voids have maxima of distribution between 1 and 3 mm, while the sub-millimetric voids are more homogeneously distributed, with peaks between 0.1 and 0.3 mm.

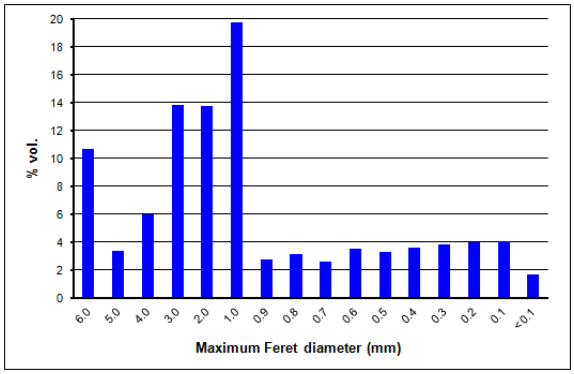

Figure 4.94. Sample RP1, pore size distribution

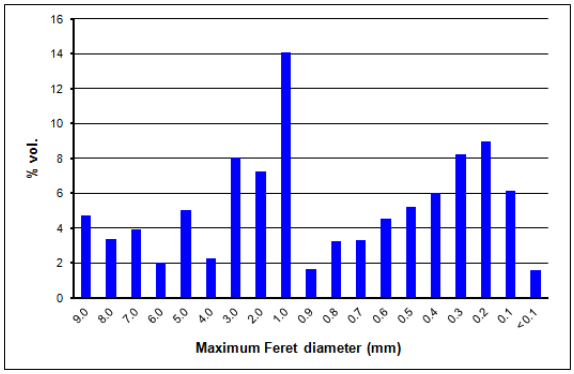

Figure 4.95. Sample RP2, pore size distribution

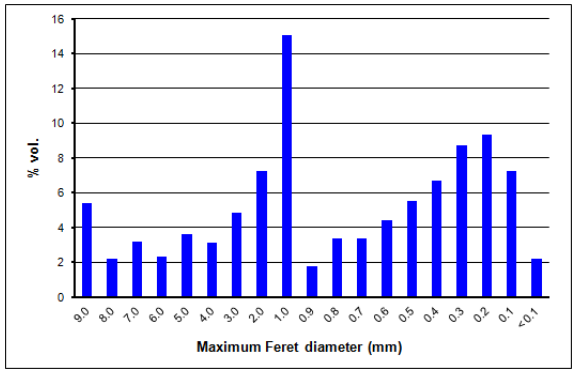

Figure 4.96. Sample RP3, pore size distribution

The main features of the aggregate fractions of the concrete beams and riddle are reported in table 4.20.

Sample	D_{max} (mm)	Fineness modulus	WMC gravel	RSD-WMC gravel	WMC sand	RSD-WMC sand
RT1	29.27	4.90	0.431	0.223	0.594	0.187
RT2	30.84	4.89	0.409	0.283	0.571	0.242
RC1	21.71	5.29	0.398	0.233	0.505	0.274

Table 4.20. Main features of the aggregate fractions of the concrete beams and riddle. WMC stands for weighted mean circularity, RSD-WMC stands for relative standard deviation of the weighted mean circularity

The analytical results confirm significant differences between the concretes of the beams and the riddle. RT1 and RT2 samples are characterized by similar D_{max} values. The high fineness modulus values clearly indicate the prevalence of coarse aggregate over sand fraction. Furthermore, all materials are manufactured with gravels of medium-high sphericity and sands of high sphericity, as indicated by the similar weighted mean circularity values. The relative standard deviation values are differentiated, being higher for RT2 sample, thus indicating a greater shape heterogeneity with respect to RT1. The characteristics of the granulometric curves and the histograms of the retained fractions confirm the similarities between the aggregates of the two concrete slab samples (figures 4.97, 4.98): they both differ strongly from the reference Füller & Thompson curves. On the contrary, a good resemblance with the reference Bolomey curves is observable, higher than the one observed for the concrete columns. Nevertheless, as indicated by the retained fractions histograms, discrepancies are observable due to enrichments in medium and fine sands, associated to depletions in medium gravels.

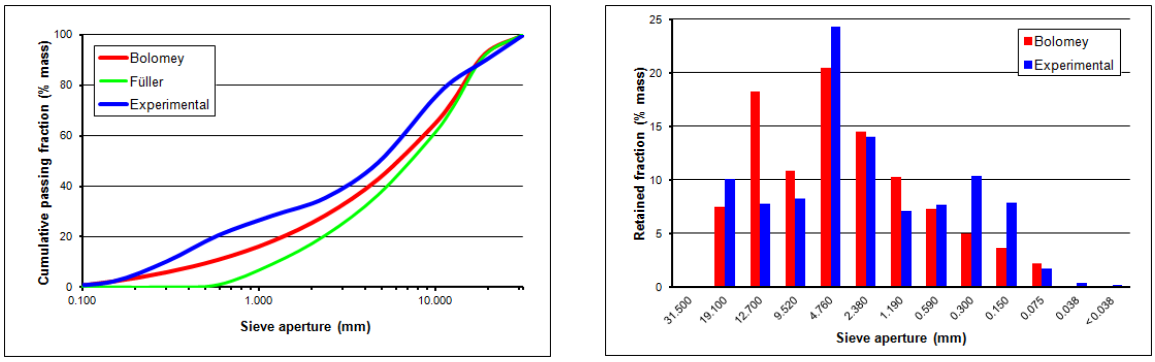

Figure 4.97. Sample RT1: granulometric curve compared with the reference ones (to the left) and retained fractions at the standard ASTM sieves compared with the reference Bolomey ones (to the right)

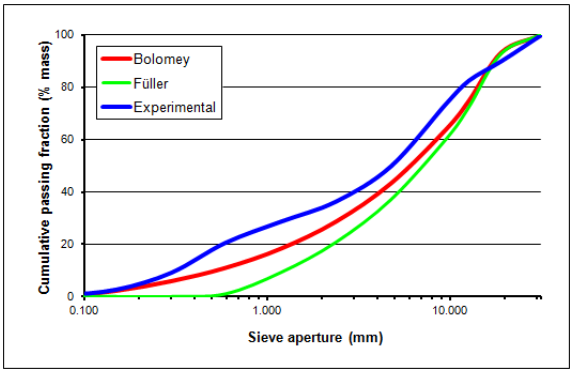

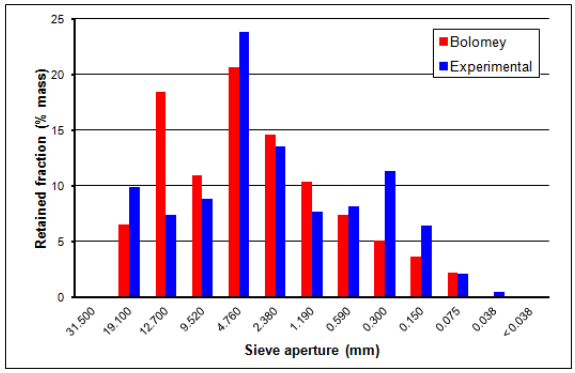

Figure 4.98. Sample RT2: granulometric curve compared with the reference ones (to the left) and retained fractions at the standard ASTM sieves compared with the reference Bolomey ones (to the right)

Higher affinity with the reference Bolomey curves with respect to the concretes of the columns is confirmed by the regression plots between experimental and Bolomey cumulative passing fractions (figures 4.99, 4.100), showing lower standard errors (4.91 for RT1, 4.94 for RT2) and higher coefficients of determination (0.984 for both RT1 and RT2).

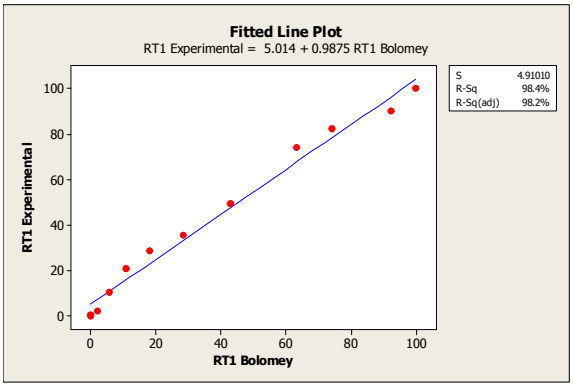

Figure 4.99. Sample RT1, relation between experimental and Bolomey cumulative passing fractions at the standard ASTM sieves

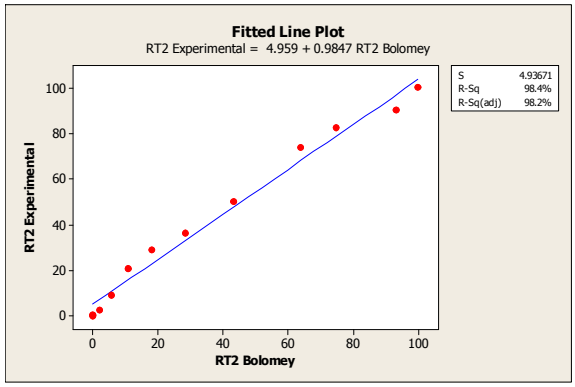

Figure 4.100. Sample RT2, relation between experimental and Bolomey cumulative passing fractions at the standard ASTM sieves

RC1 is characterized by significantly lower D_{max} values with respect to RT1 and RT2 samples. Despite this, the fineness modulus is higher, indicating greater occurrence of coarse aggregate with respect to the other samples. Furthermore, sphericity values of both coarse and fine aggregates are lower, as indicated by the weighted mean circularities. As regards the granulometric distribution, the granulometric curve shows an extremely good correspondence with the reference Bolomey curve, apart from discrepancies due to a

significant enrichment in fine gravels (figure 4.101). Nevertheless, the curve at these granulometry values is strictly affine to the reference Füller & Thompson curve.

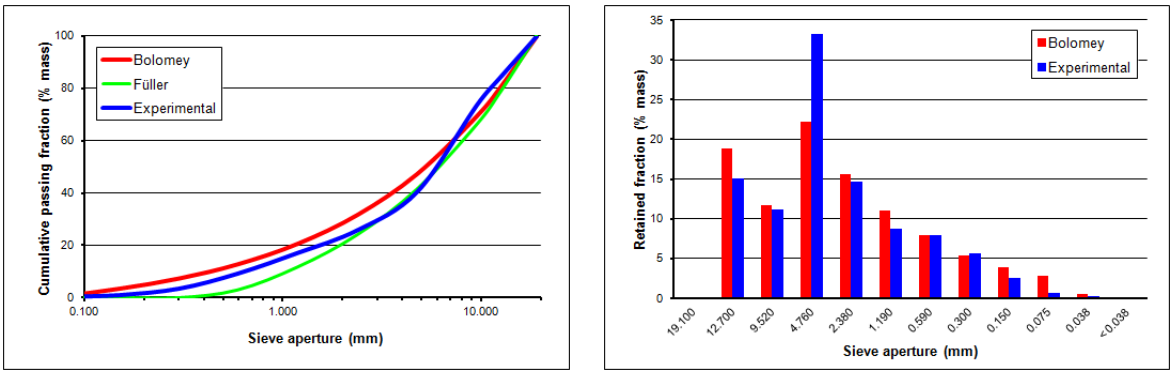

Figure 4.101. Sample RC1: granulometric curve compared with the reference ones (to the left) and retained fractions at the standard ASTM sieves compared with the reference Bolomey ones (to the right)

The higher affinity with the reference Bolomey curve with respect to the other samples is confirmed by the regression plot between experimental and Bolomey cumulative passing fractions (figure 4.102), showing a lower standard error and a higher coefficient of determination (3.38 and 0.993, respectively).

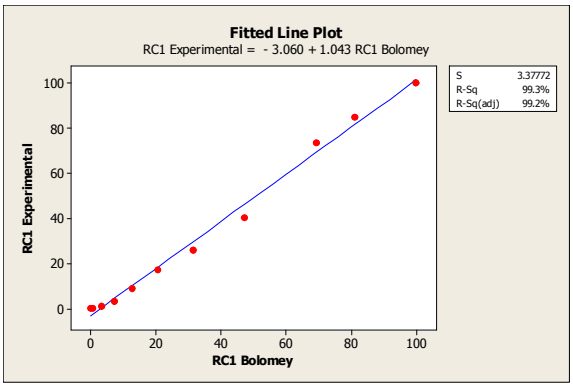

Figure 4.102. Sample RC1, relation between experimental and Bolomey cumulative passing fractions at the standard ASTM sieves

As regards the characteristics of the pore network, slight differences are observable between the samples. Beams concretes are characterized by a volumetric equivalence between over-millimetric and sub-millimetric voids, while the former are slightly prevalent in RC1 sample. Consequently, porosity modulus values are similar for RT1 and RT2 (8.11 and 7.84, respectively), higher for RC1 (10.26). Furthermore beams concretes are characterized by narrow pore size distributions, with voids of maximum dimensions

comprised between 4 and 6 mm (figures 4.103, 4.104). The size distribution of the over-millimetric voids has a maximum of distribution at 1 mm for both the samples. The sub-millimetric voids have a Gaussian distribution, with modal peak at 0.2 mm. RC1 sample is characterized by a strongly polydisperse pore size distribution, with a significant occurrence of over-centimetric voids, despite the occurrence of a maximum of distribution at 1 mm (figure 4.105). Similarly to the beams concretes, the sub-millimetric voids have a Gaussian distribution, with modal peak at 0.2 mm.

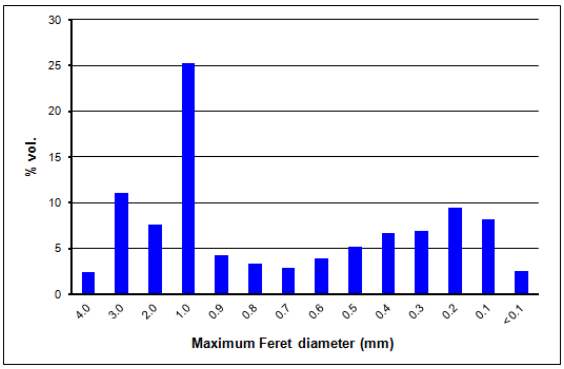

Figure 4.103. Sample RT1, pore size distribution

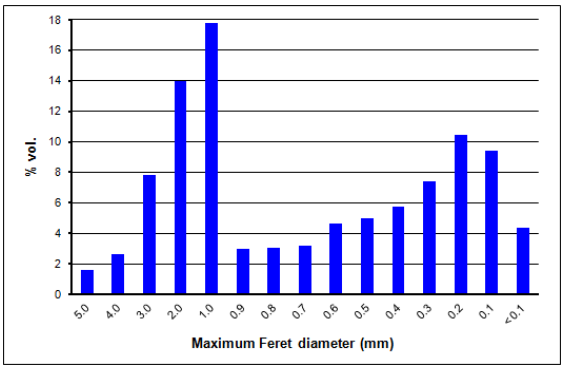

Figure 4.104. Sample RT2, pore size distribution

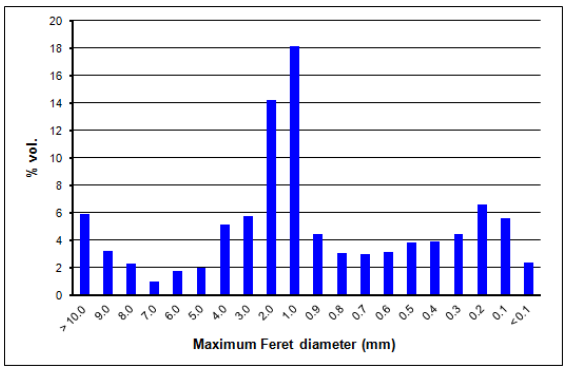

Figure 4.105. Sample RC1, pore size distribution

The main features of the aggregate fraction of RA1 sample are reported in table 4.21, while its granulometric curve, compared with the reference Füller & Thompson and Bolomey curves, and the retained fractions at the standard ASTM sieves, compared with the reference Bolomey retained fractions, are reported in figure 4.106.

Sample	D_{max} (mm)	Fineness modulus	WMC gravel	RSD-WMC gravel	WMC sand	RSD-WMC sand
RA1	23.54	4.07	0.325	0.239	0.581	0.205

Table 4.21. Main features of the aggregate fractions of RA1 sample. WMC stands for weighted mean circularity, RSD-WMC stands for relative standard deviation of the weighted mean circularity

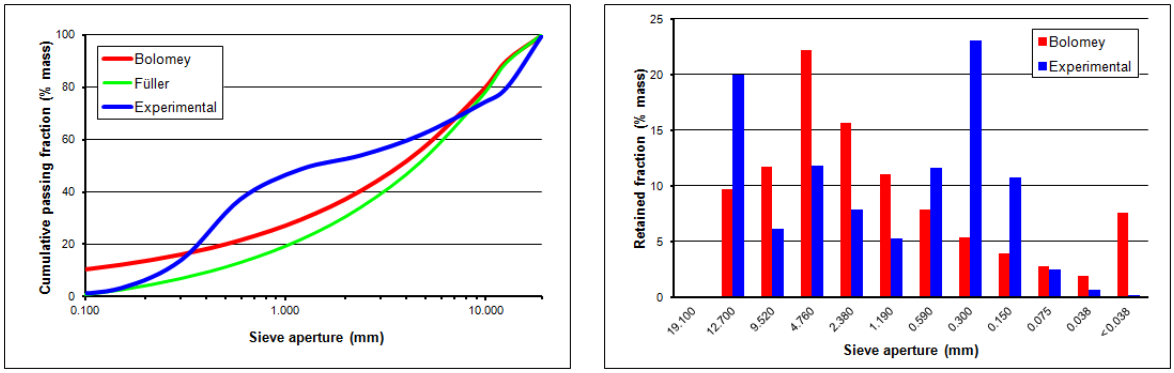

Figure 4.106. Sample RA1: granulometric curve compared with the reference ones (to the left) and retained fractions at the standard ASTM sieves compared with the reference Bolomey ones (to the right)

The characteristics of the aggregate fraction confirm the marked inadequacy of the mix design of the concrete arches. RA1 samples is characterized by a D_{max} of 23.54 mm and by fineness modulus of 4.07, significantly lower than the ones of the other concrete samples, indicating marked over-dosages of fine aggregate. The coarse aggregate is characterized by lower sphericity than the other samples, as indicated by the lower weighted mean circularity values, while the sand fraction is characterized by high sphericity. As regards the granulometric distribution, it strongly differs from the reference ones, due to marked enrichments in fine aggregate, particularly medium sands. Furthermore, the coarse aggregate is significantly enriched in medium gravels, while strong depletions in fine and very fine gravels are observable. The high discrepancy from the reference Bolomey curves is confirmed by the regression plot between experimental and Bolomey cumulative passing fractions (figure 4.107), showing a high standard error and a low coefficient of determination (11.30 and 0.905, respectively).

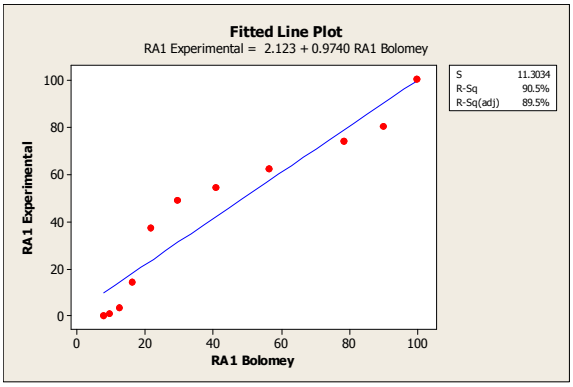

Figure 4.107. Sample RA1, relation between experimental and Bolomey cumulative passing fractions at the standard ASTM sieves

As regards the characteristics of the pore network, the sample shows a marked prevalence of over-millimetric voids, as demonstrated by the high porosity modulus (13.82). Furthermore, the voids are highly polydisperse, with a significant occurrence of over-centimetric voids (figure 4.108). The pore size distribution of the over-millimetric voids is characterized by a bimodal shape, with maxima of distribution at 2 and 8 mm. The sub-millimetric voids are more homogeneously distributed, with maxima of distribution at 0.9 and 0.1 mm.

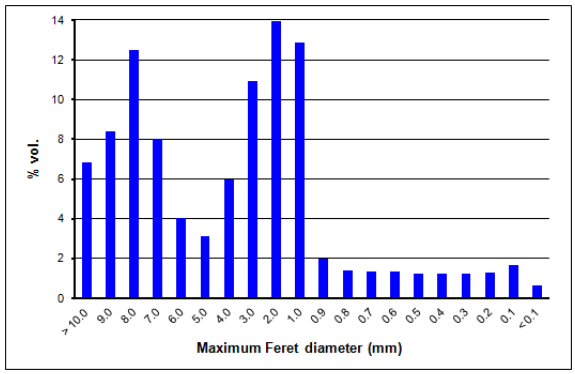

Figure 4.108. Sample RA1, pore size distribution

4.3.6 Ex-Foro Boario

The mix designs characteristics of the analyzed concrete samples, as determined by the image analysis protocol, are reported in table 4.22. The cement and aggregate contents in the original mixes, expressed in Kg/m^3, are reported, together with the water/cement (w/c) ratio, the cement/aggregate (c/a) ratio and the volumetric percentages of voids and pores in the hardened concretes.

Sample	Cement (kg/m^3)	w/c ratio	c/a ratio	Gravel (kg/m^3)	Sand (Kg/m^3)	Voids (% vol.)	Pores (% vol.)
FP1	329.61	0.58	0.17	1178.80	723.50	1.1	8.1
FP2	341.08	0.71	0.19	1068.32	752.88	0.7	10.7

Table 4.22. Mix designs of the Ex-Foro Boario concretes

The mix designs, despite being accurate and typical of standard and high performance structural concretes, show slight variations, indicating not strictly standardized production processes in the concrete mixing plant.

Cement dosages are always higher than 300 kg/m^3, but slightly variable in the two samples. Furthermore, as for the concretes of the C3 building of the Ex-Agrimont Area, it is possible to observe a direct correlation between cement dosage and w/c ratio, confirming the hypothesis of water addition in the mixtures when prepared with higher cement contents, in order to reduce the viscosity of the pastes and to maintain the consistency class of the conglomerate. These variations influenced the overall degree of micro-nanoporosity of the materials, and consequently their mechanical properties: FP1 sample, despite being characterized by the lowest cement dosage, is characterized by the highest compressive strength, thanks to the greater overall density of the conglomerate related to the low w/c ratio.

A slight variability in relative proportions between gravel and sand contents is also observable, even though all concretes were manufactured with predominant coarse aggregate fractions, necessary for the obtaining of granulometric curves in concordance with the reference ones. In particular, FP2 sample shows a limited sand over-dosage.

Finally, the volumetric percentages of macroporosity are extremely low in all samples, always around 1%. This indicates proper casting, compaction and homogenization procedures of the fresh conglomerates, confirming the elevated quality of the materials also as regards the manufacturing process.

The main features of the aggregate fractions of the Ex-Foro Boario concretes are reported in table 4.23.

Sample	**D_{max} (mm)**	**Fineness modulus**	**WMC gravel**	**RSD-WMC gravel**	**WMC sand**	**RSD-WMC sand**
FP1	15.98	4.35	0.415	0.228	0.559	0.216
FP2	15.25	4.20	0.400	0.232	0.547	0.213

Table 4.23. Main features of the aggregate fractions of the Ex-Foro Boario concretes. WMC stands for weighted mean circularity, RSD-WMC stands for relative standard deviation of the weighted mean circularity

The samples are characterized by strictly uniform and reduced D_{max} values. The fineness modulus values clearly indicate the prevalence of coarse aggregate over sand fraction, being all over 4 despite the low maximum dimensions of the inert fraction. The presence of slightly greater amounts of fine aggregate in FP2 sample is confirmed by the lower fineness modulus. Furthermore, the samples are characterized by similar weighted mean

circularities and relative standard deviations, both of the gravel and the sand fraction, indicating the utilization of aggregates of variable sphericity, generally medium-high.

As regards the granulometric distributions, the granulometric curve of FP1 strongly differs from the reference Füller & Thompson curve. On the contrary, it is characterized by an extremely good correspondence with the reference Bolomey curve, apart from slight discrepancies due to limited enrichments in medium and fine sands and in medium gravels (figure 4.109).

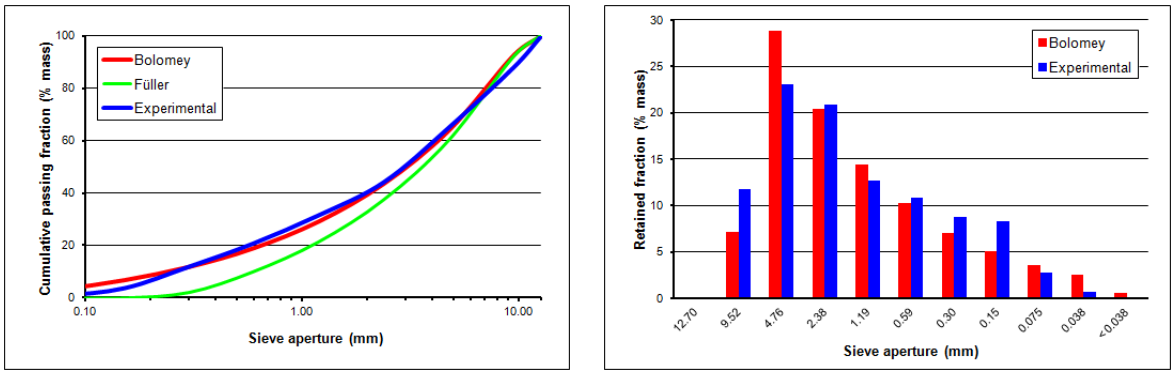

Figure 4.109. Sample FP1: granulometric curve compared with the reference ones (to the left) and retained fractions at the standard ASTM sieves compared with the reference Bolomey ones (to the right)

The affinity with the reference Bolomey curve is confirmed by the regression plot between experimental and Bolomey cumulative passing fractions (figure 4.110), showing low standard error and a high coefficient of determination (2.35 and 0.996, respectively).

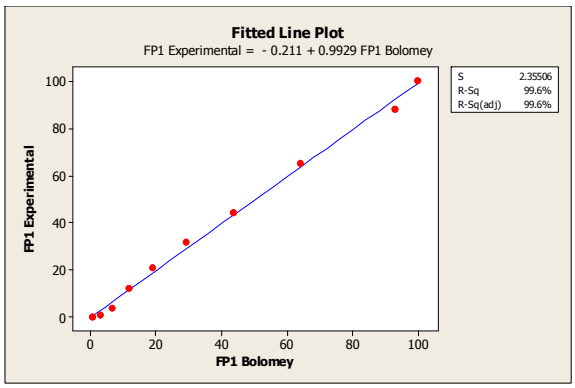

Figure 4.110. Sample FP1, relation between experimental and Bolomey cumulative passing fractions at the standard ASTM sieves

The granulometric distribution of FP2 sample is similar to the one observed for FP1 sample, being markedly affine to the reference Bolomey curve (figure 4.111).

Nevertheless, higher overall discrepancies are observable, due to more significant enrichments in coarse, medium and fine sands with respect to FP1. This experimental evidence is confirmed by the regression plot between experimental and Bolomey cumulative passing fractions (figure 4.112), showing a higher standard error and a lower coefficient of determination (3.51 and 0.992, respectively).

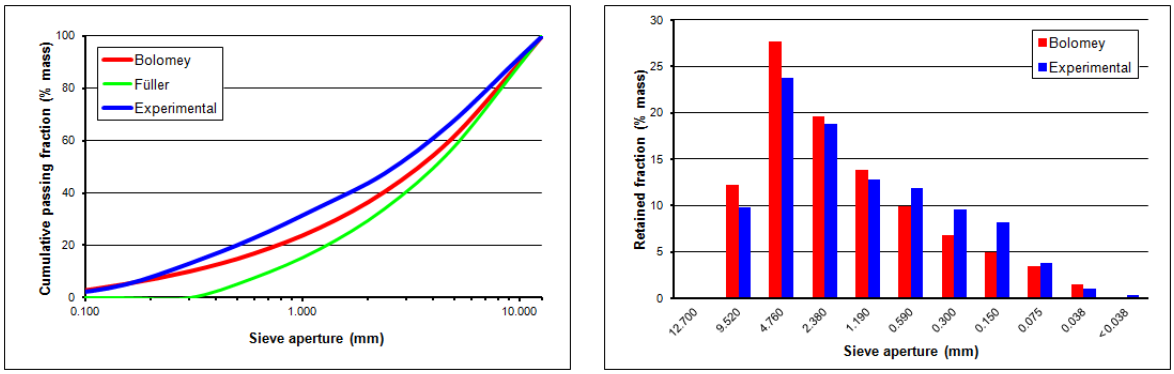

Figure 4.111. Sample FP2: granulometric curve compared with the reference ones (to the left) and retained fractions at the standard ASTM sieves compared with the reference Bolomey ones (to the right)

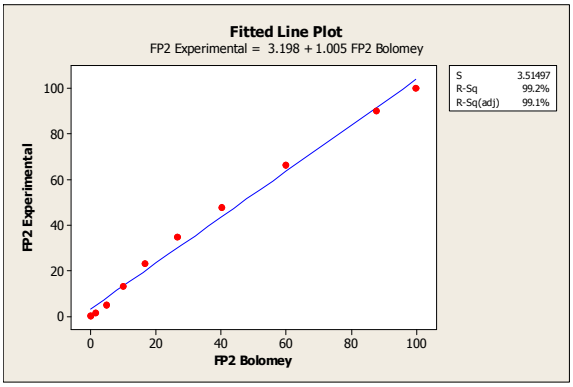

Figure 4.112. Sample FP2, relation between experimental and Bolomey cumulative passing fractions at the standard ASTM sieves

As regards the characteristics of the pore network, both samples are characterized by a substantial volumetric prevalence between over-millimetric and sub-millimetric voids. Nevertheless, FP2 is characterized by a narrower pore size distribution with respect to FP1 (figures 4.113, 4.114). Consequently, the porosity modulus of the former is lower than the one of the latter (7.71 and 8.68, respectively). The pore size distribution of the over-millimetric voids of FP1 is characterized by a bimodal shape, with maxima of distribution at 1 and 6 mm, respectively. On the other hand, the over-millimetric voids of FP2 sample are characterized by dimensions comprised between 1 and 3 mm. As regards the pore size

distributions of the sub-millimetric voids, they are quite articulated for both samples, with a main maximum of distribution at 0.1 mm and a secondary one at 0.5 mm.

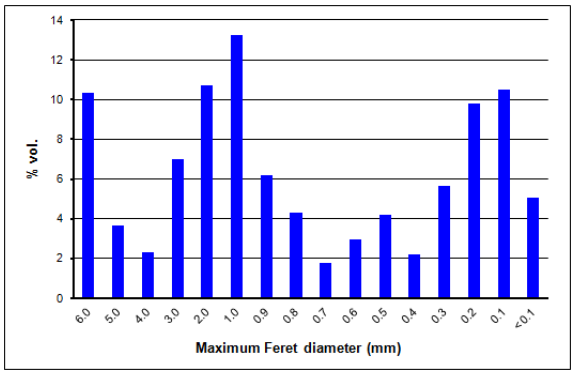

Figure 4.113. Sample FP1, pore size distribution

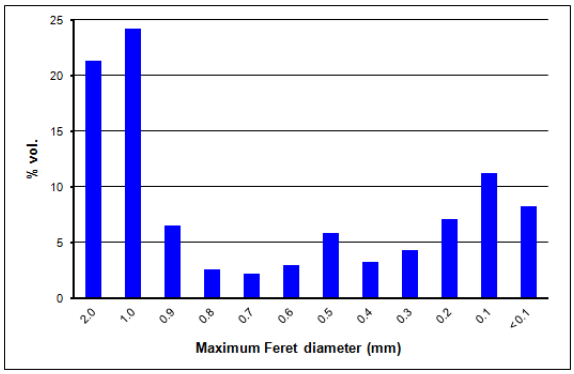

Figure 4.114. Sample FP2, pore size distribution

4.4 CONCLUSIONS

In the framework of this research project, a comprehensive and multiscale image analysis approach was conceived for the first time for the full and quantitative reconstruction of the mix designs of hardened concretes. Integrating standard microscale image analysis on BSE images taken at the electron microscope with more innovative multi-elemental image analysis processes, and extending data at the macroscale by the elaboration of a procedure of analysis of large concrete samples, the intrinsic difficulties of analysis of concretes, related to their marked polydispersity, were successfully overcome. Nevertheless, an articulated procedure of samples pre-treatment had to be developed prior to the optimization of the techniques of acquisition and analysis of the images, in order to facilitate the digital discrimination of the materials' components. As regards the segmentation strategies, the classic approach based on images thresholding was discarded, successfully experimenting a statistical approach based on maximum likelihood algorithms: this allowed an optimization of the quality of the results obtained, now strictly unbiased and operator-independent. Apart from the newly elaborated segmentation strategies, a multi-analytical protocol for the permutation of the volumetric proportions of the constituents into absolute weight amounts was elaborated, based on the relative densities of the mineral-petrographic constituents characterized by image analysis as regards the aggregate fraction, and on the extrapolation of regression functions from standard cement samples at different w/c ratios, characterized by various complementary

techniques, as regards the hardened cement pastes and, consequently, the initial anhydrous cement amounts. Furthermore, size distributions and shapes of both aggregate particles and voids were thoroughly characterized by the utilization of adequate size and shape descriptors, extrapolated by image analysis techniques.

The elaborated multiscale image analysis protocol was successfully applied for the quantitative characterization of the mix designs of the studied concrete samples. Data are in strong concordance with the ones obtained by the multi-analytical qualitative procedure and described in the previous chapter. Furthermore, the strong influence of the mix design parameters on the final mechanical properties of the materials were quantitatively demonstrated: through the simultaneous careful optimization of the compositional parameters (e.g. cement dosage, w/c ratio, c/a ratio, gravel/sand ratio, aggregate grading) and the casting and homogenization procedures, high mechanical properties, similar to the ones of modern concretes, were obtained also in some of the analyzed historical materials. Conversely, the lack of optimization of some of the compositional parameters, often related to the necessity of maintaining the desired workability properties on mixes with slightly different constituents dosages (as in the case of the excessive addition of water observed in some of the Ex-Agrimont and Ex-Foro Boario concretes related to the introduction of higher cement dosages), caused more or less marked lowering of the compressive strength values on some of the analyzed samples. In the worst cases, a total lack of optimization of the compositional parameters, associated to inadequate casting and homogenization procedures, led to the obtaining of extremely low mechanical properties, as in the case of the walls of the Victory Monument and of the arches of the Ex-Zweifel Embroidery Plant. Such characteristics did not affect significantly the static behavior of the structures when counterbalanced by structural over-dimensioning of the concrete elements, as in the case of the Victory Monument, but caused severe structural failures when adopted for relatively thin concrete elements, as in the case of the Ex-Zweifel Embroidery Plant.

Finally, mix designs characteristics are of crucial importance for the durability properties of the materials, being amongst the main causes of triggering of the alteration processes when not accurately optimized. Their influences on the conservation state of the studied materials will be thoroughly examined in the following chapters, which report the results of the characterization studies for the diagnosis of the degradation phenomena acting on the materials.

CHAPTER 5

Study of the degrade of the concrete elements

5.1 THE CONSERVATION STATE OF THE STRUCTURES

The conservation state of the concrete structural elements of the studied structures was assessed on-site during preliminary surveys by means of detailed visual inspections. The inspections enabled the recognition of macroscopic expressions of ongoing degradation phenomena and the determination of environmental and structural causes of weathering, namely temperature and relative humidity values and variations, percolation of infiltrating water and bad isolation of the structure. Furthermore, the surveys were necessary for the project of an accurate sampling campaign for the study of degradation phenomena.

5.1.1 Northern Wing of the Carraresi Castle

Concrete elements of the structure are in a surprisingly good conservation state, despite being quite old and the 20 years of total neglect of the building. This is mainly due to the fact that all columns and beams were covered during the years of utilization of the structure by multiple plaster layers of aerial lime which, reacting with environmental multipollutants and undergoing superficial exfoliation and formation of black crusts, acted as sacrificial layer and prevented extensive degrade of concrete (figure 5.1). These layers were also placed at the intrados of the concrete slabs, while the extrados was covered by a thicker multiple sacrificial layer, constituted by a layer of cement mortar of a thickness comprised between 1 and 2 cm in direct contact with the concrete, followed by a layer of sand on which a pavement of polished stone slabs was placed (figure 5.2).

Figure 5.1. Sacrificial plaster layer on ground floor concrete elements, altered by the formation of black crusts

Figure 5.2. Superficial layer of cement mortar on the second floor slab

Localized removals of the sacrificial layers showed no evidence of detachment of concrete covers. Moreover, neither horizontal nor vertical structural elements are characterized by the occurrence of superficial anomalous cracking patterns and deposition of concretions and efflorescence of secondary alteration compounds at the interfaces with the superficial layers. Localized scarifications highlighted a good conservation state of the rebars, characterized only by sporadic superficial depositions of iron hydroxides but without a clear loss of steel cross section (figure 5.3). A slightly more diffuse oxidation of rebars was observed in the beams of the second constructive phase (figure 5.4), characterized by higher permeability with respect to the other structural elements, as highlighted in chapters 3 and 4. Also, the second floor slab of the area interested by the structural collapse of the roofing is characterized by a more diffuse rebars oxidation, mainly owing to the exposition for a long time period to the external environment, with consequent subjection to excessive water percolations, and temperature and relative humidity variations which have favored degradation phenomena.

Figure 5.3. Conservation state of the rebars on a beam of the first floor (first construction phase)

Figure 5.4. Conservation state of the rebars on a beam of the ground floor (second construction phase)

5.1.2 Victory Monument

The preliminary visual inspection performed on the structure highlighted widespread degradation of the materials, particularly severe on the concrete structural elements constituting the substructure of the monument and on the intrados of the slabs and beams constituting the structural frame of the stairway.

The degrade was triggered by extremely unfavorable environmental factors, related both to massive water infiltrations diffuse in the whole substructure of the monument due to scarce isolation of the structural elements and the capillary rise of water from the ground due to the absence of isolating layers on the foundations. These factors directly influenced the occurrence of relevant relative humidity variations, both daily and seasonal, which caused repetitive saturation, mobilization and evaporation of fluids saturating concrete pore network.

The clearest manifestation of concrete degradation is the presence of widespread superficial efflorescence of secondary phases on the surfaces of all concrete elements, probably related to soluble salts crystallization phenomena (figures 5.5, 5.6). Furthermore, the progression of the degrade caused decalcification and leaching events on the cementitious matrices of the conglomerates, with associated pop-out of the inert fraction, superficial detachment and delamination of the concrete cover, and formation of superficial concretions (figure 5.7). These processes interested mainly the concrete walls, which show marked superficial loss of cohesion, with relevant scaling and dusting of the cement matrices (figure 5.8).

Figure 5.5. Superficial efflorescence on the vault of the central crypt

Figure 5.6. Superficial efflorescence of a lateral wall

Figure 5.7. Superficial concretion on a lateral wall

Figure 5.8. Superficial scaling on a lateral wall

Furthermore, the slabs and the beams are characterized by the presence of wide areas showing total detachment of the concrete cover (figure 5.9), and the exposed rebars are widely oxidized, showing massive loss of section. The presence of superficial concretion and efflorescence on the surfaces of these elements has favored further detachment of conglomerate portions (figure 5.10).

Figure 5.9. Detachment of concrete cover and rebars oxidation on the intrados of the stairway

Figure 5.10. Alteration on a beam: detachment of concrete cover, rebars oxidation and formation of superficial efflorescence

5.1.3 Ex-Agrimont Area, C3 building

Visual inspection highlighted the bad conservation state of the concrete structural frame of the building, despite the overall quality of concrete mix design and good mechanical properties, highlighted in chapters 3 and 4. All structural elements are covered by superficial black crusts, which have caused dusting and superficial scaling of cement matrices (figure 5.11). The alteration phenomenon also interested the highest portions of the structure (figure 5.12), suggesting a strong influence of atmospheric multipollutants for the development of concrete weathering.

Figure 5.11. Superficial black crusts and scaling phenomena on an arch

Figure 5.12. Superficial black crusts and scaling phenomena on non-structural beams, at an height of 12 meters

The continuous progression of the alteration phenomena caused in some cases complete consumption and detachment of concrete covers, triggering extensive oxidation on the rebars (figure 5.13). Finally, the degradation of reinforced concrete elements is further accentuated in the south-western portion of the structure, near the platform originally used for the direct load on trains of final products and by-products, where massive decalcification and detachment of concrete portions can be observed (figure 5.14). Considering the peculiarity of these manifestations of degrade, a more detailed study of the alteration dynamics acting on the concrete elements has been performed, and it will be described in detail in chapter 6.

Figure 5.13. Detachment of concrete cover and rebars oxidation on a wall

Figure 5.14. Conservation state of an arch in the south-western portion of the structure

5.3.1 Ex-Zweifel Embroidery Plant

An overall assessment of the conservation state of the structure is evidently negative, considering the structural collapse which interested half of the building. Nevertheless, considerations on the state of the concrete structural elements before the collapse can be drawn by studying the features of the building portion which overcame the collapse and of the sampled materials.

Concrete elements of the sound portion of the structure are in a good conservation state, despite the 20 years of total neglect of the building and the uncontrolled exposure to the external environment after the partial collapse of the building. No evidence of detachment of concrete covers and superficial exfoliations was found (figures 5.15, 5.16). Furthermore, neither horizontal nor vertical structural elements are characterized by the occurrence of

superficial anomalous cracking patterns and deposition of concretions and efflorescence of secondary alteration compounds. This is mainly due to the fact that all structural elements constituting the frame and the vault of the first floor have been covered during the years of utilization of the structure by multiple plaster layers which acted as a sacrificial layer and prevented extensive degrade of concrete (figures 5.15, 5.16). Coring revealed the presence of a thick cement mortar layer (between 5 and 15 mm thick) covering the riddle, the beams and the arches constituting the structural frame (figure 5.17), which acted as a further and more effective protection layer for the concrete.

Consequently, rebars still embedded in the concrete matrix remained prevalently non oxidized or, in the worst cases, were interested only by the formation of thin superficial layers of iron hydroxides, which do not cause significant loss of cross section (figure 5.18).

Figure 5.15. Sacrificial plaster layer on ground floor concrete elements

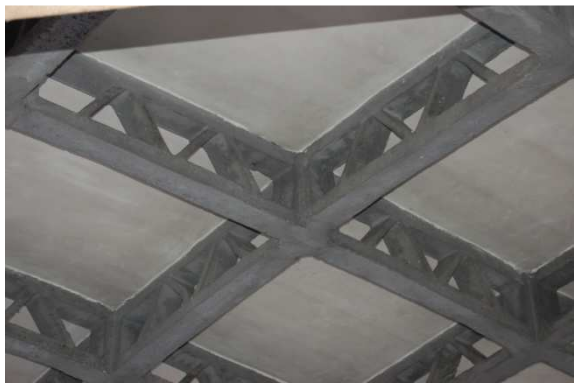

Figure 5.16. Sacrificial plaster layer on the beams of the first floor's vault

Figure 5.17. Superficial layers of cement mortar on the concrete of the beams

Figure 5.18. Conservation state on a series of rebars sampled for tensile stress tests

5.1.5 Ex-Foro Boario

A first visual analysis during surveys in the structure showed a good conservation state of the concrete.

The most damaged elements, covering slabs in cement and masonry and the floor, have no structural functions. In both cases the main cause of degradation is the infiltration of rainwater from the openings between overlapping slabs. Infiltrated water stagnated on the floor, causing efflorescence and swelling. The covering slabs were affected by percolation and water infiltration events from the extrados, which caused efflorescence, superficial detachment and breaking of hollow tiles due to freeze-thaw cycles (figures 5.19, 5.20).

Figure 5.19. Degradation at the intrados of a covering slab

Figure 5.20. Degradation at the intrados of a covering slab

As for structural elements cast on-site, the columns are in an excellent conservation state: there is no detachment of the concrete cover, superficial exfoliation or secondary phases concretions and efflorescence (figure 5.21). Local scarifications highlighted that the rebars are not affected by oxidation, which is partly due to the presence of superficial plaster layers which acted as sacrificial layers preventing the degrade of concrete (figure 5.21). Concrete beam segments, on the contrary, present a way more marked degrade, with superficial detachments, secondary phases concretions and a noteworthy oxidation of the rebars, matched by the detachment of the concrete cover (figure 5.22). This is due to

massive percolation and rainwater accumulation on structural elements, together with the inadequacy of concrete cover layers, meanly thinner than 5 mm and lacking in some areas, which prevented the preservation of the alkaline environment surrounding the rebars.

Figure 5.21. Conservation state of a reinforced concrete column

Figure 5.22. Conservation state of a concrete beam segment

5.2 EXPERIMENTAL

Preliminary colorimetric on-site tests were performed to assess the progression of the carbonation front, by means of nebulization of phenolphthalein dissolved in ethanol, at a concentration of 1 %. The solution undergoes a chromatic turning from purple to colorless at pH under 8.2, thus indicating the carbonated portions of a concrete sample. Analyses were performed both on the nuclei of the cores after the compression tests and on surfaces of concrete subjected to scarification.

Ex situ analyses have been performed on both cores and micro-cores taken for the characterization of concrete and on materials sampled for the purpose, namely superficial portions of detached concrete, scarification residuals and superficial concretions and efflorescence.

Portions of altered concrete samples were impregnated by epoxy resin and sectioned transversally to obtain 30 μm thin sections. The thin sections have been studied with a polarizing microscope to recognize petrographic features of concrete alteration

phenomena. Then, XRPD analyses were performed on the fraction under 63 μm of the samples, which were subsequently dry disaggregated and sieved. To recognize cross sectional variations of mineral assemblages due to the action of external degrading agents, various powder samples have been extracted from the sampled cores. All analyses were performed with a Philips X'Change diffractometer in Bragg-Brentano geometry equipped with a Cu X-ray tube operating at 40 kV and 40 mA (CuKa radiation), and an X'Celerator detector, both mounted on a PW1050/37 theta-2theta vertical goniometer. Data acquisition was performed operating a continuous scansion from 3.01° [2θ] to 79.99° [2θ], at an acquisition rate of 0.02° [2θ] per second. Diffraction patterns were interpreted with X'Pert HighScore Plus 3.0 software by PANalytical, reconstructing mineral profiles of the compounds by comparison with ICDD and ICSD databases.

The mineralogical and petrographic studies were integrated performing microchemical and microstructural analyses on thin sections samples using a Camscan MX 2500 scanning electron microscope (SEM), equipped with a LaB_6 electron source and an EDAX energy dispersive X-ray detector (EDS). Qualitative interpretation of spectra and semiquantitative estimation of chemical profiles were performed through SEMQuant Phizaf software. Also, chemical maps were acquired, in order to obtain spatial distributions of secondary phases inside the altered materials.

5.3 RESULTS

5.3.1 Northern Wing of the Carraresi Castle

The thickness of the carbonated portions for the sampled cores, as determined by colorimetric tests, is reported in table 5.1. Two carbonated portions are reported for cores sampled through the whole thickness of the structural element. For the slabs, carbonated portion 1 is representative for the intrados, while carbonated portion 2 is representative for the extrados. The carbonation tests on samples CT1 and CT3 are reported in figures 5.23 and 5.24.

Sample	Element	Phase	Carbonated portion 1 (mm)	Carbonated portion 2 (mm)
CC1	Slab	2	35	5
CC2	Slab	1	33	15
CC3	Slab	2	70	15
CP1	Column	2	20	-
CT1	Beam	2	80	100
CT2	Beam	3	18	-
CT3	Beam	1	35	33

Table 5.1. Northern Wing of the Carraresi Castle, thickness of the carbonated portions for the sampled cores

Figure 5.23. Colorimetric test on CT1 sample

Figure 5.24. Colorimetric test on CT3 sample

Tests highlighted the great influence of both the presence of protective layers and concrete quality on the progression of the carbonation. As for the slabs, carbonation is relevant on their intradoses, while the extradoses, protected by a thick multiple layer, underwent negligible carbonation. Also, the exposure to unfavorable environmental conditions of the slab represented by CC3 sample, due to the collapse of the roofing in the area, caused an almost total carbonation of the concrete. As for the beams, the ones of the second constructive phase, characterized by high permeability as highlighted in chapters 3 and 4, are characterized by almost total carbonation, while the others underwent carbonation in an external volume still comprised in the concrete cover portion. The column, characterized by lower overall porosity with respect to the other structural elements of the second constructive phase, underwent only a limited external carbonation.

The results of the colorimetric tests are confirmed by the petrographic analyses performed on the materials. The occurrence of carbonation fronts at the interfacial zone between external carbonated portion (characterized by a strong birefringence in thin section) and internal sound portions (isotropic when analyzed in crossed polars) have been observed for most of the samples in correspondence with the carbonation levels defined by the colorimetric tests (figure 5.25). The absence of carbonation fronts have been observed for CT1 and CC3 samples only, thus being almost totally carbonated (figure 5.26).

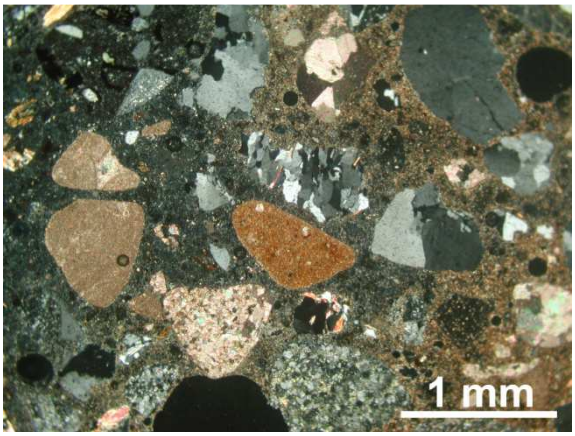

Figure 5.25. Sample CT3, carbonation front at an approximate depth of 35 mm (crossed polars microphotograph)

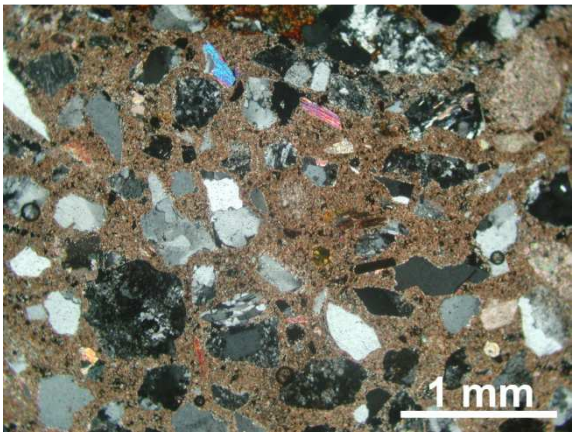

Figure 5.26. Sample CT1, total carbonation even in the core of the material (crossed polars microphotograph)

Mineralogical profiles of the finer fractions confirmed the previous observation. Most of the samples are totally carbonated in the external portions, as indicated by the total absence of portlandite in the analyzed compounds, while the occurrence of portlandite in the internal portions indicated the permanence of the alkaline environment (figure 5.27). On the contrary, CT1 and CC3 samples showed no traces of portlandite in the cores, indicating total carbonation of the calcium hydroxide (figure 5.28).

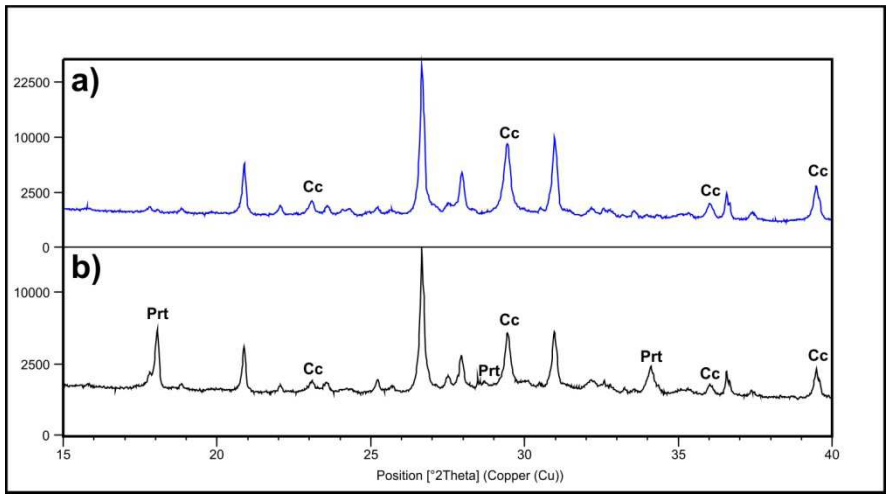

Figure 5.27. Diffraction patterns of the finer fractions of CC2 sample. a) = concrete cover, b) core.
Abbreviations: Cc = calcite, Prt = portlandite

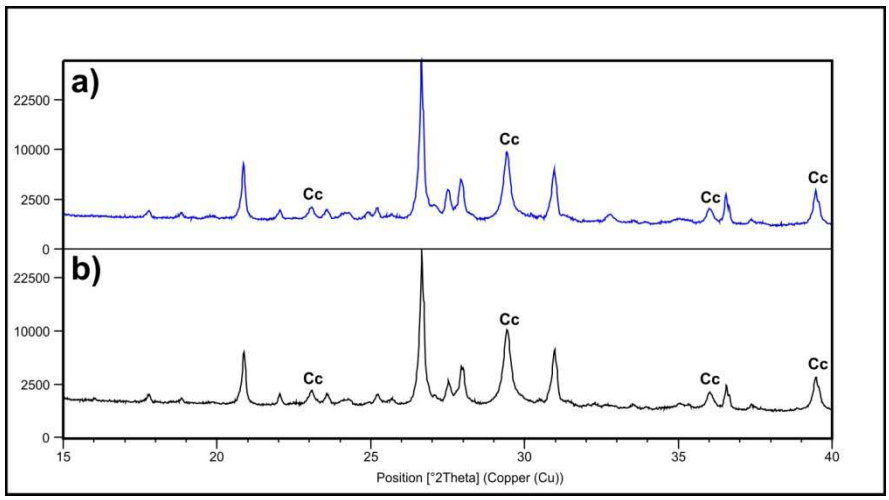

Figure 5.28. Diffraction patterns of the finer fractions of CC3 sample. a) = concrete cover, b) core.
Abbreviation: Cc = calcite

Profile chemical analyses performed by SEM-EDS, performed acquiring a series of fluorescence spectra along paths perpendicular to the external surfaces of concrete at reciprocal distances of 250 µm, confirmed the petrographic and mineralogical observations. All samples, with the exception of CT1 and CC3, are characterized by high calcium concentrations in the external carbonated portions, with Ca/Si molar ratios between 2 and 2.50, while the cores are characterized by lower values, generally between 1.30 and 1.50. Such analytical evidence suggests a progressive leaching of calcium hydroxide from the volumes of progression of the carbonation front, with mobilization of calcium ions in pore solution and subsequent precipitation in external areas characterized by lower pH with respect to the sound portions. The process is particularly evident in the

microanalyses performed on sample CP1 (figure 5.29): the external portions are characterized by high relative percentages of CaO (mean value of 55.58 %, mean Ca/Si molar ratio of 2.39), while it is possible to observe the presence of a portion of material between 20 and 22 mm from the external layers depleted in CaO (mean value of 43.20 %, mean Ca/Si molar ratio of 1.29), which constitutes the active area of leaching corresponding to the carbonation front. Beyond this portion CaO and SiO_2 relative percentages are stabilized around mean values of 48.29 % and 37.40 %, respectively, with a mean Ca/Si molar ratio of 1.38.

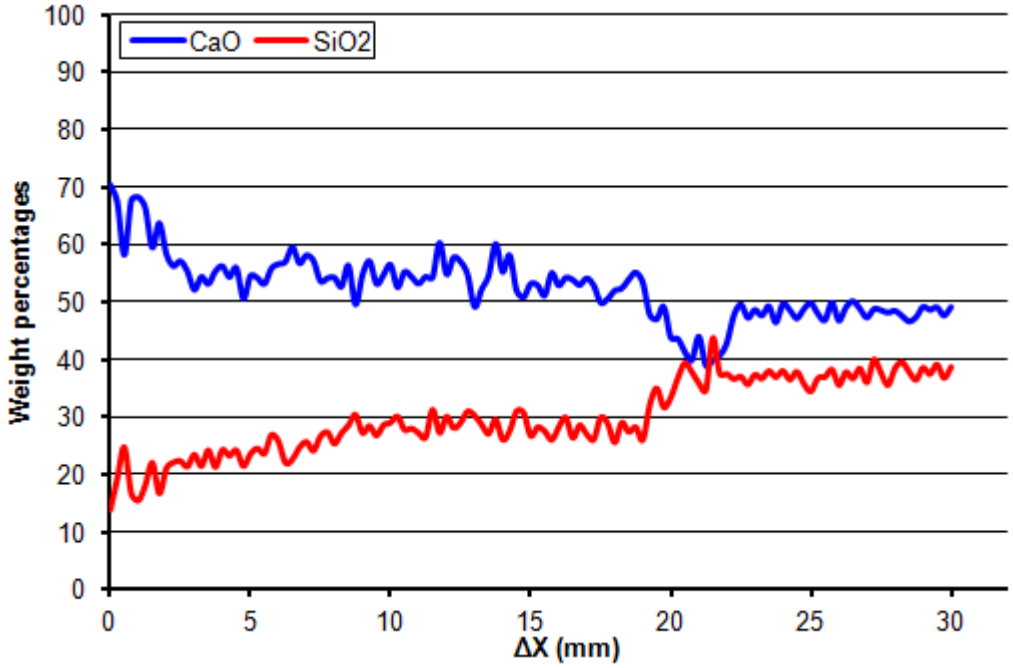

Figure 5.29. Profile chemical analysis performed on sample CP1. Relative concentrations of CaO and SiO_2 are reported, expressed in weight percentages

Besides carbonation, all concrete samples are affected by slight forms of sulfate attack, This form of alteration is highlighted by the occurrence of secondary sulfates in the most external layers of the materials, as shown by XRPD analyses on the finer fraction of the analyzed conglomerates. The alteration is limited to an initial stage of gypsum formation due to the reaction between portlandite and sulfates in pore solution, while only traces of ettringite were found (figure 5.30). No traces of secondary sulfates are detectable in the internal portions of the materials (figure 5.30), and no clear signs of cracking of the cement matrix due to the alteration phenomenon are observable in the external portions.

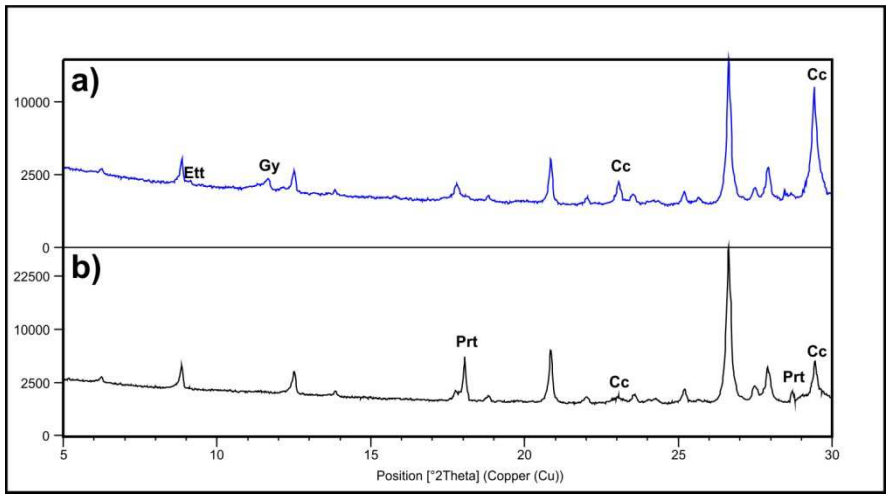

Figure 5.30. Diffraction patterns of the finer fractions of CC1 sample. a) = concrete cover, b) core.
Abbreviations: Cc = calcite, Prt = portlandite, Gy = gypsum, Ett = ettringite

5.3.2 Victory Monument

The materials underwent massive carbonation of the cement matrix, due to the reaction between portlandite and carbon dioxide from the atmosphere. The degree of carbonation is differentiated according to the typology and compositional characteristics of the concrete structural elements.

The colorimetric tests carried out on the nuclei of the sampled cores after the compression tests indicated a total carbonation of the samples of wall concrete, while the samples of stairway concrete are completely carbonated in the first 40 mm only, a value in any case greater than that of the thickness of the concrete cover. Petrographic analyses confirmed the results of the colorimetric tests: carbonation fronts were observed in the samples of the stairway concrete, at depths comparable with the ones determined by colorimetric tests (figure 5.31), while the concrete of the walls are totally carbonated even in the internal portions of the cores. Moreover, the latter are affected by a relevant precipitation of secondary carbonates inside entrained air voids, with formation of geode- and mosaic-type microstructures, mainly along the margins and in some cases completely filling the voids (figure 5.32).

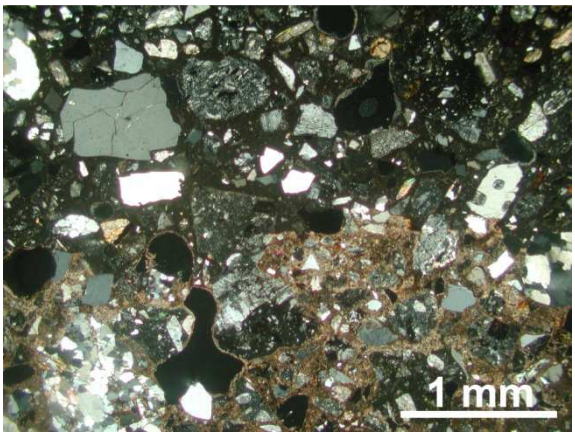

Figure 5.31. Sample BG1, carbonation front at an approximate depth of 42 mm (crossed polars microphotograph)

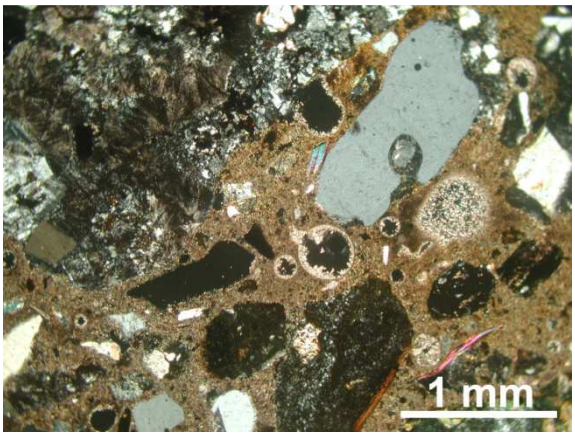

Figure 5.32. Sample BS2, total carbonation even in the core of the material, with carbonates precipitation in the voids (crossed polars microphotograph)

The diffractometric analyses confirmed the results of the colorimetric tests. Mineralogical profiles of the external portions of the beams and the slabs are constituted by predominant secondary calcite. No traces of portlandite were found. The mineralogical profiles of the internal portions are constituted mainly by quartz, whose presence is due to inadequate mechanical separation of the inert fraction from the cement matrix. As regards the calcium-bearing phases, significant amounts of calcite are present, related to carbonation processes. It is also possible to observe a progressive increase in portlandite concentrations moving towards the inner cement matrices, indicating a limited permanence of the alkaline environment of the concrete inside the materials (figure 5.33).

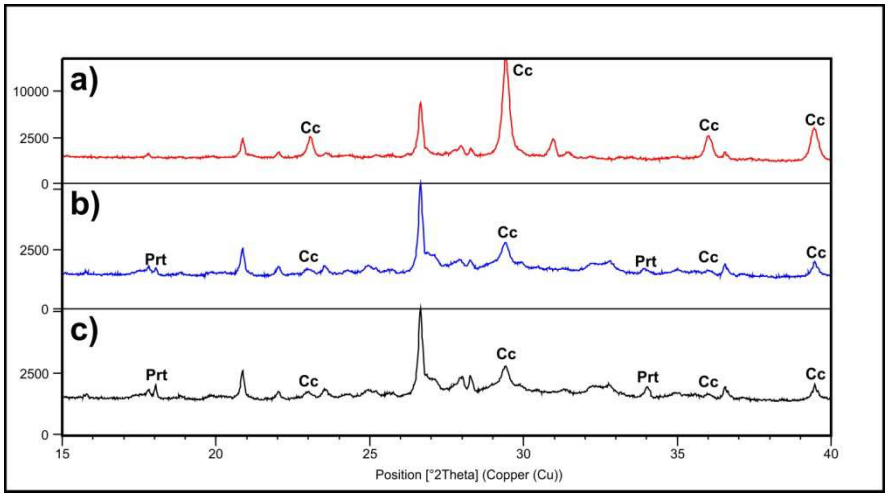

Figure 5.33. Diffraction patterns of the finer fractions of BT1 sample. a) = concrete cover, b) intermediate layer, c) core. Abbreviations: Cc = calcite, Prt = portlandite

The mineralogical profiles of the cement matrices of the walls are constituted by predominant calcite, without residual amounts of portlandite. Significant amounts of metastable calcium carbonate vaterite are present (figure 5.34). The mineral usually precipitates during the first phases of carbonation and is converted into the stable compound calcite during the progression of the alteration (St John et al., 1998). In the specific case, the occurrence of vaterite indicates degrees of carbonation greater than the degrees of phase transition between the metastable and stable compound, with permanence of nuclei of altered matrices with pH and water saturation conditions suitable for the stabilization of this phase. The presence of the compound is confirmed by SEM-EDS analyses, showing the typical framboidal morphology of vaterite aggregates (figure 5.35).

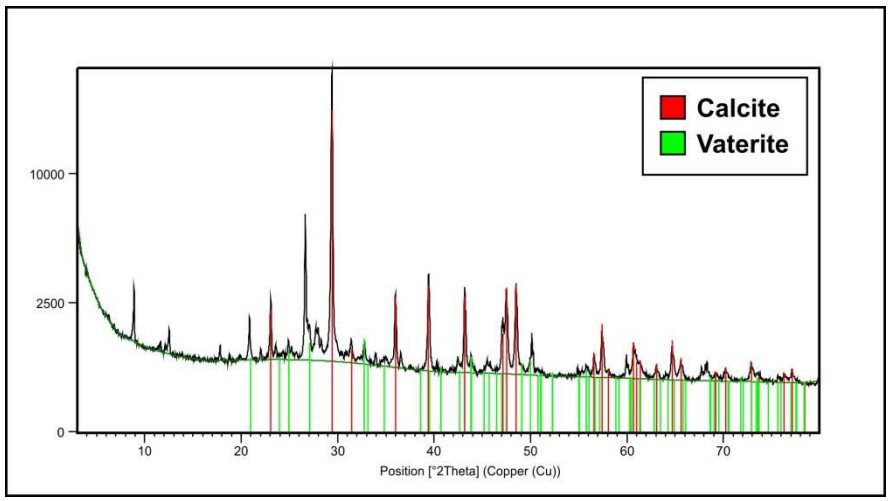

Figure 5.34. Diffraction pattern of the finer fraction of BS3 sample internal portion

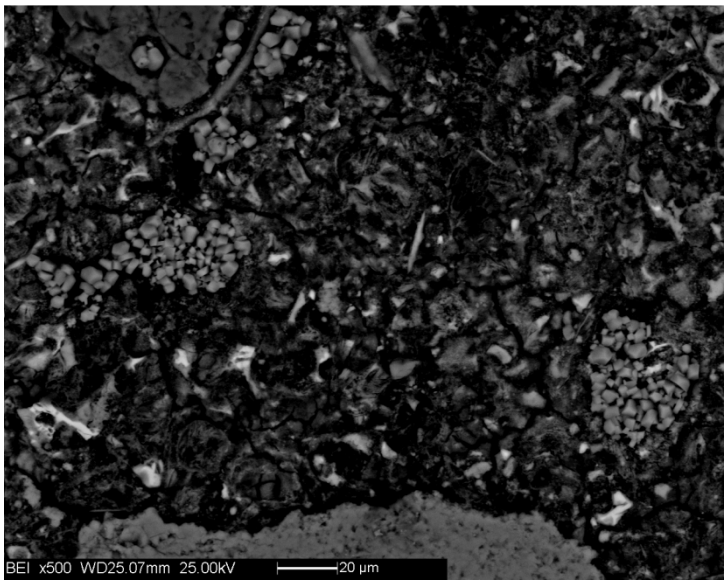

Figure 5.35.SEM-BSE image of vaterite framboids in the cement matrix of BS3 sample

Massive carbonation of the concrete of the substructure also caused the formation of typical external concrete stalactites, as confirmed by the mineralogical profiles of the external concretions occurring on the structural elements (figure 5.36). The phenomenon is due to the formation of soluble calcium bicarbonate in pore solution due to the carbonation process, with subsequent mobilization through the pore network and precipitation in form of insoluble calcium carbonate on the external portions of the concrete, due to evaporation of water caused by relative humidity changes.

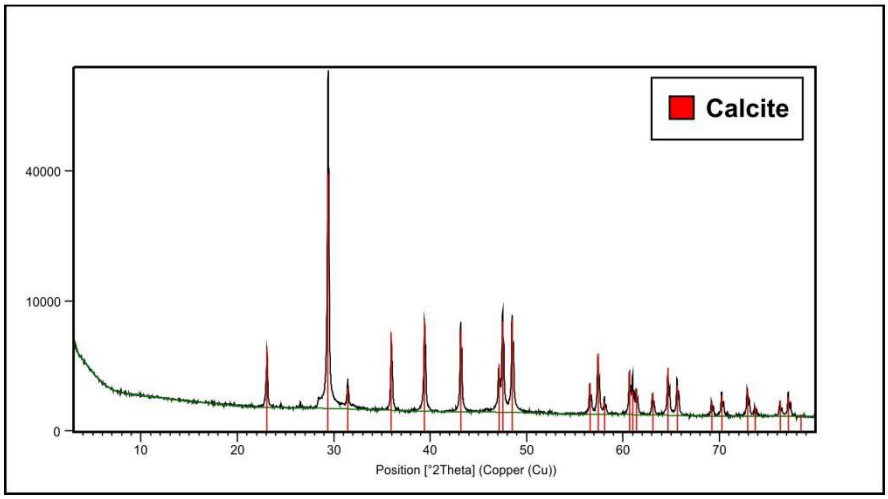

Figure 5.36. Diffraction pattern of a superficial concretion on a lateral wall (ref. figure 5.7)

The XRPD results are fully consistent with the chemical data obtained from SEM-EDS analyses. The cement matrices of the walls are characterized by the presence of high amounts of CO_2, confirming the total carbonation of the portlandite. This hypothesis is confirmed by the high Ca/Si molar ratios of the cement matrices, with medium values of 3.05. The microanalyses on the cement matrices of the beams and the slabs highlight decreasing gradients of CO_2 concentration and Ca/Si molar ratios moving towards the inner portions, with the latter showing medium values of 2.36 in the external layers, and 1.35 in the inner ones.

The analytical results indicated widespread incidence of alkali-related attacks, due to the interaction between concrete constituents and alkalis in pore solution. The incidence of such alteration phenomena is fully consistent with the environmental characteristics, as well as with the chemical and mineralogical nature of both binder and inert fraction. The enrichment of alkalis in the pore water is due to sodium and potassium leaching events in alkaline environment, both from the cement matrix and the siliceous glass of the

ignimbrites. Microanalyses on residual clinker grains highlighted the occurrence of significant amounts of sodium and potassium in the binder (mean concentrations: Na_2O = 0.30 %, K_2O = 1.70 %), generally as constituents of soluble sodium salts (figure 5.37). Moreover, volcanic glass of the ignimbrites is constituted by relevant amounts of potassium and sodium (mean concentrations: Na_2O = 3.10 %, K_2O = 6.30 %) (figure 5.38). The dissolution of these amorphous matrices in alkaline environment, due to the break-up of Si-O-Si bonds, contributes significantly to the release of alkali ions in pore solution. The mobilization of alkalis-rich solutions is favored by the high water percolation and relative humidity variations in the substructure of the Monument.

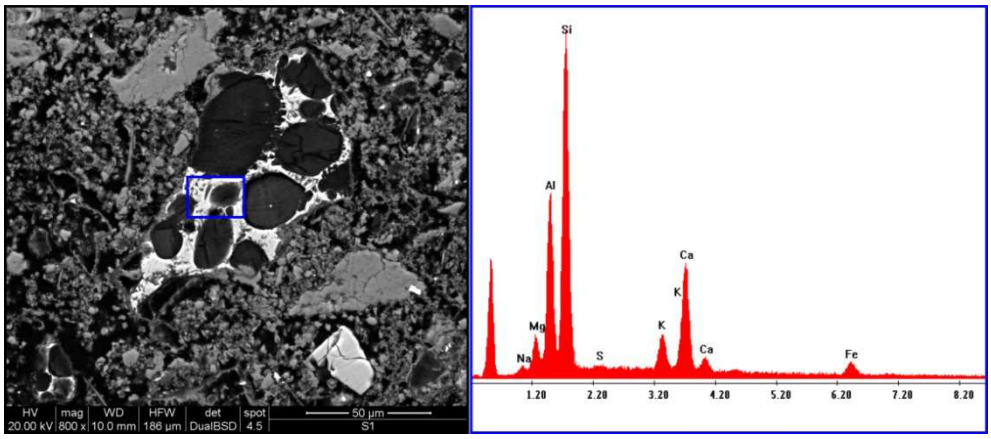

Figure 5.37. Sample BS1, SEM-BSE image and microanalysis of a residual clinker grain

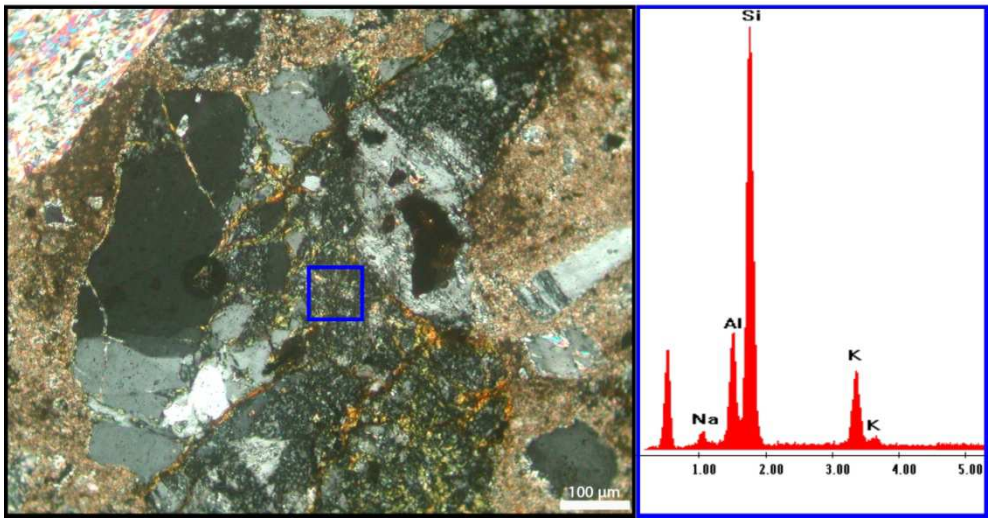

Figure 5.38. Sample BS2, corroded ignimbrite fragment and SEM-EDS microanalysis of the siliceous glass

Petrographic analyses and SEM observations show the widespread presence of stressed and strongly corroded ignimbrite and quartzite fragments with corrosion bands (figures

5.39, 5.40). The samples also exhibit many microcracks mostly oriented perpendicular to concrete external surface and interconnected with each other by a network of finer random cracks (figures 5.41, 5.42). These microscopic features suggest the occurrence of alkali-silica reactions on the materials.

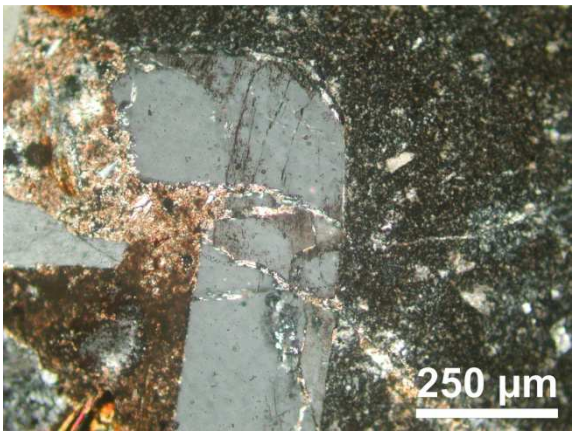

Figure 5.39. Sample BV1, corroded ignimbrite fragment (crossed polars microphotograph)

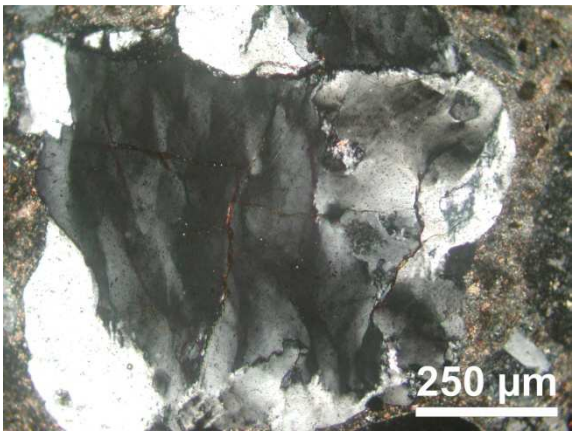

Figure 5.40. Sample S4, corroded quartzite fragment (crossed polars microphotograph)

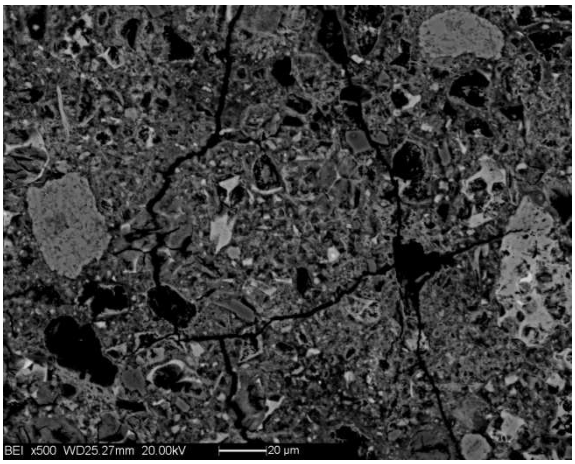

Figure 5.41. Sample BS3, cracking pattern due to ASR (SEM-BSE image)

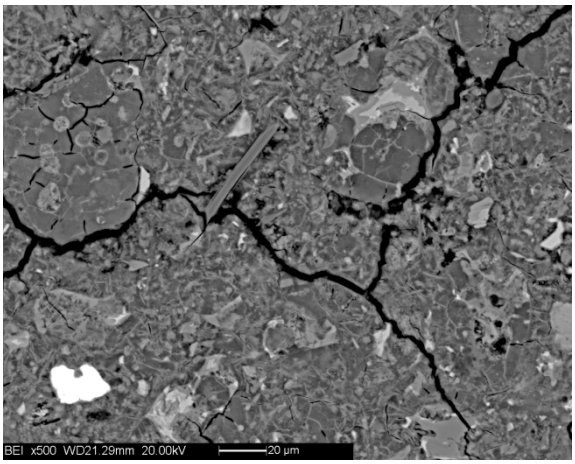

Figure 5.42. Sample BG1, Cracking pattern due to ASR (SEM-BSE image)

No clear evidence of ASR gel products is confirmed, which may be due to the fact that the gel products easily undergo desiccation processes, and subsequent elimination by water circulation. Anyway, EDS chemical mapping on the samples showed the presence of relevant amounts of sodium and potassium dispersed in the cement matrices, in areas characterized by lower density and higher overall porosity with respect to sounder portions (figure 5.43): this evidence suggests the occurrence of hydrous potassium silicates crystallized in the capillary pores of the concrete.

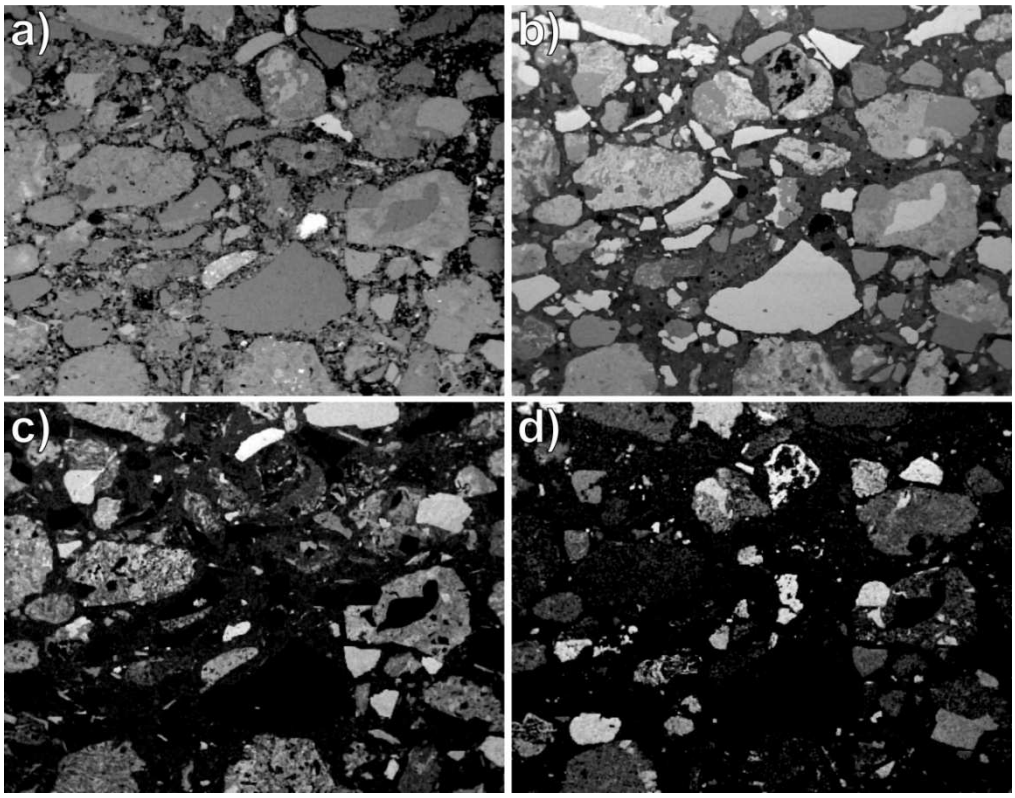

Figure 5.43. EDS chemical maps on BS2 sample (field of view: 4 mm): a) BSE image, b) Si map, c) K map, d) Na map. The simultaneous presence of Si, K and Na in the upper area, characterized by lower density, indicates the precipitation of ASR gels in the capillary porosity

The XRPD analyses of the external portions of the concrete highlight the occurrence of relevant amounts of sodium sulfate phases, mainly in anhydrous form, corresponding to the mineral thenardite, and subordinately in dihydrated and decahydrated form, corresponding to the minerals eugsterite and mirabilite, respectively. The efflorescence samples collected from the external portions of the concrete structures are of the same mineralogical nature (figure 5.44). The development of these secondary phases, responsible for the significant superficial scaling of the concrete, is due to the reaction between the alkalis of the conglomerates, leached both from the cement matrix and the volcanic glass of the ignimbrites constituting the inert fraction, and the sulfates in the solution permeating the pore network. During rapid and intense variations in relative humidity values and consequent wetting and drying cycles of the pore-water, the crystallization of the phases caused expansive dynamics in the materials. The process was due to solid volume change during transformation of anhydrous salt to its hydrous form and salt crystallization pressure development. The formation of the phases is favored in the superficial portions by the higher relative humidity variations.

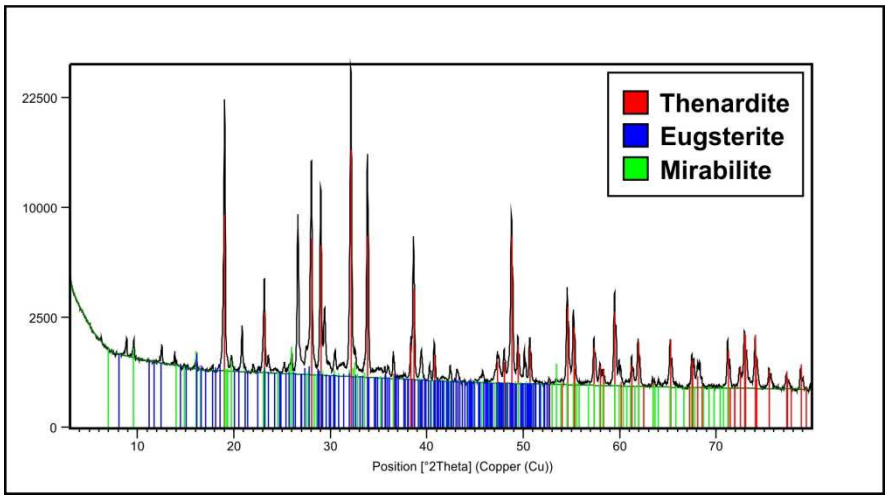

Figure 5.44. Diffraction pattern of a superficial efflorescence on a lateral wall (ref. figure 5.6)

The XRPD patterns of the cement matrices of the analyzed samples clearly show the presence of secondary sulfates, related to the incidence of sulfate attack degradation phenomena. As observed by carbonation, the degree of alteration due to sulfate attack is differentiated according to the typology of the concrete structural elements.

The alteration on the walls is limited to an initial stage of limited gypsum formation due to the reaction between portlandite and sulfates in pore solution, without ettringite formation (figure 5.45).

As regards concrete of the stairways, the mineralogical profile shows the presence of more relevant amounts of gypsum in the cement matrice, with associated traces of ettringite. The analytical results indicate a more advanced degrade of the materials due to sulfate attack with respect to the walls, even if always at an initial state of predominant gypsum formation. Also, the development of the secondary phases shows an ascending gradient moving towards the internal portions of the samples, in inverse relation with the concentration of secondary carbonates (figure 5.46). The XRPD data are consistent with the results of the microanalyses at SEM-EDS.

Experimental evidence indicates strong competitiveness between sulfate attack and other forms of concrete alteration, namely carbonation and soluble salts crystallization, with consequent hindrance of calcium sulfates formation. This is mainly due to higher precipitation rates of the secondary phases produced by carbonation and alkalis-related sulfate salts precipitation, related to kinetic factors. It is possible to hypothesize that high carbonation rates hinder sulfate attack due to the consumption of portlandite dissolved in pore solution, while crystallization of sodium sulfates in the external portions of the

materials causes a depletion of sulfates dissolved in pore solution which hinder formation of gypsum and ettringite. The consequences on the analyzed materials are an overall reduced sulfate attack rate in concrete of the walls, where carbonation is highly predominant, while in concrete of the stairways sulfate attack mainly develops in the sub-superficial portions, characterized by lower rates of secondary carbonates and sodium sulfates formation.

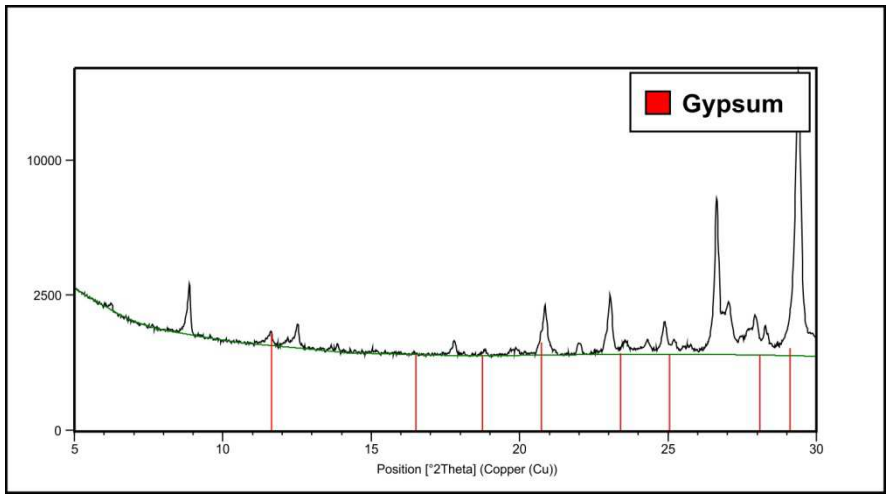

Figure 5.45. Diffraction pattern of the finer fraction of BS3 sample

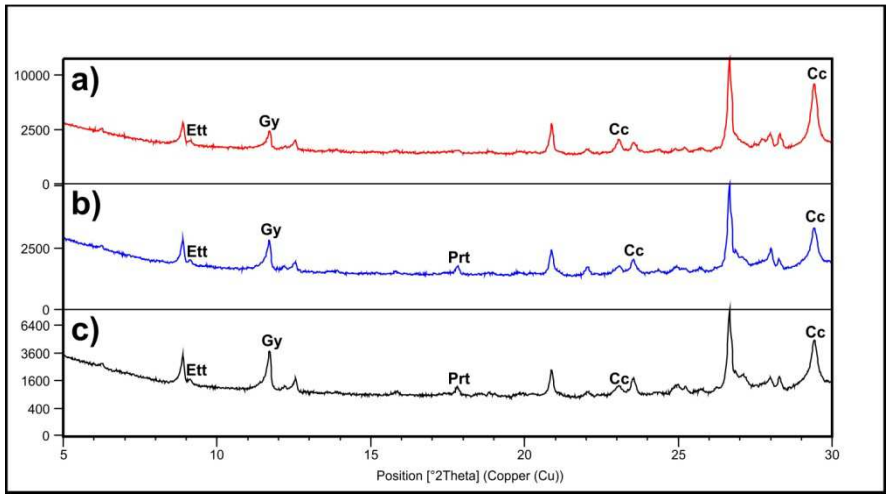

Figure 5.46. Diffraction patterns of the finer fractions of BG1 sample. a) = superficial portion, b) portion at 10 mm of depth, c) portion at 20 mm of depth. Abbreviations: Cc = calcite, Prt = portlandite, Gy = gypsum, Ett = ettringite

5.3.3 Ex-Agrimont Area, C3 building

The colorimetric tests performed on the cores and on concrete matrices after scarification indicated a lack of total carbonation of the materials, even in the most superficial portions (figure 5.47).

Figure 5.47. Colorimetric tests on MC1 and MC3 samples

The results of the colorimetric tests are confirmed by XRPD analyses, which highlighted a limited carbonation of portlandite in the external portions only, while the calcite fraction in the cores is due to carbonate of the aggregate (figure 5.48).

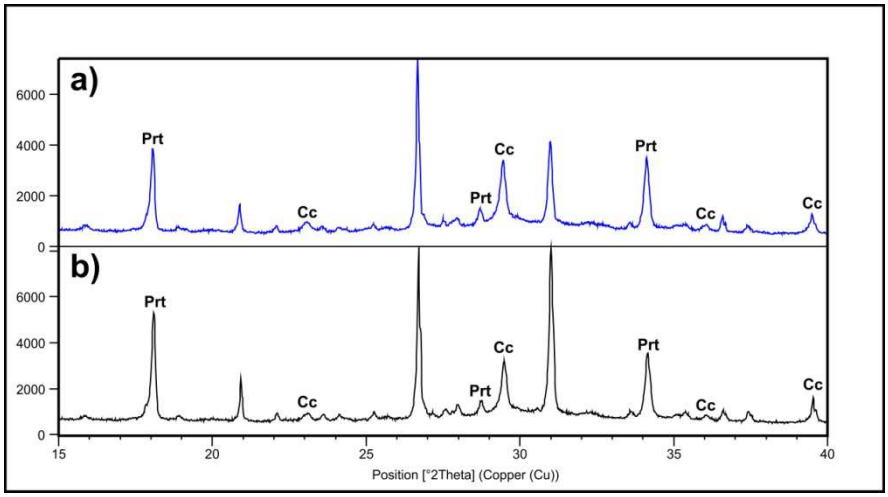

Figure 5.48. Diffraction patterns of the finer fractions of MC2 sample. a) = concrete cover, b) core. Abbreviations: Cc = calcite, Prt = portlandite

The petrographic study demonstrated the absence of marked carbonation fronts in concrete, being the cement matrix mainly isotropic when observed at the polarizing microscope in crossed polars. The presence of sporadic and isolated areas characterized by high birefringence can be observed in the external portions of the materials only, suggesting a limited carbonation process (figure 5.49).

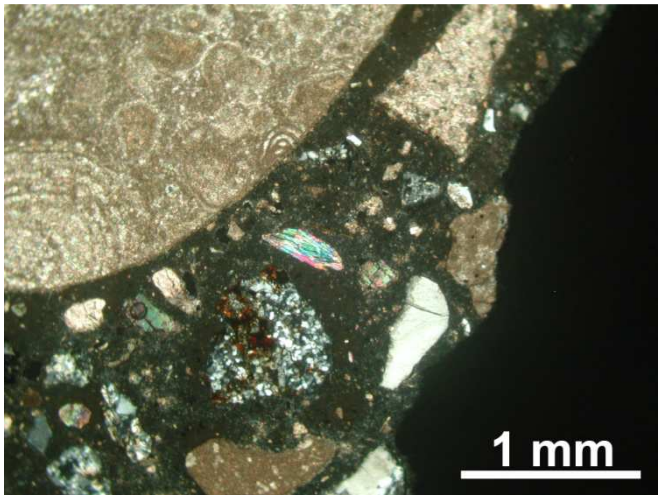

Figure 5.49. Sample MC3, external portion (crossed polars microphotograph)

SEM imaging and SEM-EDS microanalyses showed the presence in the external portions of localized areas characterized by higher Ca/Si molar ratios with respect to the surrounding matrix (figure 5.50), confirming sporadic and irregular carbonation phenomena of the matrices in the volumes of material more in contact with the external environment.

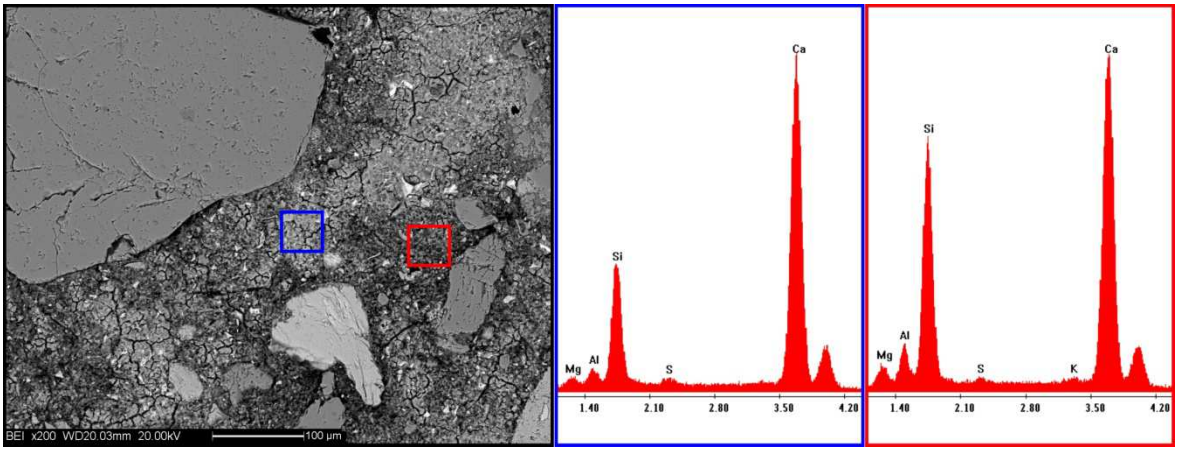

Figure 5.50. Sample MC1, SEM-BSE image of an external, partially carbonated portion of conglomerate. The carbonation of the brighter areas is confirmed by the higher Ca content with respect to the other areas, as indicated by EDS microanalyses

XRPD analyses on the finer fractions of the materials highlighted the presence of relevant amounts of sulfate phases related to sulfte attack phenomena, namely gypsum, ettringite and thaumasite. The alteration is extended to the internal portions of concrete, too (figure 5.51). Amongst the secondary phases, the prevalence of ettringite over calcium sulfate indicates an advanced state of alteration which led to the conversion of AFm monosulfate into AFt phase after dissolution of gypsum in pore solution. Furthermore, the occurrence of thaumasite justifies the relevant superficial dusting of the cement matrices, due to CSH dissolution after reaction with sulfates and carbon dioxide. These intense forms of sulfate attack indicate high tenors of sulfates in pore solution, due both to the uptake from the atmosphere polluted by industrial emissions and to capillary rise of marine water. High sulfate concentrations and water saturation of the pore network may have contributed to the hindrance of carbonation, favoring the formation of secondary thaumasite.

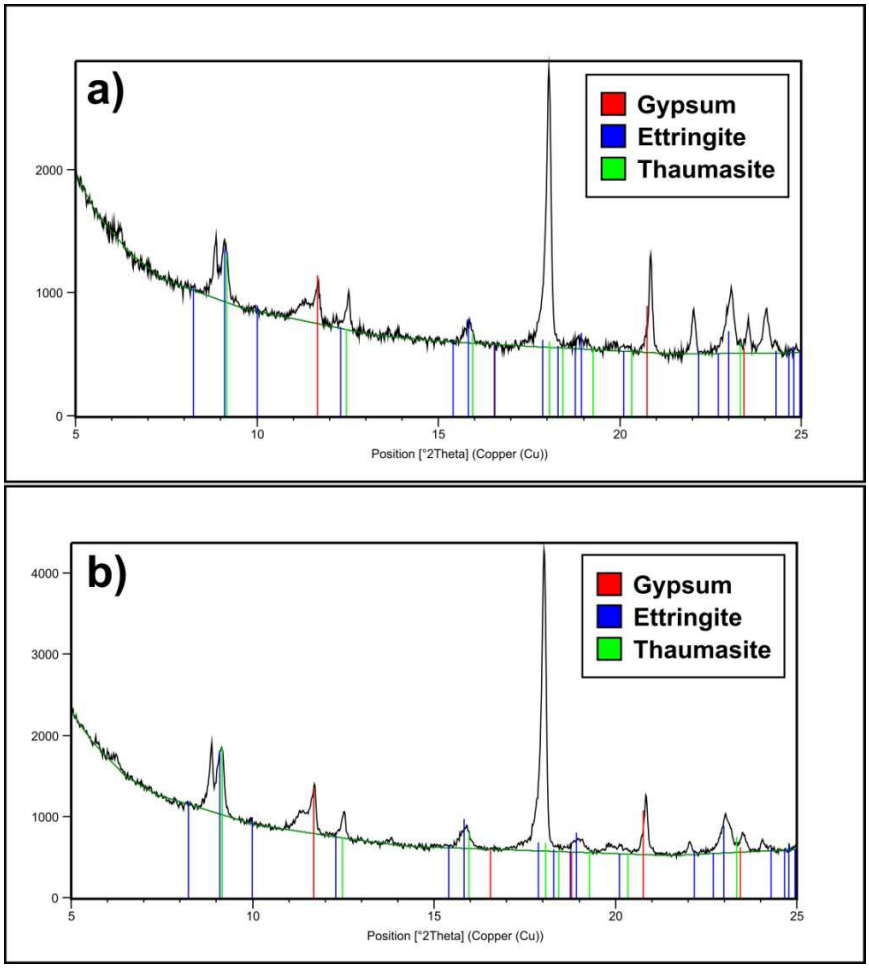

Figure 5.51. Diffraction patterns of the finer fractions of MC2 sample. a) = superficial portion, b) portion at 20 mm of depth

SEM-EDS analyses confirmed the mineralogical results. The external areas of the materials are the most affected by the degradation related to sulfate attack, being constituted by an incoherent layer of altered cement matrix, highly porous and with relevant amounts of sulfates dispersed in the capillary porosity (figure 5.52). The incorporation of organic volatile compounds into the porous matrix is the cause of the superficial dark coloring of the altered structural elements.

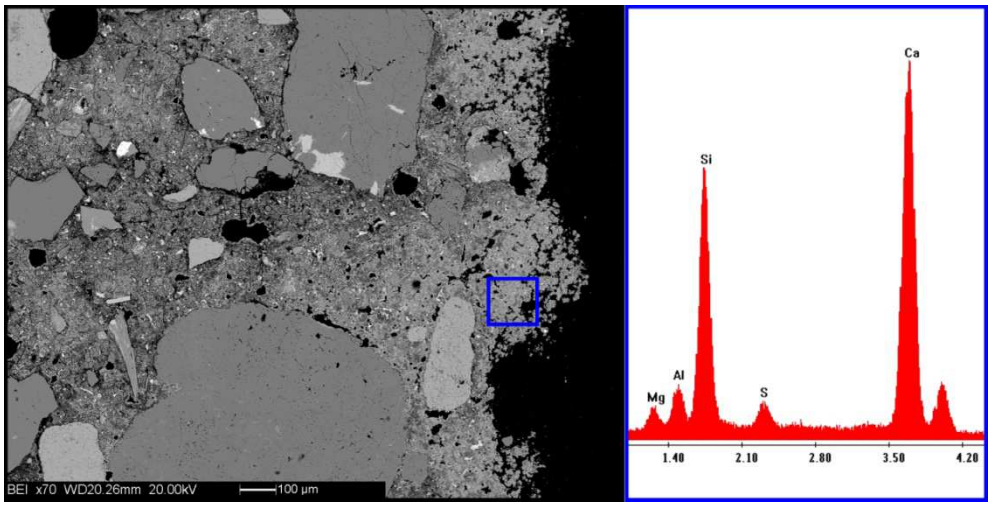

Figure 5.52. Sample MC3, SEM-BSE image of an external portion of conglomerate affected by sulfate attack and EDS microanalysis of the superficial altered layer

XRPD analyses highlighted the presence of Friedel's salt in the finer fraction of the materials (figure 5.53), due to the reaction between chlorides dissolved in pore solution and AFm phases. The presence of the secondary phase testifies the incidence of chloride attack in the conglomerates, due to capillary rise of saltwater from the soil.

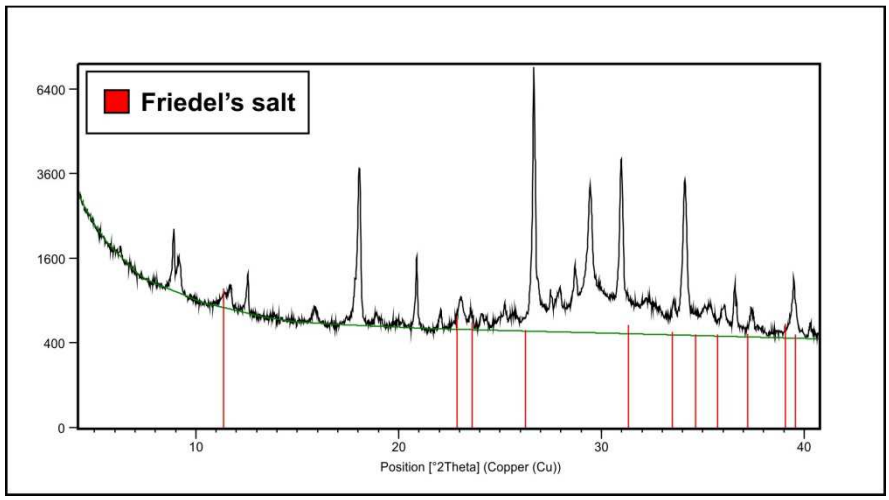

Figure 5.53. Diffraction pattern of the finer fraction of MC1 sample

Chloride attack is confirmed by SEM-EDS analyses, which showed the presence of aggregates of halite crystals precipitated in the pore network of the materials (figure 5.54).

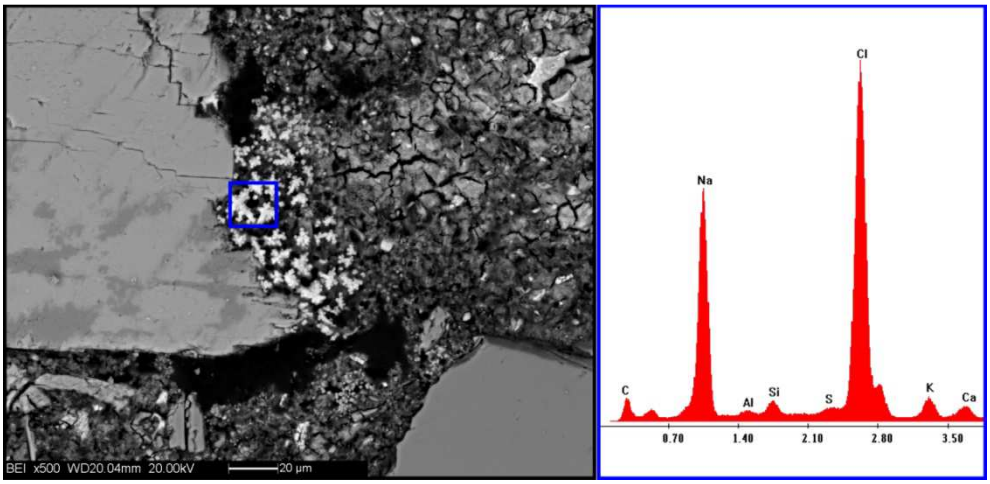

Figure 5.54. Sample MC1, SEM-BSE image and EDS microanalysis of halite crystals precipitated into the pore network

Chloride attack caused diffuse pitting corrosion of the rebars, with oxidation of the metallic iron and precipitation of secondary iron chlorides, as shown by EDS chemical maps performed on cross sections of the altered reinforcing rods (figure 5.55).

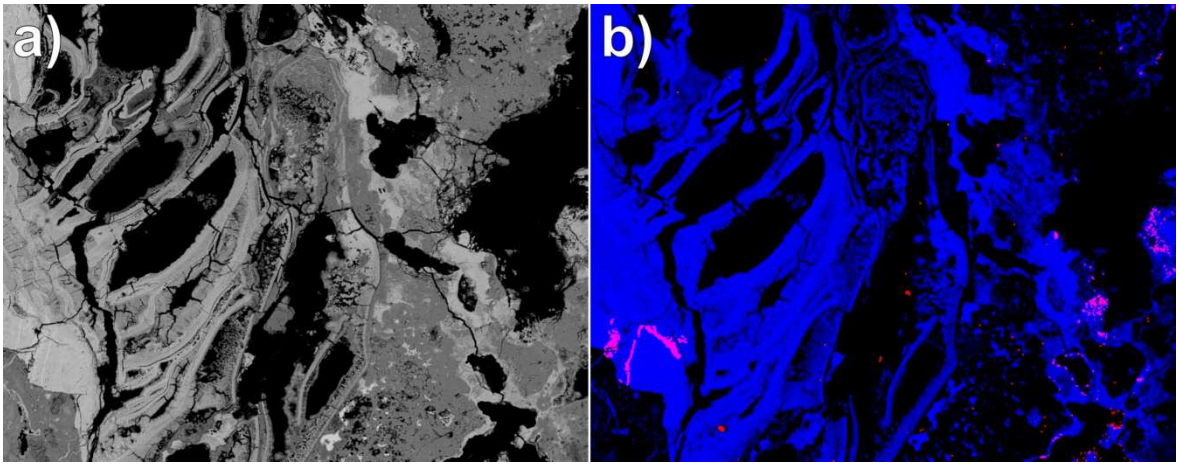

Figure 5.55. a) SEM-BSE image of an oxidized rebar in cross section (field of view: 1mm); b) false color image obtained by chemical maps merging (iron hydroxides in blue, iron chlorides in magenta, halite in red)

5.3.4 Ex-Zweifel Embroidery Plant

The thickness of the carbonated portions for the sampled cores, as determined by colorimetric tests, is reported in table 5.2.

Sample	Element	Carbonated portion (mm)
RP1	Column	18
RP2	Column	20
RP3	Column	20
RC1	Riddle	12
RT1	Beam	10
RT2	Beam	11
RA1	Arch	88

Table 5.2. Ex-Zweifel Embroidery Plant, thickness of the carbonated portions for the sampled cores

Tests highlighted the great influence of both the presence of protective layers and the quality of concrete on the progression of carbonation. The presence of the thick superficial mortar layer limited significantly the carbonation process on concrete of the beams and the riddle, while the absence of the protective layer on the columns influenced their higher carbonation, even though limited to the external portions and mainly comprised inside the concrete cover. On the contrary, concrete of the arches underwent total carbonation up to a depth of 88 mm from the external portions, despite the presence of the superficial protection layers: this is due to the poor quality of the materials and the high overall porosity, highlighted in chapters 3 and 4.

The results of the colorimetric tests are confirmed and integrated by the petrographic analyses performed on the materials. The occurrence of carbonation fronts at the interfacial zone between external carbonated portion and internal sound portions was observed for most of the samples in correspondence with the carbonation levels defined by the colorimetric tests (figure 5.56). No clear carbonation front can be observed in RA1 sample, not even in the core of the materials. Only limited, non carbonated areas are present in the core of the material (figure 5.57).

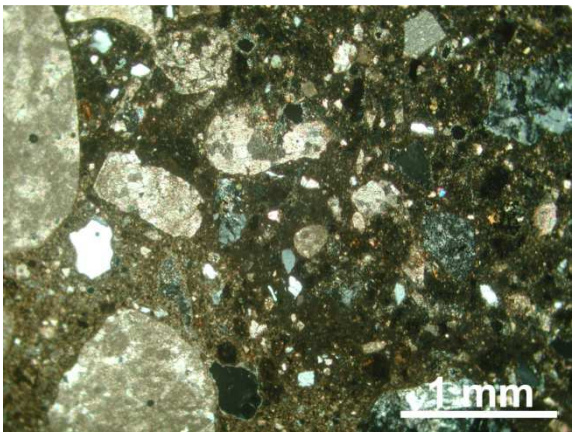

Figure 5.56. Sample RP2, carbonation front at an approximate depth of 20 mm (crossed polars microphotograph)

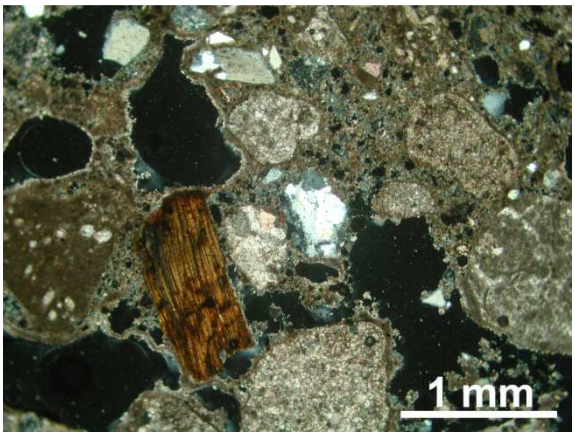

Figure 5.57. Sample RA1, intense carbonation in the core of the material, with limited presence of non carbonated areas (crossed polars microphotograph)

The mineralogical profiles of the finer fractions confirmed the previous observation. Most of the samples are totally carbonated in the external portions, as indicated by the absence of portlandite in the analyzed compounds, while the occurrence of portlandite in the internal portions indicated the permanence of the alkaline environment (figure 5.58). On the contrary, RA1 sample showed only traces of portlandite in the cores, indicating the almost total carbonation of the calcium hydroxide in these portions, too (figure 5.59).

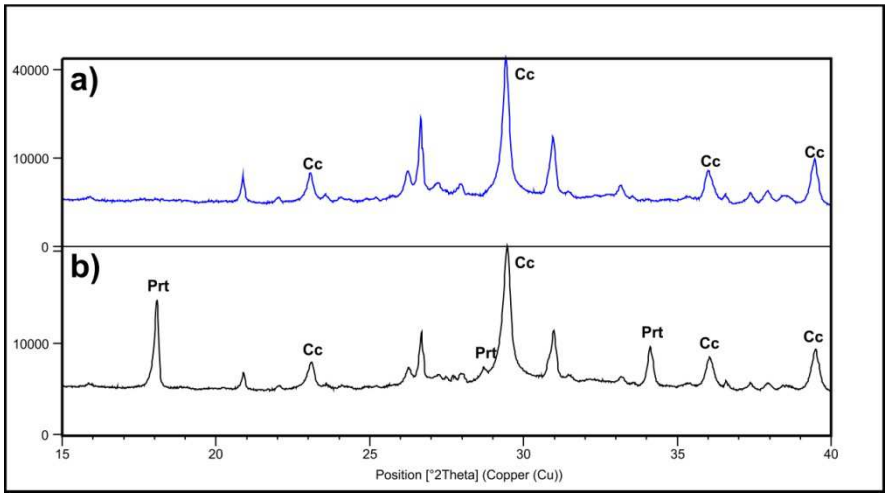

Figure 5.58. Diffraction patterns of the finer fractions of RP3 sample. a) = concrete cover, b) core. Abbreviations: Cc = calcite, Prt = portlandite

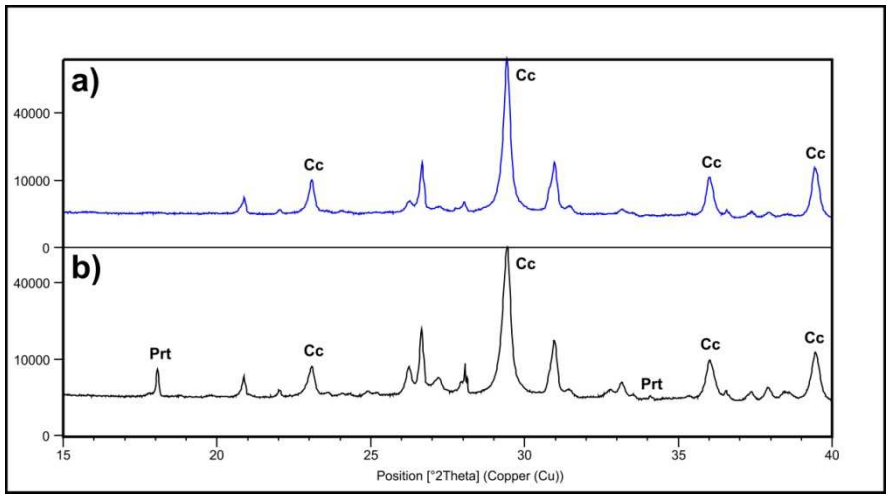

Figure 5.59. Diffraction patterns of the finer fractions of RA1 sample. a) = concrete cover, b) core. Abbreviations: Cc = calcite, Prt = portlandite

Profile chemical analyses performed on the cement matrices by SEM-EDS confirmed the petrographic and mineralogical observations. All samples, with the exception of RA1, are characterized by high calcium concentrations in the external carbonated portions, with mean Ca/Si molar ratios of 2.35, while the cores are characterized by lower values, with mean Ca/Si molar ratios of 1.39. The ratios show progressively decreasing trends moving toward the inner portions of the materials, with high variability in the most external layers and stabilization at uniform low values after the carbonation front determined by colorimetric analyses (figure 5.60). On the contrary, RA1 sample shows no clear trends in the variation of Ca/Si molar ratio along its stratigraphy, with a mean ratio of 1.98.

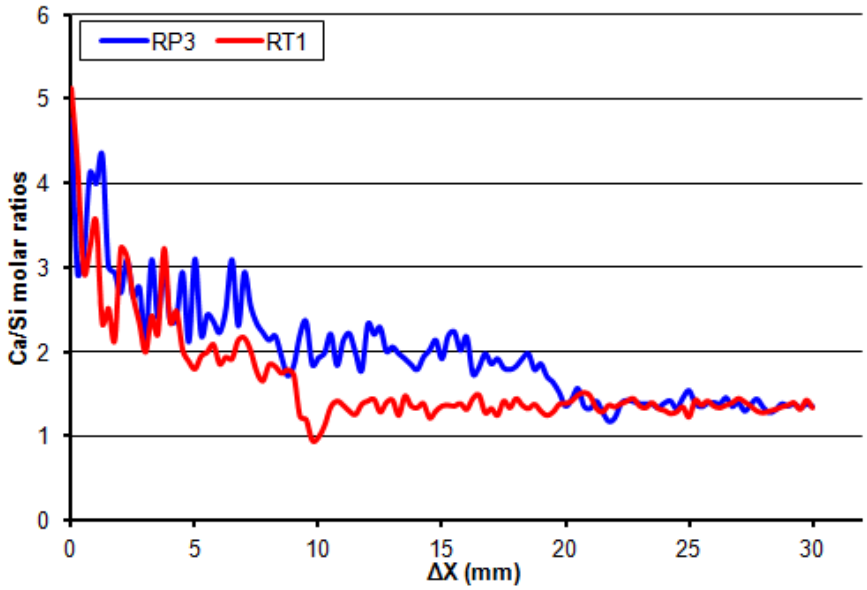

Figure 5.60. Profile chemical analysis performed on samples RP3 and RT1. Ca/Si molar ratios are reported

Besides carbonation, all concrete samples are affected by slight forms of sulfate attack, This form of alteration is highlighted by the occurrence of secondary sulfates in the most external layers of the materials, as shown by XRPD analyses on the finer fraction of the analyzed conglomerates (figure 5.61). The attack led to the formation of both gypsum and ettringite due to the reaction of sulfates in pore solution with portlandite and AFm phases, respectively. Anyway, its incidence in the conservation state of analyzed materials is reduced, as shown by the low concentrations of secondary sulfates with respect to the other crystalline phases. No traces of gypsum and ettringite are detectable in the internal portions of the materials (figure 5.61), and no clear signs of cracking of the cement matrix due to the alteration phenomenon are observable in the external portions.

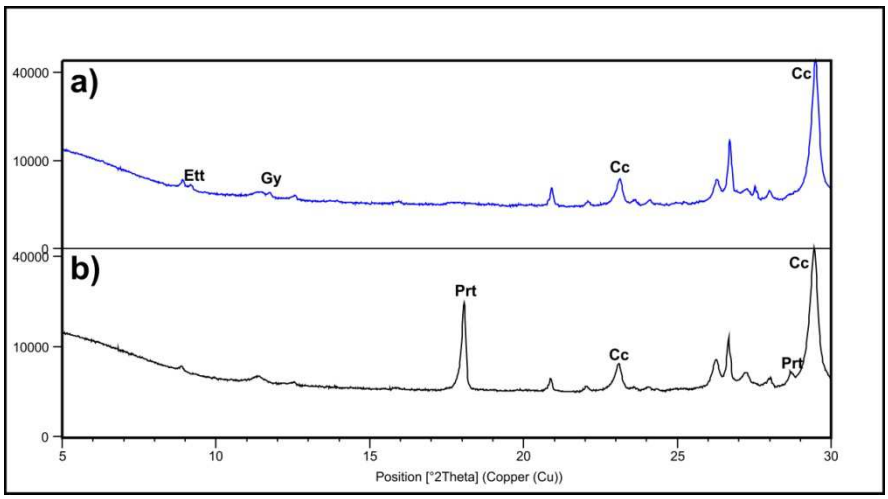

Figure 5.61. Diffraction patterns of the finer fractions of RP1 sample. a) = concrete cover, b) core.
Abbreviations: Cc = calcite, Prt = portlandite, Gy = gypsum, Ett = ettringite

5.3.5 Ex-Foro Boario

The thickness of the carbonated portions for the sampled cores and several concrete elements cross sections exposed by scarification, as determined by colorimetric tests, is reported in table 5.3. The carbonation tests on sample FP1 and scarification FP7 are reported in figures 5.62 and 5.63.

Sample	Element	Test	Carbonated portion (mm)
FP1	Column	Coring	5
FP2	Column	Coring	7
FP3	Column	Scarification	7
FP5	Column	Scarification	6
FP6	Column	Scarification	3
FP7	Column	Scarification	2
FT5	Beam segment	Scarification	12

Table 5.3. Ex-Foro Boario, thickness of the carbonated portions for the tested concrete elements

Figure 5.62. Colorimetric test on FP1 sample

Figure 5.63. Colorimetric test on FP7 scarification

Tests showed extremely limited progression of the carbonation front inside the materials, indicating a scarce incidence of carbonation phenomena on the concrete elements. For the columns, thickness is always under 10 mm, with an extension in some cases hardly detectable with the colorimetric test. Moreover, only a discoloration of the organic compound to a pinkish dye can be observed in the external portions, indicating only partial carbonation of the calcium hydroxide in the cortical layers of the materials. The partial carbonation phenomenon is always limited inside the concrete cover, thus the rebars show an excellent degree of conservation, with permanence of the superficial passivating layer (figure 5.63).

The tested beam segment is characterized by a higher extension of the carbonation front, even though limited to the external layers. Still, the limited carbonation caused intensive

scaling of the concrete elements, due to the lack of adequate concrete covering on the rebars, which underwent massive oxidation. The fracturing process caused by the alteration of the reinforcement triggered a further expansion of the carbonation front.

The results of the colorimetric tests are confirmed and integrated by the petrographic analyses performed on the materials. The occurrence of a clear carbonation front at the interfacial zone between external carbonated portion and internal sound portions have been observed for beam segment samples only, for FT5 in correspondence with the carbonation level defined by the colorimetric test (figure 5.64). No clear carbonation front can be observed for the other samples. Only limited, carbonated areas are present in the superficial portions of the materials (figure 5.65).

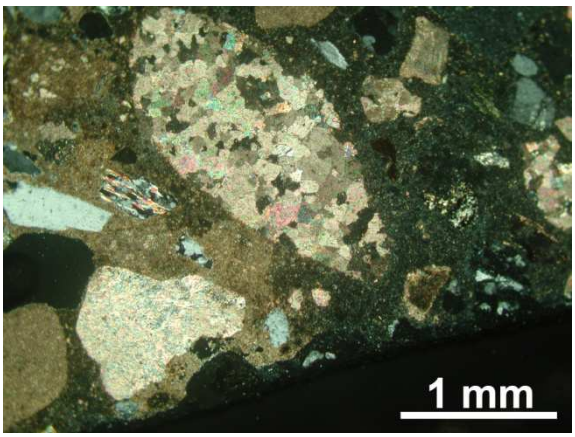

Figure 5.64. Sample FT5, carbonation front at an approximate depth of 12 mm (crossed polars microphotograph)

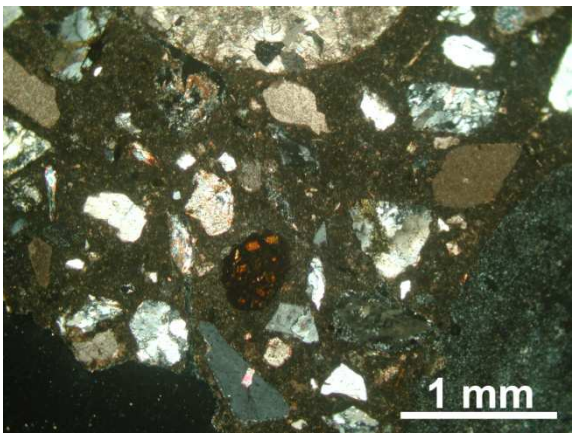

Figure 5.65. Sample FP2, limited carbonation in the external portions, absence of carbonation fronts (crossed polars microphotograph)

Mineralogical profiles of the finer fractions confirmed the previous observation. Most of the samples are only partially carbonated in the external portions, as indicated by the partial preservation of portlandite. The internal portions are completely non-carbonated in the analyzed compounds, as indicated by the presence of relevant amounts of portlandite in the finer fractions of the materials (figure 5.66). Calcite in these portions is entirely due to the finer fractions of the carbonate aggregate. Only the beam segment samples show no traces of portlandite in the external portions, indicating total carbonation in the cortical volumes of the material (figure 5.67).

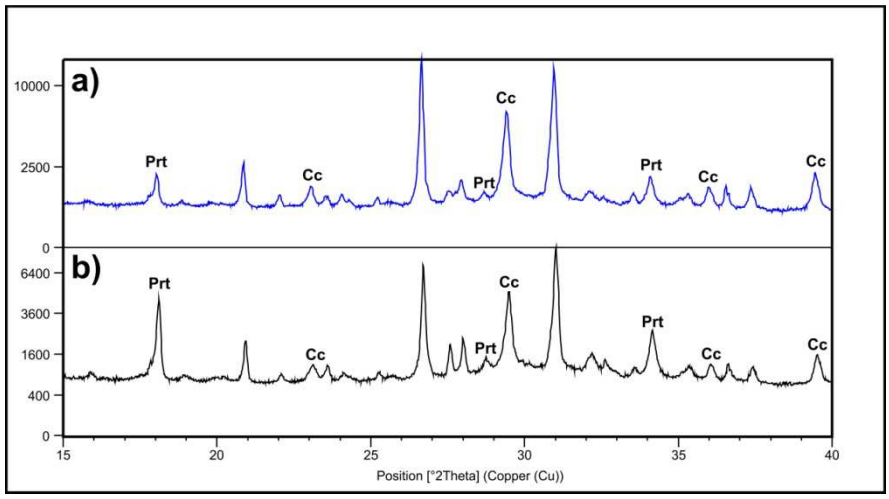

Figure 5.66. Diffraction patterns of the finer fractions of FP1 sample. a) = concrete cover, b) core.
Abbreviations: Cc = calcite, Prt = portlandite

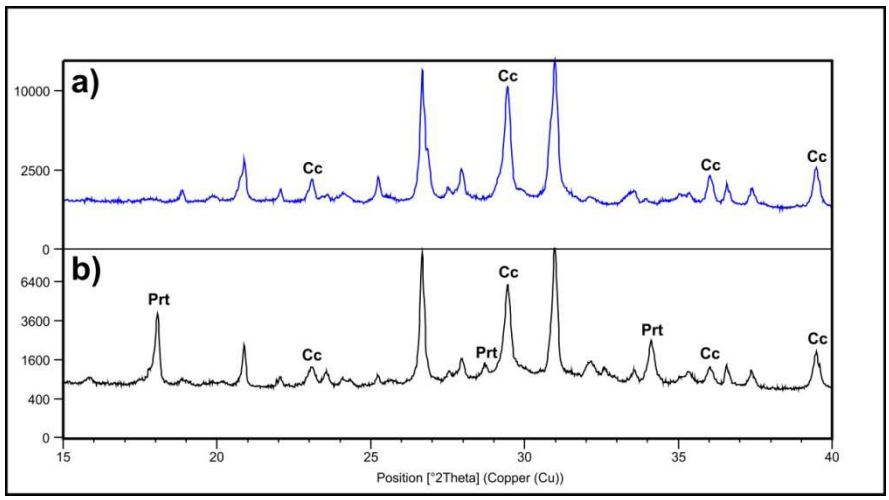

Figure 5.67. Diffraction patterns of the finer fractions of FT6 sample. a) = concrete cover, b) core.
Abbreviations: Cc = calcite, Prt = portlandite

The XRPD results are fully consistent with the chemical data obtained from SEM-EDS analyses. The cement matrices of the columns are characterized by variable but overall higher Ca/Si molar ratios in the external, partially carbonated portions, with mean values of 1.74, while the internal portions are characterized by more homogeneous Ca/Si molar ratios, with mean values of 1.40. The cement matrix of the analyzed beam segments is characterized by high Ca/Si molar ratios in the external portions, with medium values of 2.30, while the internal portions are characterized by Ca/Si molar ratios comparable with the ones of the columns, with mean values of 1.38.

All concrete samples are affected by slight forms of sulfate attack. This form of alteration is highlighted by the occurrence of secondary sulfates in the finer fractions of the

materials, as shown by XRPD analyses (figures 5.68, 5.69). As for the columns, the attack led to the formation of both gypsum and ettringite due to the reaction of sulfates in pore solution with portlandite and AFm phases, respectively. As for the beam segments, a more intense gypsum formation is observable in the external portions, without the occurrence of secondary ettringite. The concentrations of the phases show decreasing gradients moving towards the inner portions of the materials, leading to the disappearance of ettringite and the reduction of gypsum. The latter phase is detectable in traces also in the core of the materials, indicating a more intense progression of the sulfate attack with respect to the carbonation, due to saturation of the connected capillary porosity with sulfate-rich percolating solutions. Anyway, its incidence on the conservation state of the analyzed materials is reduced, as shown by the low concentrations of secondary sulfates with respect to the other crystalline phases. Confirming that, no clear signs of cracking of the cement matrix due to the alteration phenomenon are observable in the samples.

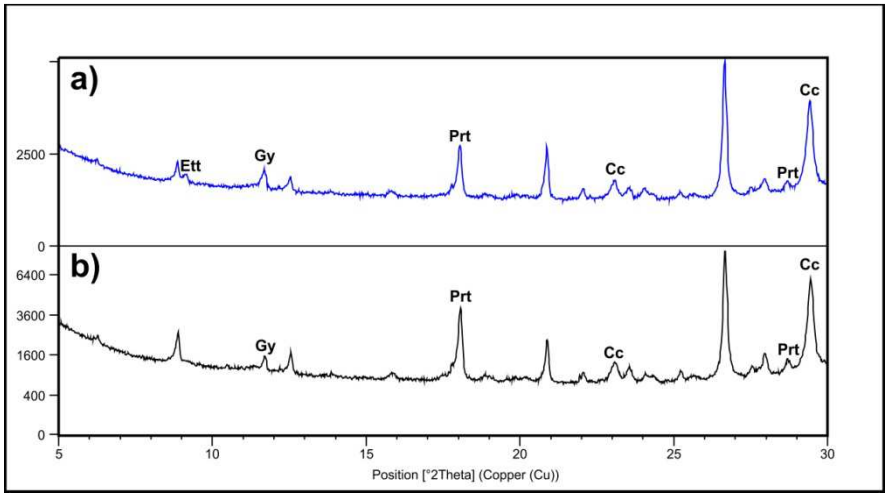

Figure 5.68. Diffraction patterns of the finer fractions of FP2 sample. a) = concrete cover, b) core.

Abbreviations: Cc = calcite, Prt = portlandite, Gy = gypsum, Ett = ettringite

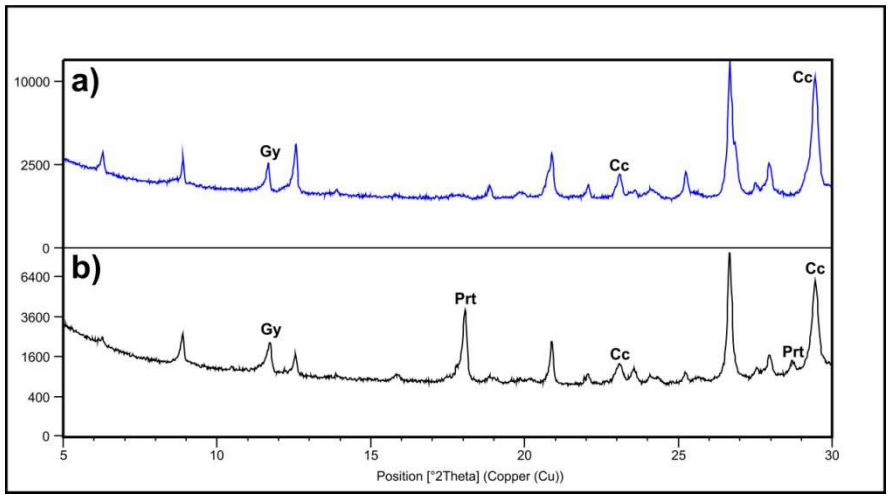

Figure 5.69. Diffraction patterns of the finer fractions of FT6 sample. a) = concrete cover, b) core.
Abbreviations: Cc = calcite, Prt = portlandite, Gy = gypsum, Ett = ettringite

The analytical results indicated a reduced incidence of alkali-aggregate reactions, due to the interaction between the inert fraction and alkalis in pore solution. The enrichment of alkalis in pore water is due to alkalis leaching events from the cement matrix in alkaline environment, deriving from the original binder. Microanalyses on residual clinker grains highlighted the occurrence of significant amounts of potassium in the cement (mean K_2O concentration of 1.23 %), generally as constituent of soluble sodium salts.

The dissolution of aggregate particles constituted by microcrystalline or amorphous silica due to the break-up of Si-O-Si bonds released silica in solution which reacted with potassium to form hydrated amorphous silica gels. ASR interested the chert fragments present in the inert fraction of the concrete as subordinate constituents. The clasts appear stressed and strongly corroded at the interface with the surrounding matrix, and several cracks develop radially to the altered grains, due to the expansive action of the secondary ASR products (figure 5.70). No clear deposition of ASR gels is observable in the cement matrix, due to the fact that the gel products easily undergo desiccation processes, and subsequent elimination by water circulation. Anyway, in several altered grains secondary pores partially filled with a mixture of amorphous silica and ASR gels are observable (figure 5.71). Given the low volumetric fraction of chert fragments over the total aggregate, the incidence of ASR on the overall conservation state of concrete is negligible, and the development of secondary cracking patterns is limited around the altered grains only.

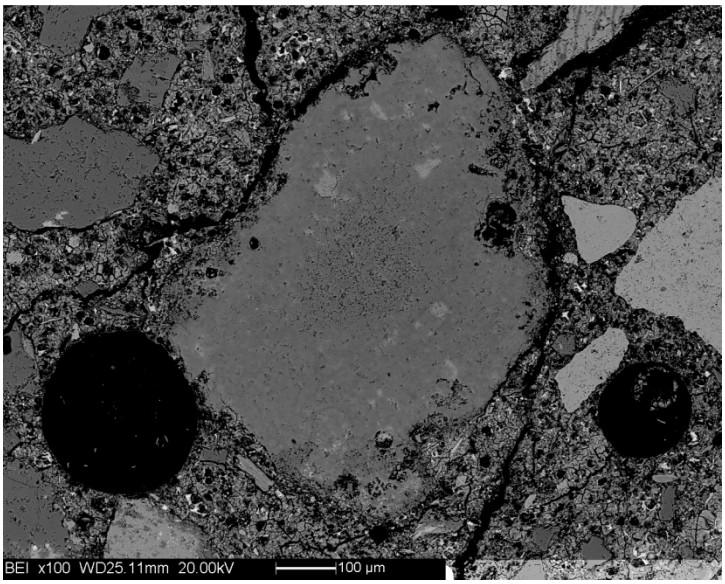

Figure 5.70. Sample FP1, chert grain altered by ASR (SEM-BSE image)

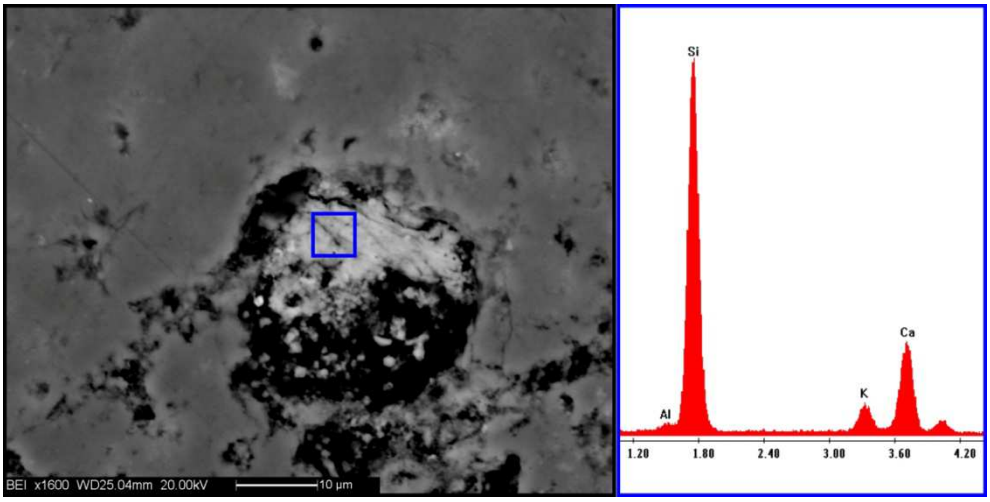

Figure 5.71. Sample FP1, SEM-BSE image and EDS microanalysis of a secondary void on a chert grain, partially filled with a mixture of ASR gels, amorphous silica and secondary carbonates

Alkali-aggregate reactions interested the carbonate fraction of the aggregate, too. Petrographic analyses and SEM observations highlighted the occurrence of interfacial dissolution of dolostones and magnesium limestone fragments, with formation of reaction rims due to the de-dolomitization processes caused by ACR (figures 5.72, 5.73). EDS microanalyses on the reaction rims showed their calcium carbonate composition (figure 5.74). The absence of magnesium secondary phases is due to the dissolution of brucite in pore solution and subsequent mobilization and diffusion through the pore network of the components.

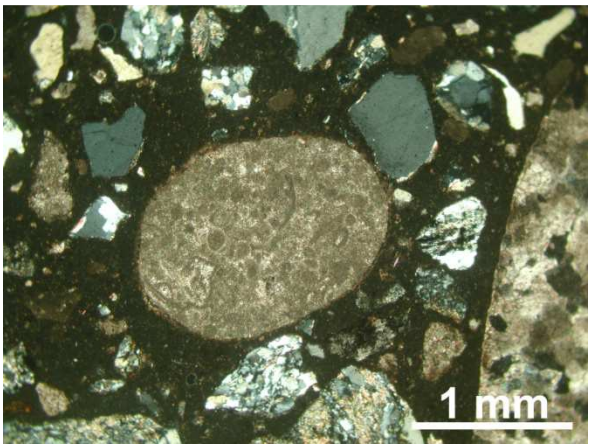

Figure 5.72. Sample FP7, dolostone grain altered by ACR (crossed polars microphotograph)

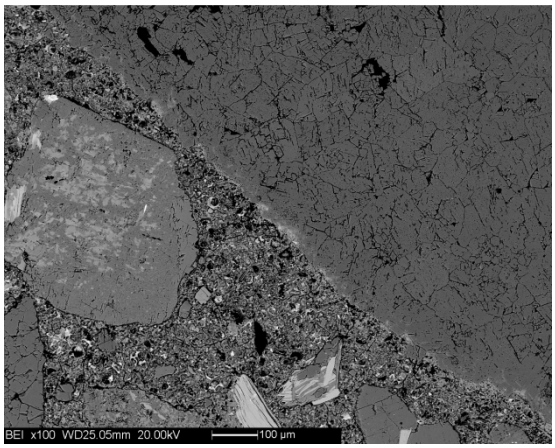

Figure 5.73. Sample FP1, magnesium limestone fragment altered by ACR (SEM-BSE image)

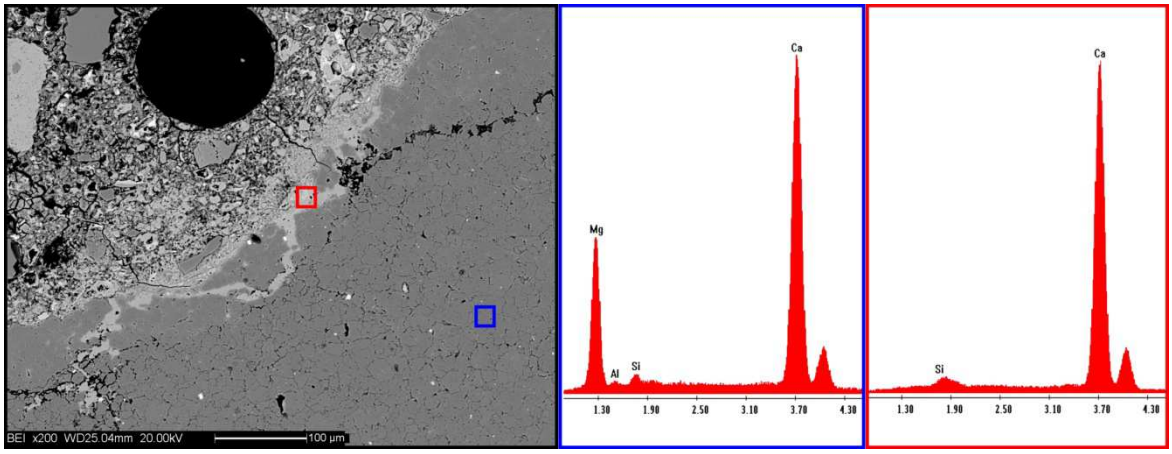

Figure 5.74. Sample FP1, SEM-BSE image of a reaction rim on an altered magnesium limestone grain and EDS microanalyses of both a sound and altered portion (highlighted in blue and red, respectively)

ACR is confirmed by the occurrence of secondary magnesite in the finer fractions of the materials (figure 5.75), due to carbonation of brucite formed after the de-dolomitization process and crystallized into the pore network during evaporation cycles of the pore-water related to environmental relative humidity variations.

Even if more diffuse than ASR, due to the predominant carbonate composition of the inert fraction, alteration by ACR did not cause severe degradation of the concrete elements, being limited only to a partial dissolution of the degraded grains, without the development of anomalous cracking patterns.

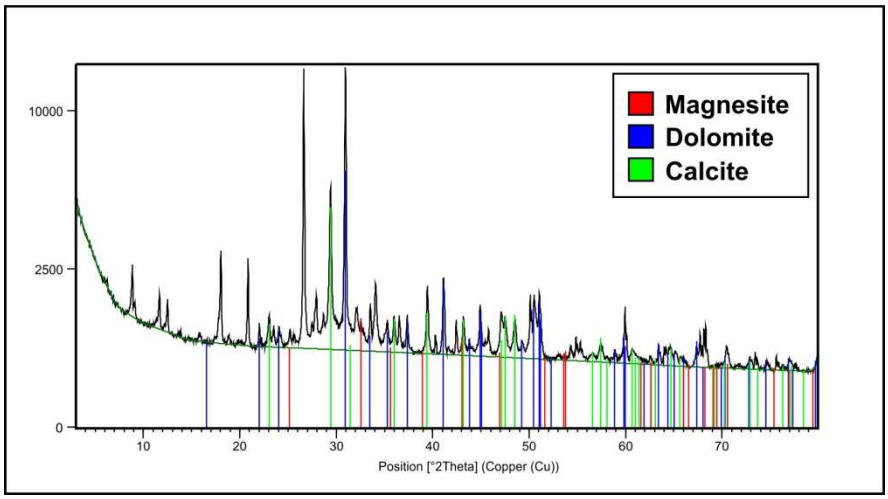

Figure 5.75. Diffraction pattern of the finer fraction of FP5 sample

5.4 CONCLUSIONS

The multianalytical approach adopted for the characterization of the conservation state of the concrete elements constituting the studied buildings highlighted the incidence of several alteration phenomena on the materials.

Amongst the various forms of degrade, carbonation resulted the most diffuse and the one responsible for the most severe damages. Moreover, its widespread diffusion hindered in some cases the development of further forms of concrete alteration.

Furthermore, external sulfate attack interested all the structures. Apart from the concrete elements of the C3 building of the Ex-Agrimont Area, this form of alteration had a limited incidence on the overall conservation state of the structures, still being at an initial and localized state of progression.

Chloride attack interested only C3 building of the Ex-Agrimont Area, being the structure built near the coastline and thus interested by capillary rise of saltwater through the pore network.

Finally, the Victory Monument and Ex-Foro Boario were interested by alkali-related attacks, for both structures in the form of alkali-aggregate reactions, and for the former also in the form of alkaline salts crystallization.

Amongst the triggering factors for the alteration phenomena, compositional and textural characteristics of the materials resulted of crucial importance: the inadequate selection of both binder and aggregate caused the development of AAR for the Victory Monument and Ex-Foro Boario, while the adoption of wrong mix designs and poor concrete casting

caused anomalous development and progression of alterative processes in several structural elements.

The protection of concrete elements with superficial sacrificial layers contributed significantly to the better static and aesthetic conservation of the buildings.

Finally, the construction of the buildings in areas characterized by unfavorable environmental exposure caused in some cases rapid and intense degradation of the concrete elements, with great consequence on the static behavior of the structures. This is the case of the Victory Monument, where a combination of poor concrete quality and exposition to massive water percolation and relative humidity variations caused severe degrade of the substructure. Furthermore, the massive degradation of C3 building of the Ex-Agrimont Area is even more significant, having caused a diffuse alteration of concrete elements characterized by excellent mix design and casting procedures. This anomalous decay is mainly related to the exposure of the structure to severe environmental and soil pollution, related to the industrial activities of Porto Marghera, and caused the development of combined and never previously described forms of alteration, which will be thoroughly analyzed in the following chapter.

CHAPTER 6

Concrete degradation by combined sulfate-phosphate attack

6.1 INTRODUCTION

The alteration of concrete structural elements due to the action of external chemical degrading agents is one of the main causes for the reduction of the service life of modern structures. These dynamics are particularly aggressive in environments characterized by heavy soil and atmospheric pollution, leading to a progressive decalcification of the cementitious matrix and oxidation of the rebars (Tulliani et al., 2002; Marinoni et al., 2003). Amongst the various forms of concrete chemical degrade, the external sulfate attack has been widely studied over the last two decades, and various theories on the effective contribution of this alteration dynamic on the physical and mechanical decay of concrete structures have been formulated (Skalny et al., 2001; Collepardi, 2003; Neville, 2004).

Yet, there are few literature references regarding phosphate attack in cementitious materials. Some authors refer to limited concrete decalcification under the action of phosphoric acid. Also, an experimental and modeling study on concrete samples in contact with phosphate-rich solutions has been carried out for the assessment of potential phosphate ions-concrete interactions (Naus et al., 2006). The results of this integrated study showed that, although the model demonstrated that the formation of hydroxylapatite after portlandite is thermodynamically favored in such systems, instead this mineral phase is not found experimentally, mainly due to unfavorable kinetic factors.

Nevertheless, the interaction between phosphates and concrete has never been evaluated taking into consideration systems far from equilibrium and characterized by local pH and chemical concentration gradients. Moreover, the interaction between phosphate attack and other forms of concrete chemical degrade has never been taken into consideration.

As stated in chapter 2, the Agrimont industrial facility produced, from 1927 to 1997, phosphate- and ammonia-based fertilizers through the classic and widely adopted wet process (Moudgil et al., 2010); the final products of the industrial facility were superphosphoric and phosphoric acids, granulated triple superphosphate, monoammonium and diammonium phosphates. Given the bad conservation state of the C3 building and the heavy pollution that interested the area over the last few decades, the building was intensively studied in order to determine the possible interaction between phosphates and concrete, recognize the correct sequences of secondary phases crystallization, and thermodynamically model the evolution of the degrade.

6.2 PRODUCTION OF PHOSPHATE-BASED FERTILIZERS

Phosphorus is one of the primary nutrients essential for plant growth and crop production. Phosphorus is highly reactive, hence it occurs in nature as phosphate ion (PO_4^{3-}), combined with various cations to form phosphate minerals, amongst which the most diffuse ones are calcium phosphates. In the biologic processes, the phosphate ion combines with various atoms and molecules within living organisms to form different compounds essential to life, such as DNA, ATP and ADP. Also, it is the main mineral constituents of bones and teeth. Plants uptake phosphate from the soil along with nitrogen, potassium and a number of other nutrients they need to thrive. Then, the compound is assimilated by animals in the food chain (Moudgil et al., 2010).

Phosphate fertilization of soils has always been important. In case of phosphate deficiency of the soil, vast areas of agricultural land may result in poor production. The phosphorus problem in soil fertility is threefold. First, the total phosphorus level of soils is low, usually no more than one-tenth to one-fourth the level of nitrogen, and one twentieth that of potassium. Second, the phosphorus compounds commonly found in soils are highly insoluble, and thus mostly unavailable for plant uptake. Third, when soluble sources of phosphorus, such as those in fertilizers and manure, are added to soils, they are fixed and form highly insoluble compounds. For all these reasons, intensive fertilization of soils has always been of crucial importance in agriculture, together with the development of effective strategies and products to improve this process (Moudgil et al., 2010).

The most readily available source of soluble phosphate for fertilization use is manure, derived from excrements of animals, and compost, the decomposed remnants of organic

materials, mainly plants. Nevertheless, manure and compost provide relatively low nutrient content, and too much manure or compost in one location will increase the likelihood of polluting the groundwater with the nitrates and/or pathogens borne by the materials. Furthermore, all the activities related to the use of these products (collection, handling, storage, transport and spreading) are highly expensive and labor-intensive on large-scale agricultural fields.

For these reasons, the production of phosphate-based fertilizers by chemical extraction from insoluble minerals became widespread since the 1840s. The main sources of phosphate minerals are naturally-occurring sedimentary deposits of phosphorites, sedimentary rocks containing significant amounts of cryptocrystalline fluorapatite and hydroxylapatite, in concentration of about 30% on the total mass. After the mining, phosphorites need to be beneficiated from accessory minerals, mainly clay minerals. To perform this, the raw material is dumped into a pit where high-pressure water guns create a slurry which is then pumped to the beneficiation plant. At the beneficiation plant the sand and clay are separated from the phosphate, and the resulting material is dried, crushed and finally sent to the chemical processing plant.

The most used technique for the production of phosphate-based fertilizers is the so-called wet process method. In a wet process facility, phosphoric acid is produced by the reaction of sulfuric acid with phosphate raw materials. Phosphate rocks powder is continuously fed into the reactor along with sulfuric acid. The reaction combines calcium from the phosphate rock with sulfate forming phosphoric acid and calcium sulfate, mainly gypsum (called phosphogypsum), according to the following simplified reaction:

$$Ca_5(PO_4)_3(OH,F,Cl) + 5H_2SO_4 + 10H_2O \rightarrow 3H_3PO_4 + 5[CaSO_4 \cdot 2H_2O]\downarrow + H(OH,F,Cl) \quad (6.1)$$

During the reaction, phosphogypsum crystals precipitate and are separated from the acid by filtration and washing. After washing, the obtained slurry is pumped into a pond for storage. Wet process phosphoric acid normally contains 26% to 30% of P_2O_5. Depending on the types of fertilizer to be produced, phosphoric acid is usually concentrated to 40% to 55% of P_2O_5 by using a series of vacuum evaporators.

Concentrated phosphoric acid reacts with ammonia and is granulated to produce diammonium phosphate (DAP) and monoammonium phosphate (MAP). Granular triple superphosphate (GTSP), a non-nitrogen fertilizer, is produced by adding phosphoric acid to ground phosphate rock. DAP fertilizer is water-soluble and is available for vegetation to take up through their roots.

The production of fertilizers requires and produces a large volume of process water. This is the water source for the phosphoric acid, gas scrubbing, phosphogypsum slurry for transportation and storage, operation of condensers, as well as other uses in the chemical complex. The process water has a pH of about 1 to 2 and contains a dilute mixture of phosphoric, sulfuric, and fluosilic acids. The process water is saturated with calcium sulfate and contains several other ions found in phosphate rock, as well as ammonia from the solid fertilizer-manufacturing process. The process water is treated with lime to raise the pH to about 4.5, then any solids formed are removed, lime is added again to raise the water's pH to about 11, again newly-formed solids are removed, the water is air stripped to remove ammonia, and acid is added to reduce the pH to about 6.5.

6.3 ENVIRONMENTAL SETTING OF THE AREA

The Porto Marghera industrial area suffered from heavy pollution during the 20th century, due to uncontrolled emissions from chemical industries and oil refineries. The dangerousness of productive activities in the industrial area was stated on the technical norms for the actuation of Venice urban planning themselves, in effect between 1962 and 1990. The document stated that "in Porto Marghera industrial area productive plants will be established, which will both spread in the atmosphere dusts and fumes dangerous for human health, and discharge in water toxic compounds, apart from producing vibrations and noise" (Chinello, 1975).

The most relevant pollution episode in the area was the uncontrolled emission of toxic by-products related to the production of vinyl chloride in the Montedison production plants. For years, the employees of the petrochemical factories were exposed to concentration of vinyl chlorides several times greater than the maximum concentrations bearable by the human body, with development of serious pathologies. Furthermore, uncontrolled discharges caused relevant phenomena of pollution of both marine and ground water.

Apart from this specific case, all production plants of the area were responsible for severe forms of water, soil and atmosphere pollution. During the years of maximum expansion of the area, the excavation of unauthorized dumps for the storage of toxic waste was common, as well as the uncontrolled dumping and dispersion of by-product slurries and non-depurated process waters. All these activities contributed to the progressive pollution of the groundwater and soils of Porto Marghera, utilized for domestic and agricultural activities,

with abnormal amounts of chlorinated and aromatic solvents, aromatic hydrocarbons, phenols, ammonia, aromatic amines, sulfates, phosphates, lead, cadmium, zinc, mercury and arsenic. Moreover, waters and sediments of the Venice lagoon underwent strong pollution, with consequent adulteration and poisoning of the fish and mollusc population.

The Ex-Agrimont area was interested by an intense soil and water pollution due to the leakage of process water from the industrial plant, rich in phosphates, sulfates and ammonia and characterized by acidic pH values, spreading from 2.1 to 6.5 according to the degree of alkalinization of the solution (table 6.1).

Parameter	**Value**
pH	2.1 – 6.5
Calcium, Ca (mg/l)	538
Magnesium, Mg (mg/l)	223
Sodium, Na (mg/l)	2260
Potassium, K (mg/l)	210
Iron, Fe (mg/l)	59
Manganese Mn (mg/l)	15
Chloride, Cl (mg/l)	140
Fluoride, F (mg/l)	4120
Sulfate, SO_4^{2-} (mg/l)	6200
Total phosphorous, P (mg/l)	6600
Ammonium nitrogen, N (mg/l)	1240

Table 6.1. Phosphate production plants, typical pond water analysis (Moudgil et al., 2010)

As for atmospheric emissions, a detailed monitoring of the years of maximum expansion of the area is not available. Yet, an intensive monitoring campaign performed by the Regional Association for the Environmental Protection (ARPA) during the years 1998-2004, when most of the factories had already closed, still showed a particularly severe atmospheric pollution from sulfates and nitrates (table 6.2).

Pollutant	**1998**	**1999**	**2000**	**2001**	**2002**	**2003**	**2004**
SO_x	19376	16468	21475	21498	21126	21238	21879
NO_x	14433	12711	15340	13968	13950	14536	14421
CO	1969	1328	1472	867	722	845	802
OVC	1664	1194	1034	981	1324	993	1088
IVC	873	568	556	464	429	492	483

Table 6.2. Porto Marghera industrial area, environmental multipollutants emissions (Tomiato & Zanardini, 2005). Values expressed in tons/year. OVC: organic volatile compounds; IVC: inorganic volatile compounds

6.4 CONSERVATION STATE OF THE STRUCTURE

Despite the overall quality of concrete and its good mechanical properties, highlighted in chapters 3 and 4, the conservation state of the structure is very bad, as all concrete elements are covered by superficial incoherent black crusts related to sulfate attack phenomena (figure 6.1), as highlighted in chapter 5.

Figure 6.1. Superficial black crusts on a concrete arch due to sulfate attack phenomena

The degradation of reinforced concrete elements is further accentuated in the south-western portion of the structure, near the platform originally used for the direct load on trains of final products and by-products. In this area, up until 2 meters of height, the reinforced concrete of the arches and other structural elements is highly exfoliated and an

almost total decalcification of the cementitious matrix can be observed, substituted by an incoherent white-yellowish material. Also, the rebars are totally oxidized, and thick globular superficial concretions are present (Figures 6.2, 6.3).

Figure 6.2. Conservation state on an arch in the south-western portion of the structure

Figure 6.3. Detail of figure 6.2. Total decalcification of the cement matrix and rebars oxidation

The alteration materials are arranged according to a marked stratigraphic heterogeneity, clearly evident in cross section (Figure 6.4): superficial concretions are clearly visible, covering a superficial black crust of variable thickness, with mean values comprised between 1 and 3 mm. The cementitious matrix in the first 3-5 cm from the outer portions is widely altered and replaced by a white-yellowish material. Furthermore, the rebars are totally oxidized and the surrounding matrix is permeated by iron hydroxide. Only limited unaltered portions are still present.

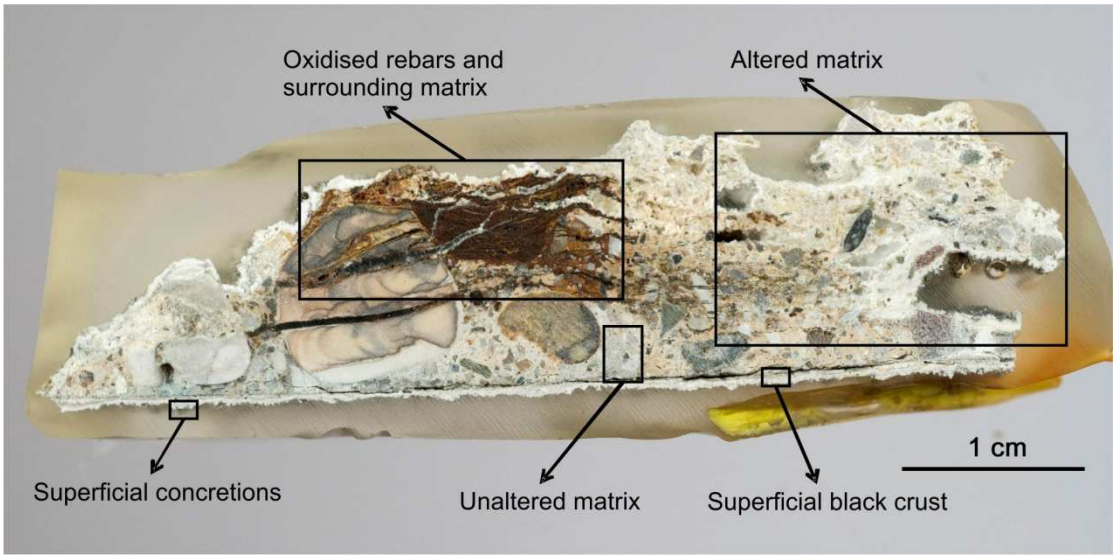

Figure 6.4. Textural aspect of the materials in cross section

6.5 CHARACTERIZATION OF THE ALTERED MATERIALS

6.5.1 Experimental

A selection of altered concrete samples was collected from different structural elements of the building, at heights below 2 meters, where the superficial scaling is more pervasive. Preliminary rebound hammer tests were carried out in order to identify the most representative sampling points. Coring was unsuccessful due to the extensive lack of coherence of the materials, so the samples were mechanically separated from the substrate with a metal chisel and superficial concretions were collected with a scalpel. 9 samples of altered concrete were taken (figure 6.5), 3 from adjacent arches (B2A1, B2A2, B2A3), 3 from the outer walls of the structure (B2M1, B2M2, B2M3) and 3 from the railway platform (B2B1, B2B2, B2B3). Moreover, 3 samples of superficial concretions (B2E1, B2E2, B2E3) were taken from areas adjacent to B2A1, B2M1 and B2B1 sampling points.

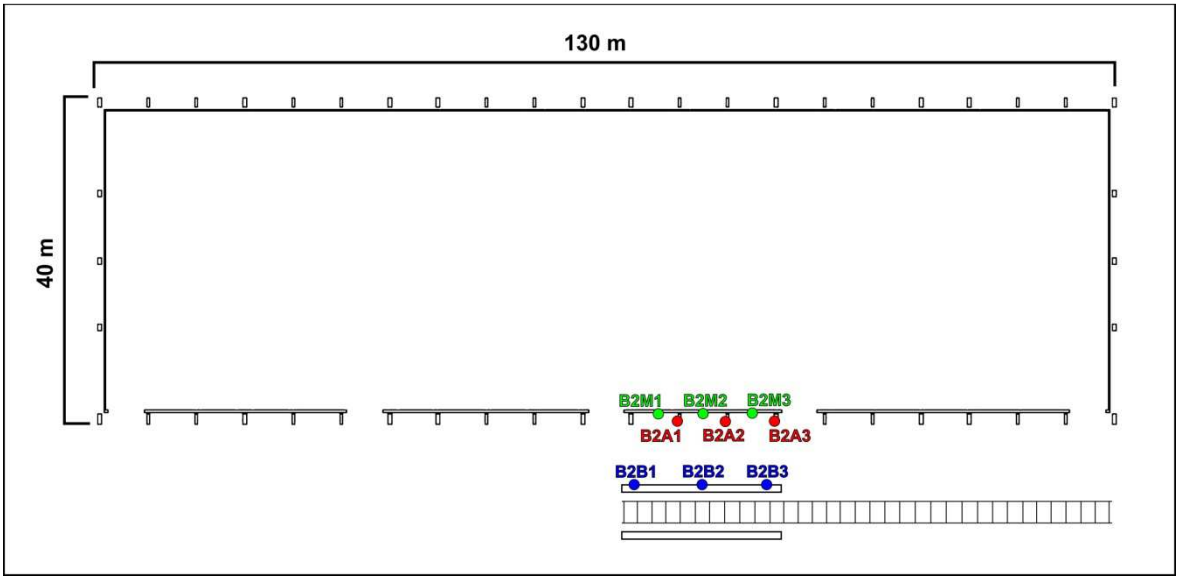

Figure 6.5. Plan of the structure and sampling locations

Portions of altered concrete samples were impregnated with epoxy resin and sectioned transversally to obtain 30 μm thin sections. The thin sections were observed with a polarizing microscope to obtain a preliminary morphological characterization of the secondary phases. Then, explorative bulk XRPD analyses were performed on the fraction under 63 μm of the samples, dry disaggregated and sieved, with a Philips X'Change

diffractometer in Bragg-Brentano geometry equipped with a Cu X-ray tube operating at 40 kV and 40 mA (CuKα radiation), and an X'Celerator detector, both mounted on a PW1050/37 theta-2theta vertical goniometer. Data acquisition was performed operating a continuous scansion from 3.01° [2θ] to 79.99° [2θ], at an acquisition rate of 0.02° [2θ] per second. Diffraction patterns were interpreted with X'Pert HighScore Plus 3.0 software by PANalytical, reconstructing mineral profiles of the compounds by comparison with ICDD and ICSD databases.

The bulk XRPD study was integrated with a detailed profile mineralogical study for the reconstruction of secondary phases stratigraphy. A series of localized profile micro-samplings was performed on the altered paste of the samples with a MicroMill® microsampling device developed by New Wave Research (figure 6.6). The precision milling device is constituted by a low-eccentricity/high-torque milling chuck with variable speed (1,200-35,000 rpm) where tungsten-carbide milling tools for sampling at high spatial resolution can be installed. The samples are fixed on a motorized 50 mm stage moving in X, Y, Z directions with sub-micron step resolution. The micro-positioning system is constituted by a high-resolution stereo microscope (6.7X to 40X optical zoom), a color CCD video camera (24.5mm to 3.3mm field of-view) and a second color CCD camera (3X digital magnification) for in-process viewing of mill bit.

Figure 6.6. MicroMill® microsampling device

Materials were sampled along 50 μm thick paths, parallel to the external surface, at a distance of about 200 μm from each other. XRPD analyses were then performed on the

micro-samples with the same instrument and the same acquisition parameters used for the execution of bulk XRPD analyses. Given the low quantities of sampled material, the diffraction patterns were acquired on a SiC zero-background.

To further integrate the profile mineralogical study, synchrotron-based space resolved profile micro-diffraction analyses were performed on samples B2A1 and B2B2, which showed the most marked stratigraphic heterogeneity. After being consolidated by epoxy resin vacuum impregnation, samples were cut transversally, mounted on 300 µm thick Plexiglas foils and reduced to a thickness of 100 µm. Measurements were performed at the µ-spot beamline of BESSY II third generation synchrotron radiation facility in Berlin. The beamline was constructed and installed by ACCEL instruments GmbH as a second branch (40 mrad off-center) of the 7 T wavelength-shifter, utilizing the optical hutch of the BAMline (Gorner et al., 2001). The accessible energy range is 1.9–30 keV, provided by a fixed exit double crystal monochromator with three sets of crystals (Si 111, Si 311 and Ge 111). The energy resolution can be varied between $\Delta E/E = 10^{-4}$ (Si 311) and $\Delta E/E = 10^{-2}$ (Si/W multilayer on Si 311). Several flexible optical schemes make it a multi-purpose beamline for applications in X-ray diffraction and X-ray spectroscopy (Erko et al., 2004).

The micro-XRPD experiments were performed in transmission geometry with a wavelength of 1.0656 Å, corresponding to a beam energy of 15 KeV. The diffracted intensities were collected by a MarMosaic 225 2D-detector with 3072 x 3072 pixels, placed at a distance of 218.458 mm from the sample. The utilized experimental setup can be seen in figure 6.7.

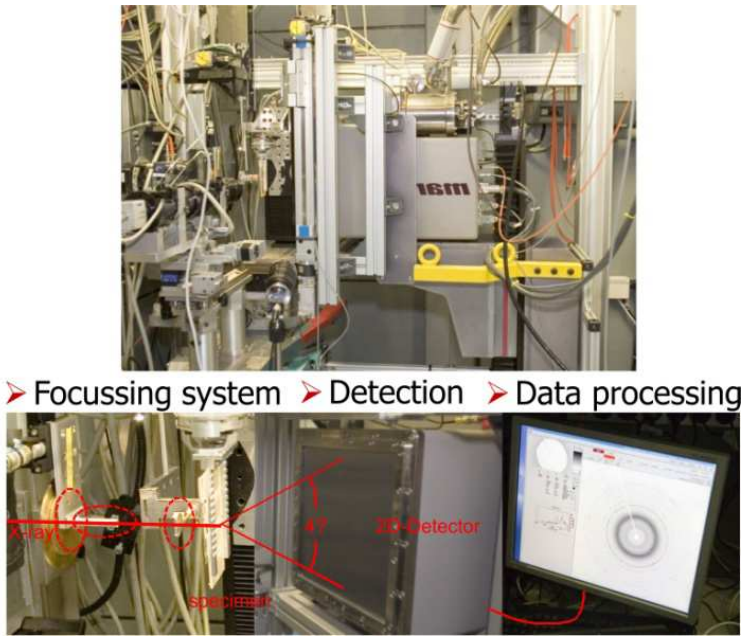

Figure 6.7. The micro-XRPD experimental setup in use at the µ-spot beamline

The spot sizes of the synchrotron radiation varied between 30 and 250 µm, according to the dimensions of mineral aggregates to be investigated and to avoid aggregate grains. Besides carrying out point analyses, a series of linear scans were performed parallel to the reaction fronts, in areas free of aggregate, with a spatial resolution of 30 µm. This allowed a significant increase in count statistics.

The mineralogical study was integrated performing profile microchemical and microstructural analyses on both thin sections and massive samples using a Camscan MX 2500 scanning electron microscope (SEM), equipped with a LaB_6 electron source and an EDAX energy dispersive X-ray detector (EDS). Qualitative interpretation of spectra and semiquantitative estimation of chemical profiles were performed through SEMQuant Phizaf software. Furthermore, chemical maps were acquired and processed by the image analysis procedure described in chapter 4, to obtain quantitative mineralogical maps.

6.5.2 Results

6.5.2.1 Explorative petrographic and mineralogical analyses

Polarizing microscope observations of thin sections highlighted the total oxidation of the reinforcement steel, even in the inner portions (figure 6.8). An almost total decalcification of cement matrix can be observed, substituted by a cryptocrystalline phase highly porous and expansive, responsible for an intense delamination with formation of incoherent superficial black crusts. This phase also permeated within the oxidized concrete steel (figure 6.8) and the residual cement portions (figure 6.9).

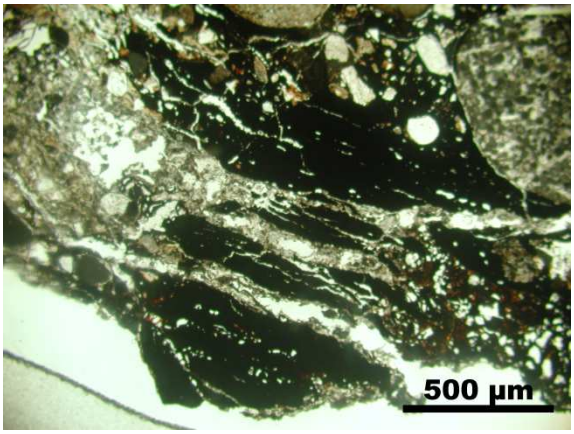

Figure 6.8. Altered rebar micrograph (PPL)

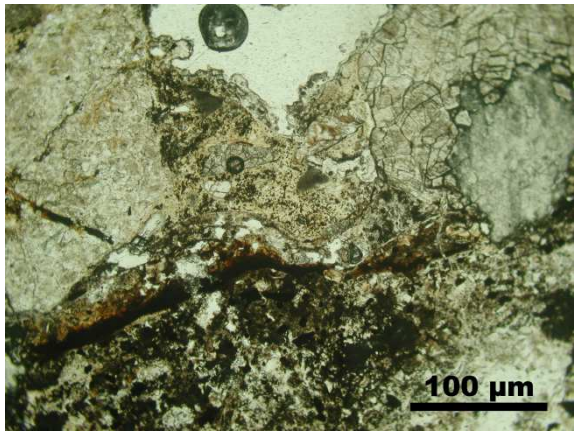

Figure 6.9. Altered cement matrix micrograph (PPL)

The diffraction patterns of the finer fraction of the altered concrete samples show a complex mineral assemblage. Besides the occurrence of aggregate-related phases (quartz, calcite, dolomite, plagioclase, biotite and chlorite), the reflexes of secondary sulfate and phosphate phases are clearly recognizable (figure 6.10). The mineralogical profile is given by hydroxylapatite (HAP), associated with gypsum and brushite ($Ca(HPO_4)\cdot 2(H_2O)$, DCPD) in solid solution, octacalcium phosphate ($Ca_8(HPO_4)_2(PO_4)_4\cdot 5(H_2O)$, OCP), a mineral phase with crystal structure similar to ardealite ($Ca_2(SO_4)(HPO_4)\cdot 4(H_2O)$) and struvite ($(NH_4)MgPO_4\cdot 6(H_2O)$). The absence of portlandite reflexes testifies the almost total decalcification of cementitious matrix.

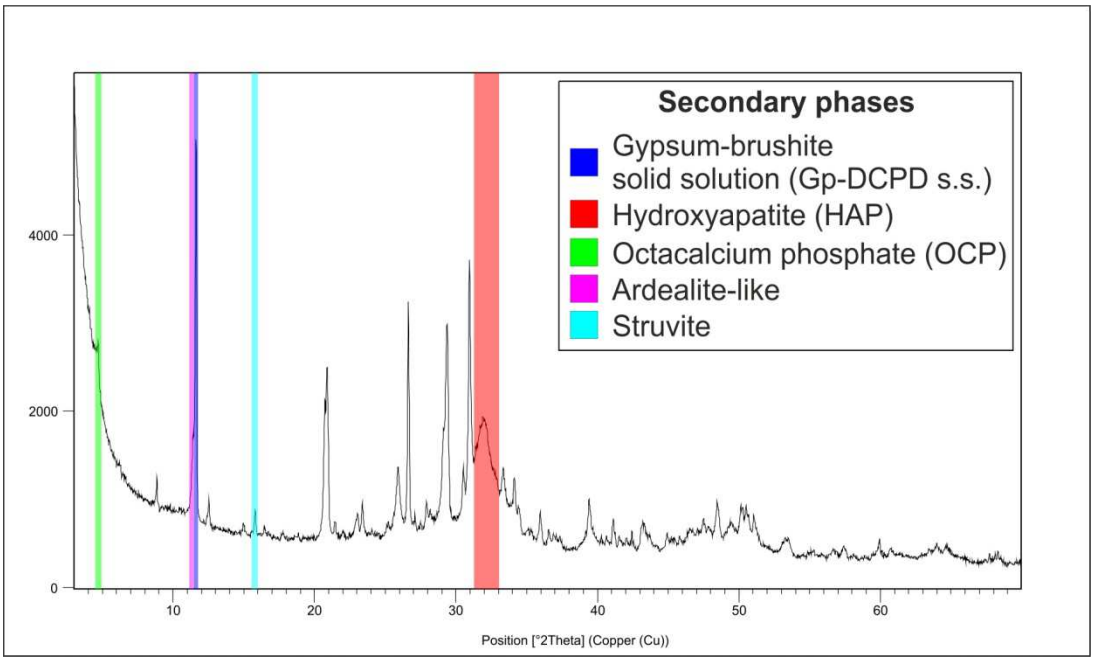

Figure 6.10. Typical diffraction pattern of the finer fraction of the altered concretes. The main reflexes of secondary phases have been highlighted

Hydroxylapatite reflexes are characterized by high FWHM values, indicating a scarce crystallinity of the phase. The occurrence of gypsum and brushite in solid solution is suggested by the observation in the diffraction patterns of remarkable displacements in reference [2θ] values of both gypsum and brushite reflexes. Gypsum and brushite both belong to the monoclinic system and have similar structures, despite not being isostructural (space groups: I2/a for gypsum, C2/c for brushite). Their structure consists of chains of SO_4 or HPO_4 tetrahedra and CaO_6 irregular octahedra, running perpendicular to the c axis. These groups are linked by sharing oxygen anions and form sheets which are held together

by hydrogen bonds established with layers of water molecules (Pinto et al., 2008). Despite having different sizes (the phosphate group is bigger than sulfate), the substitution of sulfate and phosphate groups is allowed within certain limits of composition (Rinaudo et al., 1994), generating a solid solution between the two phases which also comprehends the stoichiometric mineral ardealite, belonging to the monoclinic system and Cc space group. In the analyzed samples, remarkable displacements in reference [2θ] values of ardealite reflexes suggest the occurrence of mineral phases with a structure similar to ardealite, presenting SO_4/HPO_4 ratios close to the stoichiometric value.

Octacalcium phosphate belongs to the triclinic crystal system and P1 space group. Its structure has been described in terms of alternating apatite and hydrated layers parallel to the (100) face (figure 6.11). The apatite layer consists of two Ca^{2+} and two PO_4^{3-} groups, corresponding to each triangular set of two Ca positions in one column in apatite, thus accounting for the $Ca_6(PO_4)_4$ unit. The composition of the hydrated layer, $Ca_4(HPO_4)_4 \cdot 10(H_2O)$, corresponds to brushite with two extra water molecules (Chow & Eanes, 2001). Given its crystal structure, the phase typically forms small crystals, extremely platy and almost invariably twinned.

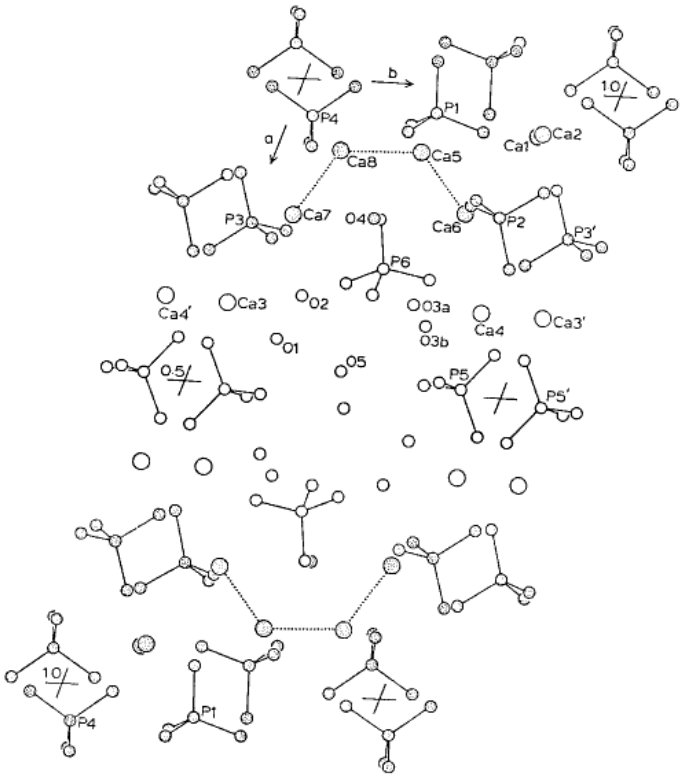

Figure 6.11. Crystal structure of OCP projected down the c-axis. The region with shaded atoms is very similar to that of HAP and has been referred to as the "apatite layer" (Chow & Eanes, 2001)

Both brushite and octacalcium phosphate are reported to be precursors of hydroxylapatite at acidic and neutral pH, respectively (Johnsson & Nancollas, 1992). The higher solubility and lower stability of the two phases with respect to hydroxylapatite cause their progressive transformation into hydroxylapatite, both by dissolution and re-precipitation processes and by epitaxial growth, possibly due to the close structural similarities between the phases.

Struvite belongs to the orthorhombic crystal system and $Pmn2_1$ space group, and is an hydrated phase consisting of magnesium, ammonium and phosphate in equal molar concentrations. The crystal structure consists of PO_4^{3-} tetrahedra, $Mg \cdot 6H_2O^{2+}$ octahedra and NH_4^+ groups held together by hydrogen bonding. Ammonium can be substituted to a certain extent by alkaline ions, in particular potassium (Whitaker & Jeffery, 1969). Struvite precipitation is controlled by pH, degree of supersaturation, temperature and the presence of other ions in solution such as calcium and can occur when the concentrations of magnesium, ammonium and phosphate ions exceed the solubility product for struvite. Among the various factors, pH is crucial for the formation of this phase, being sparingly soluble in neutral and alkaline, but readily soluble in acid conditions (Doyle & Parsons, 2002).

6.5.2.2 Profile mineralogical analyses

The profile diffraction analyses clearly show a marked mineralogical zoning through the samples: the superficial concretions (figure 6.12 a) are constituted mainly by gypsum-brushite solid solution (Gp-DCPD s.s.) and ardealite-like phases, associated with anhydrite and bassanite. The superficial crust (figure 6.12 b) is constituted mainly by monetite ($Ca(HPO_4)$, DCPA), an anhydrous calcium hydrogen phosphate that forms after dehydration of brushite. octacalcium phosphate, hydroxylapatite and gypsum-brushite solid solution are also present. The external strata under the superficial crust (figure 6.12 c, d) show a drastic decrease in monetite content, associated with an increase in gypsum-brushite solid solution and ardealite-like phases and a less marked increase in octacalcium phosphate and hydroxylapatite content. These portions are characterized by variable thickness, comprised between 2 and 4 mm. Moving towards the core of the samples (figure 6.12 e), the almost total disappearance of gypsum-brushite solid solution is observed, associated with a marked increase in octacalcium phosphate content. Also these transitional portions are characterized by variable thickness, but generally comprised

between 3 and 5 mm. In the core (figure 6.12 f) octacalcium phosphate is totally replaced by hydroxylapatite, being the only Ca-containing phase. Ammonium-magnesium phosphates, also in monohydrate form, corresponding to the mineral dittmarite, were also detected in the inner portions (figure 6.12 e, f).

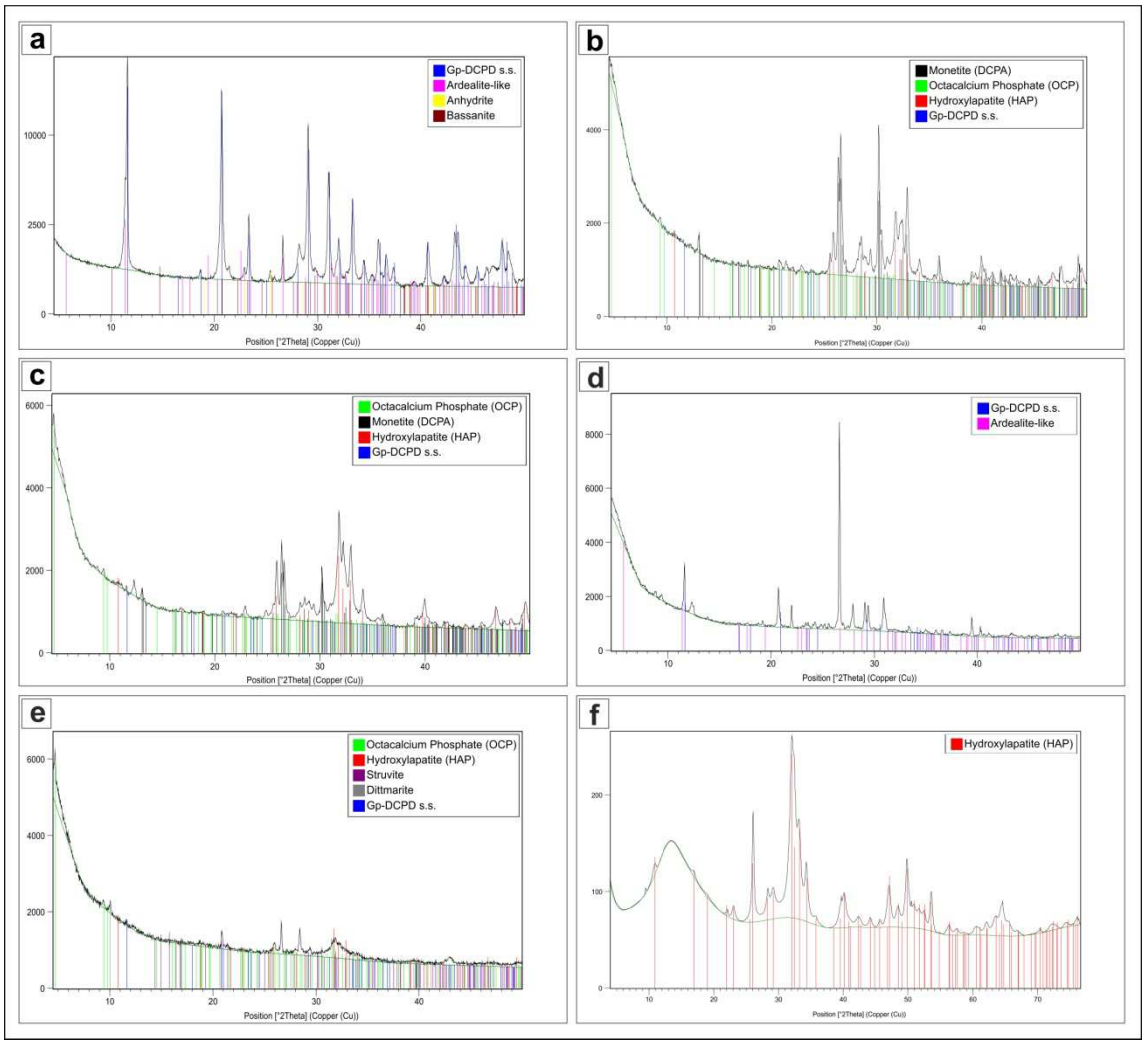

Figure 6.12. Sample B2A1, diffraction patterns of the altered matrix at different depths. a) surface; b) 100 µm; c) 200 µm; d) 1000 µm; e) 3000 µm; f) 10000 µm

A relative estimate of hydroxylapatite crystallinity was performed considering full width at half maximum (FWHM) of (002) planes diffraction peak of 15 diffraction patterns, chosen considering the absence of peak overlap with other phases. 5 diffraction patterns were relative to the superficial crust and the external strata under the superficial crust, where monetite and gypsum-brushite solid solution are the dominant phases. 5 diffraction patterns were relative to the transition zone where octacalcium phosphate is the dominant phase. Finally, 5 diffraction patterns were relative to the core of the samples, where

hydroxylapatite is the dominant phase. The data, reported in table 6.3 and figure 6.13, show a clear increase in FWHM values moving towards the inner portions of the samples, suggesting a progressive decrease in hydroxylapatite crystallinity. The difference in FWHM is particularly evident between hydroxylapatite of external portions and cores (figure 6.14). FWHM values of hydroxylapatite of the transition zones are quite disperse, as showed by the high standard deviation (table 6.3). More in detail, FWHM are divided in two groups, one with values similar to the ones observed on hydroxylapatite of the external portions, the other with values similar to the ones observed on hydroxylapatite of the cores (figure 6.13)

Dominant phase	Mean FWHM of HAP (002) peak	Standard deviation
DCPA, Gp-DCPD s.s.	0.185	0.019
OCP	0.217	0.042
HAP	0.318	0.026

Table 6.3. Mean FWHM values and relative standard deviation of HAP (002) planes diffraction peaks in relation with the dominant phase of the diffraction pattern

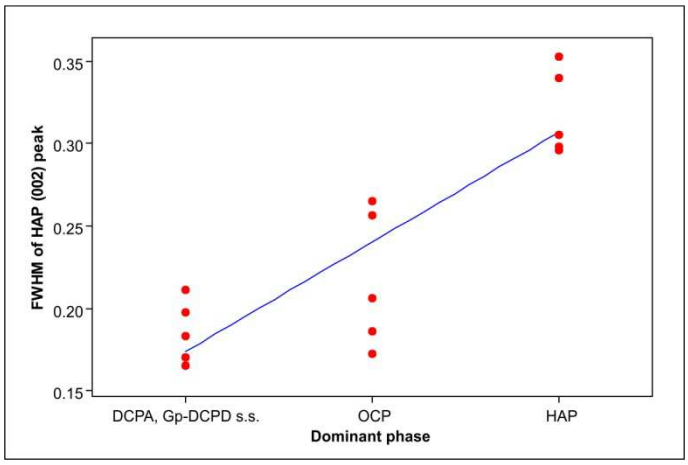

Figure 6.13 FWHM values of HAP (002) planes diffraction peaks in relation with the dominant phase of the diffraction pattern

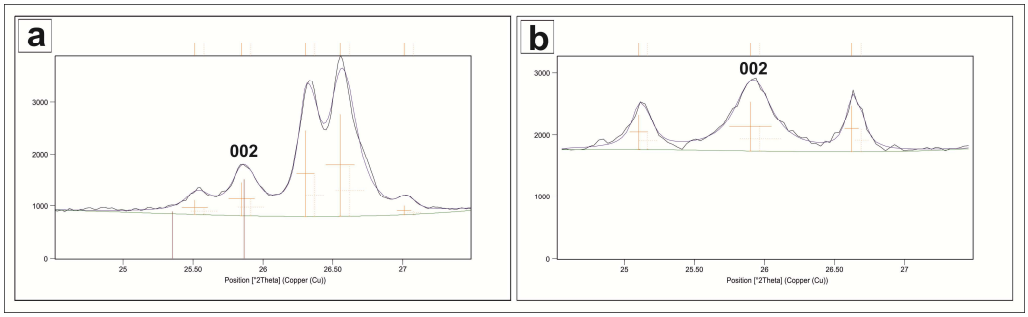

Figure 6.14. HAP (002) planes diffraction peak of external portion (a) and core (b)

The micro-diffractions performed on the altered rebars, at the interface with the surrounding matrix, gave a mineralogical assemblage constituted exclusively by iron oxides (magnetite, Fe_3O_4) and oxyhydroxides (goethite, FeO(OH), and lepidocrocite, γ-FeO(OH)), confirming the high degree of oxidation of the reinforcements. No traces of iron phosphates, like vivianite ($Fe_3(PO_4)_2 \cdot 8(H_2O)$) and mitridatite ($Ca_2Fe_3(PO_4)_3O_2 \cdot 3(H_2O)$), were found.

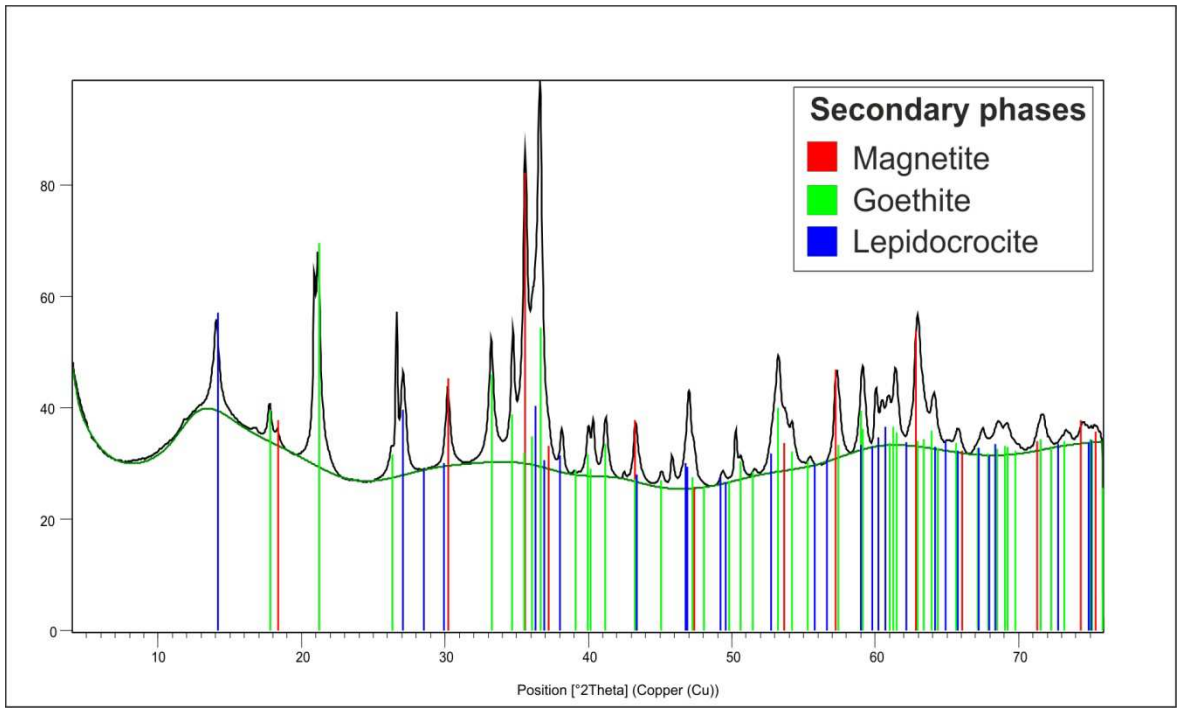

Figure 6.15. Typical diffraction pattern of the altered rebars, at the interface with the surrounding matrix

6.5.2.3 SEM-EDS analyses

Microstructural and microchemical analyses confirmed the strong decalcification of the cement matrices: cores of the hardened pastes are constituted by amorphous and incoherent silicates from which calcium has been almost totally leached (figures 6.16, 6.18., 6.19). SEM imaging (figures 6.16, 6.18) and profile microanalyses (6.19) indicated progressively increasing calcium phosphates precipitation towards the pore network of the materials, which are frequently totally filled by secondary phases. Carbonate aggregates were also heavily interested by decalcification phenomena, presenting frequently dissolution rims at the interface with the surrounding matrix (figure 6.17).

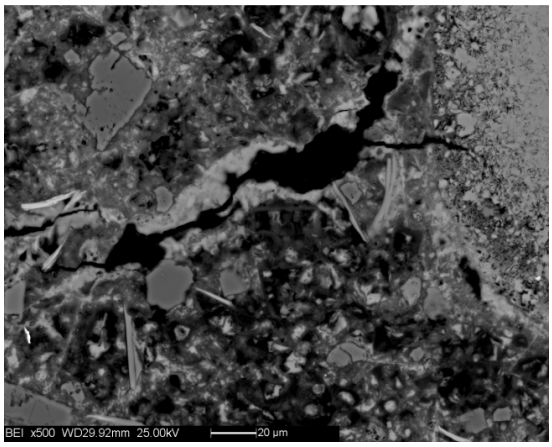

Figure 6.16. Decalcified matrix

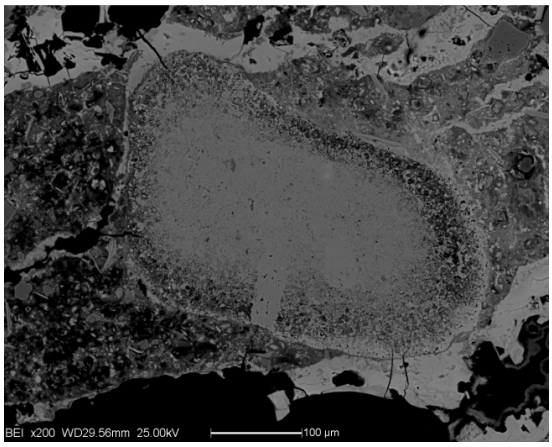

Figure 6.17. Interfacial dissolution of limestone grain

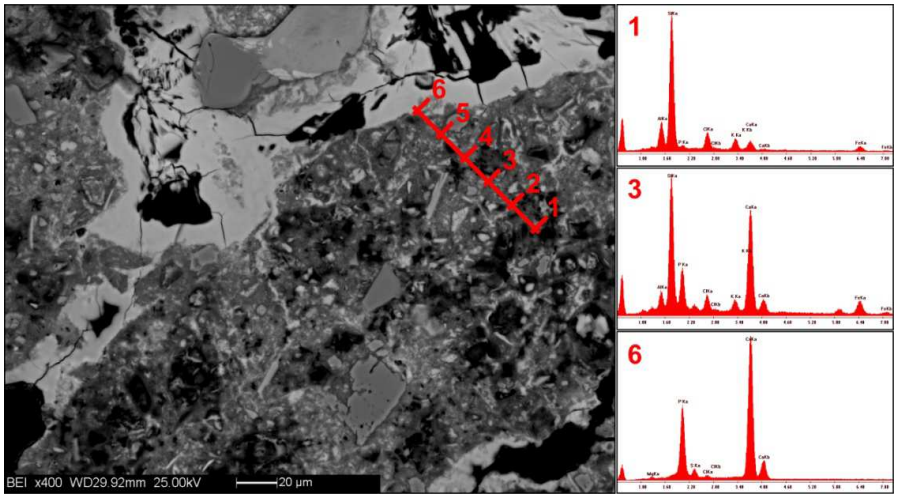

Figure 6.18. Profile microanalysis of the decalcified matrix. (1) Total decalcification in the cores; (2, 3) calcium phosphates precipitation in the pore network

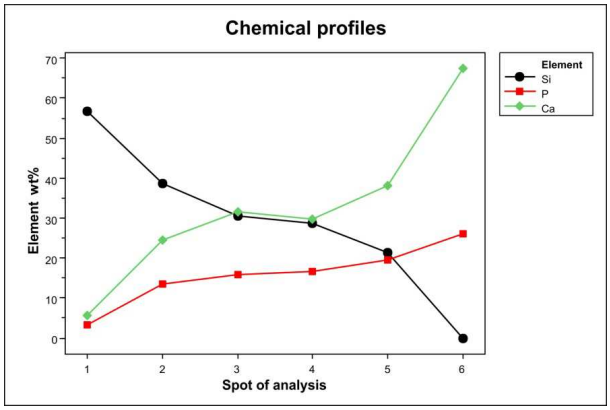

Figure 6.19. Chemical profile of Si, P and Ca of the six points of analysis in figure 6.18

The profile microstructural analyses on fresh-cut surfaces of the materials at different depths provided information on the crystallization sites, morphological features and

composition of the secondary phases. Superficial concretions are constituted by well-formed euhedral bassanite and anhydrite crystals, surrounded by a matrix of microcrystalline tabular crystals of gypsum-brushite solid solution (figures 6.20, 6.21). Superficial crusts are mainly constituted by dense aggregates of tabular monetite crystals (figures 6.22, 6.23). Moreover, cryptocrystalline aggregates of hydroxylapatite grew epitaxially on monetite seed crystals (figure 6.22). The external strata of the materials under the superficial crusts are constituted mainly by microcrystalline aggregates of tabular gypsum-brushite solid solution phases (Figure 6.24). Frequent epitaxial growths of cryptocrystalline hydroxylapatite on gypsum-brushite solid solution seed crystals are observable in these portions (figure 6.25).

Figure 6.20. External concretion: anhydrite crystals in a matrix of microcrystalline Gp-DCPD s.s.

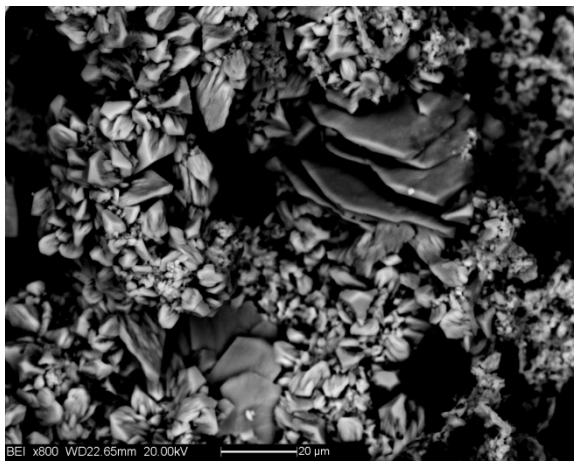

Figure 6.21. External concretion: tabular bassanite in a matrix of microcrystalline Gp-DCPD s.s.

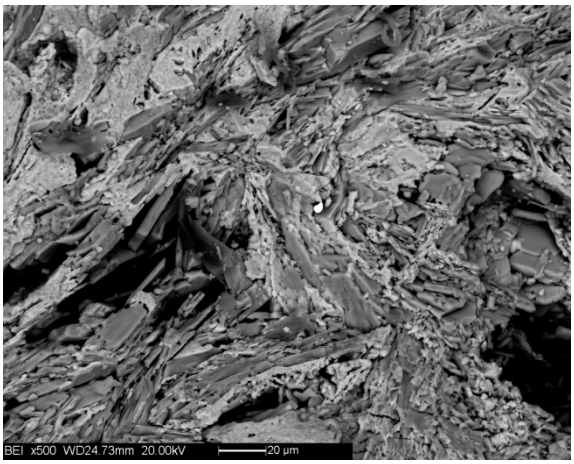

Figure 6.22. Superficial crust: DCPA crystals with HAP grown epitaxially (the latter appears whiter)

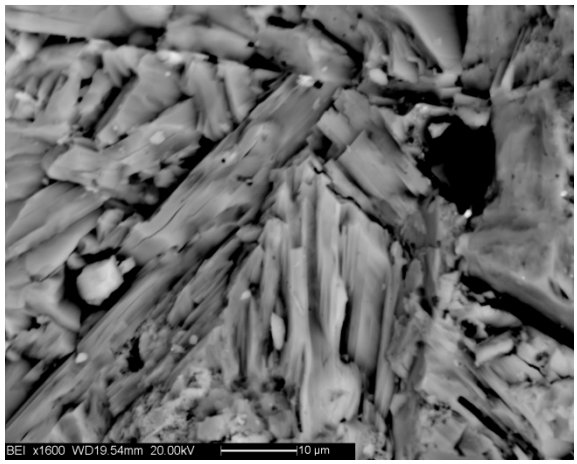

Figure 6.23. Superficial crust: detail of DCPA crystals

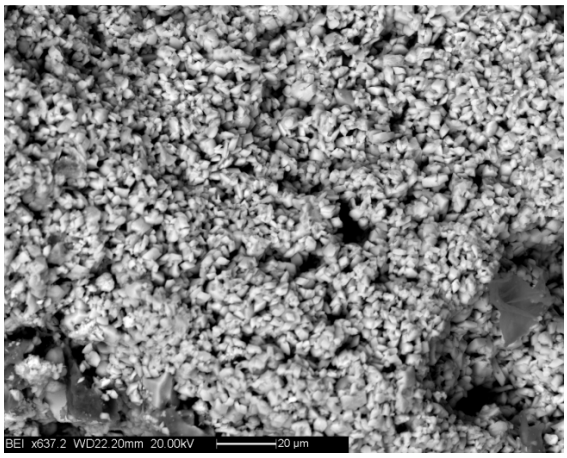

Figure 6.24. External strata under the superficial crust: aggregates of microcrystalline Gp-DCPD s.s.

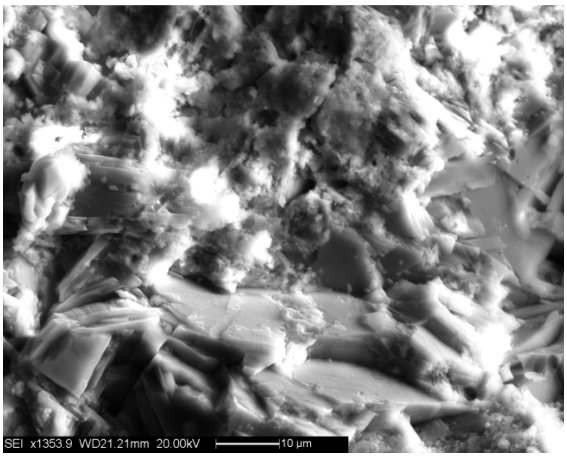

Figure 6.25. External strata under the superficial crust: epitaxial growth of HAP on Gp-DCPD s.s.

Gypsum-brushite solid solution shows high chemical variability in the relative proportions of the end-members, with mean SO_4^{2-}/HPO_4^{2-} molar ratio of 1.17, standard deviation of 0.47 and general prevalence of gypsum-rich terms and stoichiometric ardealite. Analyzing separately the chemical compositions of gypsum-brushite solid solution in the external concretions and in the external strata of altered concrete, it is possible to observe a greater homogeneity in relative proportion of end members in the former areas (standard deviation of 0.18), with prevalence of terms close to the stoichiometric compound ardealite, previously defined ardealite-like phases (mean SO_4^{2-}/HPO_4^{2-} molar ratio of 1.23) (figure 6.26). On the other hand, the latter areas show a great dispersion in SO_4^{2-}/HPO_4^{2-} molar ratios (standard deviation of 0.53), with mean values of 1.15 and general prevalence of gypsum-rich terms (figure 6.26).

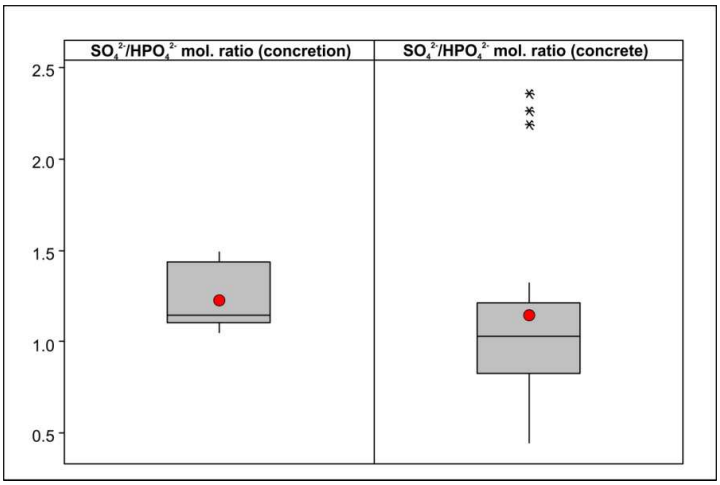

Figure 6.26. Box plots of Gp-DCPD s.s. SO_4^{2-}/HPO_4^{2-} molar ratios in the external concretions and altered concrete. Mean values are indicated by the red dot

The transition portions are mainly constituted by strongly pinacoidal octacalcium phosphate crystals, often forming fan-shaped aggregates, with associated large subhedral and euhedral struvite and dittmarite crystals (figures 6.27, 6.28). The presence of cryptocrystalline hydroxylapatite aggregates is also observable.

Finally, the cores of the altered matrices resulted to be constituted by aggregates of cryptocrystalline hydroxylapatite, characterized by globular and platy shapes (figures 6.29, 6.30). Well-formed euhedral struvite and dittmarite crystals are also present (figure 6.30).

Hydroxylapatite and ammonium-magnesium phosphates are characterized by limited isomorphic substitutions. Hydroxylapatite shows a limited PO_4^{3-}-SO_4^{2-} and OH^--Cl^- substitution, with mean PO_4^{3-}/SO_4^{2-} ratios of 19.41 (standard deviation: 3.37) and mean Cl^- molar concentrations of 0.65% over the total mass of the materials (standard deviation: 0.16). Ammonium-magnesium phosphates are characterized by a scarce NH_4^+-K^+ substitution, with mean K^+ molar concentrations of 0.84 % over the total mass (standard deviation: 0.63).

Figure 6.27. Transition portions: fan-shaped OCP aggregates, with associated struvite and dittmarite crystals (the latter appear darker)

Figure 6.28. Transition portions: OCP platy crystals, detail

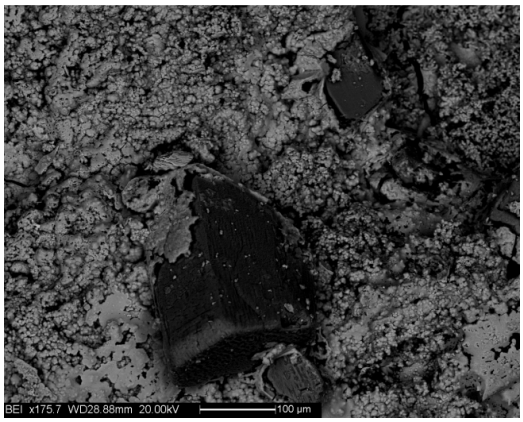

Figure 6.29. Cores: euhedral ammonium-magnesium phosphates in a matrix of cryptocrystalline HAP

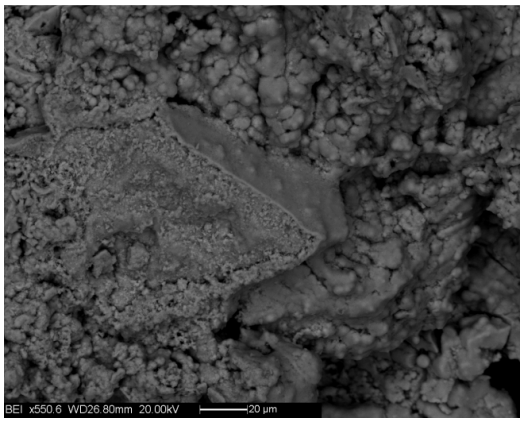

Figure 6.30. Cores: cryptocrystalline HAP aggregates, detail

The quantitative image analysis (Figure 5), performed at the interface between oxidized rebars and altered matrix, confirmed the diffuse oxidation of the rebars and the lack of iron phosphates formation, like vivianite and mitridatite. The secondary phases in contact with the iron hydroxide are constituted by gypsum-brushite solid solution, while the internal portions are constituted by hydroxylapatite and octacalcium phosphate. These microstructural features suggest the occurrence of pH gradients, related to a local acidification caused by chloride attack on the rebars, as seen in chapter 5 and confirmed by the presence of iron chlorides.

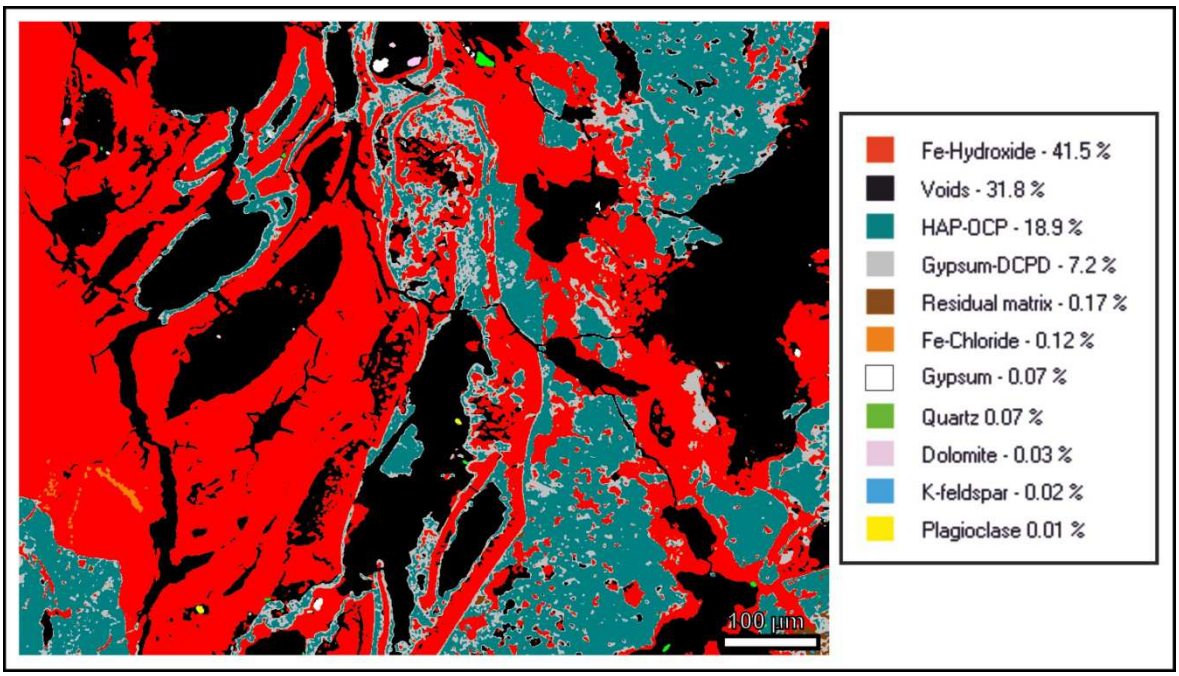

Figure 6.31. Mineralogical map of the altered rebars – matrix interface and volumetric estimation of the phases

6.6 EXPERIMENTAL STUDY OF THE DEHYDRATION BEHAVIOR OF GYPSUM-BRUSHITE SOLID SOLUTION

6.6.1 Experimental

To understand better the occurrence of bassanite, anhydrite and monetite in concretions and superficial crusts of altered concrete, a detailed study on the dehydration behavior of gypsum-brushite solid solution was performed.

A preliminary experiment was conducted on a solid solution phase synthesized for the purpose. To precipitate the compound, an aqueous solution of 0.5M $CaCl_2$ was quickly added (at 25°C) to a continuously stirred 0.5M K_2SO_4 + 0.15M K_2HPO_4 aqueous solution, previously set at pH 4 using NaOH. The resulting phase was analyzed by XRPD with a Philips X'Change diffractometer in Bragg-Brentano geometry equipped with a Cu X-ray tube operating at 40 kV and 40 mA (CuKα radiation), and an X'Celerator detector, both mounted on a PW1050/37 theta-2theta vertical goniometer. Data acquisition was performed operating a continuous scansion from 4.48° [2θ] to 70.48° [2θ], at an acquisition rate of 0.017° [2θ] per second. A structural refinement of the synthesized compound was performed through full-profile fitting according to Rietveld method, using MAUD software (Lutterotti, 1999). The phase was then thermally treated at 80°C for 24 hours. The resulting compound was analyzed by XRPD using the same experimental parameters and the diffraction pattern was interpreted using X'Pert HighScore Plus 3.0 software by PANalytical, reconstructing the mineral profile by comparison with ICDD and ICSD databases.

Starting from the results obtained from the first experiment, a second more extensive experiment was performed. A series of terms of the solid solution was synthesized by gradually adding an (x)M Na_2SO_4 + (0.5-x)M $NaH_2PO_4 \cdot H_2O$ aqueous solution to a 0.5M $CaCl_2$ aqueous solution. At each synthesis, the (x) term was varied between 0 and 0.5 in order to change the relative proportions of the end members. All the syntheses were performed at 25°C, maintaining the pH of the solution stable at 5 by gradual addition of NaOH. The two end members of the solid solution and two homogeneous solid solution terms were then analyzed.

The phases were analyzed by XRPD with a PANalytical X'PERT PRO MPD diffractometer in focalizing transmission geometry equipped with a Cu X-ray tube operating at 40 kV and 40 mA (CuKα radiation), and a PIXcel detector, both mounted on a PW1050/37 theta-theta vertical goniometer. Samples were charged in boron-silicate glass capillaries with a 200 µm diameter, and data acquisition were performed operating a continuous scan from 5° [2θ] to 105° [2θ], at an acquisition rate of 0.013° [2θ] per second. Structural refinements of the synthesized compounds were performed through full-profile fitting according to Rietveld method, using DIFFRACplus TOPAS software by Bruker AXS.

Quantitative determination of Ca, S and P concentrations on the phases were determined by inductively coupled plasma optical emission spectrometry (ICP-OES), using a Thermo Scientific iCAP 6200 spectrophotometer. The system is equipped with a charge injection device detector capable of detecting multiple spectral lines for each element, both axially and radially to the plasma-emitting ICP torch, in an interval between 175 and 847 nm. The following spectral lines were used for the quantitative determinations of main elements concentrations: 393.366 nm (Ca), 396.847 nm (Ca), 177.495 nm (P), 178.284 nm (P), 180.731 nm (S), 182.034 nm (S). Prior to the analysis, the compounds were dissolved in diluted nitric acid (2%), and the resulting solutions were again diluted in aqueous solution, given the great concentrations of the analyzed elements. Absolute concentrations were determined by the radial measurements of the emitting signals, through linear regression functions derived from calibration lines of blank samples at known concentrations.

Also, a qualitative estimation of crystal sizes of the synthesized compounds was performed through SEM imaging.

The dehydration behavior of the compounds was firstly studied by simultaneous thermogravimetric analyses (TGA) and differential thermal analyses (DTA). The analyses were performed using a NETZSCH STA 409 PC Luxx thermal analyzer, with an heating ramp rate of 10°C/min (from 20 to 1000°C) in flowing air (flow rate: 20 ml/min).

Mineralogical evolution of the phases during heating were studied by *in situ* thermal XRPD using an Anton Paar HTK 16 High-Temperature Chamber equipped with a Platinum heating filament, mounted on a Philips X'Change diffractometer in Bragg-Brentano geometry (Cu X-ray tube operating at 40 kV and 40 mA and X'Celerator detector, both mounted on a PW1050/37 theta-2theta vertical goniometer). Multiple diffraction patterns were acquired for temperatures ranging from 20°C to 300°C, with a

temperature slope of 10°C/min and 4 minutes of permanence at the target temperature prior to the data acquisition. Data acquisition was performed by operating a continuous scansion from 10° [2θ] to 54° [2θ], at an acquisition rate of 0.033° [2θ] per second. Diffraction patterns were interpreted with X'Pert HighScore Plus 3.0 software by PANalytical, reconstructing mineral profiles of the compounds by comparison with ICDD and ICSD databases.

Kinetics of dehydration of the phases were studied thermally treating the compounds at 80°C for 48 hours. Mineralogical profiles of the materials were successively determined by XRPD. Measurements were performed with a PANalytical X'PERT PRO MPD diffractometer in focalizing transmission geometry equipped with a Cu X-ray tube operating at 40 kV and 40 mA (CuKα radiation), and a PIXcel detector, both mounted on a PW1050/37 theta-theta vertical goniometer. Samples were charged in boron-silicate glass capillaries with a 200 µm diameter, and data acquisition were performed operating a continuous scansion from 3° [2θ] to 70° [2θ], at an acquisition rate of 0.026° [2θ] per second. Diffraction patterns were interpreted with X'Pert HighScore Plus 3.0 software by PANalytical, reconstructing mineral profiles of the compounds by comparison with ICDD and ICSD databases. Moreover, semiquantitative estimations of the weight fractions of the phases were performed by means of Rietveld Quantitative Phase Analysis.

To evaluate the influence of crystal size and microstrains on dehydration kinetics of the phases, the materials were grounded for 60 minutes with a Retsch Mixer Mill MM200, equipped with a steel jar and operating at a frequency of 50 Hz. The crystallinity decrease was verified both by SEM imaging and XRPD, then the samples were thermally treated at 80°C for 48 hours and analyzed by XRPD, with the same instrument and instrumental parameters utilized for the kinetics studies. Finally, the dehydration behavior of ardealite-like phase was also studied at high temperatures, thermally treating the sample in muffle at 400°C and 550°C for 4 hours and characterizing the resulting compound by XRPD, with the same instrument and instrumental parameters utilized for the kinetics studies.

6.6.2 Results

6.6.2.1 First experiment

The diffraction pattern of the solid solution phase synthesized for the first experiment was fitted by Rietveld refinement with a gypsum crystal structure, considering a partial SO_4^{2-}-HPO_4^{2-} substitution (SO_4^{2-}/HPO_4^{2-} molar ratio: 2.333) (figure 6.32). The unit cell parameters are the following: a = 5.6987 Å, b = 15.2665 Å, c = 6.5026 Å, β = 118.248°.

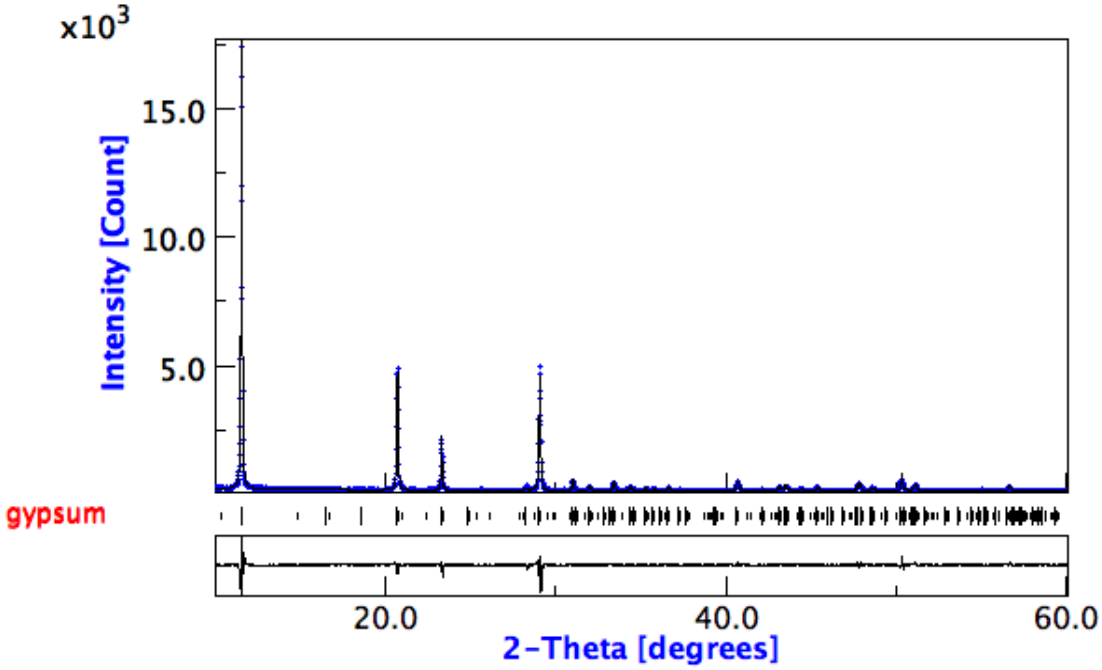

Figure 6.32. Rietveld structural refinement of the phase synthesized for the first experiment (R_{wp}: 18.28)

After the thermal treatment, the compound resulted to be constituted mainly by the gypsum-rich solid solution, with associate bassanite and monetite (figure 6.33). The thermal treatment also favored sylvite precipitation, as a residue of materials synthesis. The results suggest partial dehydration of the solid solution, even at temperature values well below the standard dehydration temperature of the end-members – two dehydration intervals for gypsum, the first at temperatures between 95°C and 170°C to form hemi-hydrated bassanite, the second at temperatures between 170°C and 220°C to form anhydrite (Strydom et. al, 1995); dehydration at 180°C for brushite, to form monetite (McIntosh & Jablonski, 1956). The dehydration process caused the separation of the sulfate and phosphate terms of the solid solution to form separated dehydration products,

and probably interested the fraction of the material characterized by lower crystallinity and higher crystal defectivity.

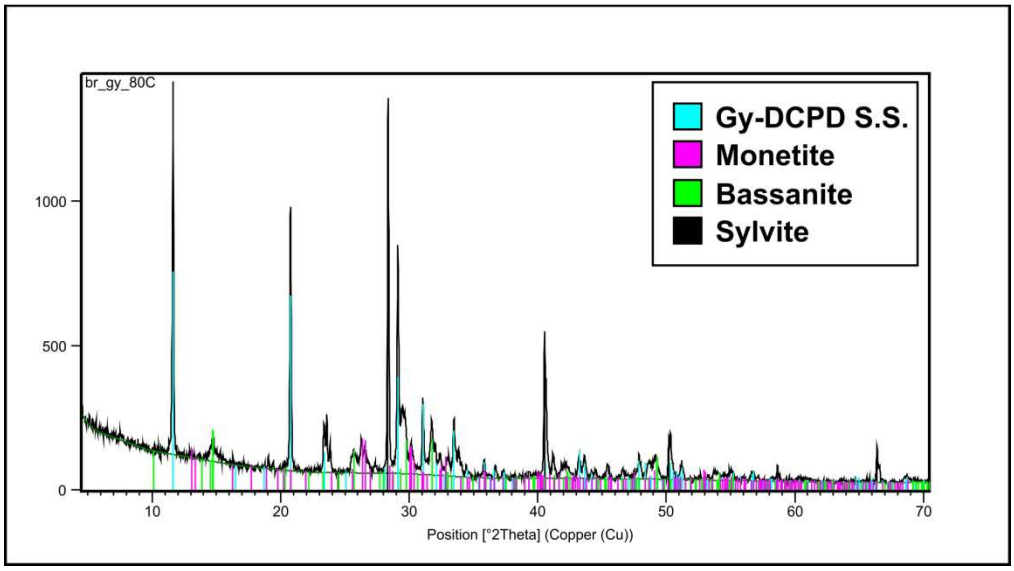

Figure 6.33. Diffraction pattern of the solid solution phase after thermal treatment at 80°C for 24 hours

6.6.2.2 Second experiment: characterization of the synthesized phases

Amongst the various phases synthesized for the second experiment, four compounds were selected for carrying out the dehydration studies, namely the two end-members of the solid solution, a term of the solid solution close to the brushite end-member (denominated brushite-near) and a term of the solid solution close to the stoichiometric compound ardealite (defined ardealite-like). The four compounds were chosen being constituted by pure phases, as confirmed by XRPD. Gypsum, brushite and brushite-near structures were determined by Rietveld refinement (figures 6.34, 6.35, 6.36). Brushite-near phase was refined starting from a brushite crystal structure. A structural refinement for ardealite-like phase was not possible, thus reflection intensities were estimated without a structural model through Le Bail method and assigning to the phase $P2_1/c$ space group (figure 6.37). Diffraction data indicated a strong anisotropic broadening of the reflections of ardealite-like phase. The reflections corresponding to the (0k0) planes of the end-member phases are characterized by lower FWHM with respect to the other reflections: this indicates a greater crystallinity of the phase along the c axis. Calculated unit cell parameters for the four phases are reported in table 6.4, together with the SO_4^{2-}/HPO_4^{2-} molar ratio determined by ICP-OES.

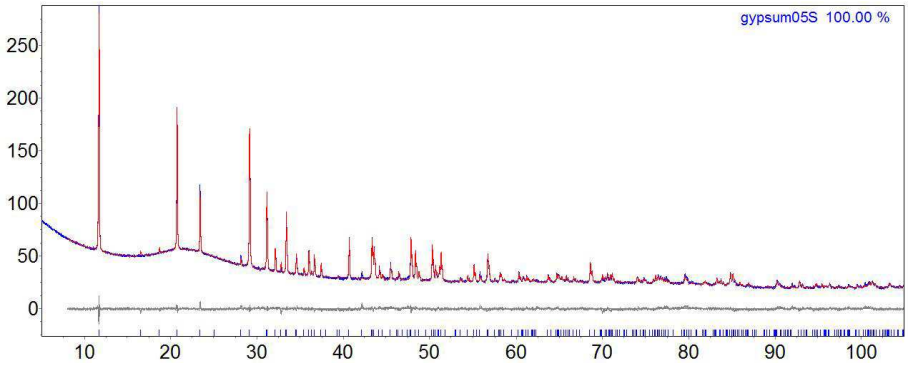

Figure 6.34. Rietveld structural refinement of gypsum (R_{wp}: 4.85)

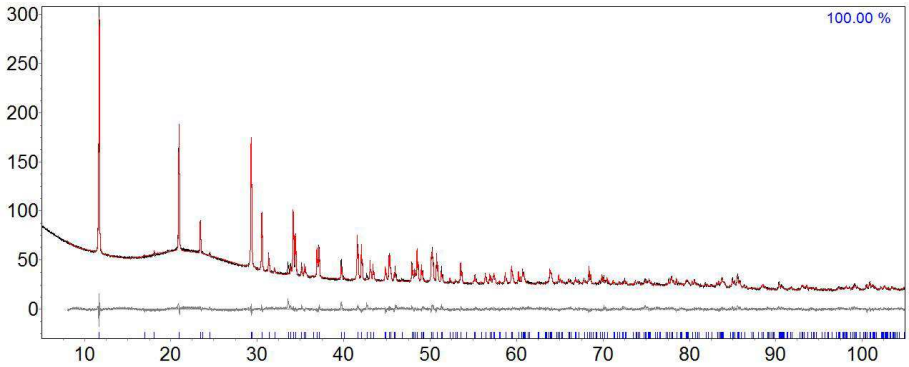

Figure 6.35. Rietveld structural refinement of brushite (R_{wp}: 5.57)

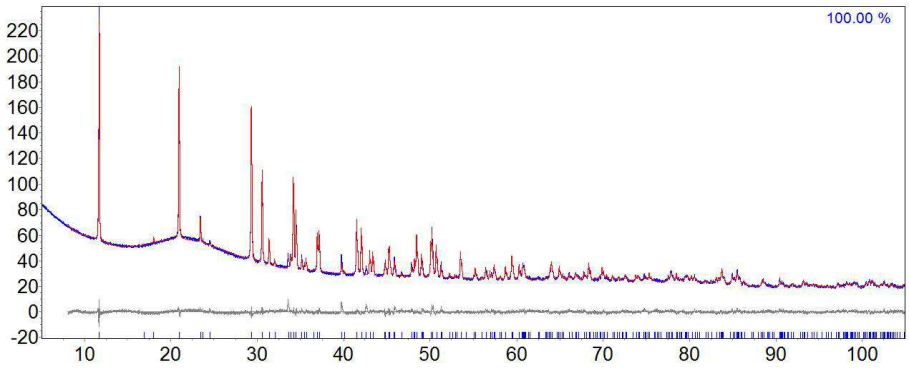

Figure 6.36. Rietveld structural refinement of brushite-near phase (R_{wp}: 5.17)

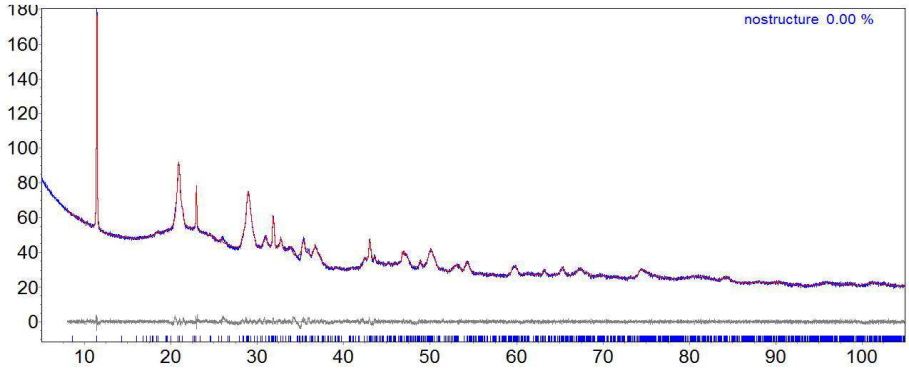

Figure 6.37. Diffraction pattern of ardealite-like phase and profile fitting through Le Bail method (R_{wp}: 3.62)

Phase	a (Å)	b (Å)	c (Å)	β	SO_4^{2-}/HPO_4^{2-} molar ratio
Gypsum	5.6866	15.2301	6.5365	118.4855	676.183
Brushite	5.8110	15.1800	6.2389	116.3902	0.004
Brushite-near	5.8075	15.1831	6.2500	116.4323	0.054
Ardealite-like	5.682	31.063	6.345	117.40	0.828

Table 6.4. Unit cell parameters and SO_4^{2-}/HPO_4^{2-} molar ratios of the synthesized phases

The four phases, despite being all quite polydisperse, are characterized by heterogeneous crystal sizes. The end-members are characterized by a good degree of crystallinity, being constituted by tabular crystals with mean dimensions of 20-30 µm (figures 6.38, 6.39). The crystallinity decreases moving towards the stoichiometric compound of the solid solution: brushite-near phase is constituted by crystals with mean dimensions of 7-10 µm (figure 6.40), while ardealite-like phase has a mean crystal size of 2-4 µm, with a significant occurrence of aggregates of cryptocrystalline particles (figure 6.41).

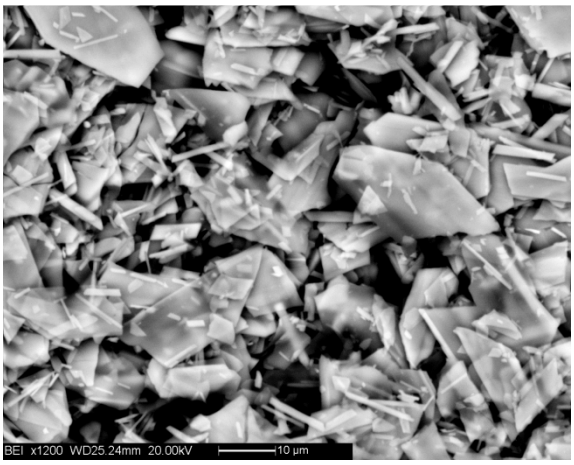

Figure 6.38. Gypsum end-member, SEM image

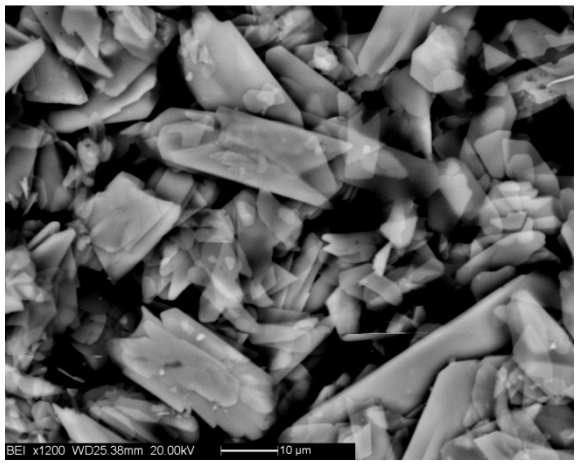

Figure 6.39. Brushite end-member, SEM image

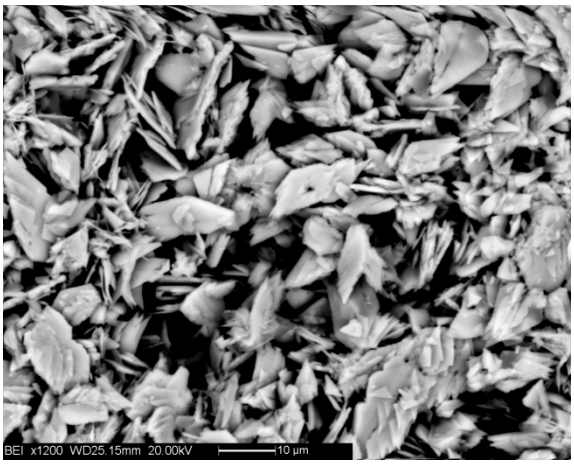

Figure 6.40. Brushite-near phase, SEM image

Figure 6.41. Ardealite-like phase, SEM image

6.6.2.3 Second experiment: thermal analyses and in situ thermal XRPD

Figures 6.42 and 6.43 display the thermogravimetric (TG), derivative thermogravimetric (DTG) and differential thermal (DTA) curves obtained for gypsum and brushite phases, respectively. Despite being both characterized by a weight loss comprised between 21 and 22% in the temperature range between 100°C and 220°C, corresponding to the loss of structural water, the dehydration process is significantly different for the two phases. The dehydration of gypsum involves an initial loss of about 75% of the water molecules and the formation of bassanite in the temperature interval comprised between 110°C and 155°C, as indicated by a strong exothermic peak in the DTA curve at 155.5°C. The complete dehydration of the phase to form anhydrite occurs between 170°C and 200°C, as indicated by a DTG peak at 177.1°C and by a shoulder in the main exothermic peak of DTA curve, centered at about 190°C. The data are in general agreement with the literature data regarding the dehydration behavior of the phase (Strydom et al., 1995).

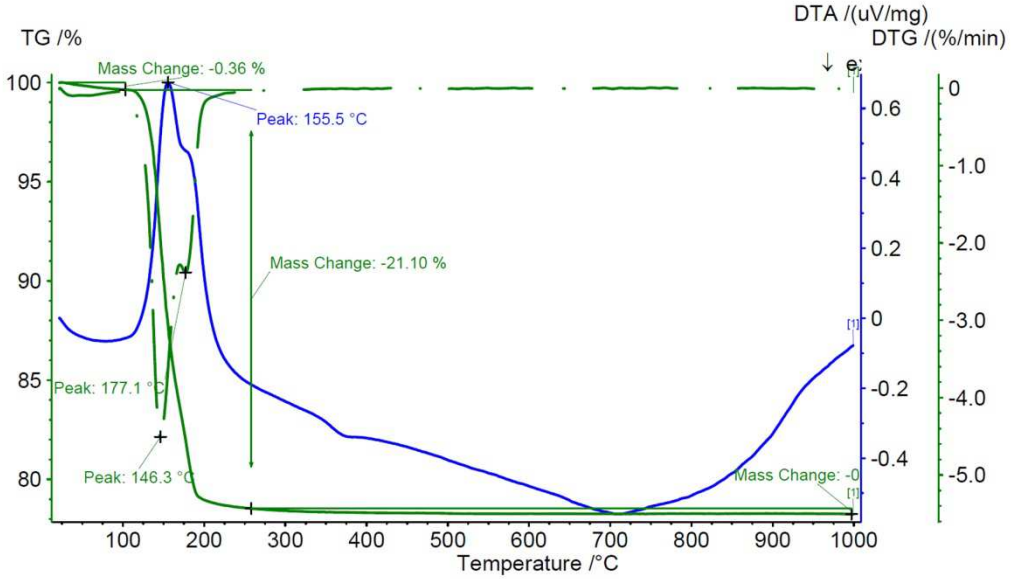

Figure 6.42. Thermogravimetric curve (green solid line), derivative thermogravimetric curve (green dotted line) and differential thermal curve (blue solid line) for the gypsum end-member

Brushite dehydrates to form monetite in two steps, a first one comprised between 110°C and 190°C, with a weight loss of 5.13%, and a second more significant one between 190°C and 200°C, as indicated by a DTG peak at 195.5°C and a strong exothermic peak in the DTA curve at 203°C. This two-step process, apparently in contrast with general literature data (McIntosh & Jablonski, 1956), may be justified by dehydration at lower temperatures

of the fraction of the material characterized by lower crystallinity. The phase is interested by a further weight loss in the temperature range between 400°C and 450°C, probably related to deprotonation of HPO_4^{2-} groups and formation of calcium pyrophosphate ($Ca_2P_2O_7$).

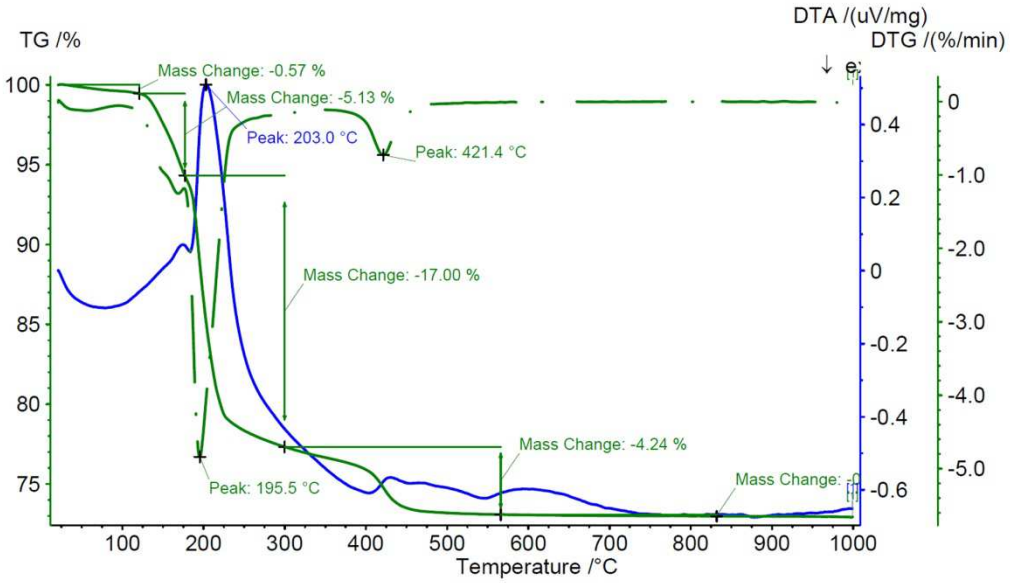

Figure 6.43. Thermogravimetric curve (green solid line), derivative thermogravimetric curve (green dotted line) and differential thermal curve (blue solid line) for the brushite end-member

The different dehydration behavior of the two end-members may be related to the structural differences between these phases, namely the presence of two crystallographically non-equivalent water molecules in brushite, where only one is responsible for establishing hydrogen bonds with oxygen from the coordination layers, and the occurrence in the brushite structure of interwater hydrogen bonds that do not occur in gypsum (Pinto et al., 2008).

Figure 6.44 display the thermogravimetric (TG), derivative thermogravimetric (DTG) and differential thermal (DTA) curves obtained for the brushite-near phase. The thermal behavior of the phase is similar to the one of the brushite end-member, with the exception that the weight loss between 100°C and 190°C is half of the one of the pure end-member, despite the lower crystallinity of the solid solution. Moreover, the main weight loss occurs at temperatures slightly higher than the ones of the end-member (DTG peak at 196.9°C, exothermic DTA peak at 204.6°C). Generally, this phase shows a better thermal stability compared to the pure end-member.

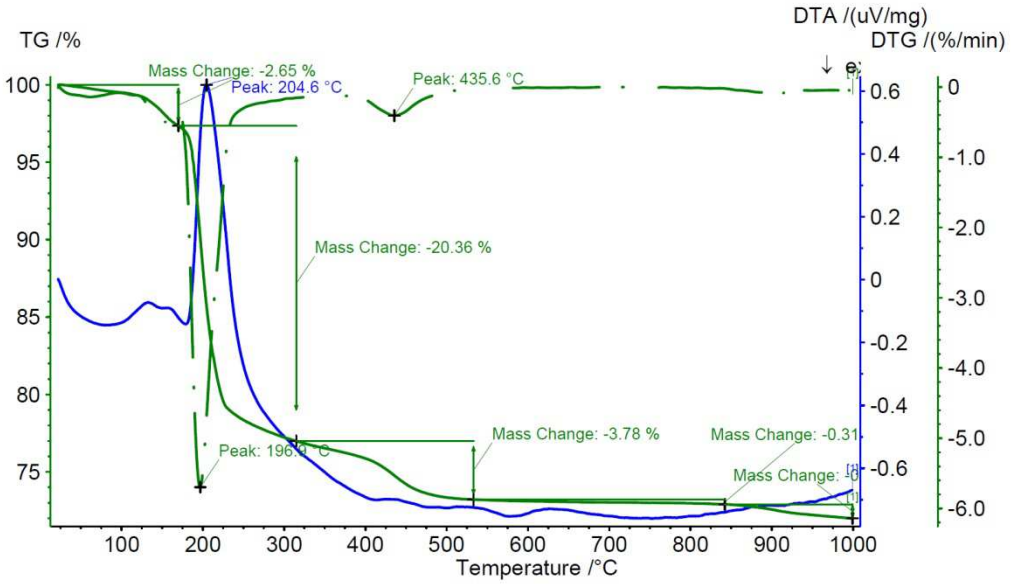

Figure 6.44. Thermogravimetric curve (green solid line), derivative thermogravimetric curve (green dotted line) and differential thermal curve (blue solid line) for the brushite-near phase

Figure 6.45 displays the thermogravimetric (TG), derivative thermogravimetric (DTG) and differential thermal (DTA) curves obtained for the ardealite-like phase. The thermal behavior of the phase is significantly different from the ones of the other compounds. The phase has a weight loss in the temperature range between 100°C and 220°C of 18.52%, lower than the ones of the other phases, and it occurs almost completely at 200°C, as showed by the DTG peak at 195.9°C and the exothermic DTA peak at 203.6°C. A further gradual weight loss of 2.54% occurs in the range between 200°C and 400°C: this can be related to a gradual loss of structural water which did not evaporate in the main dehydration event. Finally, a significant weight loss is observable in the temperature range between 850°C and 1000°C: this can be related to the deprotonation of HPO_4^{2-} groups and the formation of calcium pyrophosphate. Experimental evidence suggests a marked thermal stability of the compound with respect to the other phases, despite its low degree of crystallinity.

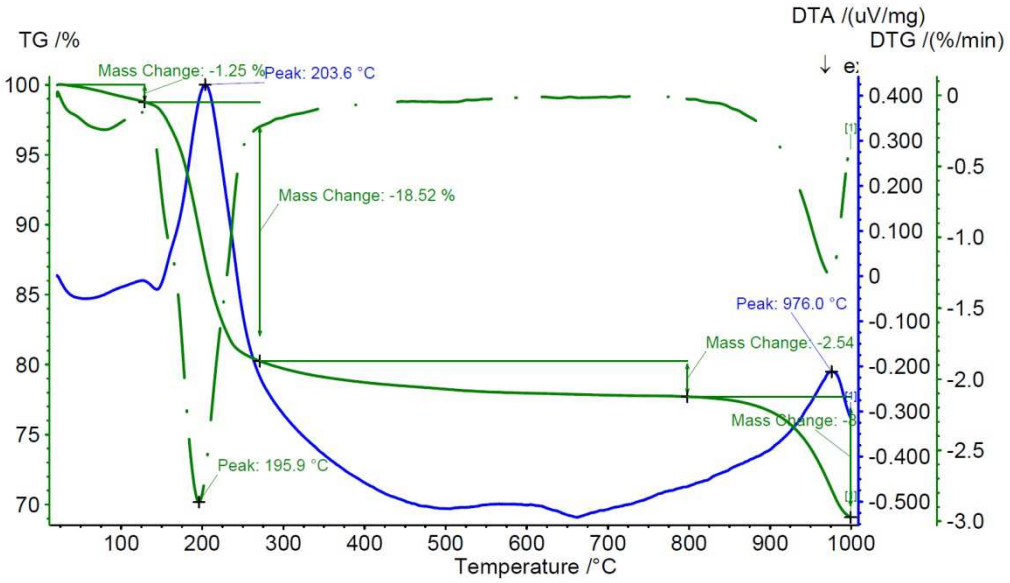

Figure 6.45. Thermogravimetric curve (green solid line), derivative thermogravimetric curve (green dotted line) and differential thermal curve (blue solid line) for the ardealite-like phase

In situ thermal XRPD of the two end-members provided results in general agreement with those of the thermal analyses. Gypsum partially dehydrates to form bassanite in a temperature interval between 110°C and 140°C, while total dehydration occurs in the interval between 190°C and 220°C, to form γ-anhydrite (figure 6.46). As regards brushite, a first limited dehydration of the cryptocrystalline fraction of the material occurs in a temperature interval between 120°C and 130°C, while the main dehydration event occurs in the temperature interval between 180°C and 190°C, where the total conversion into monetite occurs (figure 6.47).

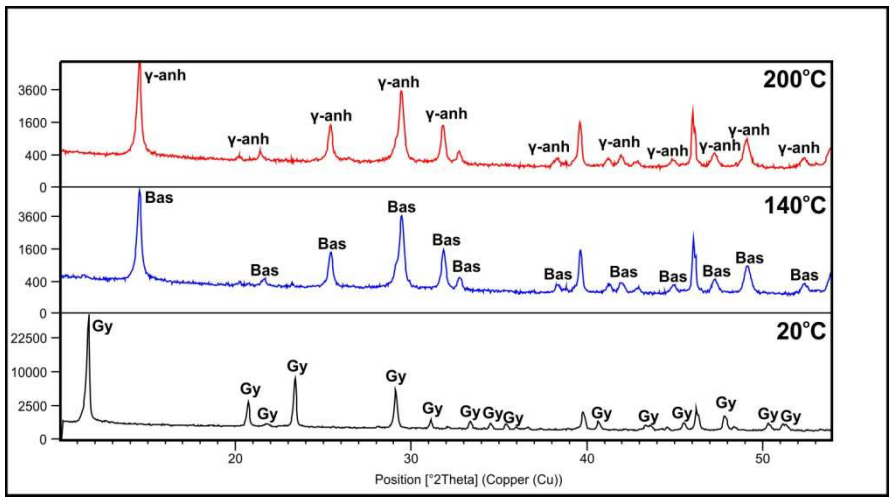

Figure 6.46. XRPD patterns obtained during the dehydration of gypsum end-member. Abbreviations: Gy = gypsum, Bas = bassanite, γ-anh = γ-anhydrite. Peaks at 39.5° and 46 ° [2θ] = platinum sample holder

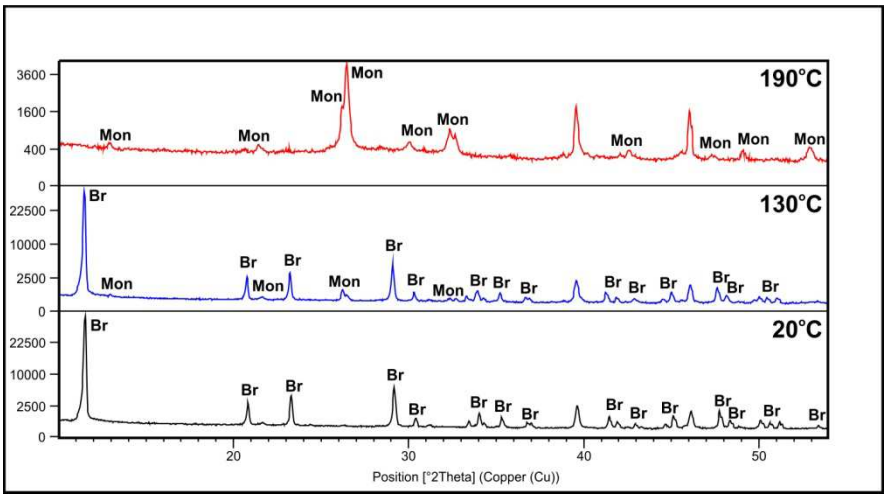

Figure 6.47. XRPD patterns obtained during the dehydration of brushite end-member. Abbreviations: Br = brushite, Mon = monetite. Peaks at 39.5° and 46 ^{o} [2θ] = platinum sample holder

Brushite-near phase dehydrates to form monetite in a single interval of temperature comprised between 180°C and 210°C, without the occurrence of dehydration phenomena at lower temperatures (figure 6.48). The formation of anhydrous calcium sulfates due to the separation of sulfate and phosphate terms of the solid solution was not observed. This is probably due to the high detection limits of the *in situ* thermal XRPD, insufficient to detect the expected formation of low amounts of calcium sulfates of a brushite-near solid solution. The analytical results confirm the better thermal stability of the solid solution with respect to the pure phosphate end-member.

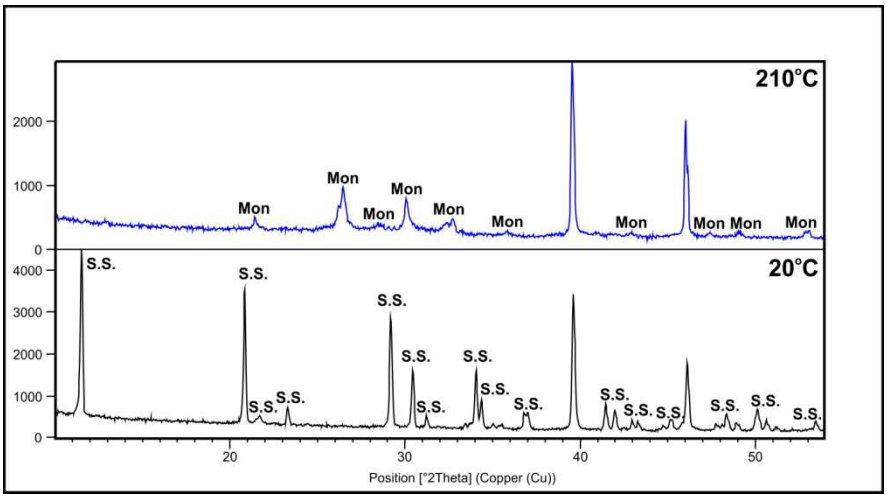

Figure 6.48. XRPD patterns obtained during the dehydration of brushite-near phase. Abbreviations: S.S. = brushite-near solid solution, Mon = monetite. Peaks at 39.5° and 46 ^{o} [2θ] = platinum sample holder

Finally, ardealite-like phase dehydrates in a single interval of temperature comprised between 180°C and 200°C, confirming the analytical results of the thermal analyses. The resulting compound is characterized by an extremely low degree of crystallinity, as indicated by the presence of few low-intensity reflexes in the diffraction pattern (figure 6.48). The reflexes find correspondence with a γ-anhydrite pattern, but remarkable displacements in reference [2θ] values suggest the occurrence of SO_4^{2-}-HPO_4^{2-} isomorphic substitution in the crystal structure of the phase. The analytical results confirm the better thermal stability of this term of the solid solution with respect to the other phases, and indicate the lack of separation of the solid solution in the investigated temperature interval, with formation of an anhydrous solid solution phase.

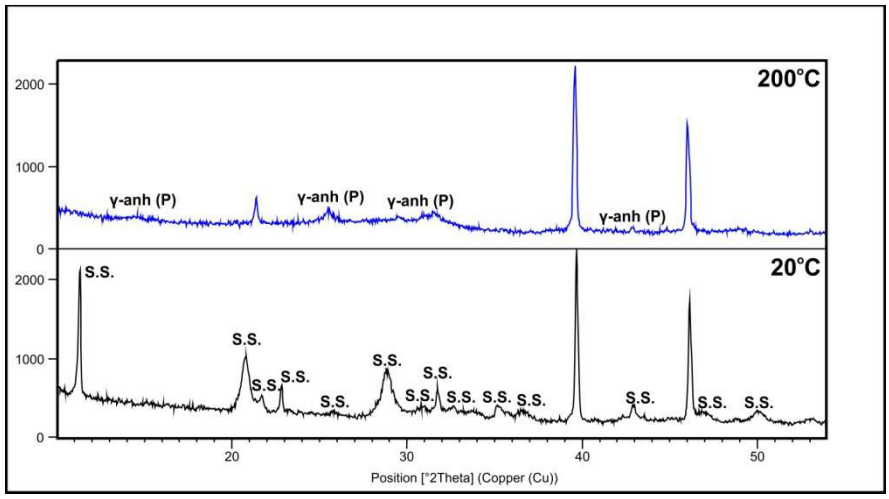

Figure 6.48. XRPD patterns obtained during the dehydration of ardealite-like phase. Abbreviations: S.S. = ardealite-like solid solution, γ-anh (P) = phosphate-substituted γ-anhydrite. Peaks at 39.5° and 46 ^{o} [2θ] = platinum sample holder, peak at 21^{o} [2θ] = cristobalite impurity formed on the sample holder

6.6.2.4 Second experiment: study of the influence of kinetics and crystal size

Gypsum end-member underwent significant dehydration after thermal treatment at 80°C for 48 hours, with the formation of a compound constituted by 71.9 % of bassanite and 28.1 % of gypsum (figure 6.49). The occurrence of dehydration at a temperature lower than the one observed during thermal XRPD analyses indicates a strong influence of kinetics for the triggering of the process. Brushite end-member underwent limited dehydration (3.6 % of monetite formation), most probably of the less crystalline fraction only (figure 6.50). Solid solution phases showed a permanence at the hydrated state (figures 6.51, 6.52), confirming a better thermal stability with respect to the end-members.

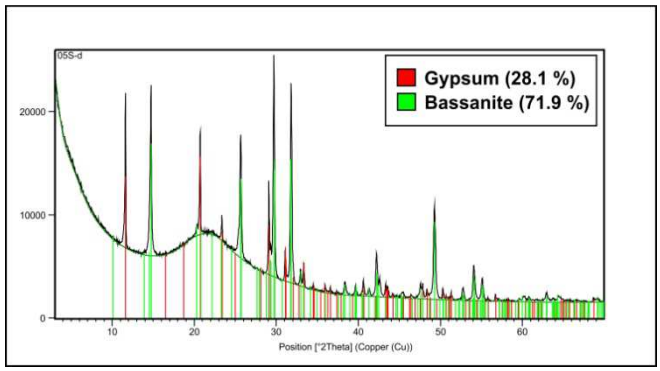

Figure 6.49. Rietveld QPA of gypsum end-member after thermal treatment at 80°C for 48 hours (R_{wp} = 6.01)

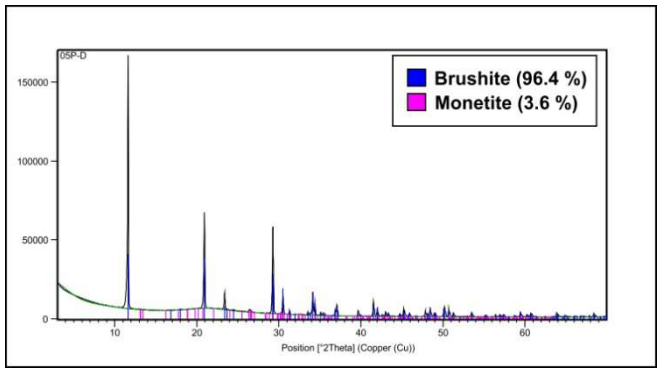

Figure 6.50. Rietveld QPA of brushite end-member after thermal treatment at 80°C for 48 hours (R_{wp} = 5.61)

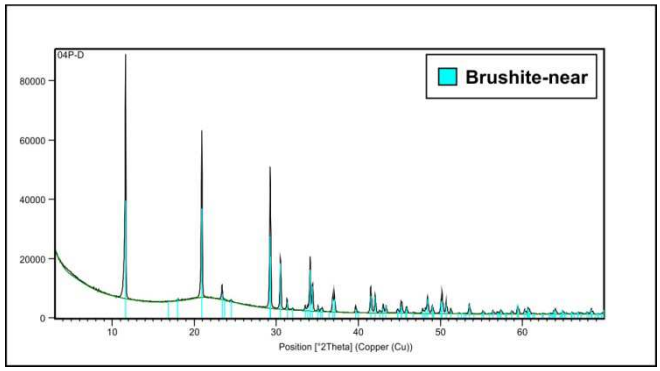

Figure 6.51. Diffraction pattern of brushite-near phase after thermal treatment at 80°C for 48 hours

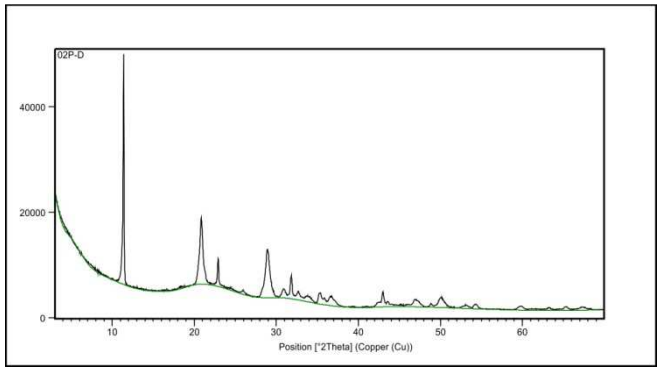

Figure 6.52. Diffraction pattern of ardealite-like phase after thermal treatment at 80°C for 48 hours

The grinding process was effective in the reduction of crystal size of the phases, as confirmed both by XRPD data (dramatic increase in FWHM of the diffraction peaks, figure 6.53) and SEM imaging (figure 6.54).

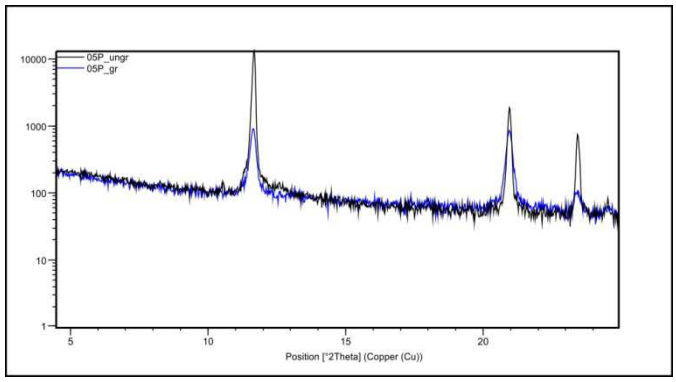

Figure 6.53. Diffraction pattern of brushite end-member before and after grinding (black and blue lines, respectively)

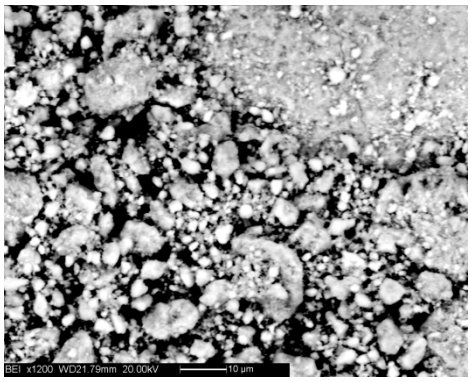

Figure 6.54. SEM image of brushite end-member after grinding

The crystal size reduction, with a consequent increase in the defectivity of crystals, caused significant changes in the thermal behavior of the synthesized phases, with an overall increase in the dehydration rate of the compounds during the 48-hour thermal treatment. Thus, the combination of crystal size and kinetic factors resulted to be fundamental for the stability of hydrated phases at temperatures below 100°C. Gypsum end-member underwent massive dehydration, with the formation of a compound constituted by 97.3% bassanite and 2.7% β-anhydrite (figure 6.55). No traces of hydrated phases have been found. The dehydration of brushite end-member increased significantly, with the formation of a compound constituted by 62.5% monetite and 37.5% brushite (figure 6.56).

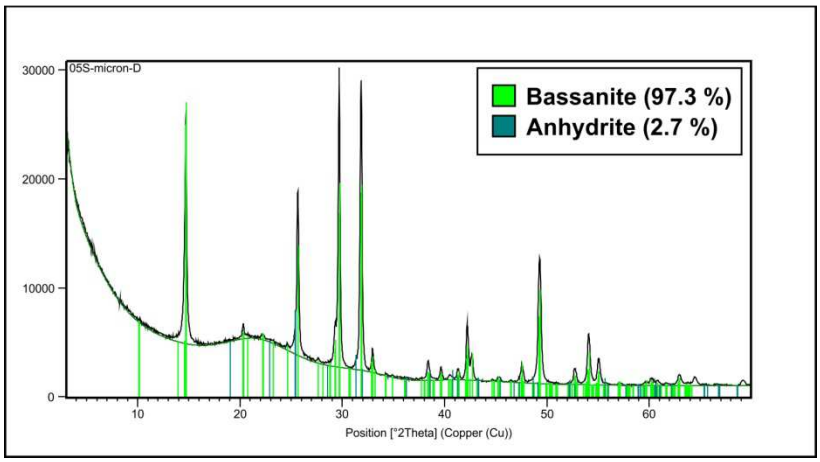

Figure 6.55. Rietveld QPA of grounded gypsum end-member after thermal treatment at 80°C for 48 hours (R_{wp} = 7.75)

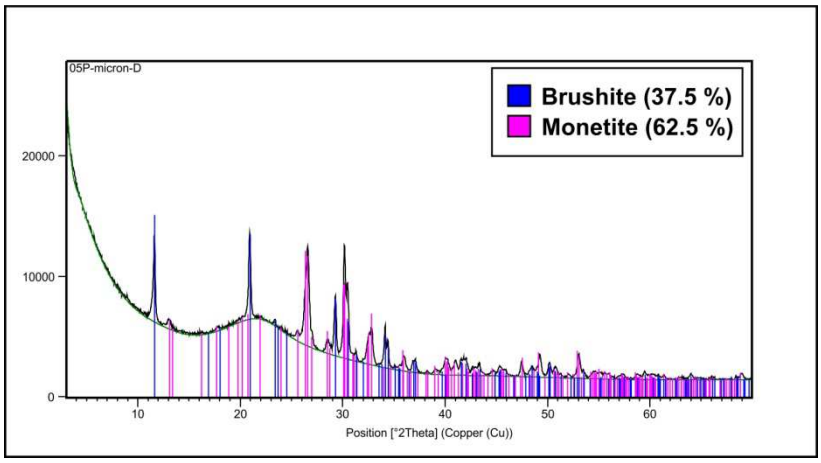

Figure 6.56. Rietveld QPA of grounded brushite end-member after thermal treatment at 80°C for 48 hours (R_{wp} = 4.10)

Also, the grinding process triggered the destabilization of the solid solution phases, which have shown so far better thermal stability with respect to the end-members. Brushite-near phase underwent a significant dehydration process, which only left 29.9% of the original phase. The dehydrated fraction of the compound is constituted by 69.6% monetite and 0.5% bassanite, indicating a separation of the sulfate and phosphate terms of the solid solution to form separated dehydration products. Mineralogical results are consistent with microstructural and microchemical analyses by SEM-EDS (figure 6.58): the compound after the thermal treatment is constituted by an association of microcrystalline crystals of hydrated solid solution phase, and aggregates of cryptocrystalline anhydrous phases, confirming the dehydration of the less crystalline fraction of the solid solution.

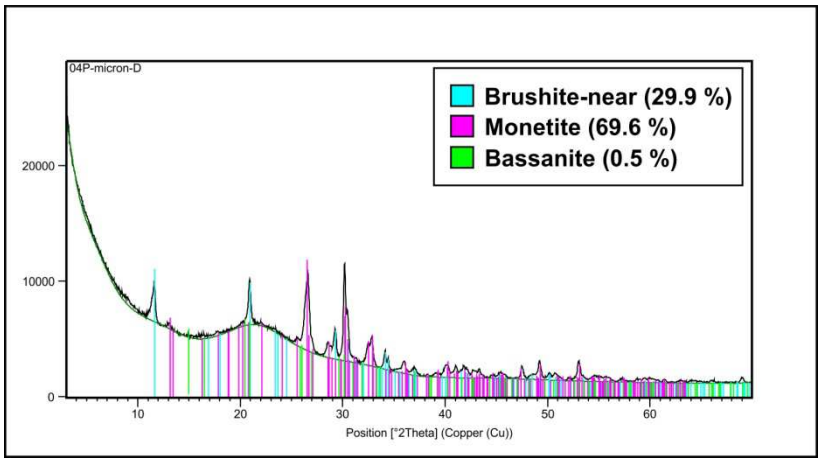

Figure 6.57. Rietveld QPA of grounded brushite-near phase after thermal treatment at 80°C for 48 hours (R_{wp} = 4.27)

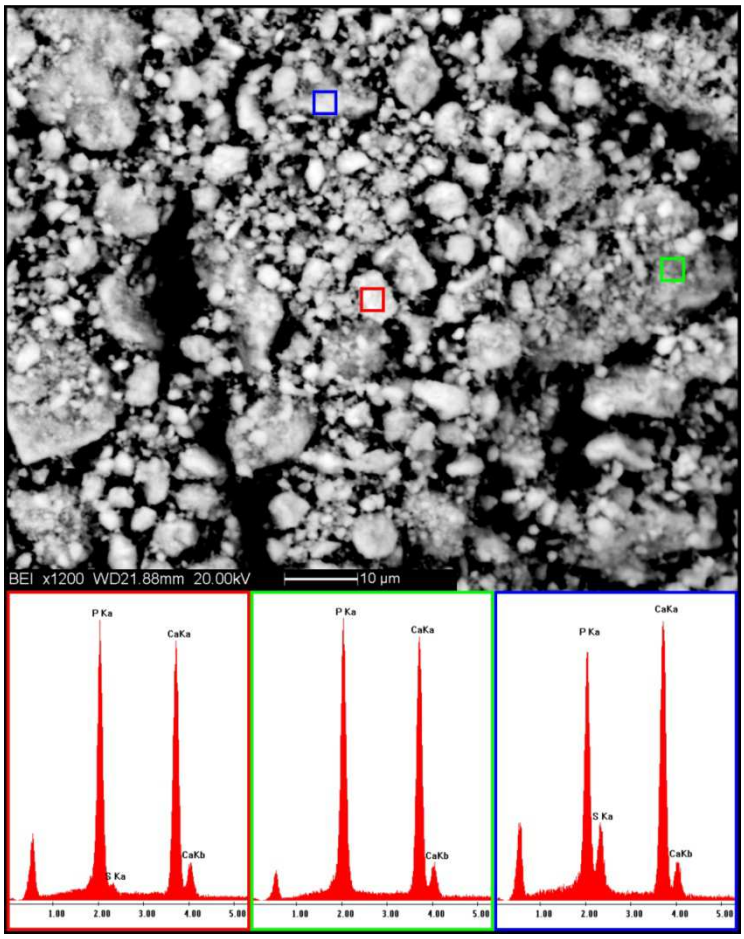

Figure 6.58. SEM-EDS image of grounded brushite-near phase after thermal treatment at 80°C for 48 hours, and microanalyses of a residual solid solution crystal (highlighted in red) and two aggregates of anhydrous phases (pure monetite highlighted in green, monetite-bassanite mix highlighted in blue)

Ardealite-like phase underwent partial dehydration, with formation of SO_4^{2-}-HPO_4^{2-}-substituted γ-anhydrite (figure 6.59). Separation of the solid solution did not take place.

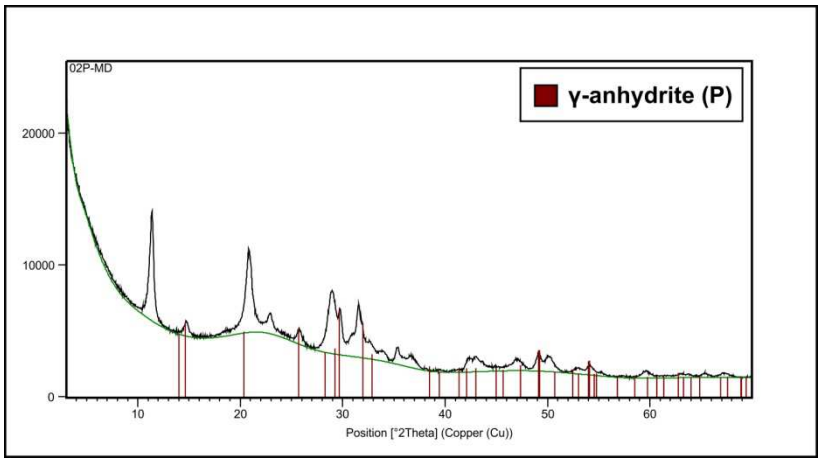

Figure 6.59. Diffraction pattern of grounded ardealite-like phase after thermal treatment at 80°C for 48 hours

Mineralogical results are consistent with microstructural and microchemical analyses by SEM-EDS (figure 6.60): after the thermal treatment the compound is constituted by an association of microcrystalline crystals of hydrated solid solution phase, and aggregates of cryptocrystalline anhydrous SO_4^{2-}-HPO_4^{2-}-substituted γ-anhydrite, confirming the dehydration of the less crystalline fraction of the solid solution and the lack of separation of the sulfate and phosphate terms.

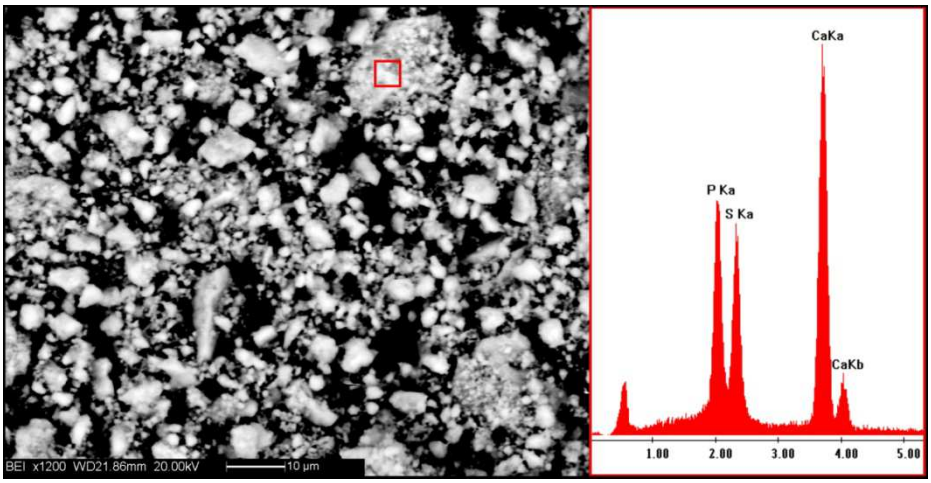

Figure 6.60. SEM-EDS image of grounded ardealite-like phase after thermal treatment at 80°C for 48 hours, and microanalysis of an aggregate of anhydrous phase

Partial separation of sulfate and phosphate terms of the solid solution occurred at high temperatures only: the diffraction pattern of the compound after 4 hours of thermal treatment at 400°C is given by SO_4^{2-}-HPO_4^{2-}-substituted γ-anhydrite, with associated pure β-anhydrite and monetite (figure 6.61). No traces of hydrated phases were found, indicating the total dehydration of the compound.

The diffraction pattern of the compound thermal treated at 550°C indicates a progression of the dissolution of the SO_4^{2-}-HPO_4^{2-}-substituted γ-anhydrite to form separated anhydrous sulfate and phosphate phases (figure 6.62).

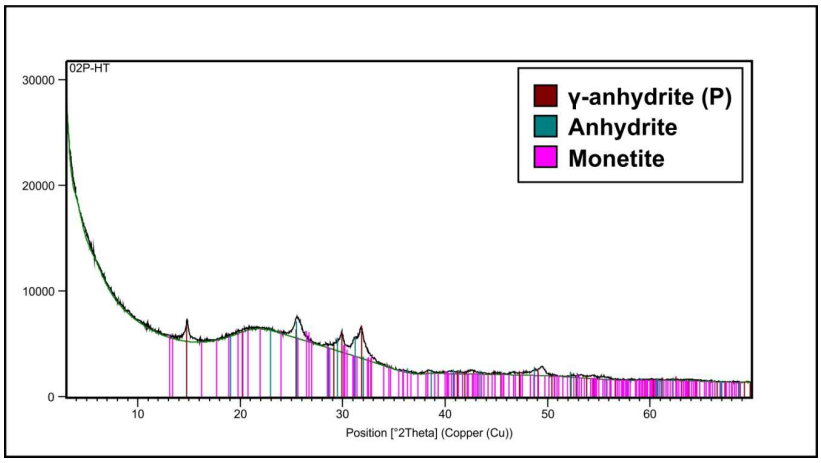

Figure 6.61. Diffraction pattern of ardealite-like phase after thermal treatment at 400°C for 4 hours

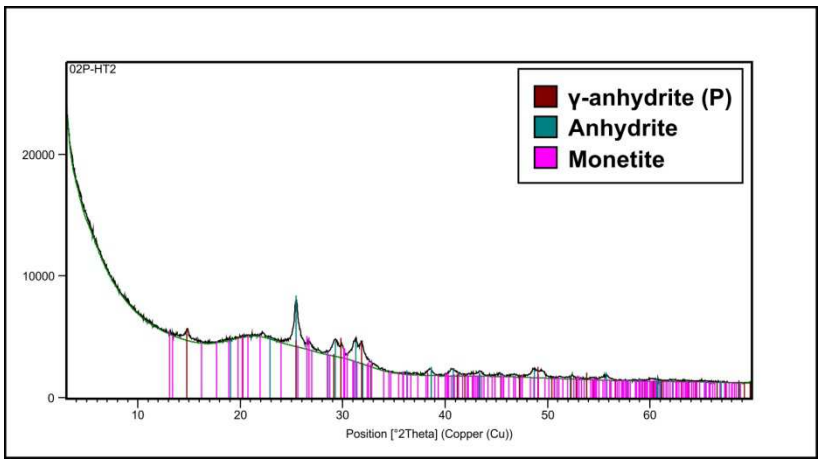

Figure 6.62. Diffraction pattern of ardealite-like phase after thermal treatment at 550°C for 4 hours

As shown by SEM-EDS analyses (figure 6.63), the compound, thermally treated at 550°C. is constituted by an association of microcrystalline crystals of SO_4^{2-}-HPO_4^{2-}-substituted γ-anhydrite and aggregates of cryptocrystalline monetite and β-anhydrite. The analytical results both confirm the partial dissolution of anhydrous solid solution and indicate a crystal growth process of the residual, more crystalline, phase during heating.

Based on all results, the better thermal stability of ardealite-like phase with respect to the other solid solution terms is confirmed.

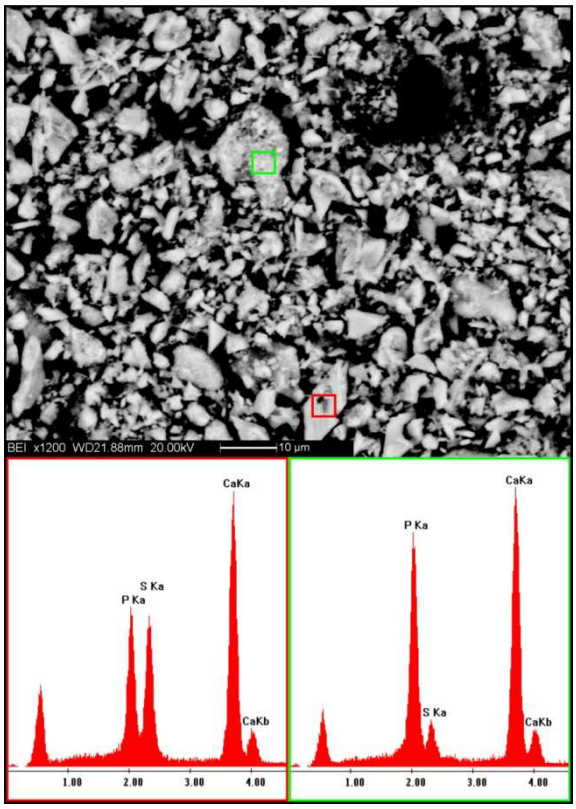

Figure 6.63. SEM-EDS image of grounded ardealite-like phase after thermal treatment at 550°C for 4 hours, and microanalyses of a residual crystal of SO_4^{2-}-HPO_4^{2-}-substituted γ-anhydrite (highlighted in red) and an aggregate of anhydrous phases, rich in monetite (highlighted in green)

6.7 THE ALTERATION MODEL

According to the analytical results and literature background, a model, based on four main alteration phases, is hereby proposed. At the unaltered state, the cementitious matrix of the concrete was constituted mainly by CSH and CH, the latter ensuring an alkaline environment capable of passivating the rebars. Under the action of environmental multipollutants, the concrete pore network was saturated through capillarity by a solution of process water and saltwater, and enriched in sulfates on the external portions in contact with atmospheric pollutants (Figure 6.64 a). Consequently, the external portions underwent stronger acidification, due to the formation of sulfuric acid in the pore-water, while the pH drop was titrated in the cores by the basic environment. All these factors caused strong mineralogical changes in the cementitious matrix. CSH, CH and carbonate minerals constituting the aggregate fraction (calcite and dolomite) underwent dissolution, and secondary phases precipitated upon reaching supersaturation conditions. The nature of the

secondary phases was strongly controlled by pH and sulfate gradients, causing heterogeneous precipitation with depth (Figure 6.64 b). More in detail, acidic precursors of hydroxylapatite like brushite (Johnsson & Nancollas, 1992) formed in the external portions, in solid solution with gypsum. The solid solution phases show high chemical variability in the relative proportions of the end-members, with general prevalence of gypsum-rich terms, and they formed also in proximity of the rebars due to the local acidification caused by chloride attack. A further consequence of this phenomenon is the absence of iron phosphates at the interface between altered rebars and surrounding matrix, as these phases are stable at higher pH (Nriagu and Dell, 1974). Moving towards the inner portions, increasingly basic hydroxylapatite precursors – octacalcium phosphate (Miller et al., 1977) and amorphous calcium phosphate ACP (Johnsson & Nancollas, 1992) – formed once their typical pH stability fields were reached. In particular, octacalcium phosphate precipitated in the intermediate layers and amorphous calcium phosphate in the inner ones. Ammonia phosphate phases, stable in alkaline systems (Taylor et al., 1963), formed in the internal portions only, where basic pH was preserved. The transformation of calcium phosphate precursors into hydroxylapatite was locally inhibited by the acidic pH and the presence of stabilizing ions in solution, such as Mg from the dissolution of dolostones and magnesium limestones (Vogel, 1986). The transformation of brushite into hydroxylapatite was only partial, and occurred by epitaxial growth on seed crystals (Koutsoukos and Nancollas, 1981), leading to a higher crystallinity of the phase (Figure 6.64 c). In the inner portions, a partial octacalcium phosphate transformation into hydroxylapatite occurred both by dissolution and reprecipitation processes (Tomazic et al., 1989) and by epitaxial growth on seed crystals (Chow & Eanes, 2001), leading to variable degrees of crystallinity of the phase. In the core, the conversion of amorphous calcium phosphate into hydroxylapatite was more effective due to the basic pH values and, according to literature data (Harries et al., 1987), it occurred by a longer range-order development process starting from the amorphous compound: this justifies the lower hydroxylapatite crystallinity in these portions. By progressive warming of concrete, due to the exposure to sun radiation, the gypsum-brushite solid solution phases underwent partial dehydration on the surfaces, with formation of concretions of partially dehydrated sulfates (bassanite, anhydrite), and crusts of anhydrous phosphates (monetite) (Figure 6.64 d). As demonstrated by the experimental study of the dehydration behavior of the solid solution, the process was highly incoherent and strictly controlled by both the chemical composition

of the phases and their crystallinity. At equal chemical composition (e.g. same relative proportions of the end-members), the dehydration process interested the low crystalline fraction of the materials only, as it is more susceptible to dehydration at temperatures below 100°C. Conversely, at equal crystallinity and varying chemical composition, the dehydration process interested the end-members and the gypsum- and brushite-rich terms of the solid solution, while terms with compositions near to the stoichiometric compound showed permanence at the hydrated state, thus being more stable.

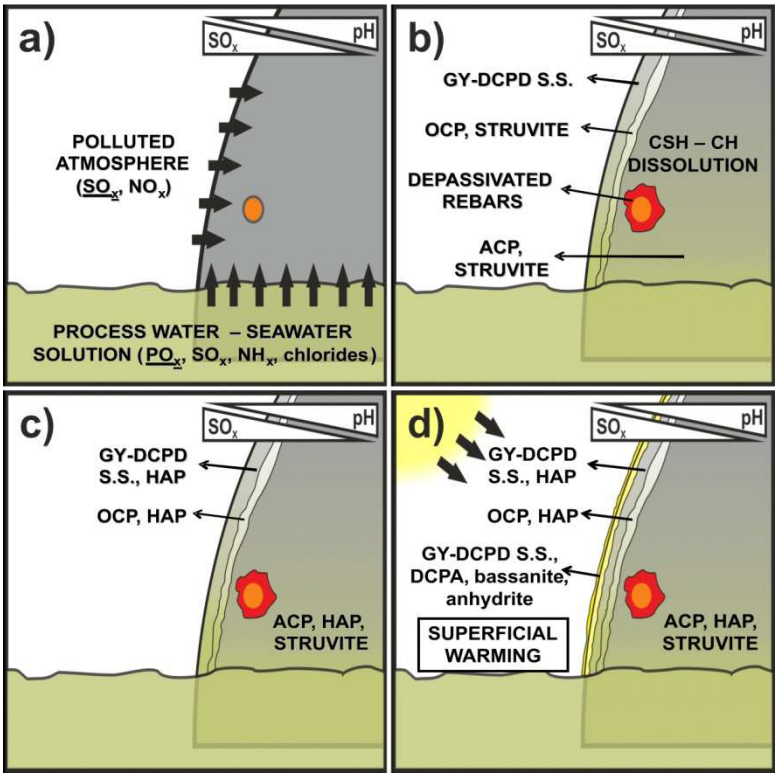

Figure 6.64. Alteration model; a) action of pollutants on concrete structures; b) first alteration phase, formation of HAP precursors; c) second alteration phase, conversion of HAP precursors; d) third alteration phase, dehydration of the solid solution.

These secondary processes were thermodynamically described with PHREEQC software (release 2.15.0), a freeware software package designed to perform low-temperature aqueous geochemical calculations (Parkhurst & Appelo, 1999). Predominance and mineral stability diagrams according to pH and concentration of reactants were calculated through simulations on several simplified pore-water compositions. Since calcium phosphates are just sparingly soluble, sulfate concentration must be much higher than phosphate to allow gypsum precipitation. Figure 6.65 shows supersaturation curves of phosphate and sulfate mineral phases as a function of pH at T = 25°C and P = 1 atm, assuming that Ca^{2+} = Mg^{2+}

and the following solution species concentrations: H_3PO_4 = 10 mmol/L, H_2SO_4 = 100 mmol/L, Ca^{2+} = Mg^{2+} = 30 mmol/L, NH_4^+ = 5 mmol/L, NaCl = 0.1M. As shown in the graph, brushite formation is favored at pH<6, while octacalcium phosphate and hydroxylapatite precipitate at higher pH values. Moreover, kinetic factors play a fundamental role in the nucleation and growth of the precursors, in particular octacalcium phosphate (Heughebaert & Nancollas, 1984), being the hydroxylapatite crystallization rate the lowest: this constitutes a limiting factor in hydroxylapatite formation inside the system. Besides the model, the hypothesis of amorphous calcium phosphate occurrence in the first phases of alteration is consistent with high pH and reagent concentration, despite the metastability of this compound (Johnsson & Nancollas, 1992). In addition, the presence of Mg in the system stabilizes amorphous calcium phosphate and brushite inhibiting hydroxylapatite and less extensively octacalcium phosphate crystallization (Salimi et al., 1985).

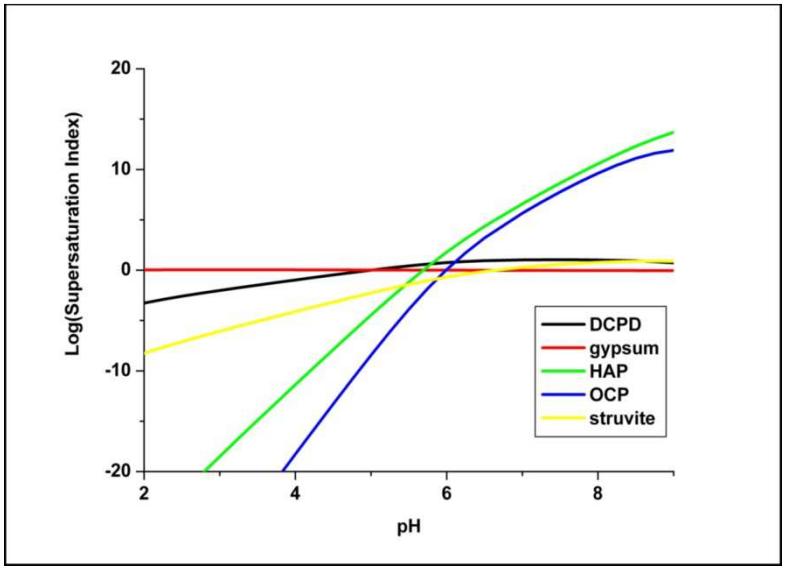

Figure 6.65. Supersaturation curves of phosphate and sulfate mineral phases as a function of pH

6.8 CONCLUSIONS

This study demonstrated that the action of multipollutants in aggressive environments caused a marked degradation of concrete structures constituting the C3 building of the Ex Agrimont area. A strong phosphate-concrete interaction was observed and verified, also thermodynamically, highlighting a form of chemical degradation not yet considered. Phosphate and sulfate attack resulted to be synergic, with formation of solid solution

phases. Moreover, heterogeneous sequences of crystallization and diffuse precipitation and permanence of apatite precursors were observed, strongly influenced by pH and concentration gradients and by the presence in pore solution of stabilizing ions like Mg. Finally, the occurrence of anhydrous calcium phosphates and sulfates in the external portions of the altered concretes was related to dehydration phenomena of the less crystalline fractions of gypsum- and brushite-rich terms of the gypsum-brushite solid solution, strongly controlled by crystal size and kinetic factors.

CONCLUSIONS

The results obtained in the framework of this research project allowed a full and quantitative characterization of the cement conglomerates constituting the structural frame of five historic buildings located in north-eastern Italy, all built between the end of the 19th and the middle of the 20th century and belonging to the first era of reinforced concrete production. Moreover, the studies allowed a detailed recognition of the conservation state of the materials, highlighting the alteration phenomena which interested the structures.

The characterization studies were performed according to an integrated multi-analytical approach, comprising both well-established analytical techniques and innovative procedures, developed on purpose. In particular, a comprehensive procedure of multiscale 2D image analysis, integrated by custom-formulated sample treatments, was conceived and applied for the first time on such polydisperse and poorly standardized materials. The results obtained allowed a precise and quantitative reconstruction of the original mix designs of the materials, overcoming, for the first time, the mere qualitative characterization of hardened concrete samples.

As regards the results obtained, the crucial importance of the mix designs' optimization procedures was clearly highlighted, showing how the project of accurate mixtures allowed reaching optimum mechanical properties also in old and low technologic concretes. On the contrary, poor mix designs, often associated with inadequate casting and homogenization procedures, were directly responsible for the low mechanical performances of more modern concretes too, causing in some cases severe structural failures (as in the case of the Ex-Zweifel Embroidery Plant). Furthermore, a low standardization of the production procedures was highlighted for the older structures, as indicated by the differences in the compositional and textural characteristics of the concretes according to the structural element and to the construction phase. As regards the concretes of the Northern Wing of the Carraresi Castle, the concretes of the first constructive phase are characterized by excellent mix design properties, namely low w/c ratios which allowed optimum mechanical properties even without cement over-dosages, and an overall good aggregate grading. The latter factor resulted particularly interesting: even though the reference Füller

& Thompson and Bolomey curves had not been formulated yet in the years of the first concrete structural elements of the building, the granulometric distributions adopted are characterized by a good approximation with the reference ones. This evidence confirms the accuracy of the still empirical Hennebique approach to the reinforced concrete construction. Despite the overall adequate properties of the materials, not strictly standardized production processes of the concrete elements were observed, as highlighted by the differences in the mix designs of the various samples analyzed. Furthermore, even though overall accurate casting procedures were adopted, difficulties related to the low viscosity of the fresh conglomerates due to the low w/c ratios caused slight segregation phenomena on the slabs, with consequent development of higher macroporosity and reduction of the mechanical properties. The concretes of the second constructive phase are characterized by less accurate mix designs, even though manufactured with higher cement dosages with respect to the Hennebique concretes. In particular, aggregate grading differs more significantly from the reference ones and w/c ratios are higher. Furthermore, casting procedures were less accurate and the production procedures were poorly standardized, as indicated by the compositional and textural differences between the concretes of the various structural elements. Surely, concrete columns were cast with a greater accuracy, as indicated by the lower overall macroporosity. This is probably related to the need of reaching better mechanical properties for these elements, due to the absence of reinforcement. Nevertheless, the result was not fully obtained, due to a significant sand over-dosage which restrained the reaching of compressive strength values higher than the ones of the slabs, characterized by higher porosity. Finally, the concretes of the third constructive phase are the ones manufactured with the best mix designs. Furthermore, casting procedures were particularly accurate, as indicated by the low degrees of macroporosity, and a higher standardization level can be observed with respect to the concretes of the other construction phases. Nevertheless, the mechanical properties obtained were not significantly higher than those of the Hennebique beams: this is mainly related to the granulometric distributions of the aggregate fractions, characterized by greater discrepancies from the reference ones with respect to the Hennebique concretes.

The low standardization procedures are even more evident in the reinforced concrete elements of the Victory Monument. High discrepancies in the adopted mix designs and in the accuracy of the casting and homogenization procedures are observable, with the concretes of the walls characterized by poor mix designs, as indicated by the low cement

dosages and by the wrong granulometric distributions of the inert fractions, reduced compactness and marked segregation phenomena. These characteristics are directly responsible for the low mechanical properties of the concretes. The concretes of the vaulted slab were manufactured with higher cement dosages and cast more accurately. Nevertheless, excessive w/c ratios and marked sand over-dosages hindered the reaching of appropriate compressive strength values. Only the concretes of the stairway are characterized by high compressive strengths, related to extremely high cement dosages, adequate w/c ratios and proper casting, compaction and homogenization procedures. Nevertheless, granulometric curves of the inert fractions strongly differ from the reference ones. All these characteristics suggest a structural conception of the walls and the vaulted slab to withstand compressive stresses only, with the poor compositional and mechanical properties counterbalanced by marked over-dimensioning, while the better mix designs and the presence of reinforcement in the concretes of the stairway indicate a more accurate structural plan for the realization of these elements, in order to optimize their flexural behavior.

The more recent buildings are characterized by a greater standardization of the compositional features of the concretes, even though differences according to the structural element are still observable, as in the case of the Ex-Zweifel Embroidery Plant. In the structure, a marked difference between the mix designs of the concrete columns, beams and riddle are observable. The former are characterized by lower cement contents, higher mix designs and less accurate aggregate grading, with consequent reaching of lower mechanical properties with respect to the concretes of the beams and the riddle. Furthermore, the concretes of the arches are characterized by very different mix design, extremely poor and inadequate. In particular, cement dosages are markedly low, w/c ratios excessive and aggregate grading totally wrong. The consequences on the microstructural and mechanical properties are the development of anomalous porosity values and the extremely poor compressive strengths.

Finally, the concretes of the C3 building of the Ex-Agrimont Area and the Ex-Foro Boario are the ones characterized by the best mix designs and, consequently, by the highest compressive strength values. Still, even though generally homogeneous, slight differences are observable in the mix designs of the various samples, indicating not strictly standardized production procedures. More in detail, variations in the granulometric distributions are observable, even though they are always comparable to the reference

ones. Furthermore, the w/c ratio resulted to be a parameter not strictly constant; the adoption of higher values was observed in several structural elements, also characterized by higher cement dosages. Consequently, it has been hypothesized that additional aliquots of water were added to the fresh pastes to reach proper workability properties, varied by the increments in viscosity caused by the introduction of higher quantities of cement in the conglomerates. These features affected the overall permeability and compressive strength values of the materials, despite being still significantly high.

As regards the conservation state of the concrete elements, the occurrence of several alteration phenomena was observed on the materials, being carbonation the most diffuse and the one responsible for the most severe damages. Furthermore, external sulfate attack interested all the structures. Nevertheless, it had a limited incidence on the overall conservation state of the structures, apart from the concrete elements of the C3 building of the Ex-Agrimont Area, struck intensely by this form of alteration due to the severe exposure to atmospheric multipollutants. In addition, the structure was also interested by chloride attack phenomena, due to its construction near the coastline and thus interested by capillary rise of saltwater through the pore network. Finally, the Victory Monument and Ex-Foro Boario were interested by alkali-related attacks, for both structures in the form of alkali-aggregate reactions, and for the former also in the form of alkaline salts crystallization.

Amongst the triggering factors for the alteration phenomena, compositional and textural characteristics of the materials resulted to be of crucial importance: the adoption of wrong mix designs and poor concrete casting procedures caused anomalous development and progression of alterative processes in several structural elements. On the contrary, the protection of concrete elements with superficial sacrificial layers contributed significantly to the better static and aesthetic conservation of the buildings. Furthermore, the construction of the buildings in areas characterized by unfavorable environmental exposure caused in some cases rapid and intense degradation of the concrete elements, as in the case of the Victory Monument, exposed to massive water percolations and relative humidity variations, and of the C3 building of the Ex-Agrimont Area, exposed to severe environmental and soil pollution related to the industrial activities of Porto Marghera. The extreme exposure conditions of the latter structure caused the development of a combined and previously undescribed form of alteration, defined as synergic sulfate-phosphate attack. The alteration process caused severe decalcification of the cement matrix and

formation of secondary sulfates and phosphates according to a marked mineralogical and textural zoning: I) gypsum-brushite solid solution, bassanite, anhydrite and ardealite-like phases in the superficial efflorescence; II) monetite in the superficial crusts; III) gypsum-brushite solid solution and ardealite-like phases in the external strata; IV) octacalcium phosphate and struvite in the intermediate layers; V) apatite and struvite in the inner altered portions. The heterogeneous microstructural development of secondary phases was interpreted taking into account the different sources of sulfate and phosphate pollutants. Moreover, the permanence of apatite acidic precursors in the external strata suggests that these portions were exposed to high acidity conditions, related to sulfuric acid formation in the pore water after reaction with sulfur dioxide, while the presence of anhydrous calcium sulfates and phosphates suggests a progressive dehydration, possibly by solar radiation warming, of the solid solution end-members and of the gypsum and brushite-rich terms.

The analytical results obtained resulted to be of crucial importance for the restoration and rehabilitation procedures which interest four of the five historic buildings, allowing the reaching of a proper level of knowledge on the structures, not only from the mechanical point of view, and facilitating the planning and performing of proper interventions with adequate restoration materials. Conversely, the studies did not allow to preserve the Ex-Zweifel Embroidery Plant from the demolition; as previously seen, the analytical results confirmed the irreparable compositional, textural and mechanical deficits of the load-bearing arches, the main causes, apart from verified human responsibilities, of the severe structural failure occurred in 2008. In this respect, the multi-analytical approach adopted, in particular the newly-developed multiscale image analysis procedure, resulted particularly effective for a quantitative evaluation of the characteristics of the structural elements, proving its full applicability for the assessment of the characteristics of pre-existing concrete structures. The analytical protocol, even though tested on historical materials, is fully applicable to modern concretes, extending its possible applications also in the fields of the modern construction technology.

REFERENCES

AA. VV. (1963). *Rock-color chart by National Research Council*. Geological Society of America Editions, New York (USA).

AA. VV. (2011). *ENVI user's guide, Version 4.77.*

Abrams, D.A. (1918). *Design of concrete mixtures*. Bulletin 1, Structural Materials Research Laboratory, Lewis Institute, Chicago.

Al-Amoudi, O.S.B., Maslehuddin, M. & Saadi, M.M. (1995). *Effect of magnesium sulfate and sodium sulfate on the durability performance of plain and blended cements*. ACI Mater J, 92, 15-24.

Andronico, D. & Lo Castro, M.D. (2008). *Operazioni di base per la misura della distribuzione granulometrica di particelle vulcaniche tramite il CAMSIZER.* Rapporti tecnici INGV, 79.

Appa Rao, G. (2001). *Generalization of Abrams' law for cement mortars*. Cement and Concrete Research, 31, 495, 502.

ASTM C33 (2003). *Standard Specification for Concrete Aggregates.* ASTM, Bridgeport (USA).

ASTM C457 (1998). *Standard Test Method for Microscopical Determination of Parameters of the Air-void System in Hardened Concrete.* ASTM, Bridgeport (USA).

ASTM C856 (2004). *Standard practice for Petrographic Examination of Hardened Concrete.* ASTM, Bridgeport (USA).

Barbisan, U. & Guardini, M. (2007). *Reinforced Concrete: A short History.* Tecnologos, Mantova (IT).

Bensted, J. & Barnes, P. (2002), *Structure and performance of cements*. Spon Press, New York (USA).

Berke, N.S. (2006). *Corrosion of Reinforcing Steel.* In: Lamond, J. F. & Pielert, J. H. (Eds.), Significance of Tests and Properties of Concrete and Concrete-Making Materials, ASTM, Bridgeport (USA).

Bertolini, L. & Pedeferri, P. (2000). *La durabilità del calcestruzzo armato.* Mc Graw-Hill, Milano (IT).

Bolomey, J. (1935). *Granulation et prevision de la resistance probable des betons*. Travaux, 19, 228-232.

Bozzo, G.P., Ragazzi, F., Vinci, I., Garlato, A., Giandon, P. & Mozzi, P. (2005). *Carta dei suoli del bacino scolante in laguna di Venezia*. ARPA, Venezia (IT).

Bressan, E. (1986). *Il castello di Padova*. Canova, Treviso (IT).

Brondi, A. (1973). *Commento al foglio geologico 027, Bolzano, 1:50000.* Studi Trentini di Scienze Naturali, rivista Museo Tridentino di Scienze Naturali, 53, 6A.

Brondi, A. (1973). *Note esplicative della Carta Geologica D'Italia, Foglio 027 Bolzano alla scala 1:50000.* Nuova Tecnica Grafica, Roma (IT).

Bullard, J.W., Jennings, H.M., Livingston, R.A., Nonat, A., Scherer, G.W., Schweitzer, J.S., Scrivener, K.L. & Thomas, J.J. (2010). *Mechanisms of cement hydration*. Cement and Concrete Research, 41(12), 1208-1223.

Carmichael, R.S. (1984). *CRC handbook of physical properties of rocks*. CRC Press Inc., Boca Raton (USA).

Castagnetti, G. (1998). *Il Ricamificio: la storia*. Verona (IT).

Chinchón, S., García, J., López-Atalaya, M., Linares, A. & Vera, R. (2004). *Cement paste colouring in concretes.* Cement and Concrete Research, 34, 1987-1991.

Chinello, C. (1975). *Storia di uno sviluppo capitalistico: Porto Marghera e Venezia 1951-1973*. Editori Riuniti, Roma (IT).

Chow, L.C. & Eanes, E.D. (2001). *Octacalcium phosphate*. Karger Publishers, Basel (CH).

Collepardi, M. (2003). *A State-of-the Art Review on Delayed Ettringite Attack on Concrete*. Cement and Concrete Composites, 25, 401–407.

Collepardi, M., Collepardi, S., Ogoumah Olagot, J.J., Simonelli, F. & Troli R. (2005). *Il calcestruzzo vulnerabile: prevenzione, diagnosi del degrado e restauro*. Enco S.r.l., Treviso (IT).

Collepardi, M., Collepardi, S., Troli, R. (2008). *Mix design del calcestruzzo*. Enco S.r.l., Treviso (IT).

Crosato, A. (2010). *Indagini ed analisi strutturali per l'aggiornamento sismico dell'ex Foro Boario di Padova*. M.Sc. thesis, Università degli Studi di Padova, Facoltà di Ingegneria, Dipartimento di Architettura, Urbanistica e Rilevamento, Padova (IT).

Daimon, M. & Roy, D.M. (1978). *Rheological properties of cement mixes: I. Methods, preliminary experiments, and adsorption studies.* Cement and Concrete Research, 8(6), 753-764.

Dal Cin, R. (1967). *Le ghiaie del Piave. Morfometria, granulometria, disposizione e natura dei ciottoli*. Memorie del Museo Tridentino di Scienze Naturali, 16(3), 121-293.

De Rose, A. S. (1995). *Marcello Piacentini. Opere (1903-1926).* Panini, Modena (IT).

Doyle, J.D & Parsons, S.A. (2002). *Struvite formation, control and recovery*. Water Research, 36, 3925–3940.

Erko, A., Schäfers, F., Firsov, A., Peatman, W.B., Eberhardt, W. & Signorato, R. (2004). *The BESSY X-ray microfocus beamline project*. Spectrochimica Acta Part B, 59, 1543-1548.

Fernández, L.L. (2008). *Aplicación de tinciones selectivas en la caracterización y cuantificación de cemento*. Ph.D. thesis, Escuela Politecnica Superior, Departimento de Costruciones Arquitectonicas, Universidad de Alicante (ES).

Ferreira, T. A. & Rasband, W. (2010). *The image J user guide, Version 1.43.*

Fontanive, F. (1974). *I materiali da costruzione delle conoidi del Brenta e dell'Astico: caratteristiche tecniche e litologiche delle ghiaie in coltivazione*. CNR, Laboratorio di Geologia Applicata, Padova (IT).

Füller, W.B. & Thompson, S.E. (1907). *The laws of proportioning concrete*. Transactions of ASCE, 59, 67-143.

Gartner, E.M., Young, J.F., Damidot, D.A. & Jawed, I. (2002). *Hydration of Portland cement*. In: Bensted, J. & Barnes, P. (Eds.), Structure and performance of cements, Spon Press, New York (USA).

Gentile, E. (2007). *Fascismo di Pietra*. Laterza, Roma (IT).

Georgali, B. & Tsakiridis, P.E. (2005). *Microstructure of fire-damaged concrete. A case study*. Cement & Concrete composites, 27, 255-259.

Gorner, W., Hentschel, M.P., Müller, B.R., Riesemeier, H., Krumrey, M., Ulm, G., Diete, W., Klein, U. & Frahm, R. (2001). *BAMline: the first hard X-ray beamline at BESSY II*. Nuclear Instruments and Methods in Physics Research A, 467–468, 703–706.

Harries, J. E., Hukins, D.W.L., Holt, C. & Hasnain, S.S. (1987). *Conversion of Amorphous Calcium Phosphate into Hydroxyapatite*. Journal of Crystal Growth, 84, 563-570.

Harris, A.W. (2001). *Testing of models of the dissolution of cements—leaching of synthetic CSH gels.* Cement and Concrete Research, 32, 267-271.

Heughebaert, J. C. & Nancollas, G. H. (1984). *Kinetics of Crystallization of Octacalcium Phosphate*. Journal of Physical Chemistry, 88, 2478-2481.

Hewlett, P. C. (2007). *Lea's chemistry of cement and concrete.* Elsevier, Amsterdam (NL).

Ingham, J. (2011). *Geomaterials under the microscope.* Manson Publishing, London (UK).

Irassar, E.F., Bonavetti, V.L. & Gonzáles, M. (2003). *Microstructural study of sulfate attack on ordinary and limestone Portland cements at ambient temperature.* Cement and Concrete Research, 33, 31-41.

Jakobsen, U.H. & Brown, D.R. (2006), *Reproducibility of w/c ratio determination from fluorescent impregnated thin sections.* Cement and Concrete Research, 36, 1567-1573.

Johnsson, M.S.A. & Nancollas, G.H. (1992). *The Role of Brushite and Octacalcium Phosphate in Apatite Formation*. Critical Reviews in Oral Biology & Medicine, 3(1/2), 61-82.

Korpa, A. & Trettin, R. (2006). *The influence of different drying methods on cement paste microstructures as reflected by gas adsorption: Comparison between freeze-drying (F-drying), D-drying, P-drying and oven-drying methods*. Cement and Concrete Research, 36, 634, 649.

Koutsoukos, P. G. & Nancollas, G.H. (1981). *Crystal Growth of Calcium Phosphates. Epitaxial Considerations.* Journal of Crystal Growth, 53, 10-19.

Landini, G. (2011). *The Threshold Color Plugin for ImageJ*.

Linares, L., López-Atalaya, M. & Chinchón, S. (2009). *Cement content determination through selective stain in hardened concrete.* Cement and Concrete Research, 39, 1105-1109.

López-Buendía, A.M., Climent, V. & Verdù, P. (2006). *Lithological influence of aggregate in the alkali-carbonate reaction.* Cement and Concrete Research, 36, 1490-1500.

Lupano, M. (1991). *Gli architetti: Marcello Piacentini*. Laterza, Roma (IT).

Lutterotti, L., Matthies, S. & Wenk, H.R. (1999). *MAUD: a friendly Java program for material analysis using diffraction*. IUCr: Newsletter of the CPD, 21, 14--15.

Marinoni, N., Pellizon Birelli, M., Rostagno, C. & Pavese, A. (2003). *The effects of atmospheric multipollutants on modern concrete.* Atmospheric Environment, 37, 4701-4712.

Massidda, L. (2005). *Analisi delle cause di degrado del calcestruzzo e delle opere in calcestruzzo armato.* Informazione, 103, 6-10.

Matschei, T., Lothenbach, B. & Glasser, F.P. (2007). *The AFm phase in Portland cement.* Cement and Concrete Research, 37, 118-130.

Maynard, D. P. & Weller, D. E. (1970). *Influence of Materials and Mix Design on the Skid Resistance Value and Texture Depth of Concrete.* Report No. LR 334, British Road Research Laboratory, London (UK).

McIntosh, A.O. & Jablonski, W.L. (1956). *X-Ray Diffraction Powder Patterns of the Calcium Phosphates*. Analytical Chemistry, 28(9), 1424, 1427.

Mei, C. (2003). *The Watershed Algorithm for ImageJ*.

Moudgil, B.M., 2010. *Phosphate Primer* [on-line]. Florida Institute of Phosphate Research. On: http://www1.fipr.state.fl.us/PhosphatePrimer [Accessed 20 October 2010].

Naus, D.J., Dole, L.R. & Mattus, C.H. (2006). *Laboratory Investigation on Effect of Phosphate Ions on Concrete*. Report to the US NRC, Oak Ridge National Laboratory, Oak Ridge, TN.

Nelva, R. & Signorelli, B. (1990). *Avvento ed evoluzione del calcestruzzo armato in Italia: il sistema Hennebique.* Edizioni di Scienza e Tecnica, Milano (IT).

Neville, A. (2004), *The confused world of sulfate attack on concrete.* Cement and Concrete Research, 34, 1275-1296.

Nicoloso, P. (2008). *Mussolini Architetto, Propaganda e paesaggio urbano nell'Italia fascista.* Einaudi, Torino (IT).

Nriagu, J. O. & Dell, C. I. (1974). *Diagenetic formation of iron phosphates in recent lake sediments*. American Mineralogist, 59, 934–46.

Ozol, M.A. (2006). *Alkali-Carbonate Rock Reaction.* In: Lamond, J. F. & Pielert, J. H. (Eds.), Significance of Tests and Properties of Concrete and Concrete-Making Materials, ASTM, Bridgeport (USA).

Parkhurst, D.L. & Appelo, C.A.J. (1999). *User's guide to PHREEQC (version 2) – A computer program for speciation, reaction-path, 1D-transport, and inverse geochemical calculations*. US Geological Survey Water-Resources Investigations Report, 99-4259, 1-312.

Pecchioni, E., Fratini, F. & Cantisani, E. (2008). *Le malte antiche e moderne tra tradizione e innovazione*. Patron, Bologna (IT).

Plank, J., Pöllmann, K., Zouaoui, N., Andres, P.R. & Schaefer, C. (2008). *Synthesis and performance of methacrylic ester-based polycarboxylate superplasticizers possessing hydroxy-terminated poly(ethylene glycol) side chains*. Cement and Concrete Research, 38, 1210-1216.

Peterson, K., Gress, D., Van Dam, T. & Lawrence, S. (2006). *Crystallized alkali-silica gel in concrete from the late 1890s.* Cement and Concrete Research, 36, 1523-1532.

Peterson, K.W. (2008). *Automated air-void system characterization of hardened concrete: helping computers to count air-voids like people count air-voids – methods for flatbed scanner calibration*. Ph.D. thesis, Michigan Technological University, Houghton (USA).

Piacentini, M. (1929). *Di alcune particolarità del Monumento alla Vittoria in Bolzano.* Architettura e Arti Decorative, 6, 255-263.

Pinto, A. J., Jimenez, A. & Prieto M. (2008). *Thermodynamics of the Gypsum-Brushite-H_2O System*. Revista de la Sociedad Española de Mineralogía, 9, 193-194.

Rear, K. (1994). *Alkali-Aggregate Reactivity, A Summary.* PCI, Committee on Durability.

Richards, J.A. (1999). *Remote Sensing Digital Image Analysis*. Springer-Verlag, Berlin (DE).

Rinaudo, C., Lanfranco, A.M. & Franchini-Angela, M. (1994). *The system $CaHPO_4 \cdot 2H_2O$-$CaSO_4 \cdot 2H_2O$: crystallization from calcium phosphate solutions in the presence of SO_4^{2-}*. Journal of Crystal Growth, 142, 184-192.

Saccomani, G. (1970). *Nuovo Foro Boario della città di Padova.* Tipolitografia Faggionato, Montebelluna (IT).

Salimi, M.H., Heughebaert J. C. & Nancollas, G. H. (1985). *Crystal Growth of Calcium Phosphate in The Presence of Magnesium Ions*. Langmuir, 1, 19-122.

Schön, J.H. (1996). *Physical properties of rocks - Fundamentals and principles of petrophysics*. Pergamon, Oxford (UK).

Skalny, J.P., Odler, I. & Marchand, J. (2001). *Sulfate Attack on Concrete*. Spon Press, New York (USA).

Soler, J.M. (2007). *Thermodynamic Description of the Solubility of C-S-H Gels in Hydrated Portland Cement - Literature Review*. Working Report 2007-88.

Soragni, U. (1993). *Il Monumento alla Vittoria di Bolzano, Architettura e Scultura per la città italiana (1926-1938).* Neri Pozza Editore, Vicenza (IT).

Soroushian, P., Elzafraney, M., Nossoni, A. (2003). *Specimen preparation and image processing and analysis techniques for automated quantification of concrete microcracks and voids*. Cement and Concrete Research, 33, 1949-1962.

St John, D.A, Poole, A.B. & Sims, I. (1998). *Concrete Petrography, A handbook of investigative techniques.* Arnold, London (UK).

Stark, D. (2006). *Alkali-Silica Reactions in Concrete*. In: Lamond, J. F. & Pielert, J. H. (Eds.), Significance of Tests and Properties of Concrete and Concrete-Making Materials, ASTM, Bridgeport (USA).

Stefanini, S. (1977). *Le ghiaie nel sottosuolo della pianura veneta ad oriente del fiume Piave*. Istituto Ricerche sulle Acque, Roma (IT).

Strydom, C.A., Hudson-Lamb, D.L., Potgieter, J.H. & Dagg, E. (1995). *The thermal dehydration of synthetic gypsum*. Thermochimica Acta, 269/270, 631-638.

Stutzman, P. (2004). *Scanning electron microscopy imaging of hydraulic cement microstructure*. Cement and Concrete Composites, 26, 957-966.

Stutzman, P. (2009). *Image Processing and Analysis for Quantitative Cement and Clinker Characterization.* NIST - Construction Materials Division.

Stutzman, P. (2009). *Specimen Preparation for Scanning Electron Microscopy and X-ray Imaging.* NIST - Construction Materials Division.

Sutter, L.L. (2007). *Procedure for Using a Flat-Bed Scanner for Performing ASTM C457*. Michigan Tech Transportation Institute, Michigan Technological University, Houghton (USA).

Szoke, S.S. (2006). *Resistance to Fire and High Temperatures*. In: Lamond, J. F. & Pielert, J. H. (Eds.), Significance of Tests and Properties of Concrete and Concrete-Making Materials, ASTM, Bridgeport (USA).

Taylor, A.W., Frazier, A.W., Gurney, E.L. & Smith, J.P. (1963). *Solubility products of di- and trimagnesium ammonium and dissociation of magnesium phosphate solutions*. Transaction of the Faraday Society Articles, 59, 1585–1589.

Taylor, H.F.W. (1990). *Cement Chemistry.* Academic Press, London (UK).

Thaulow, N. & Sahu, S. (2004). *Mechanism of concrete deterioration due to salt crystallization*. Materials Characterization, 53, 123-127.

Tomazic, B. B., Tung, M.S., Gregory, T.M. & Brown, W.E. (1989). *Mechanism of Hydrolysis of Octacalcium Phosphate*. SEM (Scanning Electron Microscopy), 3, 119-127.

Tomiato, L. & Zanardini, A. (2005). *Rapporto ambientale d'area di Porto Marghera: bilancio ambientale 1998-2004*. ARPA, Venezia (IT).

Traettino, E. (2005). *Il degrado del cemento armato: Dinamiche, recupero e prevenzione.* Ph.D. thesis, Scuola di Dottorato di Ricerca in Ingegneria delle Costruzioni, Ciclo XVIII, Università degli Studi Federico II, Napoli (IT).

Tsui, N., Flatt, R.J. & Scherer, G.W. (2003). *Crystallization damage by sodium sulphate.* Journal of Cultural Heritage, 4, 109-115.

Tulliani, J.M., Montanaro, L., Negro, A. & Collepardi M. (2002). *Sulfate attack of concrete building foundations induced by sewage waters.* Cement and Concrete Research, 32, 843-849.

UNI 11176 (2006). *Descrizione petrografica di una malta*. UNI, Milano (IT).

UNI 8520-1 (1999). Aggregati per confezione di calcestruzzi: Definizione, classificazione e caratteristiche. UNI, Milano (IT).

UNI EN 12504-2 (2001). Prove sul calcestruzzo nelle strutture - Prove non distruttive - Determinazione dell'indice sclerometrico. UNI, Milano (IT).

UNI EN 197-1 (2007). *Cemento - Parte 1: Composizione, specificazioni e criteri di conformità per cementi comuni*. UNI, Milano (IT).

UNI EN 933-1 (1999). Prove per determinare le caratteristiche geometriche degli aggregati, Determinazione della distribuzione granulometrica, Analisi granulometrica per stacciatura. UNI, Milano (IT).

UNI-EN 12390-1 (2002). Prova sul calcestruzzo indurito - Forma, dimensioni ed altri requisiti per provini e per casseforme. UNI, Milano (IT).

UNI-EN 12390-3 (2009). Prova sul calcestruzzo indurito - Resistenza alla compressione dei provini. UNI, Milano (IT).

Walker, H. N. (1992). *Petrographic methods of examining hardened concrete: a petrographic manual*. VTRC, Virginia (USA).

Whitaker, A. & Jeffery, J.W (1970). *The crystal structure of Struvite, $MgNH_4PO_4 \cdot 6H_2O$*. Acta Crystallographica Section B, 26, 1429, 1440.

Zingg, A., Winnefeld, F., Holzer, L., Pakusch, J., Becker, S., Figi, R. & Gauckler, L. (2009). *Interaction of polycarboxylate-based superplasticizers with cements containing different C3A amounts*. Cement and Concrete Composites, 31, 153-162.

Zivica, V. & Bajza, A. (2001). *Acidic attack of cement based materials – a review. Part 1. Principle of acidic attack.* Construction and Building Materials, 15, 331-340.

Zivica, V. & Bajza, A. (2002). *Acidic attack of cement based materials – a review. Part 2. Factors of rate of acidic attack and protective measures.* Construction and Building Materials, 16, 215-222.

ACKNOWLEDGEMENTS

This research project was financially supported by Mapei S.p.A. in the frame of its research agreement with the Inter-Departmental Research Center for the Study of Cement Materials and Hydraulic Binders (CIRCe) of the University of Padova. Mapei S.p.A. is acknowledged also for providing materials and facilities for many experiments during these three years.

I would like to thank the Departments of Cultural Heritage of Padova and Verona, the Municipality of Padova and La Immobiliare Veneziana S.r.l. for the helpful collaboration given for the execution of the characterization studies on the historic buildings of their competence.

All preliminary surveys, on-site tests, sampling operations and compressive strength tests were experimentally and instrumentally supported by the Structural and Transportation Engineering Department (DCT) of the University of Padova. I would like to thank all the Structural Engineering research group and all the staff of the Construction Materials Experimental Laboratory for their precious collaboration during these three years of work.

The synchrotron experimental sessions were supported by the German Federal Institute for Materials Research and Testing (BAM), VII.1 (Building Materials) division. All BAM working group, especially Moritz-Caspar Schlegel, is deeply acknowledged for its scientific contribution to this project.

Prof. Giuseppe Cruciani of the Department of Earth Sciences, University of Ferrara, is acknowledged for the execution of the thermal analyses on the studied materials.

A great acknowledgement goes to Dr. Giulio Isacco Lampronti for his fundamental contribution to the experimental study of the dehydration behavior of the gypsum-brushite solid solution and for the formulation of the thermodinamic model of the combined sulfate-phosphate attack. Dr. Lampronti is also deeply acknowledged, together with Dr. Lara Maritan, for their contribution to the theoretical and experimental characterization of this novel form of concrete degrade.

Acknowledgements are given to the staff of the Department of Geosciences of the University of Padova and of the Institute of Geosciences and Georesources of the National

Research Council (IGG-CNR), Padova branch, for their useful suggestions and their analytical support.

I would like to thank all the members of the CIRCe center at the Department of Geosciences - dr. Chiara Dalconi, Marco Favero, dr. Matteo Parisatto, dr. Luca Valentini and dr. Marco Voltolini - for their precious suggestions which allowed to enrich the scientific background of this research project, and the CIRCe secretary, Barbara Vianello, for her fundamental help on the execution of all the administrative and bureaucratic activities related to my research projects.

Finally, the biggest acknowledgements go to my supervisors, Prof. Gilberto Artioli and Prof. Claudio Mazzoli, for their useful reviews of this thesis and of all my previous publications, but especially for having given me the opportunity to investigate this extremely interesting research topic, sharing their scientific enthusiasm with me during my PhD and favoring my growth as a scientist and researcher.

RINGRAZIAMENTI

Al termine del mio (lunghissimo) periodo di formazione, desidero ringraziare profondamente le persone che al di fuori del mondo universitario hanno contribuito in maniera fondamentale, sia direttamente che indirettamente, al raggiungimento di questo mio traguardo.

Prima di tutto desidero ringraziare i miei genitori, Silveria e Gianfranco, per avermi sostenuto finanziariamente ma soprattutto moralmente lungo tutto il mio percorso di formazione universitaria e per avermi fatto capire che investire tempo e soldi nell'approfondire ed ampliare il proprio bagaglio culturale è sempre una scelta vincente. Inoltre voglio ringraziarli per avermi fatto crescere in questa famiglia bellissima, attorniato dai miei tre fratelli - Federico, Maria e Lorenzo - i quali sono stati altrettanto fondamentali, con i loro consigli ma anche con le loro critiche costruttive, nell'aiutarmi a portare avanti questo lungo e gratificante percorso formativo. Sicuramente senza il supporto di una famiglia così straordinaria non sarei qui in questo momento, quindi grazie ancora con tutto il cuore.

Desidero inoltre ringraziare i miei amici più cari nonché compagni di band - Berto, Denis e Gigi - perché sapere di poter contare su delle persone fidate con cui ci si diverte a prescindere è di aiuto fondamentale per affrontare con serenità anche le sfide professionali più impegnative.

Infine, come per le due precedenti, anche le ultime parole di questa tesi sono tutte per Fra, innanzitutto perché se ce l'ho fatta a scrivere una tesi in inglese è gran parte merito del suo training linguistico intensivo! Senza contare il fatto che le è toccato sorbirsi 300 pagine di revisione tesi, più tutti i vari paper ed abstract che mi ha revisionato in questi anni (per non dimenticare permanenze più o meno forzate a congressi e workshop...insomma se avete bisogno di un'interprete esperta di calcestruzzi e materiali da costruzione vi posso consigliare la migliore nel campo!). Ma questa non è che una delle infinite dimostrazioni di quanto straordinaria sia questa persona, il mio autentico faro negli ultimi sette anni di vita, sempre al mio fianco anche nei periodi (e sono stati tanti!) in cui era veramente difficile sopportarmi. Se sono sempre riuscito ad andare avanti per la mia strada, superando

difficoltà ed imprevisti, è in gran parte grazie al suo ottimismo e alla sua capacità di guardare sempre il bicchiere mezzo pieno, e per questo gliene sarò eternamente grato...e anche per questo so per certo che nel mio futuro non può che esserci lei.

You are my sunshine, my only sunshine...